



UNIVERSITY OF GENOVA  
PHDPROGRAM IN BIOENGINEERING AND ROBOTICS

# **Towards human-relevant preclinical models: fluid-dynamics and three-dimensionality as key elements**

Arianna Fedi

Thesis submitted for the degree of *Doctor of Philosophy* (35° cycle)

March 2023

Marco Massimo Fato  
Silvia Scaglione  
Paolo Massobrio

Supervisors

Head of the PhD program

*Thesis Jury:*

Bruno Sarmento, *Universidade do Porto*  
Riccardo Gottardi, *University of Pennsylvania*

External examiner

External examiner

**Dibris**

Department of Informatics, Bioengineering, Robotics and Systems Engineering

## **Declaration**

I hereby declare that except where specific reference is made to the work of others, the contents of this dissertation are original and have not been submitted in whole or in part for consideration for any other degree or qualification in this, or any other university. This dissertation is my own work and contains nothing which is the outcome of work done in collaboration with others, except as specified in the text and Acknowledgements. This dissertation contains fewer than 65,000 words including appendices, bibliography, footnotes, tables and equations and has fewer than 150 figures.

Arianna Fedi

March 2023

# Acknowledgements

...

## Abstract

The activity of research of this thesis focuses on the relevance that appropriate *in vitro* fully humanized models replicating physiological microenvironments and cues (e.g., mechanical and fluidic) are essential for improving human biology knowledge and boosting new compound testing.

In biomedical research, the high percentage of the low rate of successful translation from bench to bedside failure is often attributed to the inability of preclinical models in generating reliable results. Indeed, it is well known that 2D models are far from being representative of human complexity and, on the other side, although animal tests are currently required by regulatory organizations, they are commonly considered unpredictable. As a matter of fact, there is a growing awareness that 3D human tissue models and fluid-dynamic scenarios are better reproducers of the *in vivo* context.

Therefore, during this PhD, I have worked to model and validate technologically advanced fluidic platforms, where to replicate biological processes in a systemic and dynamic environment to better assess the pharmacokinetics and the pharmacodynamics of drug candidates, by considering different case studies. First, skin absorption assays have been performed accordingly to the OECD Test Guidelines 428 comparing the standard diffusive chamber (Franz Diffusion Cell) to a novel fluidic commercially available organ on chip platform (MIVO), demonstrating the importance of emulating physiological fluid flows beneath the skin to obtain *in vivo*-like transdermal penetration kinetics. On the other hand, after an extensive research analysis of the currently available intestinal models, which resulted insufficient in reproducing chemicals and food absorption profiles *in vivo*, a mathematical model of the intestinal epithelium as a novel screening strategy has been developed.

Moreover, since less than 8% of new anticancer drugs are successfully translated from preclinical to clinical trials, breast, and ovarian cancer, which are among the 5 most common causes of death in women, and neuroblastoma, which has one of the lowest survival rates of all pediatric cancers, have been considered. For each, I developed and optimized 3D ECM-like tumor models, then cultured them under fluid-dynamic conditions (previously predicted by CFD simulations) by adopting different (customized or commercially available) fluidic platforms that allowed to mimic  $u$  stimuli (fluid velocity and the fluid flow-induced shear stress) and investigate their impact on tumor cells viability and drug response. I provided evidence that such an approach is pivotal to clinically reproduce the complexity and dynamics of the cancer phenomenon (onset, progression, and metastasis) as well as to develop and validate traditional (i.e., platin-based drugs, caffeine active molecule) or novel treatment strategies (i.e., hydroxyapatite nanoparticles, NK cells-based immunotherapies).

# Table of Contents

## Sommario

<b>Section One</b> .....	1
State of the art .....	11
Innovation: Scientific and Technological Objectives .....	15
References .....	16
<b>Section Two</b> .....	19
Comparison Between Franz Diffusion Cell and a novel Micro-physiological System for In Vitro Penetration Assay Using Different Skin Models .....	20
3.1 Abstract.....	20
3.2 Introduction .....	20
3.3 Materials and Methods .....	22
3.4 Results .....	25
3.5 Discussion .....	30
3.6 References .....	33
3.7 Acknowledgments.....	35
<i>In vitro</i> models replicating the human intestinal epithelium for absorption and metabolism studies: A systematic review .....	36
4.1 Abstract.....	36
4.2 Introduction .....	36
4.3 Physiology of the GIT .....	38
4.4 2D in vitro models to evaluate intestinal absorption .....	40
4.5 3D cellular models .....	50
4.6 Mathematical modelling of absorption at the intestinal wall .....	59
4.7 Discussion .....	64
4.8 References .....	67
4.9 Acknowledgements .....	81
3D Perfusable Hydrogel Recapitulating the Cancer Dynamic Environment to in Vitro Investigate Metastatic Colonization .....	82
5.1 Abstract.....	82
5.2 Introduction .....	82
5.3 Materials and Methods .....	84
5.4 Results.....	89
5.5 Discussion .....	95
5.6 References .....	97
5.7 Acknowledgements .....	100
High blood flow shear stress values are associated with circulating tumor cells cluster disaggregation in a multi-channel microfluidic device .....	101
6.2 Abstract.....	101
6.3 Introduction .....	101
6.4 Materials and Methods .....	102
6.5 Results.....	106
6.6 Discussion .....	111
6.7 References .....	114
6.8 Acknowledgments.....	116
A multi-organ-on-chip to recapitulate the infiltration and the cytotoxic activity of circulating NK cells in 3D matrix-based tumor model .....	117
7.1 Abstract.....	117
7.2 Introduction .....	117
7.3 Materials and Methods .....	119
7.4 Results.....	122

7.5	Discussion .....	129
7.6	References .....	132
7.7	Acknowledgments.....	135
A Human Ovarian Tumor & Liver Organ-on-Chip for Simultaneous and More Predictive Toxo- Efficacy Assays.....		136
8.1	Abstract.....	136
8.2	Introduction .....	136
8.3	Materials and Methods .....	138
8.4	Results.....	140
8.5	Discussion .....	148
8.6	References .....	150
8.7	Acknowledgments.....	152
<b>Section Three</b> .....		<b>154</b>
Conclusions .....		157
PhD Achievements .....		160
10.1	List of publications.....	160
10.2	Participation to National and International Conferences.....	160
10.3	Collaboration to funded projects .....	161

# **Part I**

## **Section One**

# Chapter 1

## State of the art

In the medical and pharma research, there is an urgent challenge related to the evident and rising low rate of successful translation from bench to bedside (90% early clinical trials fail and of those that arrive to phase III only half passes to the clinical use) [3].

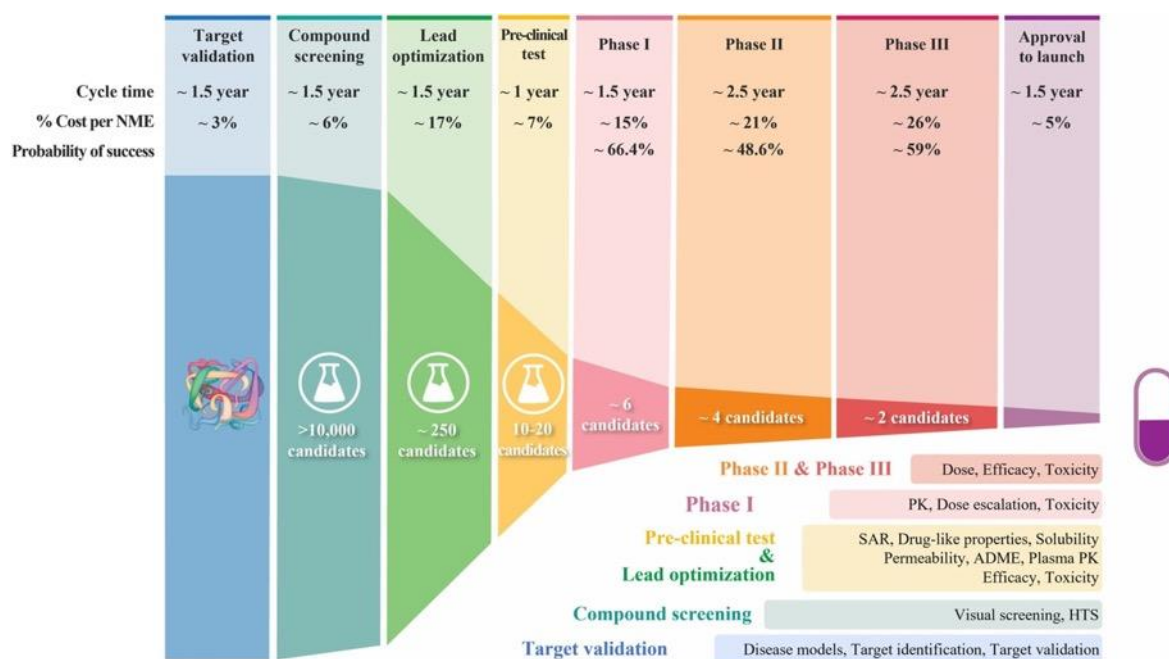


Figure 1: The process of drug discovery and development and the failure rate at each step scaled.

The highest percentage of this failure is related to lack of clinical efficacy and unmanageable organ toxicity, often attributed to the inability of preclinical models in generating results of human relevance [4].



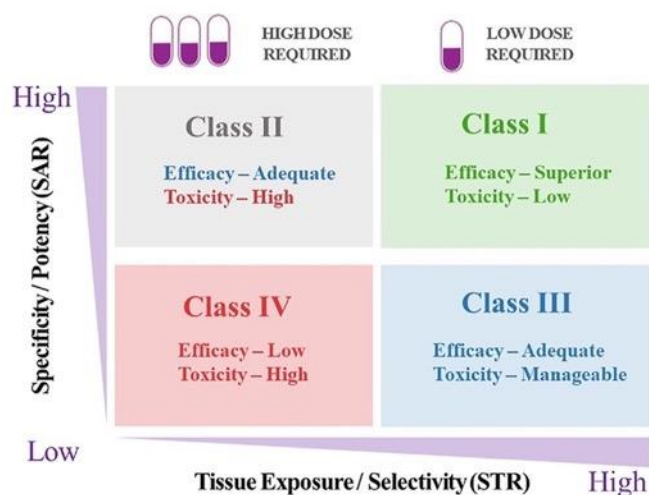


Figure 2: Structure-tissue exposure/selectivity–activity-relationship (STAR) selects drug candidates and balances clinical dose/efficacy/toxicity.

Moreover, the inaccurate prediction of dynamic responses of multiple organs to the testing compound hampers the development of new therapies.

Conventionally, the pre-clinical development of new drugs is mainly carried out through in vitro tests and trials on animals.

Indeed, it is well known that 2D models are far from being representative of human complexity [5]. For many years, 2D cell monolayers grown on flat surfaces have been widely used for in vitro screening and drug testing. These systems are affordable, simple, and offer standardized ways to reproduce biological processes and study (patho)physiological mechanisms [6]. However, 2D platforms have some major drawbacks due to the lack of 3D tissue-specific spatial features, which leads to incomplete or altered cell-to-cell and cell-to-matrix interactions, as well as tissue-specific biomechanical and biochemical cues. These deficiencies can affect normal cell proliferation, differentiation, gene and protein expression, and response to pharmacological treatments [7]. Traditional 2D culture methods on plastic may also modify the original cell morphology and heterogeneity, as cells are mainly in contact with surface coating proteins through focal adhesions. This forces a polarized and abnormally flattened shape, with fewer contacts for intercellular connection [8].

The correct spatial architecture of cell communication is essential for proper cell function, and it cannot be reproduced adequately in a 2D context. Cells in 2D cannot uniformly express adhesion molecules and receptors and are entirely exposed to nutrients and oxygen distributions, unlike the metabolic gradients experienced in vivo [9]. As a result, drugs that appear effective in vitro using 2D systems may not be as successful when given in vivo, frequently leading to false-positive outcomes [10].

On the other side, although animal tests are currently required by regulatory organizations (such as the FDA), they are commonly considered unrepresentative. As a matter of fact, there is a growing awareness of the molecular, genetic and physiological significant differences present between diverse animal species leading to species-specific responses that misrepresent the human complex processes and thus explaining this poor animal-to-human predictability [11]. In addition, animal models are time-consuming, highly labor-intensive

and related to ethical issues objections, and restrictive regulations, as evidenced by the recent ban on animal models for cosmetic testing in European Union countries [12].

For this reason, 3D models have been developed as better reproducers of several chemical, mechanical environmental *in vivo*-like cues. They are better able to replicate the *in vivo* environment than 2D cultures, while still offering the benefits of high control of experimental conditions and ease of manipulation [5]. Various types of 3D *in vitro* models can be identified, such as cellular spheroids, stable cell aggregates that recapitulates different biological features better than cell monolayers. Cells in spheroids exhibit interactions with their neighbors in all spatial directions, with a proliferation rate similar to that seen *in vivo*. However, these 3D culture systems still have some drawbacks, mainly due to a lack of a proper surrounding extracellular matrix (ECM) [13]. The tissue microenvironmental conditions, such as the matrix's mechanical rigidity and its role in modulating cell activity, cannot be finely tuned and replicated [14]. To provide cells with the necessary ECM, researchers have turned to the culture of 3D engineered tissues, adopting different types of biomaterials for this purpose. In particular, 3D hydrogel-based tissue models are emerging among others due to their potential of mimicking native ECM and their cell encapsulation capability [15].

Nevertheless, 3D models are not able to fully replicate the *in vivo* scenario because they do not mimic the fluid-dynamic stimuli that occur at the tissue and microenvironment level. As a result, they are not able to replicate the transport mechanisms for nutrients and drugs [16]. Accordingly, alternative human-relevant experimental strategies capable to better assess the pharmacokinetics (PK) and the pharmacodynamics (PD) of candidates are necessary.

To face this challenge, alternative human-relevant approaches have been emerged, first on all organ-on-chip (OOC) systems [17]. OOCs are an innovative technology that has been gaining attention in the biomedical field in recent years. These devices consist of microfluidic chambers that are designed to mimic the structure and function of specific organs in the human body. They provide a platform for studying human physiology and disease *in vitro*, with greater accuracy than conventional models and without the need for animal testing [18]. One of the main advantages of OOCs is their ability to replicate the microenvironment of the targeted organ, including the fluid dynamic stimuli. This is particularly important as fluid flow plays a crucial role in many biological processes, such as nutrient and drug transport, cellular communication, and tissue development [19]. Therefore, replicating the fluid dynamic stimuli is essential for ensuring that the OOC accurately represents the organ being studied, and also for studying disease mechanisms and drug screening. Fluid flow, in fact, provide important mechanical and chemical cues to cells and tissues [20]. Some OOCs have integrated pumps and valves that can generate pulsatile flow to mimic the physiological flow of blood through blood vessels. Other approaches include the use of magnetic or acoustic fields to generate fluid flow, the use of micro-actuators to mimic the mechanical stress experienced by cells and tissues *in vivo*, or use external pumping system with connecting tubes. Importantly, these systems could enable the development of personalized medicine by using patient-specific cells and tissues [21].

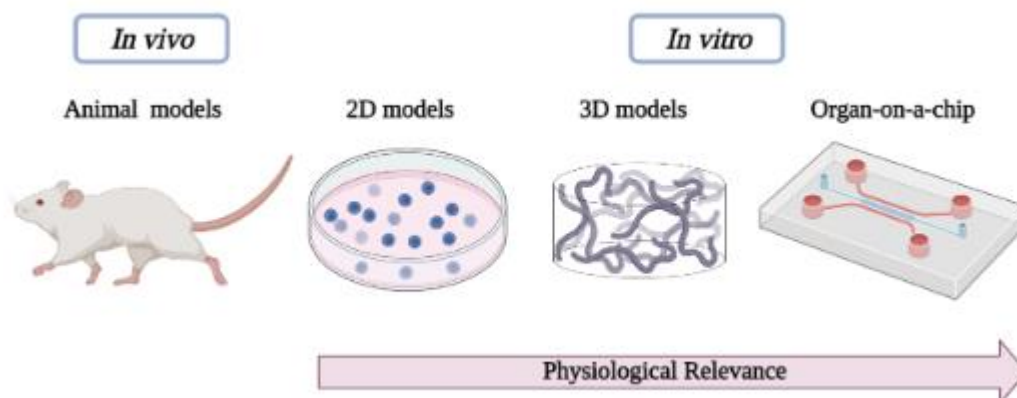


*Figure 3: Comparing preclinical models. While 2D models provide valuable insights, their physiological relevance is limited. 3D models, in particular organ-on-chips providing fluid-dynamic culture environment offer a more accurate representation of in vivo conditions being crucial in advancing preclinical research.*

Particularly, since tissues and cells within the body are anatomically connected to each other by a network of vessels and communicate by the secretion of diverse factors, organ-organ interplays are crucial in human disease understanding and should also be introduced. Specifically, multi-organ-on-chip (MOOC) systems address this need, having the potential to properly emulate the distribution, penetration, biotransformation and kinetics of drugs systemically. MOOC technologies possess the capability to accurately decouple biological mechanisms behind the cytotoxic effects of testing molecules, through a highly reproducible and less time- and cost-consuming in vitro approach [22]. Moreover, they envision to represent advanced biological contexts and thus potentially produce physiologically relevant outcomes translatable to clinical scenarios. MOOCs combine multidisciplinary aspects allowing the recapitulation of the functionality, architecture and dynamics at organ level. The integration of novel in vitro technologies with prior in silico analyses may minimize the use of animal testing, setting the stage for more efficient preclinical predictions of human responses [23].

# Chapter 2

## Innovation: Scientific and Technological Objectives

The core idea of my PhD project is to model, implement and validate technologically advanced platforms (e.g., organ-on-chips) where to replicate biological processes in a systemic and dynamic environment, for investigating the efficacy and toxicity of therapeutic compounds, by combining *in vitro* and *in silico* approaches.

To realize clinically relevant scenarios, 3D tissue models and fluid dynamic stimulations are used. Particularly, the human body fluid dynamics is emulated first performing computational fluid dynamic (CFD) simulations (ensuring optimal flow velocity and shear stress profiles, gas and nutrients gradients and the proper time-dependent drug kinetic profile) and then experimentally applied within fluidic platform, thus integrating the use of novel technologies with *in silico* analyses for developing more reliable analytical preclinical tools.

Different case studies have been considered.

1. Since skin and intestinal tissue are physiological barriers where bioactive molecules interact and permeate under certain conditions, novel transdermal and intestinal delivery platforms have been investigated [24]. Skin absorption assays have been performed accordingly to the OECD Test Guidelines 428, by comparing two different diffusive chambers (Franz Diffusion Cell and the commercially available MIVO platforms) in terms of penetration kinetics of hydrophilic and lipophilic molecules; their capacity to properly resemble physiological fluid flows beneath the skin was computationally and experimentally inspected [25] (Chapter 3).

On the other hand, since poor oral drug bioavailability is the primary cause of failures for new drugs approval, an extensive research analysis has been performed on the currently available intestinal models that resulted insufficient in emulating the compounds (chemicals, food etc.) absorption profiles *in vivo* [26], therefore a mathematical model of the intestinal epithelium as novel screening strategy has been developed (Chapter 4).

2. Although huge resources and money are spent to discover new treatments against cancer, such remains a leading cause of death worldwide. Since less than 8% of new drugs are successfully translated from preclinical to clinical trials, there is an urgent and unmet need of developing human-relevant tumor models [27]. In particular, breast and ovarian cancer, which are among the 5 most common causes of death in women [28], and neuroblastoma, which has one of the lowest survival rates of all pediatric cancers [29] have been considered. For each, I developed and optimized 3D ECM-like tumor models in terms of cells behavior *in vitro*; then, they were cultured under fluid-dynamic conditions (previously predicted by CFD simulations) through different fluidic platforms that allowed to mimic physiological stimuli and investigate the impact of fluid velocities and fluid-associated forces on tumor cells viability and drug response.

In particular, in Chapter 5 it is described a new hydrogel channel-based system that was realized and fluidically connected to an external fluidic circuit, as a preliminary 3D in vitro model, to mimic a secondary metastatic site where CTCs can migrate under a proper hemodynamic cancer environment. Once fluid-dynamic conditions and nutrients transport kinetics were optimized, the effects of physiological WSS and fluid flow on breast cancer cell line were assessed.

Subsequently, since the fluidic stimuli involved in the metastatic process still need to be deeply investigated, in particular the fluid flow-associated force named Wall Shear Stress, a novel microfluidic device have been properly designed upon theoretical and CFD modeling to simultaneously reproduce three different WSS values typical of the circulatory system (i.e. 2, 5, 20 dyn/cm<sup>2</sup>) and then realized. Once validated, the effect of the increasing levels of WSS on triple-negative breast cancer cells clusters was investigated through in silico and experimental studies, inspecting morphological variations and clusters disaggregation after circulation (Chapter 6).

In Chapter 7 it is provided a proof-of-concept of humanized and immunocompetent platform trying to bridge the gap between standard in vitro methods, advanced miniaturized organ-on-chips and animal models, by integrating CFD analyses with in vitro tests. An organ-on-chip organ on chips (OOC)-based approach is here presented for recapitulating the immune cell Natural Killer (NK) migration under physiological fluid flow, infiltration within a 3D tumor matrix, and activation against neuroblastoma cancer cells in a humanized, fluid-dynamic environment. Circulating NK cells activity and the spontaneous “extravasation” process toward the physically separated tumor niche were studied in silico and in vitro.

Finally, because of a single-organ approach is not sufficient to determine the effective response to the drug treatment, both in terms of efficacy and toxicity, a multicompartamental organ-on-chip (OOC) platform was adopted to fluidically connect 3D ovarian cancer tissues to hepatic cellular models and resemble the systemic cisplatin administration for contemporarily investigating drug efficacy and hepatotoxic effects in a physiological context. Computational fluid dynamics was performed to impose capillary-like blood flows and predict cisplatin kinetics.

By using the approach illustrated in Chapter 8, it was possible to easily combine and explore three key aspects, firstly focusing on their single role, then studying their effect when integrated:

- I. The use of 3D models with clinically relevant size.
- II. The prediction and imposing of fluidical stimuli resembling bloodstream circulation to develop a predictive pre-clinical platform that more closely reproduces human patho-physiology.
- III. Multi-organs configuration to properly emulate a systemic human-relevant scenario and properly assess the PK-PD of therapies.

## References

1. Pound, Pandora, and Merel Ritskes-Hoitinga. "Is it possible to overcome issues of external validity in preclinical animal research? Why most animal models are bound to fail." *Journal of translational medicine* 16.1 (2018): 1-8.
2. Marshall, Lindsay J., et al. "Recommendations toward a human pathway-based approach to disease research." *Drug discovery today* 23.11 (2018): 1824-1832.

3. Sun, Duxin, et al. "Why 90% of clinical drug development fails and how to improve it?." *Acta Pharmaceutica Sinica B* (2022).
4. Dowden, Helen, and Jamie Munro. "Trends in clinical success rates and therapeutic focus." *Nat. Rev. Drug Discov* 18.7 (2019): 495-6.
5. Hoarau-Véchet, J.; Raffi, A.; Touboul, C.; Pasquier, J. Halfway between 2D and animal models: Are 3D cultures the ideal tool to study cancer-microenvironment interactions? *Int. J. Mol. Sci.* 2018, 19, 181.
6. Kapalczyńska, M.; Kolenda, T.; Przybyła, W.; Zajączkowska, M.; Teresiak, A.; Filas, V.; Ibbs, M.; Bliźniak, R.; Łuczewski, Ł.; Lamperska, K. 2D and 3D cell cultures—a comparison of different types of cancer cell cultures. *Arch. Med. Sci.* 2018, 14, 910–919.
7. Cukierman, E.; Pankov, R.; Stevens, D.R.; Yamada, K.M. Taking cell-matrix adhesions to the third dimension. *Science* 2001, 294, 1708–1712.
8. Mulhall, H.J.; Hughes, M.P.; Kazmi, B.; Lewis, M.P.; Labeed, F.H. Epithelial cancer cells exhibit different electrical properties when cultured in 2D and 3D environments. *Biochim. Biophys. Acta–Gen. Subj.* 2013, 1830, 5136–5141.
9. Souza, A.G.; Ferreira, I.C. Advances in Cell Culture: More than a Century after Cultivating Cells. *J. Biotechnol. Biomater.* 2016, 6, 2–5.
10. Xu, X.; Farach-Carson, M.C.; Jia, X. Three-dimensional in vitro tumor models for cancer research and drug evaluation. *Biotechnol. Adv.* 2014, 32, 1256–1268.
11. Huh D, Hamilton GA, Ingber DE. From 3D cell culture to organs-on-chips. *Trends Cell Biol.* 2011a;21(12):745–54
12. Cheluvappa, R.; Scowen, P.; Eri, R. Ethics of animal research in human disease remediation, its institutional teaching; and alternatives to animal experimentation. *Pharmacol. Res. Perspect.* 2017, 5, e00332.
13. Herter, S.; Morra, L.; Schlenker, R.; Sulcova, J.; Fahrni, L.; Waldhauer, I.; Lehmann, S.; Reisländer, T.; Agarkova, I.; Kelm, J.M.; et al. A novel three-dimensional heterotypic spheroid model for the assessment of the activity of cancer immunotherapy agents. *Cancer Immunol. Immunother.* 2017, 66, 129–140.
14. Markovitz-Bishitz, Y.; Tauber, Y.; Afrimzon, E.; Zurgil, N.; Sobolev, M.; Shafran, Y.; Deutsch, A.; Howitz, S.; Deutsch, M. A polymer microstructure array for the formation, culturing, and high throughput drug screening of breast cancer spheroids. *Biomaterials* 2010, 31, 8436–8444.
15. Alemany-ribes, M.; Semino, C.E. Bioengineering 3D environments for cancer models. *Adv. Drug Deliv. Rev.* 2014, 79–80, 40–49.
16. Marrella, Alessandra, et al. "3D fluid-dynamic ovarian cancer model resembling systemic drug administration for efficacy assay." *ALTEX-Alternatives to animal experimentation* 38.1 (2021): 82-94.
17. Huh, D., Hamilton, G. A., & Ingber, D. E. (2011). From 3D cell culture to organs-on-chips. *Trends in cell biology*, 21(12), 745-754.
18. Skardal, A., Shupe, T., & Atala, A. (2016). Organoid-on-a-chip and body-on-a-chip systems for drug screening and disease modeling. *Drug discovery today*, 21(9), 1399-1411.
19. Maschmeyer, I., Lorenz, A. K., Schimek, K. M., Hasenberg, T., Ramme, A. P., Hübner, J., ... & Marx, U. (2015). A four-organ-chip for interconnected long-term co-culture of human intestine, liver, skin and kidney equivalents. *Lab on a Chip*, 15(12), 2688-2699.
20. Zhang, B., Radisic, M., & Organ-On-A-Chip Engineering Committee. (2017). From three-dimensional cell culture to organs-on-chips. *Trends in cell biology*, 27(11), 744-756.
21. Oleaga, C., Bernabini, C., Smith, A. S., Srinivasan, B., Jackson, M., McLamb, W., ... & Shuler, M. L. (2016). Multi-organ toxicity demonstration in a functional human in vitro system composed of four organs. *Scientific reports*, 6(1), 1-11.
22. Ingber, Donald E. "Human organs-on-chips for disease modelling, drug development and personalized medicine." *Nature Reviews Genetics* (2022): 1-25.
23. Ko, Jihoon, et al. "Engineering Organ-on-a-Chip to Accelerate Translational Research." *Micromachines* 13.8 (2022): 1200.
24. Aungst, Bruce J. "Absorption enhancers: applications and advances." *The AAPS journal* 14.1 (2012): 10-18.
25. I. Pulsoni, "Comparison Between Franz Diffusion Cell and a novel Micro-physiological System for In Vitro Penetration Assay Using Different Skin Models", *SLAS Technology*, 2022

26. A. Fedi, "In vitro models replicating the human intestinal epithelium for absorption and metabolism studies: A systematic review", *Journal of Controlled Release*, 2021
27. Mahajan, Rajiv, and Kapil Gupta. "Food and drug administration's critical path initiative and innovations in drug development paradigm: challenges, progress, and controversies." *Journal of Pharmacy And Bioallied Sciences* 2.4 (2010): 307.
28. Narod, Steven A. "Personalised medicine and population health: breast and ovarian cancer." *Human genetics* 137.10 (2018): 769-778.
29. Marrella, Alessandra, et al. "Cell-laden hydrogel as a clinical-relevant 3D model for analyzing neuroblastoma growth, immunophenotype, and susceptibility to therapies." *Frontiers in immunology* 10 (2019): 1876.

# **Part II**

## **Section Two**



# Chapter 3

## Comparison Between Franz Diffusion Cell and a novel Micro-physiological System for In Vitro Penetration Assay Using Different Skin Models

### 3.1 Abstract

In vitro diffusive models are a crucial tool for assessing the ability of active ingredients to penetrate various formulations. To achieve successful transdermal delivery, it is important to reliably assess the skin penetration enhancing properties and mechanism of action of carrier systems, as well as estimate bioavailability. To test the penetration kinetics of different compounds across the skin barrier, several in vitro models have been developed. The purpose of this study was to compare the Franz Diffusion Cell (FDC) with a new fluid-dynamic platform (MIVO) by evaluating the penetration ability of caffeine and LIP1 in both systems. Caffeine is a commonly used reference substance, while LIP1 is a testing molecule with the same molecular weight but different lipophilicity. The amount of the molecules absorbed was measured at different time points using HPLC analysis. Both diffusive systems showed similar trends for caffeine and LIP1 penetration kinetics. The Strat-M® skin model had a lower barrier function than pig skin biopsies, and the PGOA vehicle enhanced the penetration effect for both diffusive chambers and skin surrogates. Interestingly, the MIVO diffusive system was better at predicting the permeation of lipophilic molecules (such as LIP1) through highly physiological fluid flows that resemble skin models.

### 3.2 Introduction

The skin tissue is an effective barrier, representing a fundamental interface between the human body and the external environment. Based on its chemical-physical features, it forms a protective layer against harmful environmental influences such as ultra-violet light, microorganisms, pollutants and environmental toxins, pesticides, or other chemical drugs. Moreover, skin regulates temperature and homeostasis of the body, particularly by limiting the loss of water [1]. Dermal absorption assays are routinely adopted to predict risks from skin exposure to chemicals, but also to demonstrate benefits after topic application of cosmetics, medical device or therapeutic active ingredient. In this context, the Organization for Economic Co-operation and Development (OECD) and the United States Environmental Protection Agency have produced guidelines for the in vitro and in vivo assessment of percutaneous absorption [2], that establishes the passage of compounds across the skin. This process is basically divided in three steps [3]: i) penetration, which consists of the entry of the chemical compound into the stratum corneum, build up by an intracellular lipid matrix of mainly ceramides, cholesterol and free fatty acids [4,5]; ii), permeation, namely the gradual passage of the substance through the subsequent layers, which are both functionally and anatomically distinct from the stratum corneum; iii) the uptake into lymphatic and blood vessels [5], [6], [7], [8]. Interestingly, according to the skin absorption outcome, the

classification of these testing compounds may range from cosmetics to “medical devices made of substances”, that need to be absorbed in order to achieve their intended action [9], [10], [11]. Therefore, there is increasing demand for reliable and reproducible in vitro and ex vivo skin absorption methods that accelerate the chemicals testing and the measurement of their absorption percentage. In the last two decades, the European Union and national legislations have stipulated that animal experiments should be avoided whenever scientifically feasible, in line with the 3Rs (reduce, replace, refine) approach [2]. Furthermore, owing to the difference in skin structure, animal studies do not always reflect the human situation [2]. The estimation of percutaneous absorption of compounds using excised animal skin is widely accepted for the toxicological risk assessment [12]. Porcine skin has been re-cognized as an appropriate tissue for prediction of human skin permeability for some years, despite the lower barrier function of this tissue compared with human skin [13], [14], [15], [16], [17]. Recently, numerous skin surrogate systems and human skin equivalents (HSEs) have been developed to study skin penetration to overpass limits of animal sources. HSEs are typically constructed by culturing human keratinocytes on appropriate substrates [18], providing a good-quality control of the system and species relevance. Consequently, some reconstructed tissues (i.e. EpiSkin and EpiDerm) have already been validated under specific applications, such as for skin irritation [19,20]. In general, they have proved a lower barrier function than human skin [18,21,22], but for hydrophilic compounds (i.e. ethyl ascorbic acid [23] and caffeine [21]) some HSEs (i.e. LabSkin, EpiDerm, EpiSkin, SkinEthic) represent a valuable option to carry out transdermal delivery investigations, even though some regulation guidelines still have to be updated [10,24]. Artificial membranes have been also fabricated and employed as synthetic skin alternatives [25]. Non-lipid- and lipid-based membranes are cost-effective and reproducible tools to study the underlying physicochemical mechanisms of the passive drug diffusion, [24,26]. Moreover, being non-biological models, these skin models may support high-throughput screenings, without lot-to-lot variability, safety and storage limitations [4]. The parallel artificial membrane permeability assay (PAMPA) may represent an alternative to simulate dermal absorption of some compounds [25,27,28], whose results displayed a good correlation with full-thickness skin ( $R^2 > 0.7$ ). The Strat-M® membrane is an animal free, multiple layer polyether sulfone membrane, which is coated with skin lipids (e.g., ceramides, cholesterol, and free fatty acids), especially designed to mimicking the skin structure for transdermal diffusion testing. The hydrophobic lipidic structure, which is coated on the membrane is composed of the main stratum corneum lipids, paired with the polyether sulfone membrane cut-off this membrane mimics a skin penetration more closely than other membranes, which are limited only on their cut-off definition [29]. These chemico-physical properties make Strat-M® membrane a good skin model alternative to evaluate penetration flux and permeation of molecules, under infinite and finite dosing conditions [30]. However, due to their lower barrier function, artificial membranes typically lead to a higher penetration ability and penetration rate [12,13,31]. For ex vivo skin penetration studies the OECD guideline recommends pig ear skin as suitable skin surrogate to mimic human percutaneous penetration [24,32]. Pig ear skin shows similarities in morphology as well as penetration abilities and corresponds to that of human skin [33]. Typically, the passive diffusion of active ingredients is tested by culturing surrogate skin in a Franz Diffusion Cell (FDC) setup [34]. The FDC system can be either a static or flow-through setup. Although both are compliant with the OECD Test Guidelines 428, static FDC set-up remains simpler, lower-cost and more widely used diffusive system [12,24]. It consists of a receptor compartment filled with a physiological buffer solution, in which the compound is released after penetrating through the skin surrogate. Onto this surrogate a finite ( $\leq 10 \mu\text{L}/\text{cm}^2$ ) or infinite ( $\geq 10 \mu\text{L}/\text{cm}^2$ ) formulation dose can be topically applied into

the donor compartment and allows the evaluation of penetration kinetics over time [35,36]. Finite dosing represents more closely application and usage condition, whereas an infinite dosing helps to understand and elaborate permeation abilities due to a steady state penetration and a constant high formulation concentration. The penetration kinetics interpretation underlines the predicted bioavailability of the active ingredient, which is important to ensure the efficacy and the exposure to the living cell entity and a targeted drug delivery. The hydrophilic alkaloid caffeine is recommended as a model compound by the OECD guideline for in vivo, ex vivo, and in vitro percutaneous penetration testing due to its well-known penetration behaviour [32]. To optimize and ensure targeted delivery of ingredients into the skin, the formulation needs to be designed individually [37]. Most ingredients are formulated into a standard formulation (vehicle) containing water, glycols and fatty acids for penetration testing based on their physico-chemical properties and solubility characteristics [38]. Thereby, propylene glycol (PG) is the most used glycol and is often combined with other penetration enhancers like oleic acid (OA) to test ingredient penetration [39]. In this work, we compared the FDC with a novel ready-to-use, compartmental technology, named MIVO® - Multi In Vitro Organ device, compliant with the OECD 428 guideline's definition of a diffusion cell and able to properly resemble the mono-directional physiological capillary-like flow below the tissue. MIVO has been already adopted to carry out diffusion studies in gut absorption [40], tumor cells intravasation [41] and cancer drug efficacy testing [42]. Here, molecules having different lipophilicity (expressed as log p values) although same molecular weight (i.e. caffeine and LIP1, acronym for 1,3-Benzodioxol-5-ylmethylurea lipophilic molecule) have been adopted as testing molecules for skin permeation assays through two human surrogate models, the Strat-M® membrane and the pig ear skin, carried out employing both FDC, as it is the standard in vitro method for this type of study, and MIVO®. Also, computational fluid-dynamic (CFD) simulations have been performed to inspect the flow field beneath the skin in the receptor of both diffusion cells considered.

### **3.3 Materials and Methods**

#### **3.3.1 Diffusive chambers**

##### **3.3.1.1 MIVO system**

The MIVO® device is a disposable cell culture chamber able to host living tissues (e.g. cellular monolayers, 3D reconstructed tissues, tissue biopsies) or artificial membranes under physiological conditions, providing a multiple fluidic circulation that mimics the human circulatory system with the vascularization of the tissue of interest. The diffusion cell designed and implemented in this work is schematically represented in Figure 4, panel A, showing features in compliance with the OECD 428 rule for in vitro skin absorption method. Specifically, the human skin surrogate separates the donor compartment from the receiver one, exposing a surface area of 0.43 cm<sup>2</sup> suitable for drug administration. The receiver compartment has been designed to be connected to a peristaltic pump inducing a monodirectional flow: then, a capillary velocity can be set up below the skin barrier, emulating the real physiological conditions. A three-way valve placed in the fluidic circuit allows the sampling of the media over time, without affecting the sterility environment and the tissue. The whole system is hosted within the cell culture incubator with controlled atmosphere (i.e., 32°C, 5% CO<sub>2</sub>).

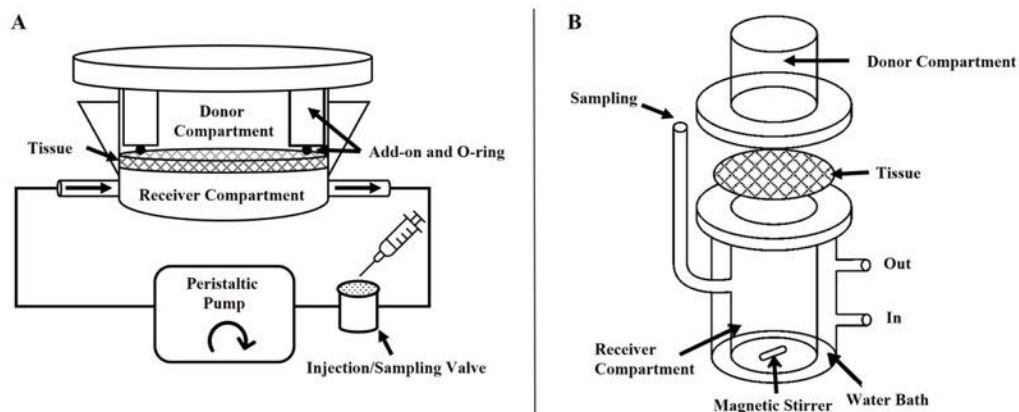


Figure 4: Diffusive chambers. Schematic representation of the diffusive chambers where the tissue (Strat-M® or pig skin) is placed for performing dynamic absorption studies. Panel A: the MIVO® fluidic chamber; Panel B: Franz Diffusion Cell.

Strat-M® membranes and pig skin biopsy discs were placed within MIVO®; an add-on equipped with a biocompatible o-ring avoiding any fluid leakage blocks the skin models inside the MIVO® chamber. The donor compartment was filled with a volume of caffeine formulations according to the infinite-dose experimental condition (780 $\mu$ L/cm<sup>2</sup>), and the receiver one was filled with 2.3 mL of calcium and magnesium enriched phosphate buffered saline (PBS), at a flow rate of 2 mL/min in order to have below the skin surrogate a mean flow velocity (of 0.1 cm/s), resembling the capillary flow [42,43]. The experiment with Strat-M® was performed in triplicate, while the one with pig ear skin was performed with 6 replicates. For both skin models, 400  $\mu$ L (or 20%) of the circulating solution in the receiver compartment were collected at different time-points (1, 2, 4, 6, 8 hours), in order to assess the quantity of caffeine/LIP1 accumulating into the receiver chamber over time. The samples were filtered through a cellulose acetate membrane filter (0.22  $\mu$ m pore size) and analyzed through High-Performance Liquid Chromatography (HPLC).

### 3.3.1.2 FDC system

The FDC system consists of a receiver compartment filled with 5 mL PBS, in which the compound is released after penetrating through the skin surrogate. Onto this surrogate the infinite-dose experimental condition (780 $\mu$ L/cm<sup>2</sup>) is topical applied into the donor compartment and allows the evaluation of penetration kinetics over time [[33], [34], [35],44]. **Errore. L'origine riferimento non è stata trovata.** shows a schematic illustration of the FDC with its magnetic stirrer and its thermostatically controlled water bath, to maintain a controlled temperature of 32°C. The Strat-M® membranes and pig skin biopsy discs as human skin surrogates were placed onto the FDC ( $\varnothing$  9 mm, diffusion area 0.64 cm<sup>2</sup>) from Logan Instruments Corp. (Somerset, USA). The Strat-M® membrane was placed shiny side up and the pig skin dermal side down onto the receiver compartment. The experiment with the Strat-M® membrane was performed with 6 replicates, while the one with pig ear skin was performed with 8 replicates. After an experimental equilibration for 30 min, different exposure times (1, 2, 4, 6, 8 hours) were adopted and 1000  $\mu$ L (or 20%) of the receiver compartment were collected and filtered through a cellulose acetate membrane filter (0.22  $\mu$ m pore size). The solution was HPLC analyzed and replaced with fresh PBS. A summary of the main features of MIVO and FDC was shown in Table 1.

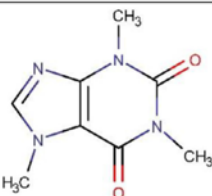
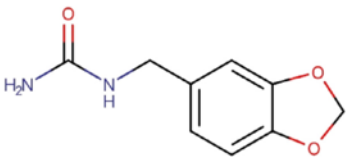
Table 1: Technical features of MIVO and FDC.

Diffusive chamber	MIVO	FDC
Flow regimes	Laminar, monodirectional, spatially homogeneous	Rotational, slight turbulent, spatially non homogeneous
Reynolds number	~20 < 2000	~1700 < 2000
Driving force	Peristaltic pump	Stirring bar
Media Sampling system	Through a three-way valve	Through the sampling port
Receptor Media volume	Flexible, ranging from 2.5 to 5 ml	From 5 to 20 ml according to the model
Skin models	Cells monolayer on inserts, membranes (eg StratM, Permeapad), 3D reconstructed skin tissues (e.g. epiDerm, epiSkin SkinEthic, Labskin), biopsies	Membranes, biopsies
Skin clamping	Auto-centering and blocking of inserts, add-on with o-ring for biopsies	Metallic clamps
Sterilization	Already sterile and ready to be used	Autoclavable, after a pre-clean/wash

### 3.3.2 Chemicals

Caffeine, 1,3-Benzodioxol-5-ylmethylurea (LIP1), Milli-Q® (water), acetonitrile, were purchased from Merck KGaA (Darmstadt, Germany). Propylene glycol (PG), Oleic acid (OA), and calcium and magnesium enriched PBS solution were purchased from Sigma Aldrich by Merck KGaA (St. Louis, USA). Formulations containing either water or PGOA (95:5) with either 0.7% caffeine (w/w) or LIP1 were prepared. Caffeine and LIP1 were selected as reference molecules having same molecular weight and different lipophilicity (Table 2).

Table 2: Physico-chemical properties of caffeine and LIP1.

	Caffeine	1,3-Benzodioxol-5-ylmethylurea (LIP1)
Chemical structure		
Molecular Formula	C <sub>8</sub> H <sub>10</sub> N <sub>4</sub> O <sub>2</sub>	C <sub>9</sub> H <sub>10</sub> N <sub>2</sub> O <sub>3</sub>
Molecular weight [g/mol]	194.19	194.19
Log P	-0.1 (exp.)	0.6 (exp.)
CAS number	58-08-2	65609-28-1

### 3.3.3 Skin models: Strat-M® and pig skin biopsies

The Strat-M® membrane purchased from Merck KGaA (Darmstadt, Germany) is a non-animal based synthetic membrane build up by multiple layers of polyether sulfones coated with skin lipids, which mimics the penetration ability of human skin (Figure 5). This lipid coating, which mimics the intercellular lipid matrix of the human stratum corneum, contains a combination of ceramides, cholesterol, free fatty acids, and other components with a similar specific lipid ratio to human skin surface [4].

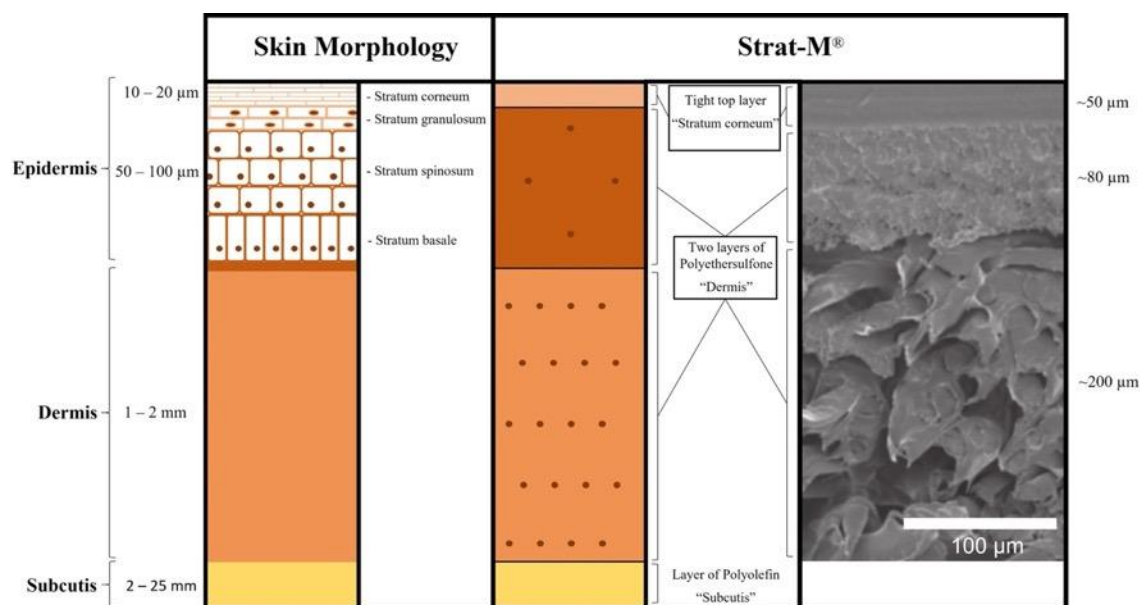


Figure 5: Strat-M® skin model. Schematic illustration of the skin morphology and the multilayered structure of the Strat-M® membrane to compare the different skin layers with a scanning electron microscopic image of a Strat-M® cross-section.

Pig ear skin was used as a human skin surrogate for penetration testing. The pig ears (German domestic pigs, 6-month-old) were obtained from a local slaughterhouse (Brensbach, Germany). Freshly slaughtered, they were cleaned with water, dried using soft tissue and stored at +4°C. The skin from the back of the pig ear was dermatomed with an electrical dermatome from Humeca BV (Borne, Netherlands). 500 µm thick split-skin punches with a diameter of 26 mm were obtained from each ear and stored for the maximum of 6 month at -20°C.

### 3.3.4 HPLC

The quantitative concentration of caffeine and LIP1 was determined using a HPLC (VWR-Hitachi ELITE LaChrom system) system. A Chromolith® Performance RP-18e 100-4.6 mm (Merck KGaA, Darmstadt) column was used as the stationary phase at 30°C and at flow rate of 2.0 mL/min, with an isocratic mobile phase of 90% water and 10% acetonitrile (HPLC gradient grade, Merck KGaA, Darmstadt) for caffeine and a mobile phase of 80:20 for LIP1. The caffeine amount was determined at a detection wavelength of 272 nm, and LIP1 at 285 nm, using a DAD I-2450 detection unit. Prior the analysis, the samples were mixed in auto sampler screw vials and analyzed with an injection volume of 60 µL of each sample (n=4). The specificity of the HPLC run was controlled via a blank injection and an internal standard solution. The quantification linearity was confirmed by a six-point calibration series (0.5-250.0 µg/mL) with linear regression confirmation of  $R^2 > 0.99$  in all cases. Accuracy and precision of the HPLC run was determined within the internal acceptance criteria variation <2 %.

## 3.4 Results

### 3.4.1 Caffeine penetration kinetics using Strat-M®

The cumulative amount of caffeine penetrated through Strat-M® was derived for the two experimental conditions (PGOA and Milli-Q® as donor solutions), showing statistical

difference between the two diffusive chambers, although similar trend were observed (Figure 6). The passage of caffeine was enhanced ( $\sim 10X$ ) when using PGOA as a vehicle (Figure 6A); moreover, the caffeine absorption through the Strat-M<sup>®</sup> membrane shows a linear trend during time in the Milli-Q<sup>®</sup> solution (Figure 6B), while in PGOA an initial plateau was observed after 6 hours.

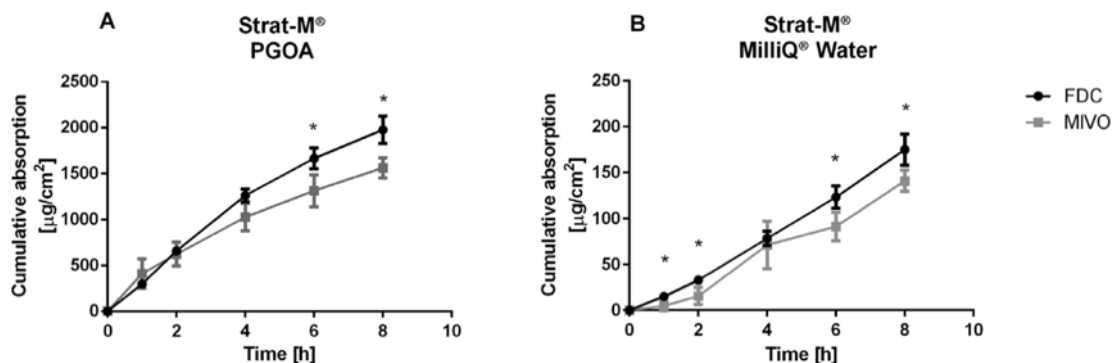


Figure 6: Cumulative amount of Caffeine penetrated through pig skin. Comparison of the caffeine penetration kinetics through pig skin biopsies in FDC and MIVO<sup>®</sup> systems with PGOA (A) and Milli-Q<sup>®</sup> water (B) as vehicle solution. Values are presented as mean  $\pm$  SD.

### 3.4.2 Caffeine penetration kinetics using Strat-M<sup>®</sup>

The cumulative amount of caffeine penetrated through pig skin tissues was measured for both formulations (PGOA and Milli-Q<sup>®</sup>), comparing the FDC and the MIVO<sup>®</sup> chambers (Figure 7) and showing statistical difference between the two diffusive systems only in MilliQ<sup>®</sup> conditions. The PGOA formulation (Figure 7A) led to an increasing amount of caffeine in the receiver chamber over time, despite the resulting penetration (ug/cm<sup>2</sup>) was overall lower than for Strat-M<sup>®</sup> ( $\sim 12X$  for FDC and  $\sim 17X$  for MIVO<sup>®</sup>). Likewise, when caffeine was topically applied within the Milli-Q<sup>®</sup> vehicle (Figure 7B), its penetration over time through the pig skin was lower than the one resulted with Strat-M<sup>®</sup> membrane.

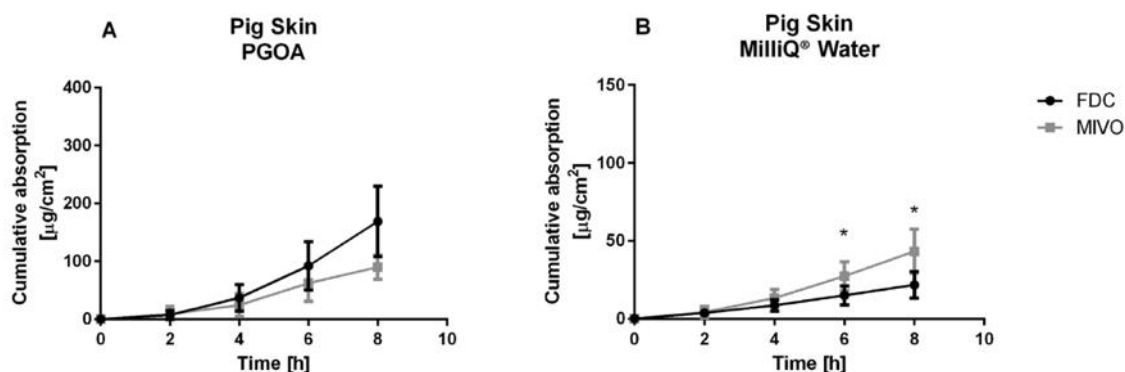


Figure 7: Cumulative amount of Caffeine penetrated through pig skin. Comparison of the caffeine penetration kinetics through pig skin biopsies in FDC and MIVO<sup>®</sup> systems with PGOA (A) and Milli-Q<sup>®</sup> water (B) as vehicle solution. Values are presented as mean  $\pm$  SD.

### 3.4.3 LIP1 penetration kinetics using Strat-M<sup>®</sup> and pig skin biopsies

Similarly to the caffeine in PGOA (Figure 6A and Figure 7A), the LIP1 in PGOA formulation displayed a gradual increase of its passage through Strat-M and pig skin, with an initial plateau observed at the ending points for Strat-M (Figure 8A) and a linear trend for pig skin (Figure 8B) for both diffusive systems. Like for caffeine, also LIP1 was more absorbed through the Strat-M than the pig skin (~6X for FDC and ~3X for MIVO®). The cumulative amount of LIP1 was statistically higher in MIVO than in FDC already after 2 hours using Strat-M and 6 hours using pig skin. Interestingly, values of caffeine in PGOA are much higher (~4X after 8hr) than those of LIP1 using Strat-M in FDC system (**Errore. L'origine riferimento non è stata trovata.**C), while no significant differences are observed between caffeine and LIP1 using pig skin in FDC system (Figure 8D). On the other side, as expected for lipophilic molecules applied onto skin tissues, MIVO displays a higher LIP1 permeation (~3X after 8hr) than caffeine using pig skin model (Figure 8D), while artificial Strat-M membrane displayed similar permeation behavior for caffeine and LIP1 (Figure 8C).

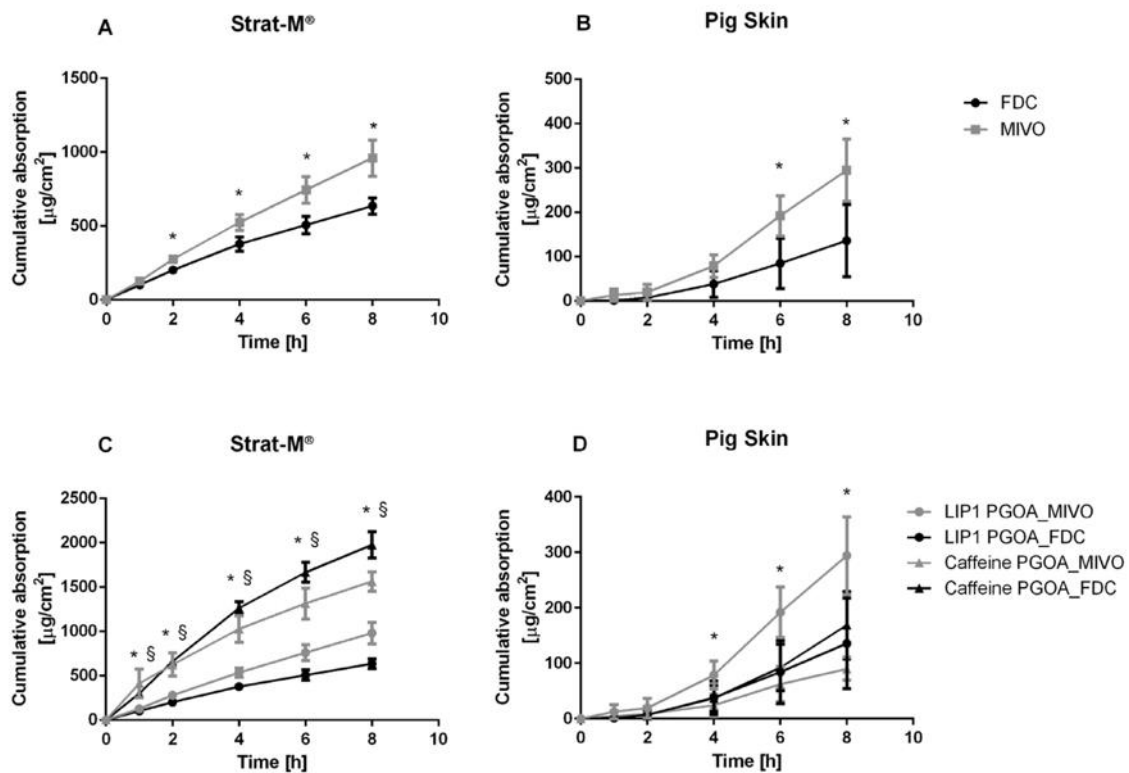


Figure 8: Cumulative amount of LIP1 penetrated through the Strat-M® membrane and pig skin. Comparison of the LIP1 penetration kinetics through Strat-M® membranes (A) and pig skin biopsies (B) with FDC and MIVO® and in comparison with Caffeine penetration kinetics through Strat-M® membranes (C) and pig skin biopsies (D). Values are presented as mean  $\pm$  SD, the values obtained by using the two systems are compared using paired t-Test statistics ( $p < 0.05$ ).

A comparison of the caffeine and LIP1 penetration for all implemented experimental conditions after 8 hours, with statistical analysis, was also shown (Figure 9).



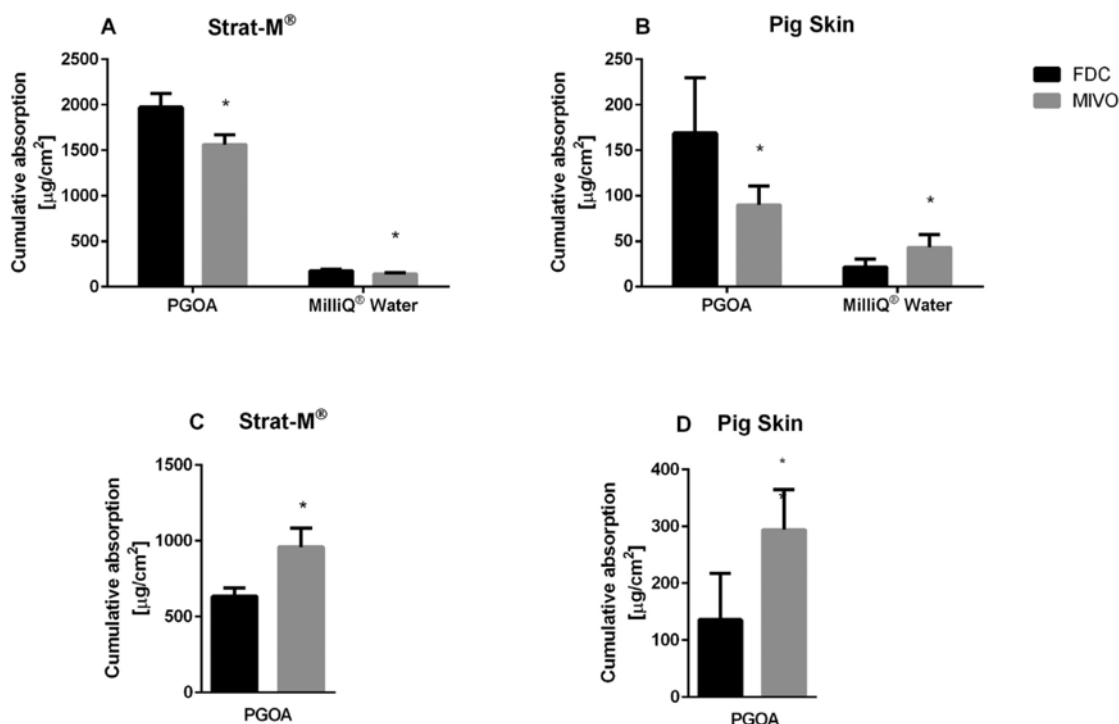


Figure 9: Caffeine and LIP1 permeation in all the experimental conditions. Quantity of caffeine penetrated after 8 hours through Strat-M<sup>®</sup> (A) and pig skin (B) with FDC and MIVO<sup>®</sup> and quantity of LIP1 through Strat-M<sup>®</sup> (C) and pig skin (D) with FDC and MIVO<sup>®</sup>. Values are presented as mean  $\pm$  SD, the values obtained by using the two systems are compared using paired t-Test statistics ( $p < 0.05$ ).

### 3.4.4 Mathematical approach to determine the diffusion coefficient

Permeation of an active ingredient through the skin's stratum corneum is described as diffusion process in which active transport plays no role [45]. Mathematically, skin absorption can be described by Fick's laws of diffusion. The first Fick's law is specific to an infinite dose condition [45], which is described for experiments with a topical amount higher than 100  $\mu\text{L}/\text{cm}^2$  (or higher than 10  $\text{mg}/\text{cm}^2$ ):

where  $J$  is the rate of transfer per unit area (flux) ( $\text{g}/\text{cm}^2/\text{h}$ ), and  $D$  is the diffusion coefficient ( $\text{cm}^2/\text{h}$ ). Thereby a steady-state flux,  $J_{ss}$ , is commonly assessed in vitro and ex vivo in diffusion cells (e.g., FDC and MIVO<sup>®</sup>), consisting of a donor compartment separated from the receiver compartment by a human skin surrogate. The ingredient is applied to the stratum corneum side of the skin, and an accumulation of active ingredient in the receiver compartment is monitored by repeated concentration measurements in the receiver medium over time. Under infinite dose conditions,  $dC$  can be replaced by the known donor concentration,  $c_D$ , and the permeated mass per time is assumed to be constant. Therefore, a plot of the permeated mass per unit area versus unit time, yields a linear function with a slope which represents the steady-state flux. The apparent permeation coefficient,  $P_{app}$ , which represents an independent measure of the skin resistance against permeation of the examined active ingredient, is frequently calculated as:

because this value only depends on the donor concentration used in the given experiment.  $J_{ss}$  and  $P_{app}$  were derived for the two skin models and the caffeine/LIP1 vehicle from the linear part of the respective absorption curves by linear regression, by using an automated approach [46], if at least four data points are within the linear part of a curve ( $R^2 > 0.92$ ).

The time to achieve steady-state conditions, under infinite dose conditions is referred as lag time (t) and the preceding period is the lag-phase. Lag time is a function of the active ingredient loading the stratum corneum and dermis, diffusivity, and thickness of the skin. Lag time is the time required for the diffusion flow to become stable. By using the Lag time calculation [47], the diffusion coefficient can be derived:

Table 3 and Table 4 report respectively the steady state flux and the percentages of caffeine and LIP1 absorbed after 8 hours under different conditions.

*Table 3: Steady-state flux and the apparent permeation coefficient for all the experimental conditions investigated.*

Steady-state Flux $J_{ss}$ and Apparent Permeation Coefficient $P_{app}$					
		Skin Model			
		Strat-M®		Pig Skin	
		FDC	MIVO®	FDC	MIVO®
LIP1 in PGOA	$J_{ss}$ ( $\mu\text{g}/\text{cm}^2/\text{h}$ )	83.59	123.13	14.53	31.97
	$P_{app}$ ( $\text{cm}/\text{s} \times 10^{-6}$ )	3.32	4.88	0.63	1.27
Caffeine in PGOA	$J_{ss}$ ( $\mu\text{g}/\text{cm}^2/\text{h}$ )	268.18	216.01	17.2	10.05
	$P_{app}$ ( $\text{cm}/\text{s} \times 10^{-6}$ )	10.64	8.57	0.68	0.40
Caffeine in Milli-Q®	$J_{ss}$ ( $\mu\text{g}/\text{cm}^2/\text{h}$ )	20.94	16.51	2.54	4.75
	$P_{app}$ ( $\text{cm}/\text{s} \times 10^{-6}$ )	0.83	0.65	0.1	0.19

*Table 4: Percentage values of penetrated caffeine and LIP1 through Strat-M® membranes and pig skin biopsies in all the experimental conditions.*

% of penetrated through the skin barrier					
		Skin Model			
		Strat-M®		Pig Skin	
		FDC	MIVO®	FDC	MIVO®
LIP1 in PGOA		11.6%	17.6%	2.5%	5.4%
Caffeine in PGOA		36.2%	28.6%	3.1%	1.7%
Caffeine in Milli-Q®		3.2%	2.6%	0.4%	0.8%

### 3.4.5 CFD simulation of fluid flow within MIVO and FDC

Fluid dynamic simulations were performed both in MIVO and in FDC environments to simulate the fluid flow profiles, mean velocities and shear stresses below the skin model (Figure 10). The 3D domain was drawn based on the dimensions of the two diffusive chambers used for skin permeation assays. The physical outputs were modeled using Comsol Multiphysics 5.6 (Laminar Fluid Flow module). The fluid was supposed to be laminar, incompressible, and not turbulent. The velocity profiles were calculated according to Navier-Stokes and the continuity equation [48,49]. In the MIVO environment, the flow rate was set to  $Q=2$  mL/min to generate velocity resembling the capillary blood flow, while in the FDC the flow was generated by a stirring bar (length of 7 mm, rotational frequency 10Hz). An iterative geometric multigrid (GMRES) algorithm was used to solve the equations. A no-slip condition was fixed on the boundary of the geometry.

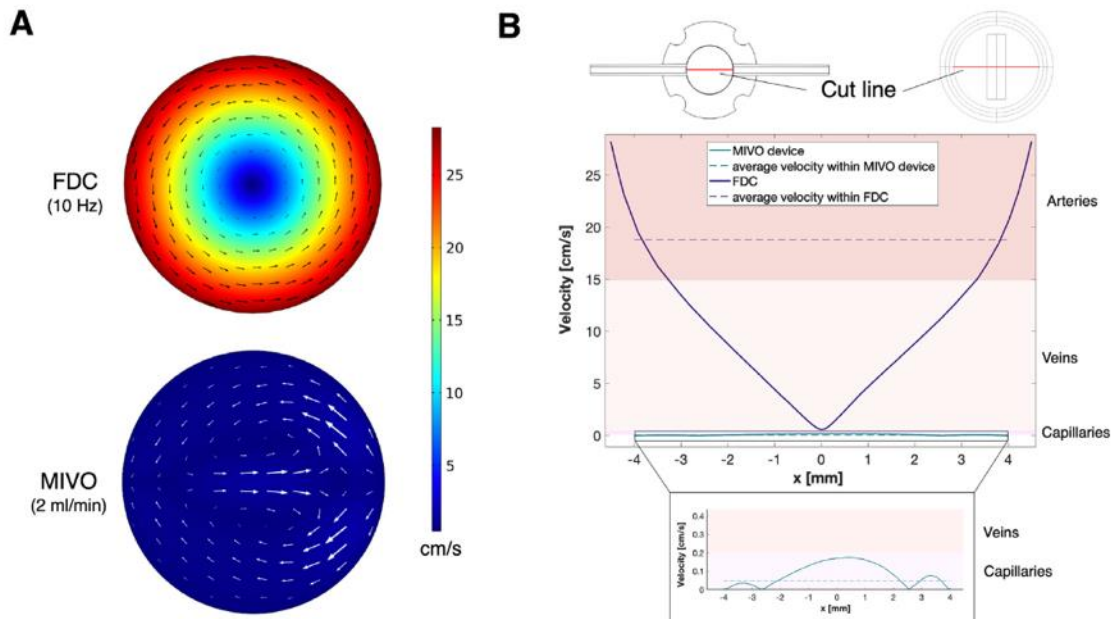


Figure 10: Computational Fluid-dynamic simulations of FDC and MIVO. Velocities distribution at the plane below the skin within FDC and MIVO (panel A). Velocity profiles at the cut line, compared to the physiological values, within FDC and MIVO (panel B).

### 3.5 Discussion

In the fields of pharmaceutical industry, reliable skin penetration data of active ingredients are indispensable, since it affects the bioavailability, defined as the amount of molecules that reaches the systemic circulation [50]. Various studies have considered the impact of different physico-chemical formulations and skin models on permeation assays. Moreover, the use of in vitro diffusion cells has evolved into a major research methodology, providing key insights towards more reliable, reproducible, and standardized in vitro and ex vivo methods. In vitro models frequently involve the use of artificial membranes to model realistic human skin penetration features. Although these membranes do not model the cellular mediated phenomena affecting the molecule passage through a living tissue, diffusion studies can be carried out. In particular, artificial membranes may be preferred to skin biopsies as they are more easily resourced, less expensive, structurally simpler and lead to a faster outcome [51]. Another challenging approach is based on in vitro human epidermis and dermis cells models, building human skin equivalent (HSE). Some commercially available HSE like Graftskin™, SkinEthic™, LAbskin™, EpiDerm and Episkin, have been already adopted for penetration assays [52,53] and to understand metabolic skin response [13,31] within exploratory assays, while regulatory bodies are currently involved in guidelines updates. Also artificial membranes, although to a higher penetration ability and penetration rate [12,13,31], are currently adopted to provide useful permeation measurement for multiple formulations with higher throughput [4]. Indeed, they exhibit superior data reproducibility, as in vivo variables such as donor age, sex and anatomical site are excluded [51]. In this context, the Strat-M® represents an interesting option among synthetic skin models, since it is a membrane-based model with diffusion characteristics well-correlated to human skin [4]. However, it does not fully resemble the heterogeneous multi-layer structure of human skin. For these reasons, an effective alternative is represented by animal skin biopsies as indicated in the OECD TG 428 guidelines [32]. Among these, pig ear skin is currently the most widely used, given its histological similarities to human skin, with a

comparable stratum corneum thickness [54,55]. In this work, a comparative study was performed by using both synthetic non-animal-based membrane (i.e., Strat-M®) and pig ear skin biopsies for assessing the penetration of two molecules with similar molecular weight but different lipophilicity: caffeine, a reference OECD 428 substance, and LIP1, a lipophilic test substance. By applying such testing molecules to the skin under infinite dose conditions, we expected that these penetrate into and diffuse through the stratum corneum, depending on their physico-chemical properties. [56,57] Indeed, a continuous increase of the caffeine and LIP1 penetration was observed up to 8 hours in all experimental conditions; in particular, Strat-M® turned out to be more permeable than pig biopsy, as already reported for synthetic membranes, especially for hydrophilic molecules [13]; this can be due to a different morphological and histological structure of the skin tissue. Moreover, despite artificial skin membranes do not fully resemble the proper passive route of molecule permeation, a lower variability, and therefore a higher reproducibility, was observed for the Strat-M® model than pig ear biopsies, as expected [31]. Although the same anatomical site (i.e., pig ear) was selected for all donors, this high variability is intrinsic to the model because of the biopsy structure, age and hydration state of the skin that may differ from one donor to another [45]. Transdermal pharmacokinetic studies allow to recognize the fate of the new formulations/drugs applied to the skin, to evaluate what fraction of the applied doses have been effectively absorbed, and to determine the bioequivalence of the generic products [58]. To better resemble the in vivo situation, where systemic circulation rapidly clears permeants, diffusion chambers hosting skin models have been widely adopted as more reliable alternative to the static condition [59]. Among these, FDC systems are used since many years, under the two available configurations: static and flow-through [34]. In both systems the receptor fluid is stirred in a non-physiological way, but the pivotal difference between the two configurations is the continuous fluid replacement in the flow-through type [10,24]. This further implementation makes the flow-through system more reliable than the static counterpart, mimicking the supply of fresh fluid media as it happens in vivo thanks to the continuous tissues vascularization. On the other side, flow-through cells are labor-intensive, introducing an additional lag time and augment experimental costs (for additional pumping equipment and larger volume of fresh media), making the use of the static device preferable and more widely diffused among testing laboratories [12,24]. Furthermore, it becomes fundamental that the fluid-dynamic environment implemented within the diffusion cell could be highly reliable and biomimetic in terms of flow velocities and mass transports profiles, that affect the diffusion kinetics of the testing ingredient [42]. For these reasons, MIVO® system has been recently employed as alternative diffusion cell, due to its ability in reproducing physiologically relevant flow culture conditions. MIVO®, as FDC systems, consist of inert non-adsorbing material with receptor compartment volumes of 2 – 10 mL and surface areas of exposed membranes of about 0.2 – 4 cm<sup>2</sup>, according to the OECD 428 guidelines. The fluid flow is imposed within MIVO through the adoption of a peristaltic pump, which allows to finely regulate the flow rate, the flow direction, and the velocity profile below the hosting tissue. In particular, based on the inner design of the receptor chamber, by setting an unidirectional flow rate of 2 mL/min it is possible to reproduce values within the capillary blood velocity range, providing a micro-physiological tool for pharmacokinetic and pharmacodynamic studies with high predictability and reproducibility outcome, as already reported for gut absorption assay [60] and drug efficacy assays [42]. As evidence of this, CFD simulations of velocity profiles below skin have been thus performed for both FDC and MIVO. A spatially homogeneous velocity profile consistent with the capillary blood flow was observed below the skin cultured within MIVO, whereas a rotational not physiological profile was detected within FDC, showing values ranging from the arterial to veins velocities in the outer and inner region, respectively, thus making MIVO

a diffusion system more suitable to recapitulate the human blood flow dynamics (Figure 10). As a matter of fact, a laminar fluid flow was noticed within the MIVO apparatus without any vortex formation [42], whereas FDC exhibited a slight turbulence (Reynolds number approximately equal to 1700). In particular, this undesirable vortex, being far from reproducing capillary physiological settings, may lead to inadequate molecule distribution throughout the receptor compartment since it has a potential to disrupt the static fluid layer adjacent to the membrane; such an effect changes one of the assumptions of Fick's law, namely that the calculation of the diffusion coefficient includes a contribution from the boundary layer [61]. Importantly, MIVO® provides a similar permeation trend to FDC system when challenged with the Strat-M® for the caffeine in PGOA as well as the Milli-Q® formulation. According to the skin-related physical features of the Strat-M®, caffeine penetration across the membrane was dependent on the vehicle used : in particular, the PGOA vehicle enhanced the ingredient penetration through both the Strat-M® (~10X for both diffusive chambers) and the pig skin (~8X and ~3X for FDC and MIVO®, respectively). Interestingly, the positive effect of PGOA was constant in the two diffusion cells where the artificial membrane was adopted, confirming the good reliability of MIVO® for permeation assays. Moreover, the percentage of caffeine permeated through pig skin in MIVO® was in line with the observed values in Schäfer-Korting [62]. However, statistically significant differences were observed between MIVO® and FDC, with higher permeation values measured in FDC. To better investigate these differences, a different molecule having the same molecular weight but different lipophilicity (i.e. LIP1) was used. By using both Strat-M® and pig skin models, MIVO® showed higher cumulative amount of LIP1 in PGOA permeation than that measured in FDC, although a similar slope was observed. In particular, by using the skin tissue as a model, the lipophilic LIP1 was more absorbed than caffeine with MIVO® system, whereas FDC showed the same permeation of caffeine and LIP1 despite their different lipophilic properties. This could be cross-correlated with a more physiologically relevant fluid flow conditions below the skin tissue hosted within MIVO rather than FDC, properly recapitulating the faster passage of lipophilic molecules than hydrophilic ones. Interestingly, a positive penetration enhancing effect of OA in increasing diffusion through skin was observed also for LIP1 molecule. This is mostly due to the hydrophobic lipidic structure of the Strat-M® top layer mimicking the tight epidermal stratum corneum [31]. Considering its barrier characteristics and water resistance, the stratum corneum is in fact the main layer that limits drug absorption through the skin [36,63,64]. The major route of skin permeation is through the intact epidermis, and two main pathways have been identified: the intercellular route through the lipids of the stratum corneum and the transcellular route through the corneocytes. In both cases, the molecules diffuse into the intercellular lipid matrix, which is recognized as the major determinant of absorption by the skin [65], [66], [67], [68], [69]. On the contrary, the Milli-Q® formulation led to a lower caffeine penetration by using the FDC, confirming the key chemical role of the PGOA: the effects of the OA penetration enhancer on skin barrier function have been widely studied. Recent studies suggested that OA may reduce reversible the stratum corneum lipid bilayer density and thickness [70] and disrupts the skin barrier facilitating water transport [71]. Besides comparing two human skin surrogate models and two vehicles, this paper aimed to compare a novel diffusion system (i.e., MIVO®) with the FDC under dynamic in vitro circumstances to provide reliable data on penetration of caffeine and LIP1, having same molecular weight but different lipophilicity, as suggested by the OECD recommendations. The results of the comparative analysis highlighted that the MIVO® diffusion chamber shows comparable penetration trend with the standard FDC system, and a possibly better prediction of the behavior of lipophilic molecules. Then, since the FDC has been adopted as a reference diffusive chamber by the OECD guidelines, the MIVO® device

could be adopted as an efficient platform for predicting the penetration kinetics of different molecules, or to perform prescreening tests before OECD acceptance.

### 3.6 References

1. Lotte C, Rougier A, Wilson DR, Maibach HI. In vivo relationship between transepidermal water loss and percutaneous penetration of some organic compounds in man: effect of anatomic site. *Arch Dermatol Res*. 1987;279(5):351-356.
2. Van de Sandt JJM, Van Burgsteden JA, Cage S, et al. In vitro predictions of skin absorption of caffeine, testosterone, and benzoic acid: a multi-centre comparison study. *Regul Toxicol Pharmacol*. 2004;39(3):271-281.
3. Pavlačková J, Egner P, Polašková J, et al. Transdermal absorption of active substances from cosmetic vehicles. *J Cosmet Dermatol*. 2019;18(5):1410-1415. doi:10.1111/jocd.12873
4. Haq A, Goodyear B, Ameen D, Joshi V, Michniak-Kohn B. Strat-M® synthetic membrane: Permeability comparison to human cadaver skin. *Int J Pharm*. 2018;547(1-2):432-437.
5. Fartasch M. The nature of the epidermal barrier: structural aspects. *Adv Drug Deliv Rev*. 1996;18(3):273-282.
6. Madison KC. Barrier function of the skin: "la raison d'être" of the epidermis. *J Invest Dermatol*. 2003;121(2):231-241.
7. Kezic S, Nielsen JB. Absorption of chemicals through compromised skin. *Int Arch Occup Environ Health*. 2009;82(6):677-688.
8. Kielhorn J, Melching-Kollmuß S, Mangelsdorf I. Dermal Absorption: WHO/International Programme on Chemical Safety. *Environ Heal Criteria*. Published online 2005.
9. Couteau C, Coiffard L. Regulation no 1223/2009 on cosmetic products. *Nouv Dermatologiques*. 2010;29(5 PART 1).
10. Hopf NB, Champmartin C, Schenk L, et al. Reflections on the OECD guidelines for in vitro skin absorption studies. *Regul Toxicol Pharmacol*. 2020;117(March):104752. doi:10.1016/j.yrtph.2020.104752
11. Union T, Journal O, Union E. (recast) (Text with EEA relevance). 2017;10(December 2016):1-21.
12. Schreiber S, Mahmoud A, Vuia A, et al. Reconstructed epidermis versus human and animal skin in skin absorption studies. *Toxicol Vitro*. 2005;19(6):813-822. doi:10.1016/j.tiv.2005.04.004
13. Schmook FP, Meingassner JG, Billich A. Comparison of human skin or epidermis models with human and animal skin in in-vitro percutaneous absorption. *Int J Pharm*. 2001;215(1-2):51-56.
14. Vallet V, Cruz C, Josse D, Bazire A, Lallement G, Boudry I. In vitro percutaneous penetration of organophosphorus compounds using full-thickness and split-thickness pig and human skin. *Toxicol Vitro*. 2007;21(6):1182-1190.
15. Barbero AM, Frasch HF. Pig and guinea pig skin as surrogates for human in vitro penetration studies: a quantitative review. *Toxicol Vitro*. 2009;23(1):1-13.
16. Luo L, Patel A, Sinko B, et al. A comparative study of the in vitro permeation of ibuprofen in mammalian skin, the PAMPA model and silicone membrane. *Int J Pharm*. 2016;505(1-2):14-19.
17. Yoshimatsu H, Ishii K, Konno Y, Satsukawa M, Yamashita S. Prediction of human percutaneous absorption from in vitro and in vivo animal experiments. *Int J Pharm*. 2017;534(1-2):348-355.
18. Mathes SH, Ruffner H, Graf-Hausner U. The use of skin models in drug development. *Adv Drug Deliv Rev*. 2014;69:81-102.
19. Fentem JH, Botham PA. ECVAM's activities in validating alternative tests for skin corrosion and irritation. *Altern to Lab Anim*. 2002;30(2\_suppl):61-67.
20. Alépée N, Tornier C, Robert C, et al. A catch-up validation study on reconstructed human epidermis (SkinEthic™ RHE) for full replacement of the Draize skin irritation test. *Toxicol Vitro*. 2010;24(1):257-266.
21. Netzlaff F, Lehr CM, Wertz PW, Schaefer UF. The human epidermis models EpiSkin®, SkinEthic® and EpiDerm®: An evaluation of morphology and their suitability for testing phototoxicity, irritancy, corrosivity, and substance transport. *Eur J Pharm Biopharm*. 2005;60(2):167-178. doi:10.1016/j.ejpb.2005.03.004
22. Van Gele M, Geusens B, Brochez L, Speeckaert R, Lambert J. Three-dimensional skin models as tools for transdermal drug delivery: challenges and limitations. *Expert Opin Drug Deliv*. 2011;8(6):705-720.
23. Iliopoulos F, Chapman A, Lane ME. A comparison of the in vitro permeation of 3-O-ethyl-L-ascorbic acid in human skin and in a living skin equivalent (LabSkin™). *Int J Cosmet Sci*. 2021;43(1):107-112. doi:10.1111/ics.12675
24. Dumont C, Prieto P, Asturiol D, Worth A. Review of the Availability of In Vitro and In Silico Methods for Assessing Dermal Bioavailability. *Appl Vitro Toxicol*. 2015;1(2):147-164. doi:10.1089/aivt.2015.0003
25. Zhang Y, Lane ME, Hadgraft J, et al. A comparison of the in vitro permeation of niacinamide in mammalian skin and in the Parallel Artificial Membrane Permeation Assay (PAMPA) model. *Int J Pharm*. 2019;556(November 2018):142-149. doi:10.1016/j.ijpharm.2018.11.065
26. Karadzovska D, Riviere JE. Assessing vehicle effects on skin absorption using artificial membrane assays. *Eur J Pharm Sci*. 2013;50(5):569-576.
27. Miki R, Ichitsuka Y, Yamada T, et al. Development of a membrane impregnated with a poly (dimethylsiloxane)/poly (ethylene glycol) copolymer for a high-throughput screening of the permeability of drugs, cosmetics, and other chemicals across the human skin. *Eur J Pharm Sci*. 2015;66:41-49.
28. Sinkó B, Garrigues TM, Balogh GT, et al. Skin-PAMPA: A new method for fast prediction of skin penetration. *Eur J Pharm Sci*. 2012;45(5):698-707. doi:10.1016/j.ejps.2012.01.011

29. Uchida T, Kadhum WR, Kanai S, Todo H, Oshizaka T, Sugibayashi K. Prediction of skin permeation by chemical compounds using the artificial membrane, Strat-MTM. *Eur J Pharm Sci.* 2015;67:113-118.
30. Arce Jr F, Asano N, See GL, Itakura S, Todo H, Sugibayashi K. Usefulness of artificial membrane, Strat-M®, in the assessment of drug permeation from complex vehicles in finite dose conditions. *Pharmaceutics.* 2020;12(2):173.
31. Zghoul N, Fuchs R, Lehr C-M, Schaefer UF. Reconstructed skin equivalents for assessing percutaneous drug absorption from pharmaceutical formulations. *ALTEX-Alternatives to Anim Exp.* 2001;18(2):103-106.
32. OECD. OECD Guideline for testing of chemicals. Skin Absorption: in vitro Method (427). *Test.* 2004;(April):1-8. <http://www.oecd-ilibrary.org/docserver/download/9742801e.pdf?expires=1455016488&id=id&accname=guest&checksum=A084AE65CC5B740E047613C22407B0B9>
33. Gerstel D, Jacques-Jamin C, Schepky A, et al. Comparison of protocols for measuring cosmetic ingredient distribution in human and pig skin. *Toxicol Vitro.* 2016;34:153-160.
34. Franz TJ. Percutaneous absorption. On the relevance of in vitro data. *J Invest Dermatol.* 1975;64(3):190-195.
35. Herbig ME, Houdek P, Gorissen S, et al. A custom tailored model to investigate skin penetration in porcine skin and its comparison with human skin. *Eur J Pharm Biopharm.* 2015;95:99-109.
36. El Maghraby GM, Barry BW, Williams AC. Liposomes and skin: from drug delivery to model membranes. *Eur J Pharm Sci.* 2008;34(4-5):203-222.
37. Wiechers JW, Kelly CL, Blease TG, Dederen JC. Formulating for efficacy 1. *Int J Cosmet Sci.* 2004;26(4):173-182.
38. Flaten GE, Palac Z, Engesland A, Filipović-Grčić J, Vanić Ž, Škalko-Basnet N. In vitro skin models as a tool in optimization of drug formulation. *Eur J Pharm Sci.* 2015;75:10-24. doi:10.1016/j.ejps.2015.02.018
39. Larrucea E, Arellano A, Santoyo S, Ygartua P. Combined effect of oleic acid and propylene glycol on the percutaneous penetration of tenoxicam and its retention in the skin. *Eur J Pharm Biopharm.* 2001;52(2):113-119.
40. Marrella A, Buratti P, Markus J, et al. In vitro demonstration of intestinal absorption mechanisms of different sugars using 3D organotypic tissues in a fluidic device. *ALTEX.* 2020;37(2):255-264. doi:10.14573/altex.1908311
41. Cavo M, Caria M, Pulsoni I, Beltrame F, Fato M, Scaglione S. A new cell-laden 3D Alginate-Matrigel hydrogel resembles human breast cancer cell malignant morphology, spread and invasion capability observed “in vivo.” *Sci Rep.* 2018;8(1):1-12. doi:10.1038/s41598-018-23250-4
42. Marrella A. 3D fluid-dynamic ovarian cancer model resembling systemic drug administration for efficacy assay. *ALTEX.* 2020;37:1-14. doi:10.14573/altex.2003131
43. Urry LA, Cain ML, Wasserman SA, Minorsky P V, Reece JB. *Campbell Biology.* Pearson Education, Incorporated; 2017.
44. Davies DJ, Heylings JR, McCarthy TJ, Correa CM. Development of an in vitro model for studying the penetration of chemicals through compromised skin. *Toxicol Vitro.* 2015;29(1):176-181.
45. Bartosova L, Bajgar J. Transdermal drug delivery in vitro using diffusion cells. *Curr Med Chem.* 2012;19(27):4671-4677.
46. Niedorf F, Schmidt E, Kietzmann M. The automated, accurate and reproducible determination of steady-state permeation parameters from percutaneous permeation data. *Altern to Lab Anim.* 2008;36(2):201-213.
47. Mitragotri S, Anissimov YG, Bunge AL, et al. Mathematical models of skin permeability: an overview. *Int J Pharm.* 2011;418(1):115-129.
48. Vitale C, Fedi A, Marrella A, Varani G, Fato M, Scaglione S. 3D perfusable hydrogel recapitulating the cancer dynamic environment to in vitro investigate metastatic colonization. *Polymers (Basel).* 2020;12(11):1-19. doi:10.3390/polym12112467
49. Id AM, Fedi A, Varani G, et al. High blood flow shear stress values are associated with circulating tumor cells cluster disaggregation in a multi-channel microfluidic device. *Published online 2021:1-19.* doi:10.1371/journal.pone.0245536
50. LUONG M-S, LUONG M-P, Lok C, Carmi E, Chaby G. Évaluation de la biodisponibilité des dermocorticoïdes par thermographie infrarouge différentielle. In: *Annales de Dermatologie et de Vénérologie.* Vol 127. ; 2000:701-705.
51. Ng S-F, Rouse JJ, Sanderson FD, Meidan V, Eccleston GM. Validation of a static Franz diffusion cell system for in vitro permeation studies. *Aaps Pharmscitech.* 2010;11(3):1432-1441.
52. Veves A, Falanga V, Armstrong DG, Sabolinski ML. Graftskin, a human skin equivalent, is effective in the management of noninfected neuropathic diabetic foot ulcers: a prospective randomized multicenter clinical trial. *Diabetes Care.* 2001;24(2):290-295.
53. Netzlaff F, Kaca M, Bock U, et al. Permeability of the reconstructed human epidermis model Episkin® in comparison to various human skin preparations. *Eur J Pharm Biopharm.* 2007;66(1):127-134. doi:10.1016/j.ejpb.2006.08.012
54. Gray GM, Yardley HJ. Lipid compositions of cells isolated from pig, human, and rat epidermis. *J Lipid Res.* 1975;16(6):434-440.
55. Wester RC, Melendres J, Sedik L, Maibach H, Riviere JE. Percutaneous absorption of salicylic acid, theophylline, 2, 4-dimethylamine, diethyl hexyl phthalic acid, and p-aminobenzoic acid in the isolated perfused porcine skin flap compared to manin vivo. *Toxicol Appl Pharmacol.* 1998;151(1):159-165.
56. Casiraghi A, Ranzini F, Musazzi UM, Franzè S, Meloni M, Minghetti P. In vitro method to evaluate the barrier properties of medical devices for cutaneous use. *Regul Toxicol Pharmacol.* 2017;90:42-50.
57. Lubda M, Zander M, Salazar A, Kolmar H, Von Hagen J. Comparison of membrane depth determination

- techniques for active ingredient skin penetration studies using microdialysis. *Skin Pharmacol Physiol*. 2021;34(4):203-213. doi:10.1159/000515113
58. Raney SG, Franz TJ, Lehman PA, Lionberger R, Chen M-L. Pharmacokinetics-based approaches for bioequivalence evaluation of topical dermatological drug products. *Clin Pharmacokinet*. 2015;54(11):1095-1106.
  59. Gajewska M, Paini A, Benito JVS, et al. In vitro-to-in vivo correlation of the skin penetration, liver clearance and hepatotoxicity of caffeine. *Food Chem Toxicol*. 2015;75:39-49.
  60. Marrella A, Buratti P, Markus J, et al. In vitro demonstration of intestinal absorption mechanisms of different sugars using 3d organotypic tissues in a fluidic device. *ALTEX*. 2020;37(2):255-264. doi:10.14573/altex.1908311
  61. Gallagher SJ, Trotter L, Carter TP, Heard CM. Effects of membrane type and liquid/liquid phase boundary on in vitro release of ketoprofen from gel formulations. *J Drug Target*. 2003;11(6):373-379.
  62. Schäfer-Korting M, Bock U, Diembeck W, et al. The use of reconstructed human epidermis for skin absorption testing: Results of the validation study. *ATLA Altern to Lab Anim*. 2008;36(2):161-187. doi:10.1177/026119290803600207
  63. Cevc G, Vierl U. Nanotechnology and the transdermal route. A state of the art review and critical appraisal. *J Control Release*. 2010;141(3):277-299. doi:10.1016/j.jconrel.2009.10.016
  64. Jepps OG, Dancik Y, Anissimov YG, Roberts MS. Modeling the human skin barrier - Towards a better understanding of dermal absorption. *Adv Drug Deliv Rev*. 2013;65(2):152-168. doi:10.1016/j.addr.2012.04.003
  65. Alexander A, Dwivedi S, Giri TK, Saraf S, Saraf S, Tripathi DK. Approaches for breaking the barriers of drug permeation through transdermal drug delivery. *J Control Release*. 2012;164(1):26-40.
  66. Desai PR, Shah PP, Hayden P, Singh M. Investigation of follicular and non-follicular pathways for polyarginine and oleic acid-modified nanoparticles. *Pharm Res*. 2013;30(4):1037-1049.
  67. Frasch HF, Barbero AM. Application of numerical methods for diffusion-based modeling of skin permeation. *Adv Drug Deliv Rev*. 2013;65(2):208-220.
  68. Notman R, Anwar J. Breaching the skin barrier—Insights from molecular simulation of model membranes. *Adv Drug Deliv Rev*. 2013;65(2):237-250.
  69. Herman A, Herman AP. Essential oils and their constituents as skin penetration enhancer for transdermal drug delivery: a review. *J Pharm Pharmacol*. 2015;67(4):473-485.
  70. Hoopes MI, Noro MG, Longo ML, Faller R. Bilayer structure and lipid dynamics in a model stratum corneum with oleic acid. *J Phys Chem B*. 2011;115(12):3164-3171.
  71. Mack Correa MC, Mao G, Saad P, Flach CR, Mendelsohn R, Walters RM. Molecular interactions of plant oil components with stratum corneum lipids correlate with clinical measures of skin barrier function. *Exp Dermatol*. 2014;23(1):39-44.

## 3.7 Acknowledgments

This work has been developed in collaboration with: Ilaria Pulsoni, Silvia Scaglione, Monica Marzagalli, Marcus Lubda, Maurizio Aiello.



# Chapter 4

## ***In vitro* models replicating the human intestinal epithelium for absorption and metabolism studies: A systematic review**

### **4.1 Abstract**

ADME studies are a crucial component of drug discovery, as they help understand how drugs are absorbed, distributed, metabolized, and excreted in the body. Absorption, specifically oral absorption, is of particular interest as poor oral bioavailability has led to drug approval failures in the past. To better simulate human physiology and reduce the use of animals, researchers have developed *in vitro* models to mimic the intestinal barrier. However, many of these models are ineffective at predicting drug absorption and metabolism during preclinical stages due to a lack of key features of the human small intestine epithelium. This chapter provides an overview of different types of *in vitro* models used for pharmaceutical screening, including conventional 2D systems, 3D models, and micro-physiological systems. The review will discuss the benefits and limitations of these models for drug absorption and metabolism studies.

### **4.2 Introduction**

Absorption, distribution, metabolism and excretion (ADME) are biological processes that involve several organs (i.e. intestine, liver, kidneys), finally determining the drug levels in tissues [1]. Presently, poor pharmacokinetic (PK) and pharmacodynamic (PD) properties of drug candidates have been identified as potential causes for high rates of drug failures, since only one compound of hundreds is normally approved by the Food and Drug Administration (FDA) [2]. For this reason, it is increasingly evident that ADME profiling represents a fundamental step in the selection of a new chemical entity (NCE). As a consequence, the assessment of ADME mechanisms became an essential part of the drug discovery pipeline, starting from the hit identification stage to lead generation and optimization, and the early pre-clinical phase of drug development [3–6]. Oral ingested compounds, which are the most commonly administered to patients, are subject to all ADME processes; in particular, the absorption, mainly occurring at the intestinal level, is the first crucial step establishing the drug fraction which successfully enters the blood circulation. It is thus fundamental to develop drugs that can efficiently penetrate the intestinal epithelium. Here, multiple cells, carriers and enzymes are involved in the transport and metabolism of the delivered substances [4]. In fact, the gastrointestinal tract (GIT) is one of the most active and dynamic organs in the body representing the first physical and chemical barrier encountered by exogenous compounds that come from the oral cavity [7]. The GIT anatomy and physiology (e.g. pH environment) together with the drug physico-chemical properties as well as the dosage form type (e.g. capsule, solution, emulsion, tablet) condition the oral absorption of natural and artificial compounds [8,9], finally affecting their bioavailability. Recent reports highlight that 90% of the orally taken drugs have poor bioavailability as a consequence of inefficient intestinal absorption, thus hampering their ultimate therapeutic

efficacy [10,11]. Basically, oral bioavailability (F) refers to the dose that reaches intact the systemic circulation. It is defined as:

$$F = F_a * F_g * F_h \quad (1)$$

where  $F_a$  is the fraction absorbed, i.e. part of the dose absorbed into the enterocytes of the intestinal membrane;  $F_g$  is the intestinal bioavailability, i.e. part of the dose escaping the metabolism in enterocytes;  $F_h$  is the hepatic bioavailability, i.e. part of dose entering the liver that escapes the hepatic metabolism [12]. The raising issue of low oral bioavailability led to increase drug doses, resulting in high toxicity and complication risks, as well as economical wastes, or even the change of the route of administration [13]. Hence, it is mandatory to clarify and predict the complex biological phenomena taking place from the mouth to the intestine, to properly conceive and design new orally delivered therapeutics. Nowadays, animal testing still represents a gold standard in pre-clinics as it is capable to reproduce ADME processes mediated by systemic blood circulation [14]. Despite this fact, it is difficult to discern and decouple all the parameters involved in the passage of a molecule across the several biological barriers encountered in vivo [15]. Furthermore, animal-based assays often fail in predicting drug absorption and first-pass metabolism in humans due to species differences in transporters and enzymes expression as well as immune responses [16,17]. Moreover, in vivo models are generally labor-intensive, expensive and time-consuming. Therefore, there is a need to develop and promote alternative in vitro platforms in pharmaceutical studies in agreement with the 3Rs principles (Reduce, Refine, Replace) [18,19]. Conventional cell monolayers are considered the leading models for evaluating the ADME effects of orally ingested drugs. These flat systems are simple, cost-effective and standardized tools for replicating biological mechanisms in vitro. However, 2D cultures cannot precisely reproduce the physiological environment of human tissues, since cells adhere to a planar surface and display incomplete or altered cell-cell and cell-matrix interactions [20]. Cells grown on plastics are over-exposed to chemicals added in the culture medium; this frequently generates false-positive results for a drug candidate thus impairing the clinical translation of NCEs [[21], [22], [23]]. As a result, 3D cell culture systems have been realized to better recreate native tissue functionalities and pave the way for more predictive in vitro drug testing platforms [24]. 3D models provide a more physiologically relevant niche for cell growth if compared with 2D cultures, still maintaining their benefits over animals. Consequently, when drugs are tested in a 2D or 3D context, their effectiveness drastically changes [25]; specifically, cells cultured in a 3D setting are often more resistant to pharmaceutical treatments than cells grown as a monolayer, similarly to what happens in the human body [22,25]. Nevertheless, despite the great improvements, 3D in vitro models (e.g. organoids, spheroids etc.) lack of organ-specific dynamic stimuli significantly affecting cells behavior. The study of ADME mechanisms particularly requires the presence of fluid flows resembling the bloodstream, and thus the drug systemic circulation and its transport kinetics. To address this need, researchers have recently fabricated micro-physiological systems (MPS) by integrating such 3D cell cultures with microfabrication techniques to impose dynamic culture conditions at the smallest biologically acceptable scale [26]. Such MPS allow to set controlled fluid flow patterns, provide mechanical forces and an efficient transport of substances as well [27]. Especially, organs-on-chips (OOCs) support the culture of substructures considerable as micro-scaled functional units of living organs under highly reliable conditions [28]. So far, these technologies offered the chance to recreate models of kidney [29], liver [30], brain [31], heart [32], skeletal muscle [33] and intestine [34] with a significantly reduced consumption of costly reagents, number of cells and drugs [35,36]. The use of MPS enhanced the automatization and parallelization of experiments for the collection of large-scale data sets of ADME profiles, potentially speeding up the drug discovery and development processes [24,28]. However, the over-miniaturization of these

models in some cases may affect the faithful reproduction of organ-level functions, requiring an experimental complexity that simultaneously hinders the practical operation and manipulation of the system [23,36,37]. Hence, this review details the intestinal models currently adopted for investigating the absorption of orally administered compounds that include 2D conventional intestinal monolayers, complex 3D tissues, and novel emerging physiologically relevant MPS culture systems. In short, we will focus on intestine models that reproduce the multiple features of the human organ and accurately predict the time-dependent drug absorption profiles occurring *in vivo*.

### 4.3 Physiology of the GIT

Drugs orally delivered follow a precise path starting from the mouth, passing through the esophagus and the stomach, terminating the travel in the large intestine. This alimentary canal is lined with a mucosa, which is composed of an epithelium covering a lamina propria where blood and lymphatic vessels reside. After traversing the first portions of the GIT, a drug (e.g. tablet) enters the stomach, where it encounters an acidic environment (pH ranges from 1.5 to 3.5 [38]) and specific enzymes involved in digesting food [39]. Muscular contractions also occur to break up the solid tablet into smaller particles, resulting in its disintegration and dissolution. In particular, the drug aqueous solubility, lipophilicity, and hydrophilicity, as well as the presence of excipients, are crucial factors in determining the successful fulfilment of these preliminary absorption phases [12]. Subsequently, the gastrointestinal content navigates to the small intestine (duodenum, jejunum, and ileum), which represents the major site of absorption of nutrients, water, electrolytes and xenobiotics [40]. Here, the absorptive mucosa is characterized by a simple columnar epithelium surmounting a highly blood perfused lamina propria, which maximize the possibility of molecules entering the systemic circulation through mesenteric vessels. Herein, the mucosa possesses a large surface area (250 m<sup>2</sup>) with wide folds, villi and microvilli (Figure 11) which significantly impact the uptake rate by augmenting the available absorptive surface area [41]. Layers of smooth muscle are also present within the lamina propria inducing the villi to undulate and the luminal content to dynamically mix, thus promoting the ingestion of the substances [42].

The intestinal epithelium consists of a single layer comprising several types of cells, as shown in Figure 11. Specifically, enterocytes are the intestine predominant cells. They are columnar-type cells held together by tight junctions, which play a pivotal role in regulating the diffusion of small compounds and the exclusion of toxic large molecules. In addition, they are characterized by the presence of about 3000-7000 microvilli over their apical membranes, which greatly benefit the absorption mechanism [43]. However, enterocytes contain also a large number of drugs- and food- metabolizing enzymes for the xenobiotics and nutrients digestion as well as for the exogenous substance protection [[44], [45], [46]]. Therefore, enzyme-guided reactions taking place in the small intestine limit the oral bioavailability of administered compounds [47]. For these reasons, taking into account intestinal metabolism is thus necessary. The enterocytic monolayer is interrupted by the residence of both enteroendocrine cells and Goblet cells. The firsts are responsible for releasing peptide hormones, which are correlated with tissue repair, angiogenesis, enterocytes differentiation and polarization [48]. Conversely, goblet cells produce mucus, a rheological substance covering the intestinal epithelium, which acts as a protective layer against noxious substances and microbial infections like bacteria or toxins. Importantly, this gel is the first barrier that filters and thus narrows the absorption of molecules, being essential in the maintenance of intestinal homeostasis [49].

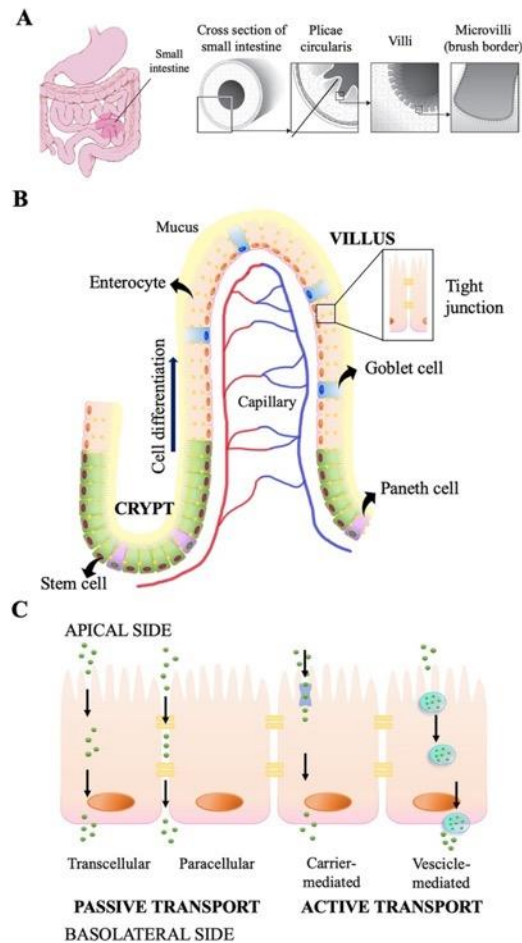


Figure 11: A cartoon depicting the architecture of the small intestine and its transport mechanisms. (A) GIT consists of the esophagus, stomach, small intestine, large intestine, and rectum (left, [62]). Schematic cross-sectional views of the small intestine tissue with an increasing magnification (right). Wide folds of mucosa (plicae circulares) are characterized by finger-like villi projections protruding into the intestinal lumen; microvilli are also present over enterocytes to increase the absorptive area; reprinted and adapted from [63], Copyright (2008) with permission from Elsevier. (B) Illustration of a typical basal crypt/villus units of the small intestinal mucosa. This columnar epithelium comprises several types of adjacent cells, which are firmly joined by tight junctions; a layer of mucus surmounts the apical cell membranes providing an additional physical and biochemical barrier, while blood vessels highly perfuse the tissue maximizing the possibility of molecules to enter the blood circulation. (C) Transport pathways of substances across the intestinal epithelium; absorption can occur in parallel involving passive (transcellular and paracellular) and active (transcellular carrier-mediated and vesicle-mediated) mechanisms.

Mucus properties and thus function vary along with the GIT; for example, the small intestinal mucus contains large pores up to  $2 \mu\text{m}^2$  for ensuring a massive absorption of nutrients [50]. Recently, researches demonstrated that alterations in the mucus architecture and content may lead to several pathologies, confirming the remarkable impact of this viscous gel on intestine health [51]. Columnar intestinal stem cells (ISCs), located in the so-called crypt base, are capable to differentiate into all other intestinal cell types, providing an extremely high intestinal self-renewal preserving the tissue integrity and function [52,53]. Finally, also Paneth cells reside in the crypt region and are specialized in supporting ISCs within the niche by secreting growth factors and producing antimicrobial peptides [54,55]. Ingested drugs travel from the luminal side of the intestinal epithelium to the basolateral one to enter the mesenteric vessel through various mechanisms involving either passive or active transports (Figure 11). Passive transport may occur via the transcellular pathway, in which

drugs pass through the cell membrane, and the paracellular pathway, in which drugs pass through the intercellular spaces. Both of them are regulated by Fick's law of diffusion. Besides this, the apparent permeability coefficient ( $P_{app}$ ) describes the amount of drug crossing the barrier per unit time and unit area ( $A$ ), and it can be calculated in either the apical to basolateral (influx) or the basolateral to apical (efflux) direction through the equation below derived by Fick's law:

$$P_{app} = \frac{dQ/dt}{A C_0} \quad (2)$$

where  $dQ/dt$  expresses the rate of drug appearance in the acceptor side and  $C_0$  is the initial drug concentration in the donor side [56]. Notably,  $P_{app}$  value is usually adopted to determine the oral fraction absorbed ( $F_a$ ) in humans [57,58]. The paracellular mechanism is the primary diffusion process for hydrophilic substances, occurring through the water-filled intercellular spaces (tight junctions). Hence, the paracellular passage is strictly referred to the integrity of the barrier, which can be monitored in vitro by measuring the trans-epithelial electrical resistance (TEER) [59,60]. On the other hand, transcellular transport mostly guides lipophilic compound uptake across the lipid cell membranes. Nonetheless, also active transport promotes the passage of compounds towards the basolateral side of the small intestine. Transcellular carrier-mediated mechanisms and the vesicular-mediated endo- or trans-cytosis actively carry drugs [61]. In addition, efflux transporters present on the apical or basolateral side can modulate the transfer from the cell cytoplasm back into the intestinal lumen, decreasing the net amount absorbed. Accordingly, complex intestinal epithelium models recapitulating these various cell dynamics are required for carrying out more predictable pharmacological investigations in vitro.

#### **4.4 2D in vitro models to evaluate intestinal absorption**

Nowadays, 2D culture systems remain widely employed to determine the bioavailability of an orally delivered drug, mainly because of their low costs, high reproducibility, and ease of manipulation. In particular, 2D in vitro models conventionally employed in pharmacology can be divided into two main categories: (i) synthetic models based on lipidic membranes, which offer a great reproducibility and stability, used to study passive diffusion processes [64], and (ii) cell-based cultures that are living and more reliable systems allowing broader spectrum analyses of intestinal absorption (Figure 12A).

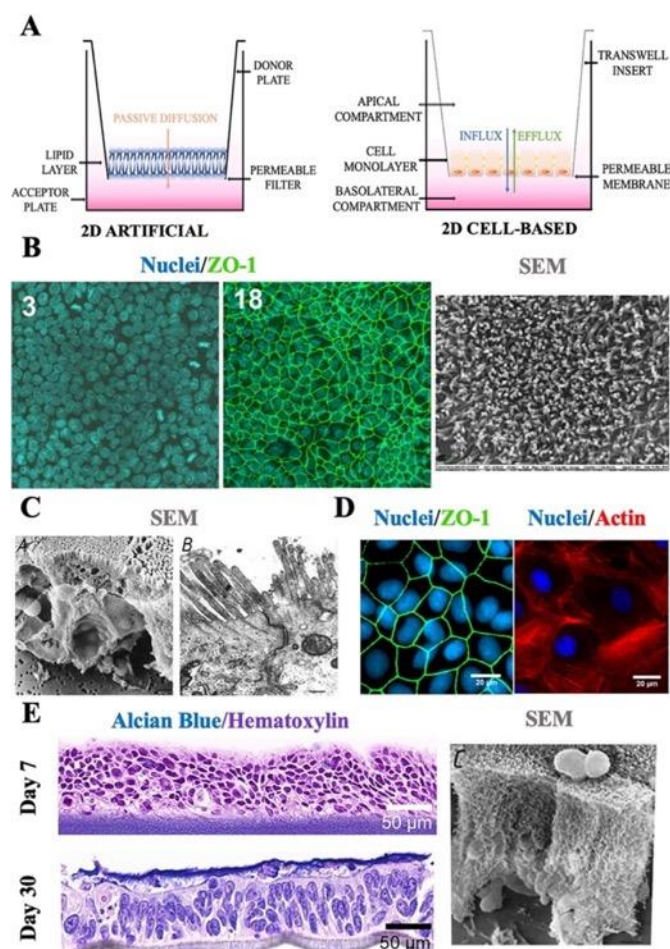


Figure 12: 2D culture systems currently used to determine the bioavailability of orally delivered drugs. (A) Scheme of artificial lipid-based (left) and cell-based (right) monolayers setup. (B) Development of tight-junctions in 2D Caco-2 cell monolayers after 3 (left) and 18 (middle) days of plating. Pictures are obtained by merging 100-frames z-stacks of the junction-mediating ZO-1 protein; reprinted and adapted from [166], Copyright (2012), with permission from Elsevier. SEM image showing a highly packed microvilli pattern over Caco-2 cells after 21 days of culture (right, [167]). (C) A side view of TC-7 cells cultured on a polycarbonate filter with brush borders and microvilli (left, SEM image); scale bar = 1.9  $\mu\text{m}$ ; two adjacent TC-7 cells displaying microvilli and strictly held by a tight junction (right, TEM image); scale bar = 0.4  $\mu\text{m}$ ; reprinted and adapted from [134] Copyright (2001), with permission from Elsevier. (D) Fluorescence images demonstrating the establishment of tight junctions (left) and a dense structure of actin filaments (right) in a 2D MDCK cell-based culture [168]. (E) Histology of an HT29-MTX cell monolayer; cells are organized in a multi-layered structure after 7 days, whereas they are well polarized and covered with mucus (stained in blue) after 30 days of static culture (left); reprinted and adapted with permission from [169] Copyright (2018) American Chemical Society. SEM image showing a lateral view of an HT29-MTX monolayer cultured on a polycarbonate filter with few microvilli and mucus droplets covering the apical membrane of the cells (right); scale bar = 2.4  $\mu\text{m}$ ; reprinted and adapted from [134] Copyright (2001), with permission from Elsevier.

## 6.5.1 Synthetic models

### 6.4.1.1 Pampa

The Parallel Artificial Membrane Permeability Assay (PAMPA) is a cell-free permeation system that reproduces in vitro the phospholipid composition of the desired human biological barrier (e.g. gut) for evaluating the passive transcellular absorption [65]. Especially, this completely artificial technology consists of two compartments separated by a membrane soaked with a mixture of phospholipids dissolved in an organic solvent,

mimicking the lipidic membrane of the enterocytes [66]. Considering that 80–95% of commercial drugs are primarily absorbed through passive diffusion, PAMPA represents a useful tool for an early-stage ADME screening of orally administered compounds [66,67]. Particularly, the rate of permeation across the lipid-based membrane represents a valid indicator of a drug absorption potential. In fact, several studies demonstrated a good relationship between the permeability data measured by PAMPA and those obtained with the Caco-2 cell-based model for drugs transcellularly transported [68]. On the other hand, PAMPA is unable to classify hydrophilic compounds transferred via paracellular pathways. To overcome this limitation, other variants of the original structure were developed by changing the key factors influencing the membrane performances (e.g. the nature of the filter support, pH conditions and lipid membrane composition) [7]. Specifically, the Double Sink PAMPA showed a stronger correlation with the human data and an improved predictive potential for poorly water-soluble drugs [69]. Hence, PAMPAs revealed to be rapid, solid and low-cost platforms for measuring permeabilities of lipophilic molecules across several biological barriers (gut but also skin, blood-brain barrier), consequently limiting cellular-based assays or animal testing in the pre-clinical scenario [70,71]. Nevertheless, their potency and applicability are hampered by their acellularity and the presence of organic solvents, which can interact with the supportive filter [64]; thus other synthetic alternatives have been recently developed [7].

#### 6.4.1.2 Pvpa

The Phospholipid Vesicle-based Permeation Assay (PVPA) is another artificial membrane-based system currently employed for the pharmaceutical characterization of NCEs [72]. As PAMPA, PVPA was introduced for *in vitro* replicating the lipid composition of biological epithelia to measure the permeability of passively delivered drugs [73,74]. Unlike PAMPAs, this is a synthetic organic solvent-free platform consisting of a tight barrier fabricated by depositing liposomes between the pores and on the top of filter support emulating the phospholipid bilayer, such as that of the intestinal cell membranes [75]. Typically, PVPA is capable to better envision the human absorbed fraction compared to PAMPA by performing experiments over a more biologically-relevant context, providing more similar results to Caco-2 cells cultures [64,73,74]. Over the years, diverse advancements of the PVPA led to remarkably enhance the biomimetism of this model. For instance, a negative charge was set up, and the lipid composition of the membrane was modified to perfectly match the composition of the intestinal barrier, thus allowing to carry out permeability tests under physiologically relevant pH conditions. In this way, an accurate capability to correctly classify at least 80% of tested compounds was exhibited accordingly to the *in vivo* absorbed fractions [74,76]. PVPAs is considered as an established approach for precisely assessing *in vitro* the absorptive potential of lipophilic drug candidates with high reproducibility and greater handling compared to cell-based models [74,76]. Nonetheless, significant morphological and physiological features are not expressed, such as the presence of villi and active transport proteins, differently from cell-based assays (Table 5). Consequently, PVPA, as well as PAMPA, remains a suitable tool only to predict the permeability of drugs transcellularly absorbed.

### 6.5.2 Cellular models

#### 6.4.2.1 Caco-2 cell line

The Caco-2 cell line, isolated for the first time by Fogh et al. [77] from a human colon adenocarcinoma, is the most widely used cell-based model to in vitro simulate the physical and biochemical barrier of the human intestine in the pharmaceutical and nutraceutical field. Caco-2 cells represent a gold standard accepted by regulatory authorities for ADME-Tox studies since they demonstrated to be particularly useful to (i) elucidate the absorption and metabolism of substances across the intestinal epithelium, (ii) predict the absorbed fraction in humans [78], and (iii) study, select and classify drug candidates under controlled conditions, according to the Biopharmaceutics Classification System (BCS) [79]. Indeed, despite their colonic origin, Caco-2 monolayers resemble most of the morphological and functional characteristics of the small bowel [80]. Conventionally, these cells display undifferentiated characteristics at the early stages of culture (after 3 or 4 days), whereas they are capable to reach an enterocytic phenotype at the late confluence (in about 3 weeks), expressing typical cytoskeleton proteins (e.g. villin [81]) and forming a polarized layer with brush-border microvilli (confirmed by sucrase immunoreactivity [82]) as well as tight junctions (confirmed by occludin antibodies staining [83]) between adjacent cells, as shown in Figure 12. However, these strict junctions entail a higher transmembrane resistance (150-400  $\Omega \cdot \text{cm}^2$  [84]) respect the small intestine (12-120  $\Omega \cdot \text{cm}^2$  [85]). This can be due to a smaller number and size of water-filled pores present in Caco-2 cells (about 3.7 Å) than the first intestinal tracts (8-13 Å) [59, [86], [87], [88]]. Accordingly, multiple studies, which investigated the paracellular uptake of hydrophilic compounds (e.g. atenolol, mannitol), indicated the inadequacy of this model in predicting the paracellular transport [[89], [90], [91]]. In fact, in literature, a systematic underestimation of the paracellular diffusion kinetics is extensively reported for Caco-2 cells. For example, remarkable divergencies respect to human jejunum regarding slowly and incompletely absorbed drugs were detected. The transport rates resulted to be 30- to 80-fold lower in the Caco-2 model, highlighting considerable limitations of such cell line in precisely replicating the physiological and anatomical jejunum properties [90]. Moreover, it is well-known that poorly absorbable drugs, which are unable to cross the villus narrow junctions, stay for a long time in the lumen, precipitating towards the crypt regions, where they can pass through the leakier crypt junctions. Nevertheless, this phenomenon cannot occur in flat monolayers because of the lack of a 3D crypt-villus structure [92]. Integrity alterations of the junctions by calcium-chelating solutions (e.g. EDTA) can be helpful to improve the permeability and thus the predictability of the paracellular pathway; however, the employment of these solvents is contraindicated [58]. Contrarily, the high similarity with absorptive enterocytes led Caco-2 monolayers to be considered an efficient intestinal membrane-mimicking model for studying the passive transcellular penetration of lipophilic compounds (e.g. propranolol and metoprolol). The permeability of rapidly and completely absorbed therapeutics differed 2- to 4-fold with respect to human intestine values for this route [90] and a high correlation was observed between Caco-2 Papp and in vivo Fa values. Surprisingly, reasonable correlations were also found for poorly absorbable compounds, fitting well human published PK data of 30 marketed compounds [58] and peptidomimetics [93,94]. Therefore, Caco-2 can be considered a valuable tool to screen passively transported compounds (correlation coefficient >83% [95]) as much as more complex models like in situ perfusion ones [96,97]. Less attractive results were obtained by using these cells to model active transport. Although some analyses provided promising outcomes about ATP-dependent paths [98] and gene profiles of intestinal transporters, such as P-glycoproteins (P-gps), involved in maintaining the intestine homeostasis by mediating xenobiotics efflux and secretion [99], expression patterns of other proteins (e.g. breast cancer resistant proteins (BCRPs) and multidrug-resistant proteins (MRPs)) [[100], [101], [102]] were observed to be considerably different from duodenal [95] and jejunal tissues [103]. For these reasons, even though FDA and



European Medicines Agency (EMA) acknowledge this cancerous line as a surrogate for in vitro permeation assays, there is still an ongoing debate on whether it represents a biorelevant model for certain applications, such as the active absorption or the transporter-mediated drug-drug interactions [103]. Moreover, an intrinsic variability between and within laboratories as well as a strong dependence on culture time was noticed in the transporters content [103]. Likewise, some defects can be observed for metabolizing enzymes responsible for the elimination of many drugs (e.g. cytochrome P450 -CYP- isoforms) [44,45]. In particular, the deficiency of CYP3A4 enzymes represents a remarkable drawback to investigate Phase I metabolism and the first-pass effect of orally taken drugs [104,105]. To solve this, some groups tried to induce CYP3A4 expression by treating Caco-2 cells with 1- $\alpha$ -25-dihydroxyvitamin D<sub>3</sub> or incorporating CYP3A4 with the NADPH into the basolateral side [106] greatly improving the relevance in estimating the first-pass metabolism in intestinal kinetics [79]. On the other hand, the presence of hydrolases associated with the microvillar membranes was verified in Caco-2 cells, allowing to accurately mimic the brush-border enzyme activity of the small intestine [81]. Thereby, controversial outcomes and disagreements can be found in literature. This could be due to the colonic cancerous origin of these cells, which show structural and functional features more similar to large intestinal cells than small bowel ones (e.g. stronger tight junctions, higher TEER values, altered enzymes and transporters expression) [104,107]. Furthermore, many works highlighted that Caco-2 cell-based systems are highly influenced by the experimental culture conditions, the cell line itself (i.e. the stage of cellular differentiation, whether the cells have reached confluency), and the passage number [108]. They are a heterogeneous population whose properties can differ between and within laboratories based on the different culture periods and the culture media used. Thus, it is fundamental to calibrate Caco-2-based experimental systems with reference compounds (chemicals with known absorbed fraction in vivo) and carefully control the environmental (temperature, pH) and barrier conditions (TEER) [78]. Currently, Caco-2 static monolayer cultures are a gold standard for in vitro assays of intestinal barrier properties following exposure to pharmaceutical and nutraceutical compounds [109]. It is commonly accepted that Caco-2 cells are the best intestinal epithelium model since they allow to exactly replicate the uptake via the transcellular pathway, which is the most common drug permeation route [14]. On the other hand, the active passage as well the metabolism of drugs in the gut is drastically underestimated [82,90]. Moreover, the absence of a mucus layer has a significant impact on this model fidelity, since it represents the first barrier that molecules meet, restricting their availability to the underlying cells [110].

#### 6.4.2.2 TC7 cell line

The TC-7 cell line is one of the Caco-2 subclones isolated to overcome the main limitations of the parental line, still maintaining its morphology (Figure 12C) [111]. Among the several advantages of TC-7 cells, the faster cellular growth due to a shorter doubling time and the lower TEER values are certainly favorable features to more closely simulate the small intestinal epithelium [82,111]. Also, being a homogeneous population, less variability between and within laboratories was observed, ameliorating the robustness of the collected data [111]. Concerning the morphological features, the TC-7 monolayer revealed an increased height ( $15.4 \pm 1.2 \mu\text{m}$ ) respect Caco-2 cells ( $13.8 \pm 2.4 \mu\text{m}$ ) more similar to the native tissue ( $25 \mu\text{m}$ ) [112]. Hence, TC-7 cells are very useful to analyze the transport biokinetics of chemicals. A good correlation between this subclone line and the Caco-2 cells was found for transcellularly absorbed drugs, indicating that the TC-7 model is an excellent alternative to Caco-2 monolayers [113,114]. Importantly, TC-7 cells also showed the ability to properly carry paracellular markers (e.g. mannitol, PEG-4000) via this passive route and

a high content of apical transporters, being capable to even reproduce the carrier-mediated delivery, unlike Caco-2 cells [115]. Multiple brush-border enzymes resembling the human enterocytic metabolism were also observed, therefore eclipsing the original model [113]. The amount of UDP-glucuronosyltransferases (phase II metabolic enzyme), hydrolase sucrase-isomaltase and CYP3A isoenzymes (e.g. CYP3A4 and CYP3A5), which reached the culmination at late confluency, were noticed to be expressed very similarly to the human tract of jejunum [116] [108,117]. Furthermore, it was observed that also P-gp-mediated efflux occurred in a more in vivo-like manner than parental line [111,115]. Consequently, it is reasonable to consider TC-7 cells as a useful option for studying intestine first-pass metabolism and active absorption paths, differently from Caco-2 monolayers [118]. However, further rigorous investigations about their employment are desirable to better evaluate their large-scale screening potential, as little permeability data are available for TC-7 cells [115].

### 6.4.2.3 MDCK cell line

The Madin-Darby canine kidney (MDCK) is another epithelial cell line used for permeability measurements, which was isolated for the first time by Madin & Darby from a canine distal renal tissue [82]. Despite their different origin, MDCK cells are morphologically analogous to Caco-2 cells, imitating the in vivo intestinal barrier topology. In fact, these cells converge to form a polarized columnar monolayer displaying brush borders and tight intercellular junctions ( $173 \pm 51 \Omega \cdot \text{cm}^2$ ) (Figure 12D) [118]. Two different strains of MDCK line were distinguished: (i) MDCK-I, which can generate a tight epithelium with high TEER values (above  $1000 \Omega \cdot \text{cm}^2$ ) and (ii) MDCK-II, which assemble a more permeable layer with lower TEER values (about  $100 \Omega \cdot \text{cm}^2$ ), thus being closer to the small intestine than Caco-2 cells [119]. In particular, these cells are less time-consuming (cells converge after 3-5 days of culture) than other epithelial cell models, consequently reducing the possibility of cell contaminations as well as costs [79]. For such benefits, MDCK cells were adopted to carry out rapid and bidirectional permeability screenings across renal and gastrointestinal epithelia during the early stages of drug discovery [119,120][118]. A clear relationship between this canine line and the human-derived Caco-2 one was demonstrated for passively absorbed drugs with a robust correlation ( $r^2=0.79$ ) [121]. Furthermore, MDCK cells well correlate human absorption data ( $r^2=0.58$ ), in line with Caco-2 cells ( $r^2=0.54$ ) [121,122]. However, several shortcomings affect the experiments carried out by using MDCK cells. Firstly, as the monolayers do not tolerate great amounts of organic solvent, poorly soluble aqueous compounds are difficult to assess by using these systems. Moreover, the non-intestinal origin of these cells as well as their heterogeneity may hamper the reliability of the results depending on cells source, culture and transport conditions. The expression levels of transporters and the metabolic activity appeared also to be very different in the MDCK line respect the native scenario and the intestinal-derived cells [120]. To solve this lack, for example, the human MDR1 gene was transferred in the MDCK-II cells to obtain similar levels to the intestinal tract [7]. Interestingly, these transfected MDR1-MDCK cells overexpressed an isoform of P-gp as well as an enhanced polarized efflux of known substrates (e.g. digoxin) compared to other MDCK clones and Caco-2 cells [123]. Hence, MDR-1 transfected MDCK cells share many common epithelial cell aspects with the human intestinal mucosa and can be a helpful model for examining the carrier activity of drug candidates, such as for the P-gps. Nevertheless, their predictability and applicability remain very low compared to Caco-2 cells [124].

### 6.4.2.4 HT-29 cell line

HT-29 cells are a human colon adenocarcinoma cell that gained increasing attention due to the typical characteristics of mature intestinal cells [125]. HT-29 cells express features of both absorptive enterocytes and intestinal secretory cells producing a gelatinous mucus-like substance. For this reason, this cellular model is broadly employed to perform bioavailability studies or to investigate the intestinal immune response to bacterial infections that may affect the properties of the secreted mucus [126]. Notably, HT-29 cells phenotype strictly depends on the culture conditions, with particular attention to the presence or absence of glucose in the culture medium. These epithelial cells form undifferentiated and unpolarized multilayers without any typical features of intestinal cells under normal glucose supply conditions [127]. Conversely, HT-29 cells undergo intestinal differentiation patterns whether modifications of the culture medium or the addition of differentiation-inducers are used. For example, they can express several characteristics similar to the human enterocytes such as polarized monolayer structures, well-developed tight junctions, brush borders and microvilli when a glucose-free culture medium is used [128]. In addition, the presence of brush border-associated enzymes was observed in enterocyte-like HT-29 cells [129]. Interestingly, most of them also express proper levels of villin as well as functional receptors for peptides and hormones existing *in vivo* [81,127,129]. Nevertheless, considering that not all hydrolases are present (e.g. lactase) and the enzymatic activity (e.g. hydrolases and sucrase-isomaltase) is lower than Caco-2 cells and the human small intestine, they cannot be properly considered as a reliable model of small bowel enterocytes [81,127]. On the other hand, they cannot be treated as colonic enterocytes since they express apical-localized hydrolases, which are normally absent in the colon [125]. The utility of this cell line is thus controversial also because several receptors naturally absent in the human epithelium (such as the neurotensin [130]) were detected in HT-29 cells, and others that are traditionally present (like that for the peptide YY or neuropeptide Y) have not been identified yet [126]. To surmount these constraints, other strategies to induce the enterocytic differentiation in HT-29 cells were carried out [131,132]. Strikingly, such efforts gave rise to other interesting lines: HT29-18-N2, HT29-H and HT-29/16E. that produce a great number of mucins, accurately resembling the *in vivo* activity of goblet cells, thus being useful to examine the influence of the mucus layer on the intestinal absorption [81]. Especially, the HT29-H clone showed a variable thickness of the layer and a paracellular permeability higher and more similar to the native tissue with respect to Caco-2 monolayers [133]. In spite of this, HT-29 cells treated with methotrexate (MTX; HT29-MTX) currently remain the most used model to inspect how foods and xenobiotics alter the mucus and vice versa [134]. In particular, the levels of secreted mucins are influenced by the applied concentration of this drug. Low doses of MTX correspond to a heterogeneous set of both columnar absorptive and mucus-secreting cells, whereas mucus-secreting cells prevail by increasing the amount of MTX [126]. Moreover, HT29-MTX-D1 and HT29-MTX-E12 sub-populations were selected due to their ability to (i) develop tight junctions, (ii) continuously secrete mucus and (iii) maintain stability for over 7 passages. Interestingly, it was noticed an inverse relationship between the permeability of lipophilic drugs (e.g. barbiturates and testosterone) and the thickness of the mucus layer. Especially, Papp values were lower in HT29-MTX-E12, which displayed a leakier but thicker mucus layer, than HT29-MTX-D1, which secreted mucus in smaller quantities [129,135]. Therefore, such cells revealed to effectively reproduce the mucus native properties. Despite the common limitations due to the human colon carcinoma source, parental and sub-derived HT-29 cells proved to be a valuable model to screen endogenous and exogenous compounds [136,137]. The mucus-secreting phenotype received a huge interest in studies focused on food digestion and drugs bioavailability since this substance influences intestinal tissue homeostasis. Along this line, HT29-MTX cells appear to be the most suitable model due to their efficient mucus production (Figure 12), and for

this reason, they are largely co-cultured with Caco-2 absorptive cells to create a more suitable in vitro intestinal-mimicking epithelium [138].

#### 6.4.2.5 IEC cell line

The group of intestinal epithelial cells (IECs) is an intestinal rat cell line that can form pseudo-monolayers exhibiting microvilli, tight junctions and an amorphous substance similar to the basement membrane [82,139,140]. Even though their differentiation can be hardly induced in vitro since they derive from undifferentiated crypt epithelial cells, IEC cells treated with fetal rat or mouse gut mesenchyme become (i) absorptive, (ii) goblet, (iii) endocrine, and (iv) Paneth's granular intestinal cellular types [81]. The IEC line includes various cellular subgroups, such as the IEC-18, IEC-6 and IEC-14 line. Specifically, the IEC-14 cell line is very helpful in examining the regulation of crypt cellular proliferation and differentiation [139]. However, the IEC-18 subline is the most common intestinal barrier model traditionally utilized for investigating in vitro amino acids, glucose and other nutrients ingestion and digestion as well as cholesterol synthesis [118]. Importantly, the TEER of these cells ( $55 \Omega \cdot \text{cm}^2$ ) was found to be comparable to the small intestine part of the ileum ( $88 \Omega \cdot \text{cm}^2$ ), where paracellular permeation massively occurs [141,142]. As a consequence, it was confirmed that IEC cells better recapitulate the paracellular pathways in comparison to Caco-2 cells [143]. Indeed, paracellular hydrophilic markers such as mannitol, dextran and PEG-4000 demonstrated greater permeability coefficients across IEC-18 monolayers and molecular radius-dependence transport, unlike colonic cells [144]. Likewise, natural compounds such as the glycosides of genistein and daidzein (i.e. genistin and diadzin, respectively) crossed the intestinal IEC-18-based epithelium via paracellular delivery with a high absorption rate [145]. Hence, IEC-18 cells provide a size-selective barrier to in vitro discriminate and classify the hydrophilic molecules based on their molecular weights [141,146]. This is striking respect to Caco-2 cells that systematically underestimate paracellular uptake. Conversely, uptake rates comparable to the in vivo scenario and Caco-2 cells were detected for lipophilic molecules transferred by the passive transcellular route, even though IEC-18 cells are less differentiated than Caco-2 cells [141,146]. Indeed, they possess less-developed tight junctional complexes and a slight polarization, and present a low expression of brush border enzymes (e.g. the sucrase-isomaltase or the intestinal isotype of alkaline phosphatase) [139,147]. This also results in an altered expression of carrier-mediated transport systems such as those of the MRP family. Besides, the quite absence of P-gps at the apical domain further correlate the low differentiated status of these rat cells with their crypt origin [141,144]. Given together, these outcomes suggest that this ileum-derived line is a useful in vitro cellular system for predicting the diffusion-mediated mechanisms of absorption, especially for hydrophilic compounds, which Caco-2 cells fail to anticipate. Notably, they precisely resemble the in vivo morphology and functionality of intestinal crypts rather than villus-localized enterocytes given the enormous lack of carriers and enzymes. As a result, these rat colon-derived cells may rapidly lose their markers of differentiations and their specific properties, thus being unstable and unpredictable [82,147].

#### 6.4.2.6 HIEC cell line

The need to resort to a new type of intestinal cells to overcome the shortcomings originating from the cancerous nature of Caco-2 and HT-29 cell lines was addressed by employing human intestinal epithelial cells (HIEC). These cells represent a valuable option being capable to show some human crypt-like features [148]. Specifically, HIECs can form monolayers of polarized columnar cells with dense microvilli and poorly organized tight junctions, resulting in a morphology very similar to the in vivo context [149]. They exhibit

low TEER values ( $98.9 \Omega \cdot \text{cm}^2$ ) as well as an aqueous pores size and distribution that determine the suitability of this line in replicating some of the crucial aspects and functioning of the human small intestine domain [150]. Accordingly, the existence of a sigmoidal relationship between  $F_a$  in vivo values and those measured in vitro for ten paracellularly delivered compounds was demonstrated, indicating a greater sensitivity and accuracy in anticipating the human paracellular uptake respect Caco-2 models. In particular, high permeability coefficients are systematically found for incompletely and poorly absorbable drugs with HIEC cells. Likewise, transcellularly transported drugs well permeate, highlighting the efficiency of this human-derived model in predicting the fractions absorbed in humans [151]. Furthermore, intestinal cell markers typical of undifferentiated crypt cells were found to be expressed in this line, such as low levels of intestinal enzymes (e.g. sucrase-isomaltase, alkaline phosphatase, CYP2C9, CYP2C19) [152,153]. Notably, other studies discovered low amounts of CYP3A4 (<7% of the human small intestine content) in HIECs and no considerable discrepancies between HIEC and Caco-2 monolayers for drug-metabolizing enzymes (e.g. CYP3A5) and transporters (e.g. BCRP, MRP1, MRP2, and MRP3) [150]. Different stages of differentiation in HIEC cells can be achieved, replicating human crypt or enterocytes aspects. This may also vary based on the tissues from which HIEC cells derive. For example, Takenaka et al. investigated the characteristics and the possible applications of these epithelial cells differentiated from adult ISCs. Such cells, which possess a long-term proliferation and high-differentiating capabilities, generate absorptive enterocytes, but also goblet, enteroendocrine and Paneth cells under appropriate culture conditions [150]. Another alternative approach may be to obtain HIEC cells from the fetal human intestine at mid-gestation of a terminated pregnancy [154] or use fetuses derived by legal abortions, which have tissues with rapid metabolism and adult differentiated markers already expressed [148]. Nonetheless, despite their advantages, these cells are forbidden to use due to related ethical issues in many countries [148].

Table 5: Advantages and disadvantages of synthetic vs cellular models.

	ADV	DIS-ADV
Synthetic models	<ul style="list-style-type: none"> <li>• Low costs</li> <li>• Rapid to use</li> <li>• Easy to manipulate</li> <li>• Robust for testing lipophilic compounds</li> <li>• Capability to reproduce passive transport</li> </ul>	<ul style="list-style-type: none"> <li>• Poor prediction of paracellular route</li> <li>• No reproduction of intestinal epithelial morphology</li> <li>• No expression of transporting proteins</li> <li>• Absence of enzymes</li> <li>• Over-simplification of the system</li> </ul>
Cellular models	<ul style="list-style-type: none"> <li>• Capacity to mimic the <i>in vivo</i> anatomical, biochemical and structural features of the small intestine</li> <li>• Capability to reproduce both passive and active transport</li> <li>• Possibility to utilize human cells</li> </ul>	<ul style="list-style-type: none"> <li>• High variability related to cell differentiation and culture conditions</li> <li>• Longer times of preparation</li> <li>• Risks of contamination hampering the entire experiment</li> <li>• Higher costs</li> </ul>

#### 6.4.2.7 Co-culture models

The aforementioned cellular models remain far from reflecting the complex heterogeneity of the human intestinal organ [82]. For this reason, conventional Caco-2 cells are often co-cultivated with other cell types to generate more predictable models and thus perform effective drugs screening assays [118,155]. For example, the integration of Caco-2 cells expressing enterocytic markers with secretory cells, such as HT-29 sub-populations, may provide an environment that better mimics the *in vivo* conditions. Their contemporary presence can modulate the structure of the junctions to be more similar to those of the small intestine [120]. Indeed, Caco-2/HT-29 and Caco-2/HT-29-H mixed monolayers display a brush border membrane with tight junctions, and sparse irregular microvilli apically [156].

Moreover, a higher permeability closer to the Fa values was showed for passively ingested compounds respect the pure Caco-2-based system, providing an improved prediction of both transcellularly and paracellularly transferred drugs [157]. Similarly, the permeabilities of drugs absorbed via paracellular, transcellular and carrier-mediated pathways were evaluated by using three different initial seeding ratios of Caco-2 and HT29-MTX cells. Although no significant differences with Caco-2 pure layers were observed for the transcellular route, augmenting the fraction of HT29-MTX cells resulted in an increased uptake of compounds paracellularly delivered [155]. Interestingly, the P-gps expression in the co-cultures was detected at a lower level compared to the Caco-2 model, and an inverse relationship was noticed between the amount of P-gps and the fraction of the goblet-like cells [155,158]. Nevertheless, this cell mixture is not the only one employed so far. For instance, the Raji-B cell line derived from Burkitt's lymphoma recently gained attention, since these B-lymphocyte-like cells can induce Microfold cells (M cells)-like phenotype in Caco-2 cells [7,159]. Particularly, they are specialized epithelial cells playing a pivotal role in mucosal immunity by transporting antigens and pathogens to the underlying lymphoid tissue [120,160]. For these reasons, the Caco-2/Raji-B co-culture model revealed to be very useful in investigating the passage nanoparticles containing therapeutic peptides and vaccines [82,161,162], and explore both intestinal enterocytes and M cells absorptive capabilities [163]. Strikingly, the three cell lines maintain their function when cultured together, establishing an asset that can faithfully recreate the human intestinal barrier complexity [164]. Accordingly, these multiple cell cultures may be employed to obtain more physiologically relevant intestinal in vitro models to better evaluate and predict intestinal absorption mechanisms [165] (Table 6).

Table 6: Characteristics of cellular models.

Model	CACO-2	TC-7	MDCK	HT-29	CO-CULTURE	HIEC	IEC
CELL SOURCE	Human colon adenocarcinoma cell line	Caco-2 subclone	Canine distal renal tissue-derived line	Human colon adenocarcinoma cell line	Human colon adenocarcinoma cell lines	Small intestinal crypt-derived human cell line	Small intestinal crypt-derived rat cell line
MORPHOLOGY	Polarized monolayer with strong tight junctions, apical brush borders and microvilli	Polarized monolayer with tight junctions, apical brush borders and microvilli	Polarized monolayer with tight junctions, apical brush borders and microvilli	Polarized monolayer with tight junctions, apical brush borders with sparse and short microvilli or a mucus layer (based on culture medium content)	Polarized monolayer with tight junctions, apical brush borders, microvilli and mucus layer	Polarized monolayer with poorly organized tight junctions, apical brush borders and dense microvilli	Polarized monolayer with poorly developed junctions, brush border, apical microvilli and an amorphous substance similar to the basement membrane
TEER [ $\Omega\text{cm}^2$ ]	250-2500	150-750	173 (parental line); ~1000 (MDCK-I subgroup); ~100 (MDCK-II subgroup)	15 (undifferentiated HT29 cell line); 280 (HT29-MTX-D1 subclone); 170 (HT29-MTX-E12 subclone)	250-400 (50% CACO-2/50% HT29-MTX); 60 (CACO-2/HT-29/Raji-B)	98.9	55 (IEC-18); 100 (IEC)
ENZYMES & TRANSPORTERS	<ul style="list-style-type: none"> <li>High expression of P-gp (MDR1), MRP2, MRP4 and BCRP, OATP1B1, OATP1B3, OATP2B1, PepT1, OCT1, OCT2 and OCT3</li> <li>Absence of CYP isoenzymes (possibility to induce CYP3A4 expression with 1-<math>\alpha</math>,25-dihydroxyvitamin D3 or NADPH)</li> <li>Proper expression of brush border enzymes</li> </ul>	<ul style="list-style-type: none"> <li>High expression of P-gps</li> <li>Expression of UDP-glucuronosyltransferases, hydrolase sucrase isomaltase</li> <li>Large quantity of CYP3A enzymes (CYP3A4 and CYP3A5)</li> </ul>	<ul style="list-style-type: none"> <li>Minimal expression of P-gp (solved with MDR1-MDCK cell line)</li> <li>Expression of MDR1, MRP1, MRP2 and MRP5</li> </ul>	<ul style="list-style-type: none"> <li>Low expression of brush border enzymes (e.g. forms of hydrolases)</li> <li>Absence of lactase</li> </ul>	<ul style="list-style-type: none"> <li>Proper expression of P-gps</li> </ul>	<ul style="list-style-type: none"> <li>Expression of BCRP, MRP1, MRP2, and MRP3</li> <li>Expression of CYP3A5 enzyme</li> <li>Low amounts of CYP3A, CYP2C9, CYP2C19, sucrase-isomaltase and alkaline phosphatase</li> </ul>	<ul style="list-style-type: none"> <li>Altered expression of carrier-mediated transport systems (e.g. MRP family)</li> <li>Poor expression of P-gps</li> <li>Low expression of brush border enzymes (e.g. sucrase-isomaltase, alkaline phosphatase)</li> </ul>
ADV	<ul style="list-style-type: none"> <li>High accuracy in replicating the enterocytic phenotype</li> <li>Long-term cell viability</li> <li>Great reproduction of the transcellular pathway</li> <li>Good reproduction of the active pathways</li> </ul>	<ul style="list-style-type: none"> <li>Fast cellular growth</li> <li>Great homogeneity ensuring consistent results</li> <li>Good reproduction of the passive pathways</li> <li>Good correlation with Caco-2 for passively transported drugs</li> <li>Possibility to study intestinal metabolism</li> </ul>	<ul style="list-style-type: none"> <li>Short culture time (3-5 days)</li> <li>Low costs</li> <li>Possibility to obtain several sub-clones</li> <li>Good reproduction of the passive pathways</li> </ul>	<ul style="list-style-type: none"> <li>No expression of P-gps</li> <li>Possibility to obtain several sub-clones by treating the culture medium with specific substances</li> <li>Possibility to obtain goblet-like cells</li> <li>Possibility to study the mucus layer</li> </ul>	<ul style="list-style-type: none"> <li>Reproduction of both absorptive and secretory epithelial cells</li> <li>Mucus production</li> <li>High permeability for passively absorbed drugs</li> <li>Possibility of modifying the permeability barrier of the cell monolayer (flexibility)</li> <li>Good reproducibility</li> <li>Cancerous origin</li> <li>Difficulties in manipulating and maintaining different cell lines contemporarily</li> </ul>	<ul style="list-style-type: none"> <li>Pore sizes and distribution similar to the human small intestine</li> <li>Long-term proliferation capability</li> <li>Ability to differentiate into several cell types</li> <li>Great accuracy in predicting the human paracellular uptake</li> </ul>	<ul style="list-style-type: none"> <li>Non-cancerous origin</li> <li>Intestinal origin</li> <li>Good reproduction of the paracellular path</li> <li>Useful model for studying cholesterol synthesis and the role of growth factors in epithelial layers</li> </ul>
DIS-ADV	<ul style="list-style-type: none"> <li>Colon cancer origin</li> <li>Long differentiation time (~3 weeks)</li> <li>Lack of physiological factors (mucus, bile salts, cholesterol)</li> <li>Inter- and intra-laboratories variability</li> <li>Underestimation of paracellular transport</li> </ul>	<ul style="list-style-type: none"> <li>Absence of large-scale data</li> </ul>	<ul style="list-style-type: none"> <li>Non-human origin</li> <li>Non-intestinal origin</li> <li>High variability</li> <li>Very low toleration of great amounts of organic solvent</li> </ul>	<ul style="list-style-type: none"> <li>Cancerous origin</li> <li>Non-small intestinal origin</li> <li>Altered glucose metabolism</li> <li>The differentiation process occurs only under specific culture conditions and require a long time</li> <li>Absence of the major metabolizing proteins</li> </ul>	<ul style="list-style-type: none"> <li>Crypt origin</li> <li>Interindividual variations</li> <li>Ethical issues prohibiting their use in several states</li> </ul>	<ul style="list-style-type: none"> <li>Non-human origin</li> <li>Crypt origin</li> <li>Long differentiation time (~3 weeks)</li> <li>Instability (rapid loss of differentiation markers)</li> <li>No transporting proteins</li> </ul>	

## 4.5 3D cellular models

Recently, remarkable progress in developing 3D cell culture platforms have been achieved by mimicking fundamental physiological cues present in the in vivo native tissue. We will present an overview of the 3D static culture systems presently adopted in pharmacology research and industry discussing their advantages and limitations (Table 7) [179,180].

Table 7: Characteristics of 3D models.

3D Static Model	Villi-shaped scaffold for intestinal mono- and co-cultures	Organoids	Epi-Intestinal
MORPHOLOGY	Structure with an increased absorptive surface area due to the villi formation; tight junctions and a mucus layer in co-cultures are present	Highly-folded differentiated epithelium with a central hollow region composed of differentiated cells (goblet, enteroendocrine cells, enterocytes) extruded into the lumen creating villi domains and apex regions (ISCs and Paneth cells)	Wall-to-wall polarized microtissue; highly differentiated epithelium including enterocytes, Paneth cells, M cells and ISCs with villi, microvilli, tight junctions, brush borders and a mucus layer
TEER [ $\Omega\text{-cm}^2$ ]	40-80 (3D hydrogel scaffold); 220 (3D nanofibers);	Not quantifiable	130-192
ENZYMES& TRANSPORTERS	<ul style="list-style-type: none"> <li>Lower presence of P-gps and higher expression of transporters (e.g BCRP, MRP) respect to 2D monocultures</li> </ul>	<ul style="list-style-type: none"> <li>Expression of GLUT2, GLUT5 and PEPT1 transporters</li> <li>High expression of CYP3A4, CYP3A5, CYP1B1, CYP2B6 and CYP2J2 enzymes</li> </ul>	<ul style="list-style-type: none"> <li>Expression of P-gps and MRP-1, MRP-2, BCRP</li> <li>Presence of most relevant enzymes (CYP3A4, CYP3A5, CYP2B6, CYP2C9, UGT)</li> </ul>
ADV	<ul style="list-style-type: none"> <li>Easy access to apical and basolateral sides</li> <li>3D large absorptive surface area</li> <li>High production of mucus</li> <li>Accurate reproduction of the intestinal villus-crypt morphology</li> <li>Use of biodegradable and bioactive material</li> </ul>	<ul style="list-style-type: none"> <li>Self-organization</li> <li>Self-renewal</li> <li>Possibility to expand indefinitely</li> <li>Long-term culture (1 year or more)</li> <li>Absence of cancerous cells</li> <li>Reproduction of the intestinal cellular heterogeneity</li> <li>Reproduction of the villus-crypt morphology</li> </ul>	<ul style="list-style-type: none"> <li>Easy access to apical and basolateral sides</li> <li>Long-term culture (up to 6 weeks)</li> <li>High reproducibility</li> <li>Low lot-to-lot tissue variability</li> <li>Relatively inexpensive</li> </ul>
DISADV	<ul style="list-style-type: none"> <li>Scaffolds may limit the absorption rate</li> <li>Hydrogels are subjected to batch variations</li> <li>Relatively complex fabrication process</li> </ul>	<ul style="list-style-type: none"> <li>Closed and hardly manipulable lumen</li> <li>Absence of a vascularization</li> <li>High costs</li> <li>High variability (source, size, shape)</li> <li>Complex experimental techniques</li> <li>Need for primary cells</li> </ul>	<ul style="list-style-type: none"> <li>Single unknown donor origin Polymorphic metabolizing enzymes not representative of a population</li> </ul>

### 4.5.1 Villi-shaped scaffold for intestinal cell mono- and co-cultures of Caco-2 cells

Mimicking the complex geometry of small intestinal epithelium in traditional monolayers of mono- and co-cultures still remains a challenge nowadays. Therefore, several attempts oriented towards 3D scaffold-based models are spreading to more closely recapitulate the intestinal architecture (Figure 13A) and thus perform more accurate pharmaceutical tests. Especially, scaffolds act as a support for cellular proliferation, differentiation and migration [181,182], playing a fundamental role in influencing cells behavior due to their chemical, mechanical and surface properties [183,184].

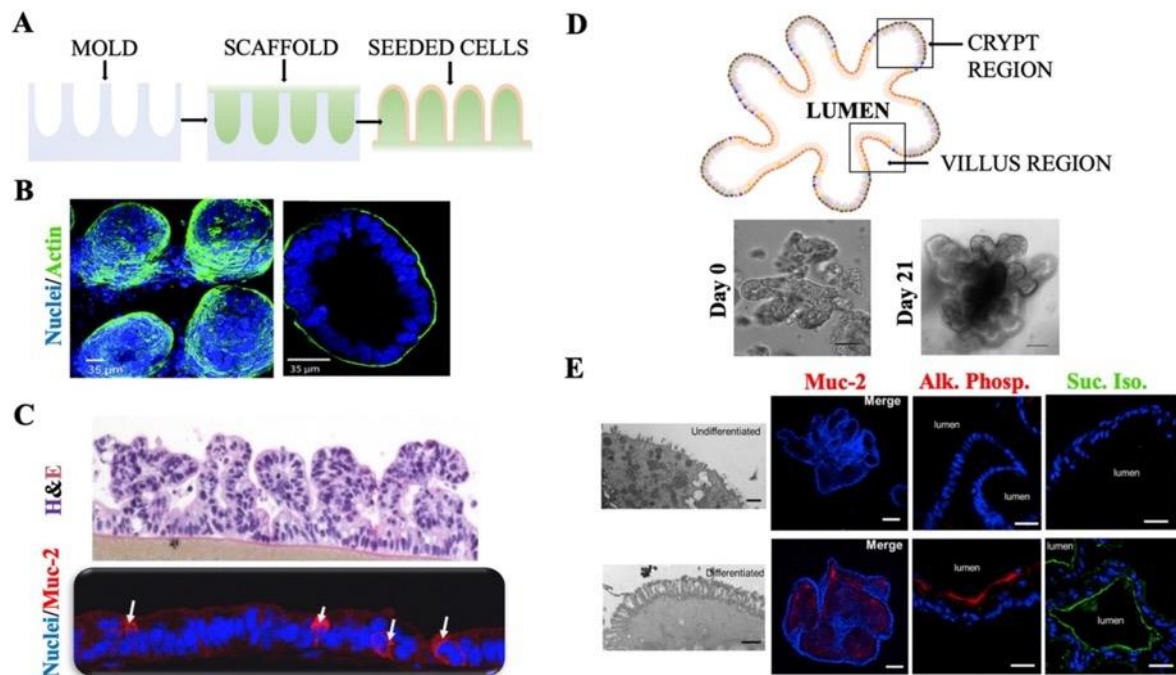


Figure 13: Intestinal 3D static culture systems resemble crucial features of differentiated intestinal tissues. (A) Schematic representation of villi-shaped scaffolds fabrication. (B) Confocal image of Caco-2 cells cultured on a collagen-based scaffold (left); hydrogel horizontal slice showing cells properly polarized and uniformly seeded on the scaffold (right); republished with permission of Royal Society of Chemistry, Copyright (2010), from [223]. (C) Illustration of intestinal organoid topography with villus-protrusions towards the lumen and crypt regions (top); such architecture can be obtained in vitro by culturing human intestinal tissue-derived crypts (bottom, left) after 21 days (bottom, right); scale bar: 100  $\mu\text{m}$  [224]. (D) Differences in Muc-2 production, Alkaline Phosphatase, and Sucrase Isomaltase expression in undifferentiated (top) and differentiated (bottom) intestinal organoids. Scale bars = 1  $\mu\text{m}$  for TEM images and 50  $\mu\text{m}$  for microscope images; reprinted and adapted from [225], Copyright (2016), with permission from Elsevier. (E) Typical histology (top) and immunohistochemistry image (bottom) of the EpiIntestinal<sup>TM</sup> (SMI-100) tissue illustrating an in vivo-like 3D structure and the simultaneous presence of both mucus-secreting and absorptive-like cells after 14 days of culture, respectively [219].

Among several materials and substrates, collagen-based hydrogels are the most widely employed for reproducing the shape of the villus-crypt axis. Caco-2 cells cultured onto these 3D structures (Figure 13B) exhibit an increased absorptive surface area due to the villi-like scaffold conformation together with a proper expression of proteins that mediate the intercellular junctions, resulting in decreased TEER values and thus a more representative model of the human small intestine respect conventional monolayers [185,186]. Interestingly, it was reported that cell differentiation varied along the villus as it is observed in vivo [185]. In this context, since the paracellular route of absorption is well-known to be seriously underestimated in flat Caco-2 cells, several drug permeability studies investigating this pathway were performed to verify whether cells growth over the 3D villi-shaped scaffolds better resemble the intestinal barrier function. In particular, the paracellular transport of slowly absorbed drugs (FITC-dextran and atenolol) and rapidly absorbed drugs (fluorescein) showed higher permeability rates in comparison to 2D well-based cultures [181,186]. Specifically, atenolol permeability coefficients were 13 times higher in 3D models than planar Caco-2 cells, being approximately 60% of that measured in the perfused human intestine, thereby proving that these 3D structures can enhance the prediction of human intestine kinetics [172,181,185]. Moreover, the activity of metabolic enzymes and drug transporters in such 3D models was found to be more similar to the in vivo scenario [186]. For example, immunohistochemistry analysis revealed a quite low presence of P-gp



proteins, while they were uniformly distributed and overexpressed in 2D cultures [[185], [186], [187]]. However, although collagen is suitable to support cellular growth and migration in a physically adequate 3D culture, this polymer can be subjected to batch variation, and its presence may limit the absorption rate of rapidly absorbed drugs. To resolve these concerns, investigations about alternative materials were proposed to recapitulate villi and crypts architectures without interfering with the permeation process [185,188]. Patient et al. fabricated polyethylene terephthalate nanofibrous scaffolds to mimic the intestinal epithelium topography. As for collagen, TEER values lower than those observed in 2D Caco-2-seeded Transwell were reported, probably due to the increased porosity of nanofibers over monolayers. Furthermore, the bidirectional absorption of FITC-dextran, lucifer yellow, rhodamine 123, propranolol, and atenolol displayed higher permeability through Caco-2 cells cultured on 3D scaffolds compared to 2D typical platforms [187]. Hence, it was widely accepted that the 3D corrugated structure fosters the establishment of a physiologically operating barrier very close to the native gut epithelium that increases the potential of the test model in predicting the intake of pharmaceuticals both via passive and active pathways, regardless of the scaffold material used [188,189]. Interestingly, the ability of these models to successfully support co-cultures of Caco-2 and HT29-MTX cells with prominent stromal cells (i.e. fibroblasts and immunocompetent macrophages) was also explored. This setting-up demonstrated a 3D larger absorptive surface area, decreased TEER values and a viscous mucus layer formation. This more physiological morphology culminated in a decreased permeability for moderately or highly absorbed drugs (propranolol, verapamil, antipyrine and carbamazepine), and an increased uptake for low absorbable compounds (ranitidine and furosemide) with a high correlation with human data ( $r^2=0.84$ ) [190]. Taken together, these outcomes denote 3D scaffold-based intestinal mucosa models as powerful and versatile systems to resemble the most important native features and functions, with a strong potential in drug screening experiments under static conditions [191]. However, additional studies should be conducted to select other materials with more suitable biochemical and mechanical properties to generate an *in vivo*-like intestinal epithelium. It would be interesting also to include other intestinal lines and culture organoids-derived stem cells, as well as to investigate whether biofabricated 3D structures or decellularized small intestinal submucosal scaffolds could control intestinal cells differentiation, proliferation and transport activity [189,192]. Finally, future developments should include fluid flows and mechanical stimulations as it happens in the living intestine [193].

#### 4.5.2 Organoids

Organoids are 3D organ-buds created *in vitro* that have a realistic microanatomy due to their *in vivo*-like self-organizing and self-renewing capabilities [183]. They brought notable ameliorations in tissue engineering by exhibiting levels of cellular complexity similarly to native organs, bridging the gap between 2D monolayers and animal testing [163,194]. To date, several 3D organotypic cultures replicating various organs involved in the GIT tract, such as the pancreas [195], stomach [196] and intestine [197], have been developed. Especially, small intestinal organoids, also called mini-guts or enteroids, are advanced technologies that are currently galvanizing the *in vitro* modelling to investigate pathophysiological mechanisms. Mini-guts can replicate the *in vivo* tissue morphology and physiology by retaining key intestinal physiological conditions and functions (e.g. crypts and protruding villi formation, cytochrome P-450 metabolizing activity, mucus secretion) for prolonged periods (Figure 13C, D) [163,198,199]. They have a central hollow region made up of differentiated cells (e.g. goblet cells, enteroendocrine cells, enterocytes), which

are extruded into the lumen forming villi- and microvilli-like domains, and an apex region where ISCs and Paneth cells reside, giving rise to crypt bases [194,200]. Enteroids are usually derived from primary tissues (either from a single ISC-expressing Lgr5 marker or isolated intestinal crypts [[201], [202], [203]]) or also from pluripotent stem cells (PSCs), both in the form of induced (iPSCs) and embryonic (ESCs) cells [204], which can differentiate into all cell types of the adult intestine thus creating a multilineage culture system [205]. Notably, in the personalized medicine scenario, intestinal patient-derived stem cells-induced organoids are very useful for establishing a patient biobank and a specific platform where to evaluate therapeutic strategies preventing any immune response [206]. However, although these 3D cellular structures faithfully resemble the human small intestine complexity, their morphology and architecture may represent a significant obstacle for studying the intestinal barrier absorptive function due to their geometry [207]. The closed lumen precludes direct access to the apical surface hampering PK assessments of endogenous and foreign substances [207,208]. It's particularly difficult to manipulate entrapped cells and conduct quantitative analyses of the transcellular and paracellular diffusion and the presence of apical carriers without altering the organoid architecture [209]. For these reasons, alternative methods to access the luminal side, such as the microinjection technique, have been conceived, particularly for examining transport phenomena of foods, toxins and drugs across the intestinal epithelium [207]. For example, the translocation of monosaccharide compounds (e.g. glucose and fructose) and peptides (e.g. Gly-Sar) was investigated by adopting this strategy and conjugating a fluorescent tracer to the substance of interest [204,210,211]. Nonetheless, the excessive costs of fluorophores and the limited reproducibility of the microinjection, which usually requires the use of micromanipulators, hinder its applicability to organoids for studying substances permeation [62,204]. Moreover, this strategy gained restricted success as it also provokes irreparable damages to the tissue [212]. Another solution was identified in mechanically disrupting the organoid 3D structure and then replating recovered cells in traditional 2D plates to obtain well-differentiated intestinal multilineage cells in an easy-to-use conformation, allowing the direct manipulation of the apical and basolateral side of the tissue [213]. Recently, this method was adopted by Yoshida et al. for evaluating the entry and metabolism of pharmaceutical compounds [214]. In particular, once an organotypic culture was established from human iPSCs, it was subsequently mechanically dissociated. Then, researchers purified the culture from mesenchymal cells, which could influence the screening activity of the model, cultured the gathered iPSC-derived IECs as a monolayer [197,214]. The potential of the established iPSC-IECs barrier was confirmed by the proper metabolization of terfenadine and midazolam, which are representative substrates of CYP3A and CYP2J2 as well as CYP3A enzymes, respectively, and cannot be reproduced with conventional 2D models. This technique revealed to be also valid to assess the uptake of other molecules, proving the reliability of the organoid-derived epithelial monolayers for investigating xenobiotics absorption [104,214]. However, the dissociation process may disrupt the stem-cell compartment and thus the continuous propagation ability of the organoid. In addition, the authors suggested that a refinement of the presented procedure is still necessary to ensure its reproducibility and replicability to perform high-throughput assays [214]. Hence, mini-guts are not the easiest-to-handle tools for investigating transport processes through an intestinal barrier model. Moreover, the absence of vasculature, which is fundamental for nutrient and waste transport, as well as fluid and mechanical stimuli (e.g. luminal flow or peristalsis motions) remarkably impact the reliability of the model [194,197]. To close this gap, a possible strategy may consist of integrating these enteroids with dynamic culture systems, such as commercial bioreactors or custom-made fluidic devices, where physical, biological and chemical parameters could accurately be imposed [215,216]. Nevertheless, the elevated

costs for the enteroid formation and maintenance must be also considered in a pre-clinical view. In this scenario, it is also well-known that outcomes derived from drug toxicity and efficacy assays, performed by using intestinal organoids, often lack reproducibility because of the intrinsic variability of the organoids source, size and shape [7,215]. All these aspects may lead to significant difficulties in gaining robust statistics of the obtained results, such as PK profiles of new drug candidates, impairing the translational potential of mini-guts as preclinical screening platforms [62]. Therefore, further efforts are certainly necessary to consider these promising organotypic systems in an increasingly present perspective of reducing as much as possible animal testing in drug discovery and development [217].

### 4.5.3 Human Reconstructed small intestinal tissues

Epi-Intestinal™ is an innovative 3D human reconstructed gut tissue model developed by MatTek Corporation which closely recapitulates several cues of the native small intestinal barrier. Indeed, it was demonstrated to be a functional biologically-relevant tool in a wide range of applications, such as drug absorption and metabolism as well as GIT toxicity and inflammatory studies [85,218]. This recent technology is emerging in the GIT in vitro research field thanks to its proven advantages over the other cell-based systems currently employed [219,220]. In fact, Epi-Intestinal, like enteroids, comprises cellular heterogeneity deriving from primary intestinal cells, which makes the reliability of data more solid compared to 2D immortalized cell-based models (Figure 13E). In particular, it includes enterocytes, Paneth cell, M cells, and intestinal stem cells into a polarized epithelium, precisely replicating the architectural and phenotypic features of the small intestine. Moreover, this organotypic microtissue possesses an open physiological luminal surface which is extremely functional in investigating drug and nutrients processing, differently from the closed geometry of organoid-based models. Importantly, this topography allows easy access to the lumen compartment which is highly profitable for bidirectional permeation studies both from the lumen to the bloodstream and vice versa [221]. To demonstrate its analogy to the human small intestine, other primary features of the Epi-intestinal were examined. For example, Ayehunie and colleagues demonstrated the formation of villi, microvilli, tight junctions and brush borders similar to the in vivo scenario by performing immunohistochemistry analyses [85]. The genetical expression of metabolizing enzymes and both uptake and efflux transporters were carefully determined with selective substrates and inhibitors. Results revealed the presence of MRP-1 and MRP-2, BCRP, and the main drug-metabolizing enzymes (CYP3A4, CYP3A5, CYP2B6, CYP2C19, CYP2C9 and UDP-glucuronosyltransferases (UGT) with very little biological differences respect the human situation [85,220]. These outcomes supported the enhanced predictability potential of the Epi-intestinal system compared to Caco-2 cell cultures, where CYP3A4 and several drug transporters are almost absent or low expressed [220]. The presence of these relevant transporters and enzymes made Epi-intestinal a suitable model also for bioavailability studies of many drugs (including talinolol, ranitidine and warfarin) with different physicochemical properties. In this context, the Epi-intestinal system was found to be very useful to rank order compounds as low (<50%), moderate (50-84%) and high (≥85%) absorbed drugs [221]. Along this line, a good correlation between the first-pass GIT availability ( $F_a \times F_g$ ) calculated in vitro with that of the human PK values was noticed for a panel of twelve drugs (e.g. atenolol and midazolam) [220]. The inability of cancerous cells-based systems in predicting human absorption was emphasized in comparison to Epi-intestinal technology. Data measured by using the organotypic intestinal tissue displayed a higher correlation with the human fractions ( $r^2=0.91$ ) respect Caco-2 cells ( $r^2=0.71$ ) [85,221]. Furthermore, high reproducibility and low lot-to-lot tissue variability

for permeability assays were demonstrated, as opposed to traditional monolayer cultures [85,222]. Therefore, Epi-intestinal microtissue represents an optimal 3D model to investigate drug absorption, by mimicking morphological and functional aspect of the small intestine. Even though it provides multiple advantages over the other available in vitro systems, some limitations hamper its use in pharmaceutical research. For example, like other 3D tissue models, Epi-intestinal is not provided with an inner vascularization and is usually employed under static incubation conditions, which do not resemble the physiological fluidic stimuli of the in vivo microenvironment [219]. Moreover, the lack of dynamic recycling of the drugs may underestimate their bioavailability, especially for drugs that are extensively metabolically cleared [220]. To our knowledge, only Marrella et al. proposed a novel approach to resolve this issue by integrating the 3D Epi-intestinal tissue into a commercialized bioreactor to better mimic the physiological fluid-dynamic microenvironment of the gut [219]. In addition, such microtissue derives from a single donor and thus it cannot be representative for a population with polymorphic metabolizing enzymes [220]. Hence, even if Epi-Intestinal is a leading in vitro technology widely accepted by formulation scientists and toxicologists as an excellent animal alternative platform for absorption and toxicity assays of pharmaceutical and nutraceutical products, additional attempts examining a larger set of compounds need to be carried out.

#### 4.5.4 3D fluid-dynamic in vitro models of the human intestinal barrier

3D fluid-dynamic in vitro models are promising tools having the potential to closely reproduce the complex physiology of the human intestine, overcoming the limits that affect static cultures. In the gastroenterology research field, they provide critical physicochemical aspects that are crucial in emulating the intestinal activity, faithfully recreating an in vivo-like dynamic microenvironment [229]. In fact, fluid flows and mechanical stimuli were demonstrated to tremendously alter the gene expression profiles (23.000 genes targeted) compared to static systems [230]. Herein, we provide an overview of the existing intestine-on-chips and, more in general, of the fluidic platforms aimed at recapitulating the human intestine physiology with an organ-scale level for absorption and metabolism investigations. OOCs of the human intestine usually consist of 2 channels, emulating the intestinal lumen and the vasculature, separated by an ECM-mimicking gel-coated porous membrane over which intestinal epithelial cells can be cultured (as represented in Figure 14A-B-C). Frequently, Polydimethylsiloxane (PDMS) is used to realize these chips since it is gas-permeable and allows fast prototyping and high-resolution imaging [62]. In these systems, dynamic culture conditions are established by imposing tailored fluid flows; in this way, the influx and efflux of substances present in the chyme and the bloodstream can be investigated across the intestinal-simulating barrier [62,207].

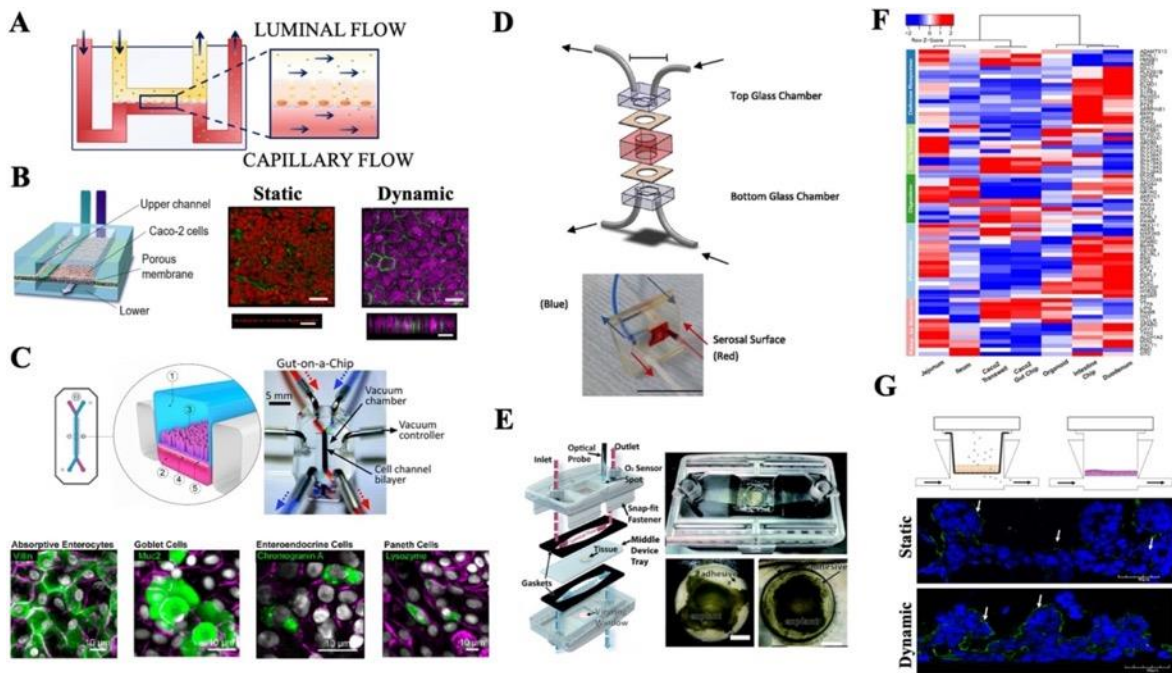


Figure 14: Intestinal OOCs provide a physiologically relevant environment: the human intestinal epithelium can be accurately recapitulated *in vitro*. (A) Typical design of an intestine-on-a-chip composed of two channels mimicking the lumen and the blood circulation, separated by a membrane over which cells are cultured. (B) 3D rendering of Caco-2 cells seeded microfluidic chip (left); immunostaining of Caco-2 cells cultured in a Transwell system (middle, static condition) at day 21 and the microfluidic device (right, dynamic condition) on day 3. Fluid flow stimulates the formation of an undulating 3D morphology with brush borders. The height of the monolayer reached  $40\ \mu\text{m} - 50\ \mu\text{m}$  on day 3 when fluidically stimulated (bottom); scale bar =  $50\ \mu\text{m}$  [231]. (C) Schematic representation (top left, [216]) and image (top right, republished and adapted with permission of Royal Society of Chemistry, Copyright (2012), from [236]) of the “Intestine Chip” by Emulate Inc. consisting of two channels separated by a gut-mimicking epithelium and surrounded by two lateral vacuum chambers which apply a cyclic strain to the cells; confocal fluorescent micrographs confirm that fluidic and mechanical stimuli induce organoids-derived cells differentiation into several intestinal cell types after 8 days of culture within the chip (bottom) [216]. (D) Exploded design of the dual flow device able to hold and perfuse a full-thickness intestinal tissue section (top); Red and blue dyes demonstrating the dual independent fluidic circuits (bottom); reprinted from [243], with the permission of AIP Publishing. (E) Schematic illustration of a microfluidic chip capable to maintain an intestinal tissue explant *ex vivo* in a physiologically relevant environment (left); Image of a mouse colon explant inside the device (right, top) at 0 h and 72 h through a viewing window (right, bottom). Scale bars: 2 mm; republished with permission of Royal Society of Chemistry, Copyright (2020), from [244]. (F) A heatmap of gene expression profiles comparing *in vivo* tissues (jejunum, ileum, duodenum) and *in vitro* reconstructed epithelial models (Caco-2-based Transwell, Caco-2-based chip, 3D organoid, organoid-based intestine chip). Combining organoid-derived epithelial cells with fluidic and mechanical stimulations allows to better recreate intestinal organ-level physiology [247]. (G) Schematic representation of the MIVO® fluidic system hosting either a Caco-2 monolayer and the EpiIntestinal™ (SMI-100) tissue and resembling the capillary flow below the gut model (top); immunohistochemistry analysis demonstrating that EpiIntestinal™ (SMI-100) tissue develops an *in vivo*-like morphology (presence of villi and microvilli) when properly stimulated by a biologically relevant fluid flow [219].

Interestingly, although immortalized cell lines (e.g. Caco-2 cells) displayed several limitations under static culture conditions, they can develop a compact intestinal epithelial layer with 3D villi-like structures and basal crypts when properly stimulated by a fluid-dynamic active environment [179,231], [232], [233], [234]]. Moreover, Caco-2 cells complete their differentiation already after 5-7 days under fluid flow, unlike planar monolayers that exhibit a complete mature phenotype after 21 days (Figure 14B) [56,179,233,235,236]. When the fluidic stimuli are also combined with mechanical cyclic

strains to perform peristalsis-like deformations, intestinal cells undergo a spontaneous differentiation reprogramming themselves into 4 different small intestinal cell types (enterocytes, enteroendocrine, Paneth and Goblet cells), presenting a columnar in vivo-like cell morphology [179]. In this context, several studies aimed at investigating xenobiotics and food-related entities transport across the intestinal epithelium were performed and compared with traditional Transwell- or Ussing chamber-based cultures. For example, Kulthong et al. carried out biokinetic studies of high (antipyrine, ketoprofen and digoxin) and low (amoxicillin) permeability compounds in the two opposite culture conditions. Results revealed that a lower drug uptake occurred in the gut-on-a-chip with respect to the static condition with permeability values in line with the BCS. Similarly, the absorption rates of several compounds (curcumin, mannitol, dextran, caffeine and atenolol) in Caco-2 cells-seeded microfluidic devices were reported to be comparable with human data [56,231,234]. Moreover, under dynamic stimulation, Caco-2 cells revealed to be efficient to in vitro inspect and reproduce PK profiles of orally-delivered chemotherapeutic agents, which often fail to pass the intestinal barrier because of their low solubility and permeability. New insights were provided for lipophilic chemotherapeutic prodrugs such as SN-38 (7-ethyl-10-hydroxycamptothecin) and approved antineoplastic drugs like 5-FU [56,237]. In particular, for this latter, a concentration-time curve with an in-vivo like pattern of absorption and excretion was generated by applying a peristaltic flow on the top channel, and its therapeutic effect on target lung cancer cells was verified within the same chip. Therefore, it is clear that fluid flows significantly regulate the transport of drugs, for example limiting their diffusion due to the recirculation of the luminal content. Dynamic conditions trigger a 3D intestinal in vivo-like morphogenesis, increasing the available absorptive surface and, consequently, the absorptive efficiency of the tissue [238]. In fact, it was recently demonstrated that fluid flow-associated forces such as shear stress play a pivotal role in epithelial cells growth and microvilli formation [239,240]. Notably, Caco-2 cells secrete mucus, unlike standard static cultures in microfluidic chips [179]. Furthermore, it was shown that luminal and basal flows are responsible for the proper expression of transporters on the apical and basolateral side of the barrier [231]. Likewise, biomimetic chips promote the establishment of the main intestinal metabolic pathways, differently from Transwell systems, where cells lack the expression of the majority of enzymes [232]. For example, 3D collagen-based scaffolds seeded with Caco-2 cells were integrated within the chips to couple a 3D intestinal topography with fluid flow patterns [193,241]. However, hydrogels are challenging to inject in microdevices at low concentrations, and, at the same time, increased volumes subsequently alter the stiffness of the mimetic matrix. For this reason, this technique is currently rarely used [62]. In addition, it is necessary to keep in mind that Caco-2 cells exhibit a specific mutated genetic profile also when fluidically stimulated [242]. Therefore, another valuable approach was identified in incorporating mammalian full-thickness explants in dual-flow platforms [[243], [244], [245]] (Figure 14D-E). Despite the promising results obtained in faithfully mimicking all aspects of the intestinal pathophysiology, their employment still remains extremely restricted due to the remarkable difficulties in their usability and maintenance in culture, hampering the possibility to perform pharmacology assays [207,243]. To date, advancements in the GIT research and the hopeful outcomes arising from the microfluidic devices determined the circumstances to recreate intestinal organ-level physiology by combining organoids and fluidic devices. In this scenario, some researchers were able to culture primary stem cells (derived from fragmented enteroids) within these platforms, overcoming the challenges shown by human organoids in performing screening assays due to the enclosed geometry, as discussed before [246]. In this way, a well-formed intestinal epithelium with tight junctions, brush borders and elongated villus-like protrusions, as well as a complete

intestinal differentiation can be developed in response to fluidic and mechanical stimulations within 8-12 days [[246], [247], [248]]. Fluorescence microscopy confirmed the successful maturation of all major intestinal epithelial cell types, such as proliferative cells in the basal regions, mucin-producing cells, enterocytes covered with densely-packed microvilli, and enteroendocrine and Paneth cells [216,247,248] (Figure 14C). Strikingly, a human intestinal endothelial-parenchymal tissue-tissue interface was also be successfully recapitulated by seeding human intestinal microvascular endothelial cells (HIMECs) in the lower channel, enabling the investigation of drug passage and nutrients ingestion across a more natural barrier [216,247]. Therefore, organoids-derived intestine chips are very useful tools to realize clinically relevant human intestine models. A transcriptomic analysis indicated that these human primary cells-based systems more closely emulate the human small intestine scenario compared to Caco-2-based gut-on-a-chip and duodenum biopsy-derived enteroids [216,247]. Kasendra et al. [216,247] found that a subset of 305 genes associated with fundamental biological intestine functions (e.g. digestion, metabolism, transport, detoxification) was expressed in their Duodenum Intestine-Chip similarly to the duodenal native tissue, highlighting the potential of this platform to investigate biokinetics and biotransformation processes of nutrients and drugs (as illustrated in Figure 14F). As matter of fact, the apical localization and function of the major drug transporters, such as MDR1, BCRP and PEPT1, and a high expression of the cytochrome CYP450 (CYP3A4) were confirmed. Microfluidic devices thus offer the possibility to *in vitro* thoroughly reproduce the biochemical processes that dynamically occur in the human intestine. Clearly, the synergistic use of primary cells and fluidic chips allows the establishment of physiologically relevant pre-clinical platforms for better predictions of human PK, toxicity risks as well as an improved *in vitro*-to-*in vivo* data extrapolation compared to immortalized cell lines-based chips. Unfortunately, to date, some technical limitations persist in these systems, such as fluid leakages, pump requirements, difficulties in performing robust and high-throughput experiments [249]. Moreover, even though PDMS holds advantageous properties, it can adsorb small and hydrophobic molecules, influencing PK and PD evaluations [250]. Therefore, there remains a compelling need to further improve intestinal OOC systems for increasing their robustness and reliability as drugs screening platforms (Table 8). Alternative manufacturing techniques have already been adopted to realize other types of micro-physiological systems for drug delivery and toxicity assays [[251], [252], [253]]. An innovative research was recently published by Marrella et al. to *in vitro* elucidate the absorption mechanisms of different sugars (mannitol and lactulose) in healthy and pathological conditions by incorporating the Epi-Intestinal tissue within a commercial fluidic device (named MIVO®), presented in Figure 14G, capable to resemble the physiological stimuli of the intestinal environment [219].

Table 8: Characteristics of fluid-dynamic models.

Model	Cell source	Features	Adv	Dis-adv
Gut-on-a chip	Cell lines (mono- and co-cultures)	PDMS-based chip with 2 channels reproducing the intestinal lumen and the vasculature, separated by an ECM-mimicking gel-coated porous membrane	<ul style="list-style-type: none"> <li>• Mucus layer</li> <li>• Formation of 3D villi-like structures</li> <li>• Reproduction of physiological levels of fluid flows and shear forces</li> <li>• Spontaneous and rapid differentiation due to the dynamic stimuli (5-7days)</li> </ul>	<ul style="list-style-type: none"> <li>• Possible non-specific binding of hydrophobic molecules onto PDMS surface</li> <li>• Altered gene expression profiles</li> </ul>
3D scaffolds on chip	Cell lines (mono- and co-cultures)	Microfluidic device (PDMS sheets with fluidic channels) integrated with 3D hydrogel-based villi-like scaffold	<ul style="list-style-type: none"> <li>• Combination of a 3D villi geometry with fluid flows positively impacting cell differentiation</li> </ul>	<ul style="list-style-type: none"> <li>• Possible non-specific binding of hydrophobic molecules onto PDMS surface</li> <li>• Scaffolds may limit the absorption rate</li> <li>• Hydrogels are subjected to batch variations</li> <li>• High complex fabrication process</li> </ul>
Microfluidic organotypic device	Full-thickness intestinal tissue section and tissue explant	Dual flow perfusing full-thickness intestinal tissue sections or tissue explants <i>ex vivo</i> in a physiologically relevant environment	<ul style="list-style-type: none"> <li>• Biomimetic and organotypic intestinal culture models</li> <li>• Simultaneous presence of muscular, neural, immune and epithelial components</li> <li>• Double fluid flows mimicking the intestinal lumen and the vasculature</li> </ul>	<ul style="list-style-type: none"> <li>• High costs</li> <li>• Short-term assays (72 h)</li> <li>• Poor scalability and repeatability</li> </ul>
"Intestine Chip" by Emulate Inc.	Cell lines (mono- and co-cultures), organoid-derived cells	PDMS-based chip with 2 channels reproducing the intestinal lumen and the vasculature, separated by an ECM-mimicking gel-coated porous membrane and supported with two lateral vacuum chambers which apply a cyclic strain to the cells	<ul style="list-style-type: none"> <li>• Combination of organoid-derived intestinal cells of three independent donors with microfluidic chips technology</li> <li>• Well-formed <i>in vivo</i>-like intestinal epithelium</li> <li>• Simultaneous fluidic and mechanical stimulations</li> <li>• Proper gene expression profiles</li> </ul>	<ul style="list-style-type: none"> <li>• Longer intestinal differentiation (8-12 days)</li> <li>• Complex experimental techniques</li> <li>• High costs</li> </ul>
"MIVO" by React4life	Cell lines (mono- and co-cultures), organoid-derived cells, biopsies, 3D commercial reconstructed tissues	Optical-transparent <i>in vitro</i> multi-chamber platform easily accommodating 2D cell monolayer or 3D human tissues and biopsies with clinically relevant sizes	<ul style="list-style-type: none"> <li>• Physiological mass transport and remotion of waste due to the dynamic fluid flows</li> <li>• Clinically relevant sizes of tissue model</li> <li>• Possibility to study the passage of molecules across the healthy or pathological small intestinal barrier</li> </ul>	<ul style="list-style-type: none"> <li>• Use of a greater volume than microfluidic chips</li> <li>• Low throughput</li> </ul>

## 4.6 Mathematical modelling of absorption at the intestinal wall

### 4.6.1 Motivation

The inner wall of the small intestine is covered by villi. These are protruding, approximately cylindrical structures with a length of approximately 1 mm and a diameter of 0.1 mm. The role of villi is thought to be that of increasing the surface available for exchanges between the fluid inside the intestine and blood vessels perfusing the intestinal wall. The surface available for exchanges in the presence of villi is increased by a factor 40 with respect to the case of a flat wall. One would expect that the absorption rate at the wall scales with the surface available for exchanges. However, preliminary two-dimensional simulations that we have carried out show that the presence of villi alone thus not support this statement: only a very small increase of absorption is predicted and in some cases villi are even found to decrease absorption. This implies that some ingredients are missing from our simple models, which motivates our interest on this problem. Indeed, similar results have been reported in a recent work Wang and Brasseur (2017).

### 4.6.2 Existing models



- Wang et al. (2010): The model and the results are the same of the work developed by Wang and Brasseur (2017) but in 2 dimensions. Thus, please refer to such a work, which is described below.
- Lim et al. (2015): The model is three-dimensional and considers a small group of 5 villi, which are assumed to be rigid structures. Authors solve the equation of fluid motion and the advection/diffusion equation for Newtonian and non-Newtonian fluids. Fluid flow is produced by a longitudinal contraction of the wall and solved by a Lattice-Boltzmann method. The wall movement is defined by a strain rate function in the form of a sinusoidal wave. Absorption is assumed to be passive and occurs instantaneously when the nutrient reaches the wall. Zero radial velocity and pressure as well as non-diffusive boundary conditions are imposed at the left and right of the domain. Non-slip conditions are applied at the solid boundaries. Results show that the wall action causes fluid to be drawn into the inter-villus region during the wall relaxation period and ejected from it during contraction, triggering a continuous replacement of the fluid in the inter-villus space during each cycle of wall activity. The rheology of the fluid can significantly alter the degree of shear rate: the shear rate in the inter-villus space increases when the index of the power-law decreases. The movement of the villi increases the mass absorbed by one order of magnitude, compared to the situation where villi are static and the only mechanism for nutrient transport is molecular diffusion.
- Wang and Brasseur (2017): The model is three-dimensional and considers a series of small group of 5 villi, modelled as rigid structures. The authors solve the equation of fluid motion and the advection/diffusion equation. Fluid flow is produced by the axial movement of the upper wall with a constant speed (roughly mimicking the peristaltic or segmental contractions), together with an axial or lateral movement of the villi, and it has been solved by a Lattice-Boltzmann method. The villi movement is sinusoidal, and each villus group oscillates 180° out of phase with its neighbours. No-slip and no-flux boundary conditions are applied at the front a rear wall, whereas periodic boundary conditions are applied laterally. Concentration boundary conditions are applied at the surfaces over and between the villi, to model immediate nutrient absorption. Zero radial velocity and pressure as well as non-diffusive boundary conditions are imposed at the left and right of the domain. Concentration at the lid is fixed in order to model a source of molecules. Results show that the wall action generates macro-scale eddies that interact with micro-scale eddies created by the villi movement. These interactions enhance the absorption: macro-scale eddies continuously recharge with new molecules the micro-scale ones. The layer adjacent to the villi surface over which this macro–micro-scale interaction takes place is what the authors refer to as the "Micro Mixing Layer". In particular, the enhancement is higher when the villi move laterally and thus perpendicularly to the upper wall: the net adsorption is increased by 25% when the villi move laterally vs axially.
- Zhang et al. (2020): The model is two-dimensional and mimics the rat duodenum structure (pipe with villi). The authors solve the equation of fluid motion and the advection/diffusion equation. Fluid flow is produced by pendular wall activity, caused by the longitudinal contraction of the muscles, considered in the model by a moving mesh method. The effect of a net inlet velocity is also considered. Wall motion is in the form of stationary sinusoidal waves. This generates circulation

structures in the pipe. The pendular activity enhances absorption by up to  $\approx 70\%$ ; this figure reduces to  $\approx 10\%$  in the presence of a net inlet velocity.

- Zha et al. (2021): The model is two-dimensional and mimics the human duodenum structure (pipe with circular folds of  $\approx 8\text{mm}$ ). The authors solve the equation of fluid motion and the advection/diffusion equation for an incompressible fluid assuming a laminar fluid flow. Fluid flow is produced by a segmentation contraction of the wall, considered in the model by a moving mesh method. No-slip and no flux boundary conditions are applied. The segmentation divides the tube into sections, where contraction and relaxation occur sequentially and alternatively at the same location. Wall motion is in the form of sinusoidal waves. To find out the role of circular folds the results have been compared with a smooth tube with the same length and volume of the pipe, with folds but with a different radius. Moreover, the Peclet number has been quantified to examine the dominant mechanism of mass transfer. The presence of circular folds intensifies radial and axial mixing under segmentation: prominent and long-lasting vortices can be identified together with higher velocity and shear rates than in the smooth pipe (larger  $Re$  e  $Pe$  values). Circular folds enhance absorption by up to  $\approx 10\%$  after 10 periods. The optimal shape of circular folds is such that wave height  $\approx 5\text{ mm}$  and wave length  $\approx 2\text{ mm}$ .

### 4.6.3 Mathematical formulation and results

Fluid flow is governed by the Navier-Stokes equation:

$$\begin{cases} \rho \left[ \frac{\partial u_f}{\partial t} + u_f \times (\nabla u_f) \right] = -\nabla p + \mu(\nabla^2 u_f) & (1a) \\ (\nabla \times u_f) = 0 & (1b) \end{cases}$$

where  $t$  is time,  $u_f$  is fluid velocity,  $p$  pressure,  $\rho$  density and  $\mu$  viscosity. We are therefore assuming that the fluid has Newtonian properties. The flow has been generated by imposing a constant gradient of pressure between the fluid inlet and outlet, together with a physiological longitudinal velocity at the inlet,  $U = 0.1\text{ m/s}$ . This is coupled with the advection diffusion equation for the transport of a passive species.

$$\left[ \frac{\partial c}{\partial t} + \nabla \times (\nabla u_f c) \right] - \nabla \times (D \nabla c) = 0 \quad (2)$$

where  $c$  denotes the species concentration and  $D$  the diffusion coefficient. At the intestinal wall we impose the no slip condition ( $u = u_{\text{wall}}$ ), where  $u_{\text{wall}}$  is wall velocity, which as now now has been assumed equal to zero. We also impose that the concentration is fixed to the value  $c_{\text{wall}}$  ( $c = c_{\text{wall}}$ ). This condition implies that blood flow very effectively removes the species from the tissue. The condition can be obtained as a limiting case of the more general condition, for the case of  $\Gamma \rightarrow \infty$ :

$$(c u_f - D \nabla c) \times n = \Gamma(c - c_{\text{wall}}). \quad (3)$$

#### 4.6.3.1 Steady flow through a channels of constant width

We considered a two-dimensional channel with physiologically relevant dimensions: a length of  $100\text{ mm}$  and a height of  $12.5\text{ mm}$ . The case of a flat wall (without villi) and the case of a geometry provided with rectangular-shaped structures resembling the villi have been investigated (Figure 15). The single villus is  $1\text{ mm}$  long and  $0.1\text{ mm}$  thick. The distance

between the villi is 0.2 mm. To compare the absorption efficiency of the wall with or without villi, we defined an absorption efficiency parameter  $e$  as:

$$e = \frac{Q_{in} - Q_{out}}{Q_{in}}, \quad (4)$$

where  $Q_{in}$  and  $Q_{out}$  are the inlet and outlet species fluxes.

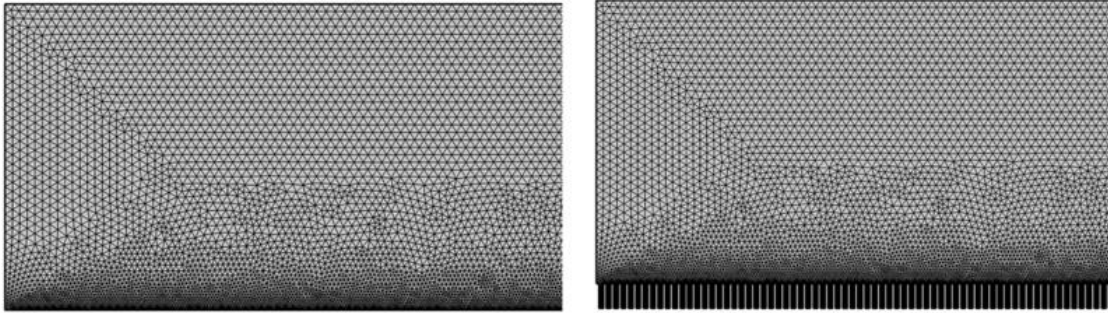


Figure 15: Geometries considered and computational mesh.

Results of simulations performed by using Comsol Multiphysics (Figure 16) showed only a slightly higher absorption value for the case of wall covered with villi, as shown in Table 9: Evaluation of absorption efficiency. Thus, in this simple case the presence of villi has little effect on adsorption. This is since diffusion smooths out gradients within the tightly packed villi, and the channels work almost as if it was just narrower than in the flat wall case. This suggests for villi to effectively increase adsorption some mechanism that generates species gradients in the spaces among villi is needed.

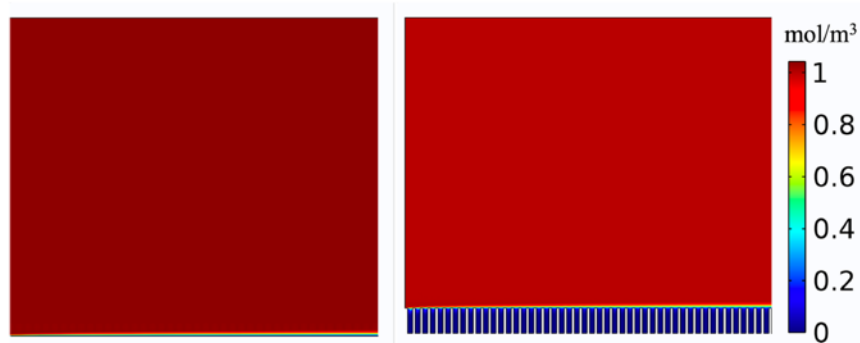


Figure 16: Concentration profiles in the case of a flat (left) and rough (right) wall.

Table 9: Evaluation of absorption efficiency.

Parameter	Flat	Villi
$e$	$4.33 \cdot 10^{-4}$	$5.05 \cdot 10^{-4}$

For this reason, a transverse water flux across the wall was added to the model to consider the water absorption that occurs across the intestinal wall. This flux is indeed likely to exist as it is normally the case that molecules and ion transport across cell layers is accompanied by water flux. This flux has been modelled by imposing a fixed, normal velocity at the wall. The absorption efficiency parameter  $e$  has been evaluated for different physiological values of such a transverse flux and diffusion coefficient. Results reported in Figure 17: Absorption efficiency of the wall in the different cases inspected. display a clear enhancement effect in

the ability of the wall to absorb substances when the presence of villi is combined with the existence of a transverse water flux, even is this transverse flux is very small ( $10^{-6}$  m/s) compared to the longitudinal velocity present in the channel ( $10^{-2}$  m/s).

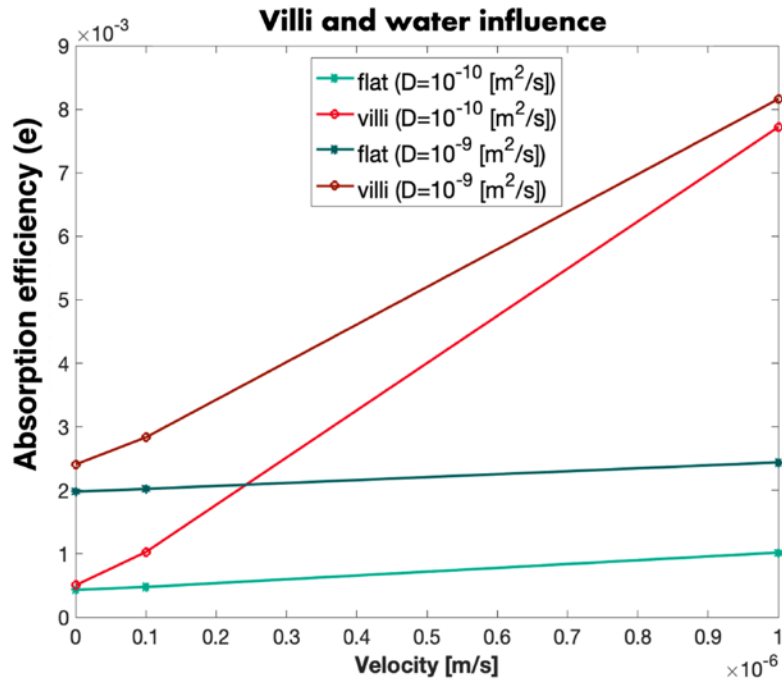


Figure 17: Absorption efficiency of the wall in the different cases inspected.

#### 4.6.3.2 Steady flow through a wavy channel

In order to account for the presence of folds (also known plicae circulares) in the small intestine we modify our two-dimensional intestinal model as shown in the figure below. Three different wavy designs for the absorptive wall have been created, keeping the amplitude of the folds constant (4 mm) and varying the distance between them (4, 6, 10 mm), as depicted in Figure 18: Absorption efficiency of the wall in the different cases inspected.. The absorption efficiency of these wavy walls was therefore compared with the flat wall in the presence of villi and water absorption (normal velocity equal to  $10^{-6}$  m/s).

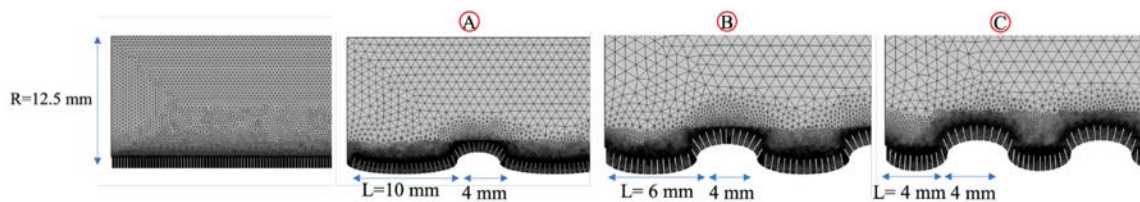


Figure 18: Absorption efficiency of the wall in the different cases inspected.

Results are reported in Figure 19: Comparison between the absorption efficiency of the wavy walls and the flat one. It seems that there may be an optimal distance between the folds of the intestinal wall to increase absorption. In general, the wavy wall augments the absorption efficiency of the intestinal wall, independently from the geometry selected.

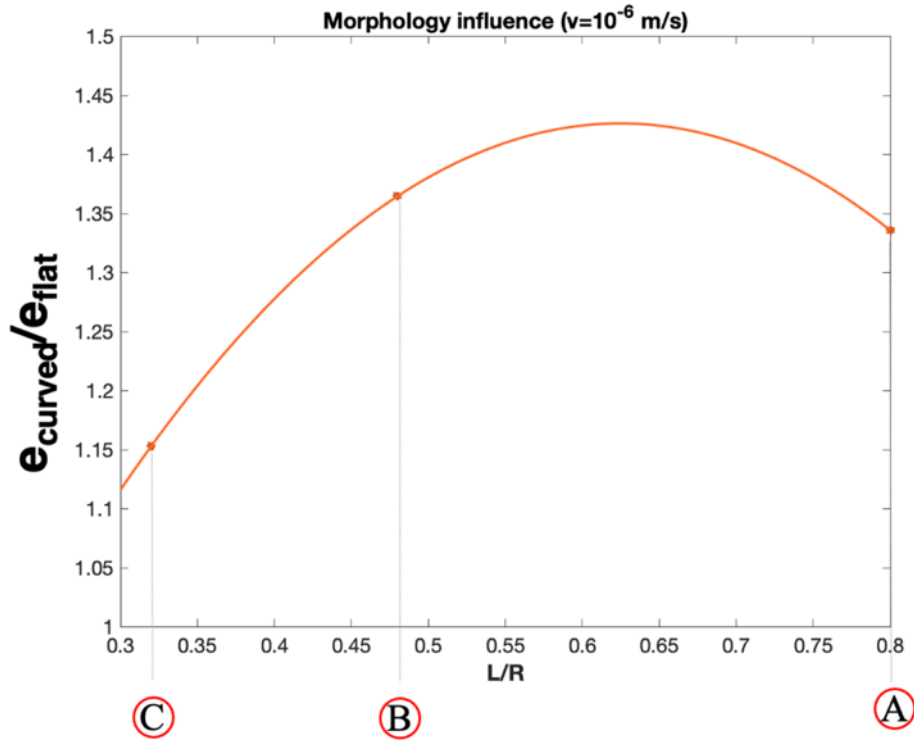


Figure 19: Comparison between the absorption efficiency of the wavy walls and the flat one.

## 4.7 Discussion

It is commonly recognized that ADME properties are crucial to a drug candidate clinical success. To date, poor oral bioavailability - due to inefficient intestinal absorption - has been identified as the primary cause of the high rate of new drug approval failures. For this reason, several in vitro culture systems mimicking the intestinal epithelium have largely spread in the early stages of drug discovery and development to predict intestinal permeability more rapidly and simultaneously reduce animal testing, thus accelerating pharmaceuticals translation into clinics.

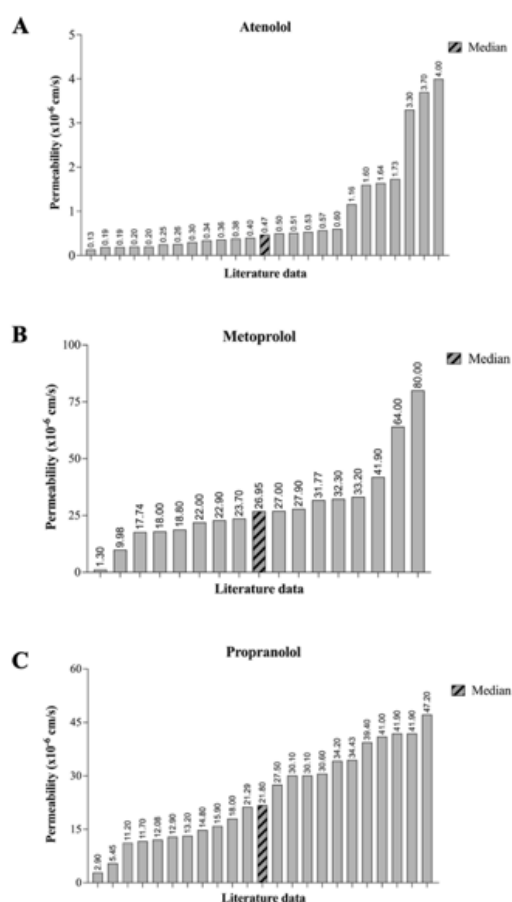


Figure 20: Caco-2 literature data variability. (A) Atenolol, (B) Metoprolol and (C) Propranolol apparent permeability data obtained from Caco-2 cells in different studies/laboratories. The bar graphs show the enormous variability of data present in literature for these three largely employed model compounds. The median of the data set was selected as best representative value and reported in Table 5.

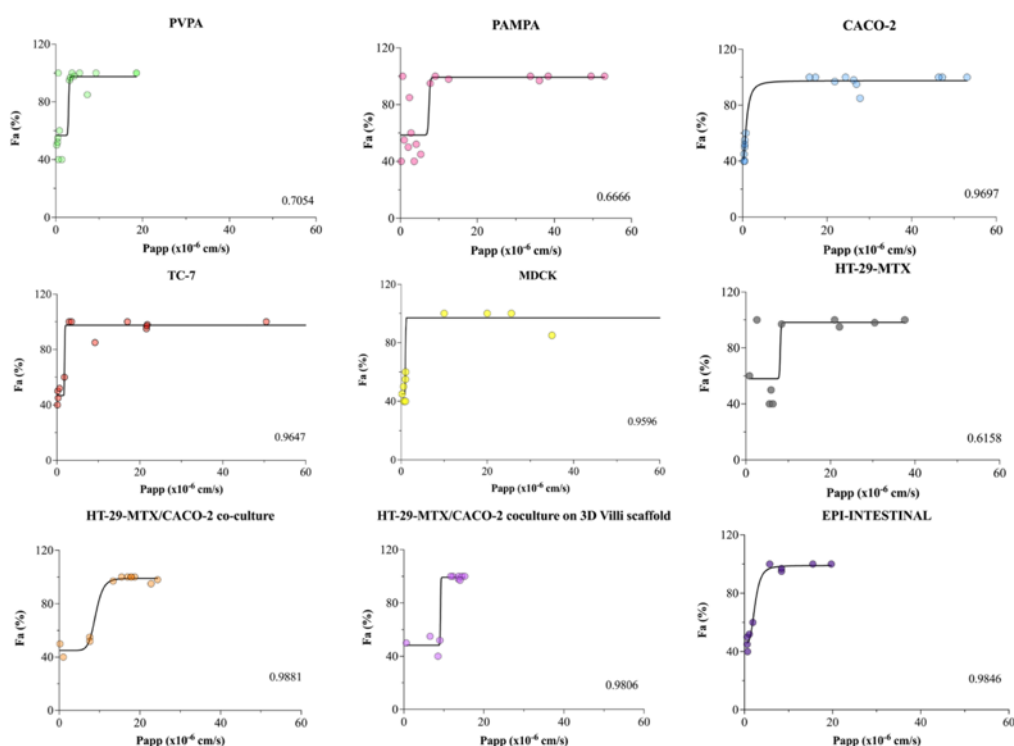
Table 10 shows Papp values obtained from different studies and laboratories by adopting the intestinal epithelium in vitro models previously described, focusing on 17 model drugs that belong to different BCS class and are characterized by various pKa.

Table 10: Summary of model drugs permeation throughout the intestinal epithelium in vitro models. For Caco-2 model, the median of the Papp data set considered from literature was selected as representative value to be reported, as shown in Figure 20.

	pKa	BCS Class	Fa	Papp (x10 <sup>-6</sup> cm/s)												
				PAMPA	PVPA	CACO-2	TC-7	MDCK	MDCK-MDR	HT29-MTX	HIEC	HT-29-MTX/ CACO-2 10%	HT-29-MTX/ CACO-2/ RAJI	3D Villi CACO-2/HT- 29-MTX	EPI-INTESTINAL	CACO-2 on chip
Atenolol	9,6	III	50	2,06	0,22	0,47	0,21	0,58	0,13	5,93	0,68	0,2	16	-	0,6	60
Acetaminophen	9,9	I	85	2,39	7,3	31,9	9,2	35	-	-	-	-	-	-	-	28
Amoxicillin	2,4	III	45	5,3	-	0,33	0,32	0,24	-	-	-	-	-	-	0,6	0,58
Antipyrine	2,2	I	100	9,12	18,6	47,23	50,5	150	19,35	37,6	33	17,82	-	12,3	-	950
Caffeine	14	I	98	12,54	4,32	26,3	21,8	79,3	20	30,5	-	24,38	55,7	13,67	-	3450
Carbamazepine	15,96	II	100	53	18,6	50,3	17,01	-	19,62	-	62	18,74	36,4	13,65	19,7	150
Cimetidine	6,8	III	60	2,8	0,89	0,74	1,86	1,04	0,97	0,86	1,4	-	24,3	-	1,9	20
Furosemide	4,7	IV	40	3,6	1,41	0,29	-	0,62	1,97	5,6	-	1,03	12,4	8,55	0,7	110
Hydrochlorothiazide	7	IV	55	1,02	0,51	-	-	1	-	-	3,3	7,58	-	6,56	-	270
Ketoprofen	3,88	II	100	33,8	5,51	24,36	61	20	-	21	-	16,93	-	14,6	-	5,9
Metoprolol	9,7	I	95	7,8	3,23	26,95	21,6	150	-	22,13	-	22,77	32,3	-	8,4	-
Naproxen	4,19	II	100	49,5	3,79	53,07	89,9	-	-	-	-	17,88	45,7	15,26	15,5	1080
Propranolol	9,5	I	97	36,1	3,41	21,8	21,65	170	34,19	8,45	22	13,38	-	14,07	8,4	390
Ranitidine	8,2	III	52	4,13	0,4	0,49	0,68	-	0,95	-	0,89	7,63	-	9,02	1,1	-
Salicylic Acid	3	I	100	0,59	0,59	15,8	3,55	10	-	2,61	-	-	-	-	-	-
Terbutaline	10,1	III	40	0,23	0,64	0,47	0,128	1	-	6,37	0,7	-	-	-	-	-
Verapamil	8,92	I	100	38,4	9,3	17,2	2,98	25,6	15,2	-	-	15,48	-	11,73	5,7	5,2

2D models are currently the most standardized platforms since they allow for cost-effective and high-throughput screenings. In particular, Caco-2 cells have been accepted as a gold

standard due to their capability to closely resemble the enterocytic phenotype. In fact, Caco-2 and TC-7 cellular models displayed a much higher correlation with in vivo data if compared to synthetic models (Figure 21).



*Figure 21: Human bioavailability and in vitro apparent permeability (Papp) correlation. Graphs illustrating the Papp-Fa sigmoidal relationships for each in vitro system analyzed. The correlation was calculated only for those in vitro models which had a data set composed of at least ten values. The goodness of the fit and, consequently, the goodness of the in vitro model in predicting the human absorption, has been evaluated considering the coefficient of determination R2.*

However, while these conventional cell cultures demonstrated good quantitative correlations with absorbed fraction in humans for drugs transcellularly transported, solely good qualitative results were achieved for other routes, due to their colonic origin and the altered expression of fundamental metabolizing and transporting proteins. Nevertheless, the co-culture of Caco-2 and HT-29-MTX cells - with or without the presence of a 3D scaffold displayed an improved correlation with in vivo data (R2), as depicted in Figure 21. Hence, with the increasing evidence that 3D multicellular in vitro models better recapitulate the in vivo environment, several groups have developed more predictive tools for studying xenobiotics ingestion and digestion through the intestinal barrier. Among them, organoids are capable of reproducing multilineage differentiation as well as the 3D morphology of native tissue; nevertheless, their use is limited in this field because of the inaccessible luminal surface. As a result, easier-to-use human reconstructed intestinal tissues have been commercialized to perform bidirectional permeation studies from the lumen to the bloodstream and vice versa. The relationship between Papp and Fa was found to be higher than 0.98 by using the Epi-Intestinal™ tissue, where multiple cells are present. Anyhow, the lack of dynamic stimuli that mediate ADME processes in the human body prompted the manufacture of micro-physiological technologies capable of emulating chemical gradients, luminal flow and peristaltic movements in a highly controllable manner. Tremendous progress has been recently obtained by coupling organotypic grafts with fluid-dynamic systems in the GIT research. However, many challenges to gain reproducible assays need to

be faced by using these platforms. Indeed, a systematic characterization of drugs, standardized protocols for culturing epithelial and organoid-derived cells, as well as a clear metrics of choice of manufacturing techniques and materials are lagging behind to translate such devices to the market. In light of this, a plethora of efforts will have to be done to improve the experimental reproducibility between and within laboratories and thus the in vitro to in vivo data extrapolation, finally obtaining a robust data set through which the reliability of these models could be demonstrated. Accordingly, the future implementation of these aspects, together with the realization of more in vivo-like models that should include the entire microbiome, a mucus layer and other cell types (e.g. immune cells), will increase the robustness and the predictive potential of these systems.

Regarding in silico models, one of the ingredients that are likely to play an important role in governing absorption at the intestinal wall is villi motility. Villi motion is mostly passive and it is induced by fluid flow. In the presence of an unsteady flow villi deformation might create local fluid circulations that could significantly enhance exchanges between the fluid and the wall. In the next steps, it would therefore be interesting to develop a model that accounts for the following ingredients:

- Three-dimensional fluid and solute transport.
- Unsteady flow conditions where fluid motion would be induced by motion of the wall.
- Villi flexibility. Villi are slender bodies that can be treated as beams with a given bending stiffness.

## 4.8 References

1. Physiologically based pharmacokinetic and pharmacodynamic analysis enabled by microfluidically linked organs-on-chips, *Annu. Rev. Pharmacol. Toxicol.* 58 (2018) 37–64.
2. J. Wang, L. Urban, The impact of early ADME profiling on drug discovery and development strategy, *Drug Discov. World.* (2004) 73–86.
3. D.B. Kassel, Applications of high-throughput ADME in drug discovery, *Curr. Opin. Chem. Biol.* 8 (2004) 339–345, <https://doi.org/10.1016/j.cbpa.2004.04.015>.
4. A.P. Li, Screening for human ADME/Tox drug properties in drug discovery, *Drug Discov. Today.* 6 (2001) 357–366, [https://doi.org/10.1016/S1359-6446\(01\)01712-3](https://doi.org/10.1016/S1359-6446(01)01712-3).
5. H. Yu, A. Adedoyin, ADME-Tox in drug discovery: integration of experimental and computational technologies, *Drug Discov. Today.* 8 (2003) 852–861, [https://doi.org/10.1016/S1359-6446\(03\)02828-9](https://doi.org/10.1016/S1359-6446(03)02828-9).
6. S. Balani, G. Miwa, L.-S. Gan, J.-T. Wu, F. Lee, Strategy of utilizing in vitro and in vivo ADME tools for lead optimization and drug candidate selection, *Curr. Top. Med. Chem.* 5 (2005) 1033–1038, <https://doi.org/10.2174/156802605774297038>.
7. P.A. Billat, E. Roger, S. Faure, F. Lagarce, Models for drug absorption from the small intestine: where are we and where are we going? *Drug Discov. Today.* 22 (2017) 761–775, <https://doi.org/10.1016/j.drudis.2017.01.007>.
8. L. Lin, H. Wong, Predicting oral drug absorption: Mini review on physiologically- based pharmacokinetic models, *Pharmaceutics* 9 (2017), <https://doi.org/10.3390/pharmaceutics9040041>.
9. D.M. Mudie, G.L. Amidon, G.E. Amidon, Physiological parameters for oral delivery and in vitro testing, *Mol. Pharm.* 7 (2010) 1388–1405, <https://doi.org/10.1021/mp100149j>.
10. P. Fasinu, V. Pillay, V.M.K. Ndesendo, L.C. du Toit, Y.E. Choonara, Diverse approaches for the enhancement of oral drug bioavailability, *Biopharm. Drug Dispos.* 32 (2011) 185–209.
11. T. Hou, Y. Li, W. Zhang, J. Wang, Recent developments of in silico predictions of intestinal absorption and oral bioavailability, *Comb. Chem. High Throughput Screen.* 12 (2009) 497–506, <https://doi.org/10.2174/138620709788489082>.
12. S.E. Rosenbaum, Basic pharmacokinetics and pharmacodynamics: An integrated textbook and computer simulations, John Wiley & Sons, 2016.



13. S. Majumdar, A.K. Mitra, Chemical modification and formulation approaches to elevated drug transport across cell membranes, *Expert Opin. Drug Deliv.* 3 (2006) 511–527, <https://doi.org/10.1517/17425247.3.4.511>.
14. D. Dahlgren, H. Lennernas, Intestinal permeability and drug absorption: “ predictive experimental, computational and in vivo approaches, *Pharmaceutics* 11 (2019), <https://doi.org/10.3390/pharmaceutics11080411>.
15. L. Meigs, L. Smirnova, C. Rovida, M. Leist, T. Hartung, Animal testing and its alternatives - the most important omics is economics, *ALTEX* 35 (2018) 275–305, <https://doi.org/10.14573/altex.1807041>.
16. R. Negoro, K. Takayama, Y. Nagamoto, F. Sakurai, M. Tachibana, H. Mizuguchi, Modeling of drug-mediated CYP3A4 induction by using human iPS cell-derived enterocyte-like cells, *Biochem. Biophys. Res. Commun.* 472 (2016) 631–636.
17. L. Romero, J.M. Vela, Alternative models in drug discovery and development part I: in silico and in vitro models, *Vivo Model. Drug Discov.* 9783527333 (2014) 27–58, <https://doi.org/10.1002/9783527679348.ch02>.
18. G. Dothel, V. Vasina, G. Barbara, F. De Ponti, Animal models of chemically induced intestinal inflammation: predictivity and ethical issues, *Pharmacol. Ther.* 139 (2013) 71–86, <https://doi.org/10.1016/j.pharmthera.2013.04.005>.
19. S.K. Doke, S.C. Dhawale, Alternatives to animal testing: a review, *Saudi Pharm. J.* 23 (2015) 223–229, <https://doi.org/10.1016/j.jsps.2013.11.002>.
20. H. Lee, D.S. Kim, S.K. Ha, I. Choi, J.M. Lee, J.H. Sung, A pumpless multi-organ-on- a-chip (MOC) combined with a pharmacokinetic–pharmacodynamic (PK–PD) model, *Biotechnol. Bioeng.* 114 (2017) 432–443, <https://doi.org/10.1002/bit.26087>.
21. M. Kapalczynska, T. Kolenda, W. Przybyła, M. Zajączkowska, A. Teresiak, V. Filas, M. Ibbs, R. Bliźniak, Ł. Łuczewski, K. Lamperska, 2D and 3D cell cultures – a comparison of different types of cancer cell cultures, *Arch. Med. Sci.* 14 (2018) 910–919, <https://doi.org/10.5114/aoms.2016.63743>.
22. A. Marrella, 3D fluid-dynamic ovarian cancer model resembling systemic drug administration for efficacy assay, *ALTEX* 37 (2020) 1–14, <https://doi.org/10.14573/altex.2003131>.
23. C. Vitale, A. Fedi, A. Marrella, G. Varani, M. Fato, S. Scaglione, 3D perfusable hydrogel recapitulating the cancer dynamic environment to in vitro investigate metastatic colonization, *Polymers (Basel)*. 12 (2020) 1–19, <https://doi.org/10.3390/polym12112467>.
24. D. Huh, G.A. Hamilton, D.E. Ingber, From 3D cell culture to organs-on-chips, *Trends Cell Biol.* 21 (2011) 745–754.
25. R. Edmondson, J.J. Broglie, A.F. Adcock, L. Yang, Three-dimensional cell culture systems and their applications in drug discovery and cell-based biosensors, *Assay Drug Dev. Technol.* 12 (2014) 207–218, <https://doi.org/10.1089/adt.2014.573>.
26. U. Marx, T. Akabane, T.B. Andersson, E. Baker, M. Beilmann, S. Beken, S. Brendler-Schwaab, M. Cirit, R. David, E.M. Dehne, I. Durieux, L. Ewart, S. Fitzpatrick, O. Frey, F. Fuchs, L.G. Griffith, G.A. Hamilton, T. Hartung, J. Hoeng, H. Hogberg, D.J. Hughes, D.E. Ingber, A. Iskandar, T. Kanamori, H. Kojima, J. Kuehn, M. Leist, B. Li, P. Loskill, D.L. Mendrick, T. Neumann, G. Pallocca, I. Rusyn, L. Smirnova, T. Steger-Hartmann, D.A. Tagle, A. Tonevitsky, S. Tsyb, M. Trapecar, B. Van de Water, J. Van den Eijnden-van Raaij, P. Vulto, K. Watanabe, A. Wolf, X. Zhou, A. Roth, Biology-inspired microphysiological systems to advance patient benefit and animal welfare in drug development, *ALTEX* 37 (2020) 364–394, <https://doi.org/10.14573/altex.2001241>.
27. A.M. Id, A. Fedi, G. Varani, I. Vaccari, M.F. Id, G. Firpo, P. Guida, N. Aceto, S. S. Id, High blood flow shear stress values are associated with circulating tumor cells cluster disaggregation in a multi-channel microfluidic device, *PLoS One* (2021) 1–19, <https://doi.org/10.1371/journal.pone.0245536>.
28. D. Huh, H.J. Kim, J.P. Fraser, D.E. Shea, M. Khan, A. Bahinski, G.A. Hamilton, D. E. Ingber, Microfabrication of human organs-on-chips, *Nat. Protoc.* 8 (2013) 2135–2157, <https://doi.org/10.1038/nprot.2013.137>.
29. K.J. Jang, K.Y. Suh, A multi-layer microfluidic device for efficient culture and analysis of renal tubular cells, *Lab Chip*. 10 (2010) 36–42, <https://doi.org/10.1039/b907515a>.
30. J. Deng, W. Wei, Z. Chen, B. Lin, W. Zhao, Y. Luo, X. Zhang, Engineered liver-on- a-chip platform to mimic liver functions and its biomedical applications: a review, *Micromachines*. 10 (2019) 676.
31. L.M. Griep, F. Wolbers, B. De Wagenaar, P.M. Ter Braak, B.B. Weksler, I. A. Romero, P.O. Couraud, I. Vermes, A.D. Van Der Meer, A. Van Den Berg, BBB on CHIP: Microfluidic platform to mechanically and biochemically modulate blood- brain barrier function, *Biomed. Microdevices*. 15 (2013) 145–150, <https://doi.org/10.1007/s10544-012-9699-7>.

32. M. Kitsara, D. Kontziampasis, O. Agbulut, Y. Chen, Heart on a Chip: Micro- Nanofabrication and Microfluidics Steering the Future of Cardiac Tissue Engineering, 2019, <https://doi.org/10.1016/j.mee.2018.11.001>.
33. M.B. Esch, J.H. Sung, J. Yang, C. Yu, J. Yu, J.C. March, M.L. Shuler, On chip porous polymer membranes for integration of gastrointestinal tract epithelium with microfluidic 'body-on-a-chip' devices, *Biomed. Microdevices*. 14 (2012) 895–906.
34. C. Beurivage, E. Naumovska, Y.X. Chang, E.D. Elstak, A. Nicolas, H. Wouters, G. van Moolenbroek, H.L. Lanz, S.J. Trietsch, J. Joore, Development of a gut-on-a- chip model for high throughput disease modeling and drug discovery, *Int. J. Mol. Sci.* 20 (2019) 5661.
35. P. Neužil, S. Giselbrecht, K. Lange, T.J. Huang, A. Manz, Revisiting lab-on-a-chip " technology for drug discovery, *Nat. Rev. Drug Discov.* 11 (2012) 620–632, <https://doi.org/10.1038/nrd3799>.
36. E.W. Esch, A. Bahinski, D. Huh, Organs-on-chips at the frontiers of drug discovery, *Nat. Rev. Drug Discov.* 14 (2015) 248–260, <https://doi.org/10.1038/nrd4539>.
37. N. Khalid, I. Kobayashi, M. Nakajima, Recent lab-on-chip developments for novel drug discovery, *Wiley Interdiscip. Rev. Syst. Biol. Med.* 9 (2017), e1381.
38. E.N. Marieb, *Human Anatomy and Physiology 1*, CA Benjamin/Cummings Publ. Company, Inc., Redwood City, 1992, pp. 306–307.
39. J.B. Dressman, H. Lennernas, Oral Drug Absorption: Prediction and Assessment," 2000.
40. P.R. Kiela, F.K. Ghishan, Physiology of intestinal absorption and secretion, *Best Pract. Res. Clin. Gastroenterol.* 30 (2016) 145–159, <https://doi.org/10.1016/j. bpg.2016.02.007>.
41. L. Shargel, B.C. Andrew, S. Wu-Pong, *Applied Biopharmaceutics & Pharmacokinetics*, Appleton & Lange Stamford, 1999.
42. C.A.M. Fois, T.Y.L. Le, A. Schindeler, S. Naficy, D.D. McClure, M.N. Read, P. Valtchev, A. Khademhosseini, F. Dehghani, Models of the gut for analyzing the impact of food and drugs, *Adv. Healthc. Mater.* 8 (2019) 1–23, <https://doi.org/10.1002/adhm.201900968>.
43. R.E. McConnell, J.N. Higginbotham, D.A. Shifrin Jr., D.L. Tabb, R.J. Coffey, M. J. Tyska, The enterocyte microvillus is a vesicle-generating organelle, *J. Cell Biol.* 185 (2009) 1285–1298.
44. M.F. Paine, H.L. Hart, S.S. Ludington, R.L. Haining, A.E. Rettie, D.C. Zeldin, The human intestinal cytochrome P450 "pie", *Drug Metab. Dispos.* 34 (2006) 880–886.
45. K.E. Thummel, Gut instincts: CYP3A4 and intestinal drug metabolism, *J. Clin. Invest.* 117 (2007) 3173–3176.
46. M.V.S. Varma, R.S. Obach, C. Rotter, H.R. Miller, G. Chang, S.J. Steyn, A. El- Kattan, M.D. Troutman, Physicochemical space for optimum oral bioavailability: Contribution of human intestinal absorption and first-pass elimination, *J. Med. Chem.* 53 (2010) 1098–1108, <https://doi.org/10.1021/jm901371v>.
47. D. Onozato, M. Yamashita, A. Nakanishi, T. Akagawa, Y. Kida, I. Ogawa, T. Hashita, T. Iwao, T. Matsunaga, Generation of intestinal organoids suitable for pharmacokinetic studies from human induced pluripotent stem cells, *Drug Metab. Dispos.* 46 (2018) 1572–1580.
48. G. Roda, A. Sartini, E. Zambon, A. Calafiore, M. Marocchi, A. Caponi, A. Belluzzi, E. Roda, Intestinal epithelial cells in inflammatory bowel diseases, *World J. Gastroenterol. WJG.* 16 (2010) 4264.
49. M. Herath, S. Hosie, J.C. Bornstein, A.E. Franks, E.L. Hill-Yardin, The role of the gastrointestinal mucus system in intestinal homeostasis: implications for neurological disorders, *Front. Cell. Infect. Microbiol.* 10 (2020), <https://doi.org/10.3389/fcimb.2020.00248>.
50. B.H. Bajka, N.M. Rigby, K.L. Cross, A. Macierzanka, A.R. Mackie, The influence of small intestinal mucus structure on particle transport ex vivo, *Colloids Surfaces B Biointerfaces.* 135 (2015) 73–80.
51. M. Kebouchi, Z. Hafeez, Y. Le Roux, A. Dary-Mouro, M. Genay, Importance of digestive mucus and mucins for designing new functional food ingredients, *Food Res. Int.* 131 (2020) 108906, <https://doi.org/10.1016/j.foodres.2019.108906>.
52. N. Barker, Adult intestinal stem cells: critical drivers of epithelial homeostasis and regeneration, *Nat. Rev. Mol. Cell Biol.* 15 (2014) 19–33.
53. N. Barker, J.H. Van Es, J. Kuipers, P. Kujala, M. Van Den Born, M. Cozijnsen, A. Haegebarth, J. Korving, H. Begthel, P.J. Peters, Identification of stem cells in small intestine and colon by marker gene *Lgr5*, *Nature.* 449 (2007) 1003–1007.
54. R. Sakamori, S. Yu, X. Zhang, A. Hoffman, J. Sun, S. Das, P. Vedula, G. Li, J. Fu, F. Walker, CDC42 inhibition suppresses progression of incipient intestinal tumors, *Cancer Res.* 74 (2014) 5480–5492.

55. J. Wehkamp, N.H. Salzman, E. Porter, S. Nuding, M. Weichenthal, R.E. Petras, B. Shen, E. Schaeffeler, M. Schwab, R. Linzmeier, Reduced Paneth cell  $\alpha$ -defensins in ileal Crohn's disease, *Proc. Natl. Acad. Sci.* 102 (2005) 18129–18134.
56. K. Pocock, L. Delon, V. Bala, S. Rao, C. Priest, C. Prestidge, B. Thierry, Intestine- on-a-chip microfluidic model for efficient in vitro screening of oral chemotherapeutic uptake, *ACS Biomater. Sci. Eng.* 3 (2017) 951–959, <https://doi.org/10.1021/acsbiomaterials.7b00023>.
57. P. Prieto, S. Hoffmann, V. Tirelli, F. Tancredi, I. Gonzalez, M. Bermejo, I. De ´ Angelis, An exploratory study of two Caco-2 cell models for oral absorption: a report on their within-laboratory and between-laboratory variability, and their predictive capacity, *ATLA Altern. to Lab. Anim.* 38 (2010) 367–386, <https://doi.org/10.1177/026119291003800510>.
58. C. Li, T. Liu, X. Cui, A.S. Uss, K.C. Cheng, Development of in vitro pharmacokinetic screens using Caco-2, human hepatocyte, and Caco-2/human hepatocyte hybrid systems for the prediction of oral bioavailability in humans, *J. Biomol. Screen.* 12 (2007) 1084–1091, <https://doi.org/10.1177/1087057107308892>.
59. S. Tavelin, J. Taipalensuu, L. Soderberg, R. Morrison, S. Chong, P. Artursson, Prediction of the oral absorption of low-permeability drugs using small intestine- like 2/4/A1 cell monolayers, *Pharm. Res.* 20 (2003) 397–405.
60. V. Gupta, N. Doshi, S. Mitragotri, Permeation of insulin, calcitonin and exenatide across Caco-2 monolayers: measurement using a rapid, 3-day system, *PLoS One.* 8 (2013), e57136.
61. S. Fowler, W.L.K. Chen, D.B. Duignan, A. Gupta, N. Hariparsad, J.R. Kenny, W. G. Lai, J. Liras, J.A. Phillips, J. Gan, Microphysiological systems for ADME-related applications: current status and recommendations for system development and characterization, *Lab Chip.* 20 (2020) 446–467, <https://doi.org/10.1039/c9lc00857h>.
62. S.N. Steinway, J. Saleh, B.K. Koo, D. Delacour, D.H. Kim, Human microphysiological models of intestinal tissue and gut microbiome, *Front. Bioeng. Biotechnol.* 8 (2020), <https://doi.org/10.3389/fbioe.2020.00725>.
63. J.M. DeSesso, A.L. Williams, Chapter 21 - contrasting the gastrointestinal tracts of mammals: factors that influence absorption, in: M.C. Macor (Ed.), J.E.B.T.-A.R., Academic Press, 2008, pp. 353–371, [https://doi.org/10.1016/S0065-7743\(08\)00021-3](https://doi.org/10.1016/S0065-7743(08)00021-3).
64. S.P. Gantzsch, B. Kann, M. Ofer-Glaessgen, P. Loos, H. Berchtold, S. Balbach, T. Eichinger, C.M. Lehr, U.F. Schaefer, M. Windbergs, Characterization and evaluation of a modified PVPA barrier in comparison to Caco-2 cell monolayers for combined dissolution and permeation testing, *J. Control. Release.* 175 (2014) 79–86, <https://doi.org/10.1016/j.jconrel.2013.12.009>.
65. J.M. Reis, B. Sinko, C.H.R. Serra, Parallel artificial membrane permeability assay (PAMPA) - is it better than Caco-2 for human passive permeability prediction? Mini-Reviews *Med. Chem.* 10 (2012) 1071–1076, <https://doi.org/10.2174/1389557511009011071>.
66. P. Sciences, Examination of Permeability of Drugs by PAMPA Method in Theoretical and Practical Aspects Gabor Vizse´ ralek, 201´ 6.
67. H. Yu, Q. Wang, Y. Sun, M. Shen, H. Li, Y. Duan, A new PAMPA model proposed on the basis of a synthetic phospholipid membrane, *PLoS One.* 10 (2015) 1–13, <https://doi.org/10.1371/journal.pone.0116502>.
68. M. Kansy, F. Senner, K. Gubernator, Physicochemical high throughput screening: parallel artificial membrane permeation assay in the description of passive absorption processes, *J. Med. Chem.* 41 (1998) 1007–1010.
69. A. Avdeef, The rise of PAMPA, *Expert Opin. Drug Metab. Toxicol.* 1 (2005) 325–342.
70. J. Mensch, A. Melis, C. Mackie, G. Verreck, M.E. Brewster, P. Augustijns, Evaluation of various PAMPA models to identify the most discriminating method for the prediction of BBB permeability, *Eur. J. Pharm. Biopharm.* 74 (2010) 495–502, <https://doi.org/10.1016/j.ejpb.2010.01.003>.
71. B. Sinko, T.M. Garrigues, G.T. Balogh, Z.K. Nagy, O. Tsinman, A. Avdeef, ´ K. Takacs-Nov´ ak, Skin-PAMPA: A new method for fast prediction of skin ´ penetration, *Eur. J. Pharm. Sci.* 45 (2012) 698–707, <https://doi.org/10.1016/j.ejps.2012.01.011>.
72. M. Falavigna, M. Klitgaard, C. Brase, S. Ternullo, N. Skalko-Basnet, G.E. Flaten, ´ Mucus-PVPA (mucus Phospholipid Vesicle-based Permeation Assay): An artificial permeability tool for drug screening and formulation development, *Int. J. Pharm.* 537 (2018) 213–222, <https://doi.org/10.1016/j.ijpharm.2017.12.038>.
73. P. Berben, A. Bauer-Brandl, M. Brandl, B. Faller, G.E. Flaten, A.C. Jacobsen, J. Brouwers, P. Augustijns, Drug permeability profiling using cell-free permeation tools: Overview and applications, *Eur. J. Pharm. Sci.* 119 (2018) 219–233, <https://doi.org/10.1016/j.ejps.2018.04.016>.

74. G.E. Flaten, A.B. Dhanikula, K. Luthman, M. Brandl, Drug permeability across a phospholipid vesicle based barrier: a novel approach for studying passive diffusion, *Eur. J. Pharm. Sci.* 27 (2006) 80–90, <https://doi.org/10.1016/j.ejps.2005.08.007>.
75. G.E. Flaten, Z. Palac, A. Engesland, J. Filipović-Grčić, Z. Vanić, N. Skalko-Basnet, In vitro skin models as a tool in optimization of drug formulation, *Eur. J. Pharm. Sci.* 75 (2015) 10–24, <https://doi.org/10.1016/j.ejps.2015.02.018>.
76. E. Naderkhani, J. Isaksson, A. Ryzhakov, G.E. Flaten, Development of a biomimetic phospholipid vesicle-based permeation assay for the estimation of intestinal drug permeability, *J. Pharm. Sci.* 103 (2014) 1882–1890, <https://doi.org/10.1002/jps.23954>.
77. J. Fogh, T. Orfeo, J. Tiso, F.E. Sharkey, Establishment of human colon carcinoma lines in nude mice, *Pathobiology.* 47 (1979) 136–144.
78. I. de Angelis, L. Turco, Caco-2 cells as a model for intestinal absorption, *Curr. Protoc. Toxicol.* (2011) 1–15, <https://doi.org/10.1002/0471140856.tx2006s47>.
79. M. Hu, J. Ling, H. Lin, J. Chen, Use of Caco-2 Cell monolayers to study drug absorption and metabolism, *Optim. Drug Discov.* (2004) 19–35, <https://doi.org/10.1385/1-59259-800-5:019>.
80. I.J. Hidalgo, T.J. Raub, R.T. Borchardt, Characterization of the human colon carcinoma cell line (Caco-2) as a model system for intestinal epithelial permeability, *Gastroenterology.* 96 (1989) 736–749, [https://doi.org/10.1016/0016-5085\(89\)90897-4](https://doi.org/10.1016/0016-5085(89)90897-4).
81. A. Zweibaum, M. Laburthe, E. Grasset, D. Louvard, Use of cultured cell lines in studies of intestinal cell differentiation and function, *Compr. Physiol.* (2011), <https://doi.org/10.1002/cphy.cp060407>.
82. B. Sarmiento, F. Andrade, S.B. Da Silva, F. Rodrigues, J. Das Neves, D. Ferreira, Cell-based in vitro models for predicting drug permeability, *Expert Opin. Drug Metab. Toxicol.* 8 (2012) 607–621, <https://doi.org/10.1517/17425255.2012.673586>.
83. P. Dowdell, S. Chankhamhaengdech, W. Panbangred, T. Janvilisri, A. Aroonnu, Probiotic activity of enterococcus faecium and lactococcus lactis isolated from thai fermented sausages and their protective effect against clostridium difficile, *Probiotics Antimicrob. Proteins.* 12 (2020) 641–648, <https://doi.org/10.1007/s12602-019-09536-7>.
84. B. Srinivasan, A.R. Kolli, M.B. Esch, H.E. Abaci, M.L. Shuler, J.J. Hickman, TEER measurement techniques for in vitro barrier model systems, *J. Lab. Autom.* 20 (2015) 107–126, <https://doi.org/10.1177/2211068214561025>.
85. S. Ayejunie, T. Landry, Z. Stevens, A. Armento, P. Hayden, M. Klausner, Human primary cell-based organotypic microtissues for modeling small intestinal drug absorption, *Pharm. Res.* 35 (2018), <https://doi.org/10.1007/s11095-018-2362-0>.
86. P. Artursson, A.-L. Ungell, J.-E. Lofroth, Selective paracellular permeability in two models of intestinal absorption: cultured monolayers of human intestinal epithelial cells and rat intestinal segments, *Pharm. Res.* 10 (1993) 1123–1129, <https://doi.org/10.1023/A:1018903931777>.
87. Y. Tanaka, Y. Taki, T. Sakane, T. Nadai, H. Sezaki, S. Yamashita, Characterization of drug transport through tight-junctional pathway in Caco-2 monolayer: comparison with isolated Rat Jejunum and colon, *Pharm. Res.* 12 (1995) 523–528, <https://doi.org/10.1023/A:1016245711557>.
88. J. Linnankoski, J. Mäkelä, J. Palmgren, T. Mauriala, C. Vedin, A. Ungell, L. Lazorova, P. Artursson, A. Urtili, M. Yliperttula, Paracellular porosity and pore size of the human intestinal epithelium in tissue and cell culture models, *J. Pharm. Sci.* 99 (2010) 2166–2175, <https://doi.org/10.1002/jps.21961>.
89. G. Wilson, I.F. Hassan, C.J. Dix, I. Williamson, R. Shah, M. Mackay, P. Artursson, Transport and permeability properties of human Caco-2 cells: an in vitro model of the intestinal epithelial cell barrier, *J. Control. Release* 11 (1990) 25–40, [https://doi.org/10.1016/0168-3659\(90\)90118-D](https://doi.org/10.1016/0168-3659(90)90118-D).
90. P. Artursson, K. Palm, K. Luthman, Caco-2 monolayers in experimental and theoretical predictions of drug transport, *Adv. Drug Deliv. Rev.* 64 (2012) 280–289, <https://doi.org/10.1016/j.addr.2012.09.005>.
91. A.L. Rao, G.G. Sankar, Caco-2: an overview, *Jprhc.* 1 (2009) 260–275.
92. J.L. Madara, G. Hecht, Tight (occluding) junctions in cultured (and native) epithelial cells, *Funct. Epithel. Cells Cult.* (1989) 131–163.
93. D.-C. Kirn, P.S. Burton, R.T. Borchardt, A correlation between the permeability characteristics of a series of peptides using an in vitro cell culture model (Caco-2) and those using an in situ perfused rat ileum model of the intestinal mucosa, *Pharm. Res.* 10 (1993) 1710–1714, <https://doi.org/10.1023/A:1018961828510>.

94. R.A. Conradi, K.F. Wilkinson, B.D. Rush, A.R. Hilgers, M.J. Ruwart, P.S. Burton, In vitro/in vivo models for peptide oral absorption: comparison of Caco-2 cell permeability with rat intestinal absorption of renin inhibitory peptides, *Pharm. Res.* 10 (1993) 1790–1792, <https://doi.org/10.1023/A:1018990602102>.
95. D. Sun, H. Lennernas, L.S. Welage, J.L. Barnett, C.P. Landowski, D. Foster, D. Fleisher, K.D. Lee, G.L. Amidon, Comparison of human duodenum and Caco-2 gene expression profiles for 12,000 gene sequences tags and correlation with permeability of 26 drugs, *Pharm. Res.* 19 (2002) 1400–1416, <https://doi.org/10.1023/A:1020483911355>.
96. W. Rubas, J. Villagran, M. Cromwell, A. McLeod, J. Wassenberg, Correlation of solute flux across Caco-2 monolayers and colonic tissue in vitro, *STP Pharma Sci.* 5 (1995) 93–97.
97. P. Wils, A. Warnery, V. Phung-Ba, D. Scherman, Differentiated intestinal epithelial cell lines as in vitro models for predicting the intestinal absorption of drugs, *Cell Biol. Toxicol.* 10 (1994) 393–397.
98. G. Wilson, I.F. Hassan, C.J. Dix, I. Williamson, R. Shah, M. Mackay, Transport and permeability properties of human Caco-2 cells: an in vitro model of the intestinal epithelial cell barrier \* and P. Artursson When on nitrocellulose filters, in chambers, Caco-2 cells form a confluent monolayer with several proper, *Science* 11 (1990) 25–40.
99. J. Hunter, M.A. Jepson, T. Tsuruo, N.L. Simmons, B.H. Hirst, Functional expression of P-glycoprotein in apical membranes of human intestinal Caco-2 cells. Kinetics of vinblastine secretion and interaction with modulators, *J. Biol. Chem.* 268 (1993) 14991–14997.
100. N. Maubon, M. Le Vee, L. Fossati, M. Audry, E. Le Ferrec, S. Bolze, O. Fardel, Analysis of drug transporter expression in human intestinal Caco-2 cells by real-time PCR, *Fundam. Clin. Pharmacol.* 21 (2007) 659–663, <https://doi.org/10.1111/j.1472-8206.2007.00550.x>.
101. C. Hilgendorf, G. Ahlin, A. Seithel, P. Artursson, A.-L. Ungell, J. Karlsson, Expression of thirty-six drug transporter genes in human intestine, liver, kidney, and organotypic cell lines, *Drug Metab. Dispos.* 35 (2007) 1333–1340.
102. J. Taipalensuu, H. Tornblom, G. Lindberg, C. Einarsson, F. Sjöqvist, H. Melhus, P. Garberg, B. Sjöström, B. Lundgren, P. Artursson, Correlation of gene expression of ten drug efflux proteins of the ATP-binding cassette transporter family in normal human jejunum and in human intestinal epithelial Caco-2 cell monolayers, *J. Pharmacol. Exp. Ther.* 299 (2001) 164–170.
103. S. Brück, J. Strohmeier, D. Busch, M. Drozdzik, S. Oswald, Caco-2 cells—expression, regulation and function of drug transporters compared with human jejunal tissue, *Biopharm. Drug Dispos.* 38 (2017) 115–126.
104. M.H. Macedo, F. Araújo, E. Martínez, C. Barrias, B. Sarmiento, iPSC-derived enterocyte-like cells for drug absorption and metabolism studies, *Trends Mol. Med.* 24 (2018) 696–708, <https://doi.org/10.1016/j.molmed.2018.06.001>.
105. A.-L.B. Ungell, Caco-2 replace or refine? *Drug Discov. Today Technol.* 1 (2004) 423–430.
106. R.B. Van Breemen, Y. Li, Caco-2 cell permeability assays to measure drug absorption, *Expert Opin. Drug Metab. Toxicol.* 1 (2005) 175–185, <https://doi.org/10.1517/17425255.1.2.175>.
107. N.J. Darling, C.L. Mobbs, A.L. Gonzalez-Hau, M. Freer, S. Przyborski, Bioengineering novel in vitro co-culture models that represent the human intestinal mucosa with improved Caco-2 structure and barrier function, *Front. Bioeng. Biotechnol.* 8 (2020) 1–15, <https://doi.org/10.3389/fbioe.2020.00992>.
108. V. Meunier, M. Bourrié, Y. Berger, G. Fabre, The human intestinal epithelial cell line Caco-2; pharmacological and pharmacokinetic applications, *Cell Biol. Toxicol.* 11 (1995) 187–194, <https://doi.org/10.1007/BF00756522>.
109. H. Sun, E.C.Y. Chow, S. Liu, Y. Du, K.S. Pang, The Caco-2 cell monolayer: Usefulness and limitations, *Expert Opin. Drug Metab. Toxicol.* 4 (2008) 395–411, <https://doi.org/10.1517/17425255.4.4.395>.
110. P. Artursson, Cell cultures as models for drug absorption across the intestinal mucosa, *Crit. Rev. Ther. Drug Carrier Syst.* 8 (1991) 305–330.
111. A.V. Lyubimov, E. Le Ferrec, O. Fardel, Applications using Caco-2 and TC7 cells for drug metabolism studies, *Encycl. Drug Metab. Interact.* (2012), <https://doi.org/10.1002/9780470921920.edm061>.
112. W. Jee, L. Weiss, Histology: cell and tissue biology, *Histol. Cell Tissue Biol.* 5 (1983) 200–255.
113. L. Turco, T. Catone, F. Caloni, E. Di Consiglio, E. Testai, A. Stamatii, Caco-2/TC7 cell line characterization for intestinal absorption: how reliable is this in vitro model for the prediction of the oral dose fraction absorbed in human? *Toxicol. Vit.* 25 (2011) 13–20, <https://doi.org/10.1016/j.tiv.2010.08.009>.
114. H. Lennernas, K. Palm, U. Fagerholm, P. Artursson, Comparison between active and passive drug transport in human intestinal epithelial (Caco-2) cells in vitro and human jejunum in vivo, *Int. J. Pharm.* 127 (1996) 103–107.

115. M.-C. Gr`es, B. Julian, M. Bourri'e, V. Meunier, C. Roques, M. Berger, X. Boulenc, Y. Berger, G. Fabre, Correlation between oral drug absorption in humans, and apparent drug permeability in TC-7 cells, a human epithelial intestinal cell line: comparison with the parental Caco-2 cell line, *Pharm. Res.* 15 (1998) 726–733, <https://doi.org/10.1023/A:1011919003030>.
116. X. Liu, V.H. Tam, M. Hu, Disposition of flavonoids via enteric recycling: determination of the UDP-glucuronosyltransferase isoforms responsible for the metabolism of flavonoids in intact Caco-2 TC7 cells using siRNA, *Mol. Pharm.* 4 (2007) 873–882.
117. I. Caro, X. Boulenc, M. Rousset, V. Meunier, M. Bourrie, B. Julian, H. Joyeux, Roques, Y. Berger, A. Zweibaum, Characterisation of a newly isolated Caco-2 clone (TC-7), as a model of transport processes and biotransformation of drugs, *Int. J. Pharm.* 116 (1995) 147–158.
118. E. Le Ferrec, C. Chesne, P. Artusson, D. Brayden, G. Fabre, P. Gires, F. Guillou, M. Rousset, W. Rubas, M.L. Scarino, In vitro models of the intestinal barrier, *ATLA Altern. to Lab. Anim.* 29 (2001) 649–668, <https://doi.org/10.1177/026119290102900604>.
119. M.J. Cho, D.P. Thompson, C.T. Cramer, T.J. Vidmar, J.F. Scieszka, The Madin Darby canine kidney (MDCK) epithelial cell monolayer as a model cellular transport barrier, *Pharm. Res.* 6 (1989) 71–77.
120. F. Antunes, F. Andrade, D. Ferreira, H. Morck Nielsen, B. Sarmiento, Models to predict intestinal absorption of therapeutic peptides and proteins, *Curr. Drug Metab.* 14 (2012) 4–20, <https://doi.org/10.2174/138920013804545160>.
121. J.D. Irvine, L. Takahashi, K. Lockhart, J. Cheong, J.W. Tolan, H.E. Selick, J. R. Grove, MDCK (Madin-Darby canine kidney) cells: A tool for membrane permeability screening, *J. Pharm. Sci.* 88 (1999) 28–33, <https://doi.org/10.1021/js9803205>.
122. P.V. Balimane, S. Chong, R.A. Morrison, Current methodologies used for evaluation of intestinal permeability and absorption, *J. Pharmacol. Toxicol. Methods.* 44 (2000) 301–312, [https://doi.org/10.1016/S1056-8719\(00\)00113-1](https://doi.org/10.1016/S1056-8719(00)00113-1). [123] F. Tang, K. Horie, R.T. Borchardt, Are MDCK cells transfected with the human MRP2 gene a good model of the human intestinal mucosa? *Pharm. Res.* 19 (2002) 773–779, <https://doi.org/10.1023/A:1016192413308>.
123. D.A. Volpe, Drug-permeability and transporter assays in Caco-2 and MDCK cell lines, *Future Med. Chem.* 3 (2011) 2063–2077, <https://doi.org/10.4155/fmc.11.149>.
124. D. Mart´inez-Maqueda, B. Miralles, I. Recio, HT29 cell line, *Impact Food Bioact. Heal.* (2015) 113–124.
125. D. Mart´inez-Maqueda, B. Miralles, I. Recio, HT29 Cell Line BT, in: K. Verhoeckx, P. Cotter, I. Lopez-Exp´osito, C. Kleiveland, T. Lea, A. Mackie, H. Wichers (Eds.), *The Impact of Food Bioactives on Health: in vitro and ex vivo models*, Springer International Publishing, Cham, 2015, pp. 113–124, [https://doi.org/10.1007/978-3-319-16104-4\\_11](https://doi.org/10.1007/978-3-319-16104-4_11).
126. M. Rousset, The human colon carcinoma cell lines HT-29 and Caco-2: two in vitro models for the study of intestinal differentiation, *Biochimie.* 68 (1986) 1035–1040, [https://doi.org/10.1016/S0300-9084\(86\)80177-8](https://doi.org/10.1016/S0300-9084(86)80177-8).
127. C. Huet, C. Sahuquillo-Merino, E. Coudrier, D. Louvard, Absorptive and mucus-secreting subclones isolated from a multipotent intestinal cell line (HT-29) provide new models for cell polarity and terminal differentiation, *J. Cell Biol.* 105 (1987) 345–357, <https://doi.org/10.1083/jcb.105.1.345>.
128. T. Lesuffleur, A. Barbat, E. Dussaulx, A. Zweibaum, Growth adaptation to methotrexate of HT-29 human colon carcinoma cells is associated with their ability to differentiate into columnar absorptive and mucus-secreting cells, *Cancer Res.* 50 (1990) 6334–6343.
129. P. Kitabgi, C. Poustis, C. Granier, J. van Rietschoten, J. Rivier, J.-L. Morgat, P. Freychet, Neurotensin binding to extraneural and neural receptors: comparison with biological activity and structure—activity relationships, *Mol. Pharmacol.* 18 (1980) 11–19.
130. P. Wils, S. Legrain, E. Frenois, D. Scherman, HT29-18-C1 intestinal cells: A new model for studying the epithelial transport of drugs, *BBA - Mol. Cell Res.* 1177 (1993) 134–138, [https://doi.org/10.1016/0167-4889\(93\)90032-K](https://doi.org/10.1016/0167-4889(93)90032-K).
131. C. Augeron, C.L. Laboisse, Emergence of permanently differentiated cell clones in a human colonic cancer cell line in culture after treatment with sodium butyrate, *Cancer Res.* 44 (1984) 3961–3969.
132. A. Wikman, J. Karlsson, I. Carlstedt, P. Artursson, A drug absorption model based on the mucus layer producing human intestinal goblet cell line HT29-H, *Pharm. Res. An Off. J. Am. Assoc. Pharm. Sci.* 10 (1993) 843–852, <https://doi.org/10.1023/A:1018905109971>.
133. C. Pontier, J. Pachot, R. Botham, B. Lenfant, P. Arnaud, HT29-MTX and Caco-2/TC7 monolayers as predictive models for human intestinal absorption: Role of the mucus layer, *J. Pharm. Sci.* 90 (2001) 1608–1619, <https://doi.org/10.1002/jps.1111>.

135. I. Behrens, P. Stenberg, P. Artursson, T. Kissel, Transport of lipophilic drug molecules in a new mucus-secreting cell culture model based on HT29-MTX cells, *Pharm. Res.* 18 (2001) 1138–1145, <https://doi.org/10.1023/A:1010974909998>.
136. R. Dupak, I. Spevakova, M. Capcarova, Use of HT-29 cell line to investigate toxicological effects of mycotoxins: a mini review, *Sci. Pap. Anim. Sci. Biotechnol. Stiint. Zooteh. Si Biotehnl.* 53 (2020).
137. L. Mahlert, J. Anderski, D. Mulac, K. Langer, The impact of gastrointestinal mucus on nanoparticle penetration – in vitro evaluation of mucus-penetrating nanoparticles for photodynamic therapy, *Eur. J. Pharm. Sci.* 133 (2019) 28–39, <https://doi.org/10.1016/j.ejps.2019.03.010>.
138. E. Walter, S. Janich, B.J. Roessler, J.M. Hilfinger, G.L. Amidon, HT29-MTX/Caco-2 cocultures as an in vitro model for the intestinal epithelium: In vitro-in vivo correlation with permeability data from rats and humans, *J. Pharm. Sci.* 85 (1996) 1070–1076, <https://doi.org/10.1021/js960110x>.
139. S. The, C. Biology, N. Feb, Epithelioid Cell Cultures from Rat Small Intestine: Characterization by Morphologic and Immunologic Criteria Author (s): Andrea Quaroni, Jack Wands, Robert L. Trelstad and Kurt J. Isselbacher 80, 2014, pp. 248–265.
140. A. Quaroni, K.J. Isselbacher, Cytotoxic effects and metabolism of benzo [a] pyrene and 7, 12-dimethylbenz [a] anthracene in duodenal and ileal epithelial cell cultures, *J. Natl. Cancer Inst.* 67 (1981) 1353–1362.
141. E. Duizer, A.H. Penninks, W.H. Stenhuis, J.P. Groten, Comparison of permeability characteristics of the human colonic Caco-2 and rat small intestinal IEC-18 cell lines, *J. Control. Release.* 49 (1997) 39–49, [https://doi.org/10.1016/S0168-3659\(97\)00058-8](https://doi.org/10.1016/S0168-3659(97)00058-8).
142. D.W. Powell, Barrier function of epithelia, *Am. J. Physiol. Liver Physiol.* 241 (1981) G275–G288.
143. P. Artursson, J. Karlsson, Correlation between oral drug absorption in humans and apparent drug permeability coefficients in human intestinal epithelial (Caco-2) cells, *Biochem. Biophys. Res. Commun.* 175 (1991) 880–885.
144. C.H.M. Versantvoort, R.C.A. Ondrewater, E. Duizer, J.J.M. Van de Sandt, A. Gilde, J.P. Groten, Monolayers of IEC-18 cells as an in vitro model for screening the passive transcellular and paracellular transport across the intestinal barrier: comparison of active and passive transport with the human colon carcinoma Caco-2 cell line, *Environ. Toxicol. Pharmacol.* 11 (2002) 335–344.
145. A. Steensma, H.P.J.M. Noteborn, H.A. Kuiper, Comparison of Caco-2, IEC-18 and HCEC cell lines as a model for intestinal absorption of genistein, daidzein and their glycosides, *Environ. Toxicol. Pharmacol.* 16 (2004) 131–139, <https://doi.org/10.1016/j.etap.2003.11.008>.
146. T.Y. Ma, D. Hollander, D. Bhalla, H. Nguyen, P. Krugliak, IEC-18, a nontransformed small intestinal cell line for studying epithelial permeability, *J. Lab. Clin. Med.* 120 (1992) 329–341.
147. C.H.M. Versantvoort, R.C.A. Ondrewater, E. Duizer, J.J.M. Van De Sandt, A. Gilde, J.P. Groten, Erratum: monolayers of IEC-18 cells as an in vitro model for screening the passive transcellular and paracellular transport across the intestinal barrier: comparison of active and passive transport with the human colon carcinoma Caco-2 cell line (Environm), *Environ. Toxicol. Pharmacol.* 13 (2003) 55, [https://doi.org/10.1016/S1382-6689\(02\)00123-0](https://doi.org/10.1016/S1382-6689(02)00123-0).
148. Z. Liu, P. Zhang, Y. Zhou, H. Qin, T. Shen, Culture of human intestinal epithelial cell using the dissociating enzyme thermolysin and endothelin-3, *Brazilian J. Med. Biol. Res.* 43 (2010) 451–459, <https://doi.org/10.1590/S0100-879X2010007500036>.
149. N. Perreault, J.F. Beaulieu, Use of the dissociating enzyme thermolysin to generate viable human normal intestinal epithelial cell cultures, *Exp. Cell Res.* 224 (1996) 354–364, <https://doi.org/10.1006/excr.1996.0145>.
150. T. Takenaka, N. Harada, J. Kuze, M. Chiba, T. Iwao, T. Matsunaga, Human small intestinal epithelial cells differentiated from adult intestinal stem cells as a novel system for predicting oral drug absorption in humans, *Drug Metab. Dispos.* 42 (2014) 1947–1954, <https://doi.org/10.1124/dmd.114.059493>.
151. T. Takenaka, N. Harada, J. Kuze, M. Chiba, T. Iwao, T. Matsunaga, Application of a human intestinal epithelial cell monolayer to the prediction of oral drug absorption in humans as a superior alternative to the Caco-2 cell monolayer, *J. Pharm. Sci.* 105 (2016) 915–924, <https://doi.org/10.1016/j.xphs.2015.11.035>.
152. L. Pageot, N. Perreault, N. Basora, C. Francoeur, P. Magny, J. Beaulieu, Human cell models to study small intestinal functions: recapitulation of the crypt-villus axis, *Microsc. Res. Tech.* 49 (2000) 394–406.
153. F. Escaffit, N. Perreault, D. Jean, C. Francoeur, E. Herring, C. Rancourt, N. Rivard, P.H. Vachon, F. Paré, M.-P. Boucher, Repressed E-cadherin expression in the lower crypt of human small intestine: a cell marker of functional relevance, *Exp. Cell Res.* 302 (2005) 206–220.
154. J.-F. Beaulieu, D. Menard, Isolation, characterization, and culture of normal human intestinal crypt and villus cells, in: *Hum. Cell Cult. Protoc.*, Springer, 2012, pp. 157–173.

155. C. Hilgendorf, H. Spahn-Langguth, C.G. Regårdh, E. Lipka, G.L. Amidon, P. Langguth, Caco-2 versus Caco-2/HT29-MTX co-cultured cell lines: Permeabilities via diffusion, inside- and outside-directed carrier-mediated transport, *J. Pharm. Sci.* 89 (2000) 63–75, [https://doi.org/10.1002/\(SICI\)1520-6017\(200001\)89:1<63::AID-JPS7>3.0.CO;2-6](https://doi.org/10.1002/(SICI)1520-6017(200001)89:1<63::AID-JPS7>3.0.CO;2-6).
156. A. Wikman-Larhed, P. Artursson, Co-cultures of human intestinal goblet (HT29- H) and absorptive (Caco-2) cells for studies of drug and peptide absorption, *Eur. J. Pharm. Sci.* 3 (1995) 171–183.
157. C. Pereira, J. Costa, B. Sarmiento, F. Araújo, Cell-based in vitro models for intestinal permeability studies, in: *Concepts Model. Drug Permeability Stud. Cell Tissue Based Vitr. Cult. Model*, 2016, pp. 57–81, <https://doi.org/10.1016/B978-0-08-100094-6.00005-5>.
158. A. Béduneau, C. Tempesta, S. Fimbel, Y. Pellequer, V. Jannin, F. Demarne, A. Lamprecht, A tunable Caco-2/HT29-MTX co-culture model mimicking variable permeabilities of the human intestine obtained by an original seeding procedure, *Eur. J. Pharm. Biopharm.* 87 (2014) 290–298.
159. S. Kern´eis, A. Bogdanova, J.-P. Kraehenbuhl, E. Pringault, Conversion by Peyer’s patch lymphocytes of human enterocytes into M cells that transport bacteria, *Science* (80) 277 (1997) 949–952.
160. A. Frey, K.T. Giannasca, R. Weltzin, P.J. Giannasca, H. Reggio, W.I. Lencer, M. R. Neutra, Role of the glycocalyx in regulating access of microparticles to apical plasma membranes of intestinal epithelial cells: implications for microbial attachment and oral vaccine targeting, *J. Exp. Med.* 184 (1996) 1045–1059.
161. A. Des Rieux, V. Fievez, I. Th´eate, J. Mast, V. Pr´eat, Y.J. Schneider, An improved in vitro model of human intestinal follicle-associated epithelium to study nanoparticle transport by M cells, *Eur. J. Pharm. Sci.* 30 (2007) 380–391, <https://doi.org/10.1016/j.ejps.2006.12.006>.
162. A. Des Rieux, E.G.E. Ragnarsson, E. Gullberg, V. Preat, Y.J. Schneider, ´ P. Artursson, Transport of nanoparticles across an in vitro model of the human intestinal follicle associated epithelium, *Eur. J. Pharm. Sci.* 25 (2005) 455–465, <https://doi.org/10.1016/j.ejps.2005.04.015>.
163. J. Costa, A. Ahluwalia, Advances and current challenges in intestinal in vitro model engineering: a digest, *Front. Bioeng. Biotechnol.* 7 (2019) 1–14, <https://doi.org/10.3389/fbioe.2019.00144>.
164. F. Araújo, B. Sarmiento, Towards the characterization of an in vitro triple co- culture intestine cell model for permeability studies, *Int. J. Pharm.* 458 (2013) 128–134, <https://doi.org/10.1016/j.ijpharm.2013.10.003>.
165. F. Antunes, F. Andrade, F. Araújo, D. Ferreira, B. Sarmiento, Establishment of a triple co-culture in vitro cell models to study intestinal absorption of peptide drugs, *Eur. J. Pharm. Biopharm.* 83 (2013) 427–435, <https://doi.org/10.1016/j.ejpb.2012.10.003>.
166. M. Natoli, B.D. Leoni, I. D’Agnano, F. Zucco, A. Felsani, Good Caco-2 cell culture practices, *Toxicol. Vitr.* 26 (2012) 1243–1246, <https://doi.org/10.1016/j.tiv.2012.03.009>.
167. T. Lea, Caco-2 cell line BT, in: K. Verhoeckx, P. Cotter, I. Lopez-Exp´ osito, ´ C. Kleiveland, T. Lea, A. Mackie, H. Wichers (Eds.), *The Impact of Food Bioactives on Health: In Vitro and Ex Vivo Models*, Springer International Publishing, Cham, 2015, pp. 103–111, [https://doi.org/10.1007/978-3-319-16104-4\\_10](https://doi.org/10.1007/978-3-319-16104-4_10).
168. M. Kaiser, L. Pohl, S. Ketelhut, L. Kastl, C. Gorzelanny, M. Gotte, ”
169. Schneidenburger, F.M. Goycoolea, B. Kemper, Nanoencapsulated capsaicin changes migration behavior and morphology of madin darby canine kidney cell monolayers, *PLoS One.* 12 (2017), e0187497.
170. S. Kootala, L. Filho, V. Srivastava, V. Linderberg, A. Moussa, L. David, S. Trombotto, T. Crouzier, Reinforcing mucus barrier properties with low molar mass chitosans, *Biomacromolecules.* 19 (2018) 872–882, <https://doi.org/10.1021/acs.biomac.7b01670>.
171. D.A. Volpe, Application of method suitability for drug permeability classification, *AAPS J.* 12 (2010) 670–678, <https://doi.org/10.1208/s12248-010-9227-8>.
172. S. Youhanna, V.M. Lauschke, The past, present and future of intestinal in vitro cell systems for drug absorption studies, *J. Pharm. Sci.* 110 (2021) 50–65, <https://doi.org/10.1016/j.xphs.2020.07.001>.
173. D.A. Volpe, Advances in cell-based permeability assays to screen drugs for intestinal absorption, *Expert Opin. Drug Discov.* 15 (2020) 539–549.
174. L. Shuler, J.J. Hickman, TEER Measurements in Cells, 2016, <https://doi.org/10.1177/2211068214561025>.TEER.
175. K. Verhoeckx, P. Cotter, I. Lopez-Exp´ osito, C. Kleiveland, T. Lea, A. Mackie, ´ T. Requena, D. Swiatecka, H. Wichers, The impact of food bioactives on health: in vitro and ex vivo models, *Impact Food Bioact. Heal. Vitr. Ex Vivo Model.* (2015) 1–327, <https://doi.org/10.1007/978-3-319-16104-4>.
176. E. Le Ferrec, C. Chesne, P. Artusson, D. Brayden, G. Fabre, P. Gires, F. Guillou, M. Rousset, *In Vitro Models of the Intestinal Barrier*, 2001, pp. 649–668. [176] *The Madin Darby Canine Kidney.pdf*, 2020.



177. E. Le Ferrec, C. Chesne, P. Artusson, D. Brayden, G. Fabre, P. Gires, F. Guillou, M. Rousset, W. Rubas, M.L. Scarino, In vitro models of the intestinal barrier: The report and recommendations of ECVAM workshop 461,2, *ATLA Altern. to Lab. Anim.* 29 (2001) 649–668, <https://doi.org/10.1177/026119290102900604>.
178. S.C. Pearce, H.G. Coia, J.P. Karl, I.G. Pantoja-Feliciano, N.C. Zachos, K. Racicot, Intestinal in vitro and ex vivo models to study host-microbiome interactions and acute stressors, *Front. Physiol.* 9 (2018), <https://doi.org/10.3389/fphys.2018.01584>.
179. H.J. Kim, D.E. Ingber, Gut-on-a-Chip microenvironment induces human intestinal cells to undergo villus differentiation, *Integr. Biol. (United Kingdom)*. 5 (2013) 1130–1140, <https://doi.org/10.1039/c3ib40126j>.
180. A. Skardal, T. Shupe, A. Atala, Organoid-on-a-chip and body-on-a-chip systems for drug screening and disease modeling, *Drug Discov. Today*. 21 (2016) 1399–1411, <https://doi.org/10.1016/j.drudis.2016.07.003>.
181. K.A. Fitzgerald, M. Malhotra, C.M. Curtin, F.J. O'Brien, C.M. O'Driscoll, Life in 3D is never flat: 3D models to optimise drug delivery, *J. Control. Release*. 215 (2015) 39–54.
182. D.W. Hutmacher, Scaffolds in tissue engineering bone and cartilage, *Biomaterials*. 21 (2000) 2529–2543.
183. J.S. Joseph, S.T. Malindisa, M. Ntwasa, Two-dimensional (2D) and three-dimensional (3D) cell culturing in drug discovery, *Cell Cult.* 2 (2018) 1–22.
184. E. Piskin, Biodegradable polymers as biomaterials, *J. Biomater. Sci. Polym. Ed.* 6 (1995) 775–795.
185. J. Yu, S. Peng, D. Luo, J.C. March, In vitro 3D human small intestinal villous model for drug permeability determination, *Biotechnol. Bioeng.* 109 (2012) 2173–2178, <https://doi.org/10.1002/bit.24518>.
186. B. Yi, K.Y. Shim, S.K. Ha, J. Han, H.H. Hoang, I. Choi, S. Park, J.H. Sung, Three-dimensional in vitro gut model on a villi-shaped collagen scaffold, *Biochip J.* 11 (2017) 219–231, <https://doi.org/10.1007/s13206-017-1307-8>.
187. J.D. Patient, H. Hajiali, K. Harris, B. Abrahamsson, C. Tannergren, L.J. White, A. M. Ghaemmaghami, P.M. Williams, C.J. Roberts, F.R.A.J. Rose, Nanofibrous scaffolds support a 3D in vitro permeability model of the human intestinal epithelium, *Front. Pharmacol.* 10 (2019) 456.
188. R.H. Dosh, A. Essa, N. Jordan-Mahy, C. Sammon, C.L. Le Maitre, Use of hydrogel scaffolds to develop an in vitro 3D culture model of human intestinal epithelium, *Acta Biomater.* 62 (2017) 128–143, <https://doi.org/10.1016/j.actbio.2017.08.035>.
189. T. Nakajima, K. Sasaki, A. Yamamori, K. Sakurai, K. Miyata, T. Watanabe, Y. Matsunaga, A simple three-dimensional gut model constructed in a restricted ductal microspace induces intestinal epithelial cell integrity and facilitates absorption assays, *Biomater. Sci.* 8 (2020) 5615–5627, <https://doi.org/10.1039/d0bm00763c>.
190. N. Li, D. Wang, Z. Sui, X. Qi, L. Ji, X. Wang, L. Yang, Development of an improved three-dimensional in vitro intestinal mucosa model for drug absorption evaluation, *Tissue Eng. - Part C Methods*. 19 (2013) 708–719, <https://doi.org/10.1089/ten.tec.2012.0463>.
191. I. Pereira, A. Lechanteur, B. Sarmento, 3D model replicating the intestinal function to evaluate drug permeability, in: *Epithel. Cell Cult.*, Springer, 2018, pp. 107–113.
192. S.A. Shaffiey, H. Jia, T. Keane, C. Costello, D. Wasserman, M. Quidgley, J. Dziki, S. Badylak, C.P. Sodhi, J.C. March, Intestinal stem cell growth and differentiation on a tubular scaffold with evaluation in small and large animals, *Regen. Med.* 11 (2016) 45–61.
193. K.Y. Shim, D. Lee, J. Han, N.T. Nguyen, S. Park, J.H. Sung, Microfluidic gut-on-a-chip with three-dimensional villi structure, *Biomed. Microdevices* 19 (2017), <https://doi.org/10.1007/s10544-017-0179-y>.
194. P.H. Dedhia, N. Bertaux-Skeirik, Y. Zavros, J.R. Spence, Organoid models of human gastrointestinal development and disease, *Gastroenterology*. 150 (2016) 1098–1112, <https://doi.org/10.1053/j.gastro.2015.12.042>.
195. C. Greggio, F. De Franceschi, M. Figueiredo-Larsen, S. Gobaa, A. Ranga, H. Semb, M. Lutolf, A. Grapin-Botton, Artificial three-dimensional niches deconstruct pancreas development in vitro, *Development*. 140 (2013) 4452–4462.
196. N. Barker, M. Huch, P. Kujala, M. van de Wetering, H.J. Snippert, J.H. van Es, T. Sato, D.E. Stange, H. Begthel, M. van den Born, Lgr5+ stem cells drive self-renewal in the stomach and build long-lived gastric units in vitro, *Cell Stem Cell*. 6 (2010) 25–36.
197. Y. Fang, R.M. Eglén, Three-dimensional cell cultures in drug discovery and development, *SLAS Discov.* 22 (2017) 456–472, <https://doi.org/10.1177/1087057117696795>.
198. K.L. Fair, J. Colquhoun, N.R.F. Hannan, Intestinal organoids for modelling intestinal development and disease, *Philos. Trans. R. Soc. B Biol. Sci.* 373 (2018), <https://doi.org/10.1098/rstb.2017.0217>.
199. R. Conder, Intestinal organoid culture: the history of intestinal organoids using intestinal organoids as a model culture system, *Stem Cell Rev.* (2015) 1–4.

200. J.R. Spence, C.N. Mayhew, S.A. Rankin, M.F. Kuhar, J.E. Vallance, K. Tolle, E. E. Hoskins, V.V. Kalinichenko, S.I. Wells, A.M. Zorn, N.F. Shroyer, J.M. Wells, Directed differentiation of human pluripotent stem cells into intestinal tissue in vitro, *Nature*. 470 (2011) 105–110, <https://doi.org/10.1038/nature09691>.
201. M. Noben, W. Vanhove, K. Arnauts, A. Santo Ramalho, G. Van Assche, S. Vermeire, C. Verfaillie, M. Ferrante, Human intestinal epithelium in a dish: current models for research into gastrointestinal pathophysiology, *United Eur. Gastroenterol. J.* 5 (2017) 1073–1081, <https://doi.org/10.1177/2050640617722903>.
202. T. Sato, R.G. Vries, H.J. Snippert, M. Van De Wetering, N. Barker, D.E. Stange, J. H. Van Es, A. Abo, P. Kujala, P.J. Peters, H. Clevers, Single Lgr5 stem cells build crypt-villus structures in vitro without a mesenchymal niche, *Nature*. 459 (2009) 262–265, <https://doi.org/10.1038/nature07935>.
203. T. Sato, H. Clevers, Growing self-organizing mini-guts from a single intestinal stem cell: mechanism and applications, *Science* (80) 340 (2013) 1190–1194, <https://doi.org/10.1126/science.1234852>.
204. T. Zietek, P. Giesbertz, M. Ewers, F. Reichart, M. Weinmüller, E. Urbauer, D. Haller, I.E. Demir, G.O. Ceyhan, H. Kessler, E. Rath, Organoids to study intestinal nutrient transport, drug uptake and metabolism – update to the human model and expansion of applications, *Front. Bioeng. Biotechnol.* 8 (2020) 1–14, <https://doi.org/10.3389/fbioe.2020.577656>.
205. S. Rahmani, N.M. Breyner, H.M. Su, E.F. Verdu, T.F. Didar, Intestinal organoids: a new paradigm for engineering intestinal epithelium in vitro, *Biomaterials*. 194 (2019) 195–214, <https://doi.org/10.1016/j.biomaterials.2018.12.006>.
206. K. Takahashi, S. Yamanaka, Induced pluripotent stem cells in medicine and biology, *Development*. 140 (2013) 2457–2461.
207. A. Bein, W. Shin, S. Jalili-Firoozinezhad, M.H. Park, A. Sontheimer-Phelps, A. Tovaglieri, A. Chalkiadaki, H.J. Kim, D.E. Ingber, Microfluidic organ-on-a-chip models of human intestine, *Cmgh*. 5 (2018) 659–668, <https://doi.org/10.1016/j.jcmgh.2017.12.010>.
208. A. Sontheimer-Phelps, B.A. Hassell, D.E. Ingber, Modelling cancer in microfluidic human organs-on-chips, *Nat. Rev. Cancer*. 19 (2019) 65–81, <https://doi.org/10.1038/s41568-018-0104-6>.
209. S.N. Bhatia, D.E. Ingber, Microfluidic organs-on-chips, *Nat. Biotechnol.* 32 (2014) 760–772.
210. H. Uchida, M. Machida, T. Miura, T. Kawasaki, T. Okazaki, K. Sasaki, S. Sakamoto, N. Ohuchi, M. Kasahara, A. Umezawa, H. Akutsu, A xenogeneic-free system generating functional human gut organoids from pluripotent stem cells, *JCI Insight*. 2 (2017) 1–13, <https://doi.org/10.1172/jci.insight.86492>.
211. T. Zietek, E. Rath, D. Haller, H. Daniel, Intestinal organoids for assessing nutrient transport, sensing and incretin secretion, *Sci. Rep.* 5 (2015) 1–10, <https://doi.org/10.1038/srep16831>.
212. I.A. Williamson, J.W. Arnold, L.A. Samsa, L. Gaynor, M. DiSalvo, J.L. Cocchiari, I. Carroll, M.A. Azcarate-Peril, J.F. Rawls, N.L. Allbritton, A high-throughput organoid microinjection platform to study gastrointestinal microbiota and luminal physiology, *Cell. Mol. Gastroenterol. Hepatol.* 6 (2018) 301–319.
213. T. Roodsant, M. Navis, I. Aknouch, I.B. Renes, R.M. van Elburg, D. Pajkrt, K. C. Wolthers, C. Schultsz, K.C.H. van der Ark, A. Sridhar, V. Muncan, A human 2D primary organoid-derived epithelial monolayer model to study host-pathogen interaction in the small intestine, *Front. Cell. Infect. Microbiol.* 10 (2020) 1–14, <https://doi.org/10.3389/fcimb.2020.00272>.
214. S. Yoshida, H. Miwa, T. Kawachi, S. Kume, K. Takahashi, Generation of intestinal organoids derived from human pluripotent stem cells for drug testing, *Sci. Rep.* 10 (2020) 1–11, <https://doi.org/10.1038/s41598-020-63151-z>.
215. M. Kasendra, J.M. Wells, A window into your gut: biologically inspired engineering of mini-gut tubes in vitro, *Dev. Cell*. 55 (2020) 522–524, <https://doi.org/10.1016/j.devcel.2020.11.015>.
216. M. Kasendra, R. Luc, J. Yin, D.V. Manatakis, G. Kulkarni, C. Lucchesi, J. Sliz, A. Apostolou, L. Sunuwar, J. Obrigewitch, K.J. Jang, G.A. Hamilton, M. Donowitz, K. Karalis, Duodenum intestine-chip for preclinical drug assessment in a human relevant model, *Elife*. 9 (2020) 1–23, <https://doi.org/10.7554/eLife.50135>.
217. Y.B. Yin, H.R. de Jonge, X. Wu, Y.L. Yin, Mini-gut: a promising model for drug development, *Drug Discov. Today*. 24 (2019) 1784–1794, <https://doi.org/10.1016/j.drudis.2019.06.006>.
218. D. Jirova, M. Dvorakova, K. Kejlova, L. Kasparova, D. Kresk, H. Kolarova, Safety evaluation of nanosilver using reconstructed human GIT tissues, in: *World Congr. Expo Nanotechnol. Mater. Sci.*, 2015.
219. A. Marrella, P. Buratti, J. Markus, G. Firpo, M. Pesenti, T. Landry, S. Ayehunie, S. Scaglione, H. Kandarova, M. Aiello, In vitro demonstration of intestinal absorption mechanisms of different sugars using 3d organotypic tissues in a fluidic device, *ALTEX* 37 (2020) 255–264, <https://doi.org/10.14573/altex.1908311>.

220. Y. Cui, S. Claus, D. Schnell, F. Runge, C. Maclean, In-depth characterization of epiintestinal microtissue as a model for intestinal drug absorption and metabolism in human, *Pharmaceutics* 12 (2020), <https://doi.org/10.3390/pharmaceutics12050405>.
221. J. Markus, T. Landry, Z. Stevens, H. Scott, P. Llanos, M. Debatis, A. Armento, M. Klausner, S. Ayehunie, Human small intestinal organotypic culture model for drug permeation, inflammation, and toxicity assays, *Vitr. Cell. Dev. Biol. - Anim.* (2020), <https://doi.org/10.1007/s11626-020-00526-6>.
222. J. Markus, T. Landry, M. Klausner, H. Kandarova, Z. Stevens, C. Donovan, S. Ayehunie, Lab to lab reproducibility in the production of physiologically relevant reconstructed small intestine tissue for in vitro testing of toxicity, permeation and inflammation, *Toxicol. Lett.* 280 (2017) S324, <https://doi.org/10.1016/j.toxlet.2017.08.077>.
223. J.H. Sung, J. Yu, D. Luo, M.L. Shuler, J.C. March, Microscale 3-D hydrogel scaffold for biomimetic gastrointestinal (GI) tract model, *Lab Chip.* 11 (2011) 389–392.
224. L.M. Gonzalez, I. Williamson, J.A. Piedrahita, A.T. Blikslager, S.T. Magness, Cell lineage identification and stem cell culture in a porcine model for the study of intestinal epithelial regeneration, *PLoS One.* 8 (2013), e66465.
225. J. Foulke-Abel, J. In, J. Yin, N.C. Zachos, O. Kovbasnjuk, M.K. Estes, H. de Jonge, M. Donowitz, Human enteroids as a model of upper small intestinal ion transport physiology and pathophysiology, *Gastroenterology* 150 (2016) 638–649, e8, <https://doi.org/10.1053/j.gastro.2015.11.047>.
226. S. Ayehunie, Z. Stevens, T. Landry, M. Klausner, P. Hayden, S. Letasiova, Novel 3- D human small intestinal tissue model to assess drug permeation, inflammation, and wound healing, *Toxicol. Lett.* 229 (2014) S144, <https://doi.org/10.1016/j.toxlet.2014.06.505>.
227. A.W.F. Janssen, L.P.M. Duivenvoorde, D. Rijkers, R. Nijssen, A.A.C.
228. M. Peijnenburg, M. van der Zande, J. Louise, Cytochrome P450 expression, induction and activity in human induced pluripotent stem cell-derived intestinal organoids and comparison with primary human intestinal epithelial cells and Caco-2 cells, *Arch. Toxicol.* (2020), <https://doi.org/10.1007/s00204-020-02953-6>.
229. F. Yu, *Micromachines Engineering Microfluidic Organoid-on-a-Chip Platforms Engineering Microfluidic Organoid-on-a-Chip Platforms*, 2019, <https://doi.org/10.3390/mi10030165>.
230. M. Mehling, S. Tay, Microfluidic cell culture, *Curr. Opin. Biotechnol.* 25 (2014) 95–102. H.J. Kim, H. Li, J.J. Collins, D.E. Ingber, Contributions of microbiome and mechanical deformation to intestinal bacterial overgrowth and inflammation in a human gut-on-a-chip, *Proc. Natl. Acad. Sci. U. S. A.* 113 (2016) E7–E15, <https://doi.org/10.1073/pnas.1522193112>.
231. H.Y. Tan, S. Trier, U.L. Rahbek, M. Dufva, J.P. Kutter, T.L. Andresen, A multi- chamber microfluidic intestinal barrier model using Caco-2 cells for drug transport studies, *PLoS One.* 13 (2018) 1–23, <https://doi.org/10.1371/journal.pone.0197101>.
232. Y. Guo, Z. Li, W. Su, L. Wang, Y. Zhu, J. Qin, A biomimetic human gut-on-a-chip for modeling drug metabolism in intestine, *Artif. Organs.* 42 (2018) 1196–1205, <https://doi.org/10.1111/aor.13163>.
233. K. Kulthong, L. Duivenvoorde, H. Sun, S. Confederat, J. Wu, B. Spenkelink, L. de Haan, V. Marin, M. van der Zande, H. Bouwmeester, Microfluidic chip for culturing intestinal epithelial cell layers: characterization and comparison of drug transport between dynamic and static models, *Toxicol. Vitr.* 65 (2020), <https://doi.org/10.1016/j.tiv.2020.104815>.
234. D. Gao, H. Liu, J.M. Lin, Y. Wang, Y. Jiang, Characterization of drug permeability in Caco-2 monolayers by mass spectrometry on a membrane-based microfluidic device, *Lab Chip.* 13 (2013) 978–985, <https://doi.org/10.1039/c2lc41215b>.
235. K. Kulthong, L. Duivenvoorde, B.Z. Mizera, D. Rijkers, G. Ten Dam, G. Oegema, T. Puzyn, H. Bouwmeester, M. Van Der Zande, Implementation of a dynamic intestinal gut-on-a-chip barrier model for transport studies of lipophilic dioxin congeners, *RSC Adv.* 8 (2018) 32440–32453, <https://doi.org/10.1039/c8ra05430d>.
236. H.J. Kim, D. Huh, G. Hamilton, D.E. Ingber, Human gut-on-a-chip inhabited by microbial flora that experiences intestinal peristalsis-like motions and flow, *Lab Chip.* 12 (2012) 2165–2174, <https://doi.org/10.1039/c2lc40074j>.
237. Y. Guo, P. Deng, W. Chen, Z. Li, Modeling pharmacokinetic profiles for assessment of anti-cancer drug on a microfluidic system, *Micromachines* 11 (2020), <https://doi.org/10.3390/M11060551>.
238. W. Shin, C.D. Hinojosa, D.E. Ingber, H.J. Kim, Human intestinal morphogenesis controlled by transepithelial morphogen gradient and flow-dependent physical cues in a microengineered gut-on-a-chip, *IScience.* 15 (2019) 391–406, <https://doi.org/10.1016/j.isci.2019.04.037>.
239. S. Miura, K. Sato, M. Kato-Negishi, T. Teshima, S. Takeuchi, Fluid shear triggers microvilli formation via mechanosensitive activation of TRPV6, *Nat. Commun.* 6 (2015), <https://doi.org/10.1038/ncomms9871>.

240. L.C. Delon, Z. Guo, A. Oszmiana, C.C. Chien, R. Gibson, C. Prestidge, B. Thierry, A systematic investigation of the effect of the fluid shear stress on Caco-2 cells towards the optimization of epithelial organ-on-chip models, *Biomaterials*. 225 (2019) 119521, <https://doi.org/10.1016/j.biomaterials.2019.119521>.
241. S.H. Kim, J.W. Lee, I. Choi, Y.C. Kim, J.B. Lee, J.H. Sung, A microfluidic device with 3-D hydrogel villi scaffold to simulate intestinal absorption, *J. Nanosci. Nanotechnol.* 13 (2013) 7220–7228, <https://doi.org/10.1166/jnn.2013.8088>.
242. J.P. Mochel, A.E. Jergens, D. Kingsbury, H.J. Kim, M.G. Martín, K. Allenspach, Intestinal stem cells to advance drug development, precision, and regenerative medicine: a paradigm shift in translational research, *AAPS J.* 20 (2018) 1–9, <https://doi.org/10.1208/s12248-017-0178-1>.
243. A. Dawson, C. Dyer, J. Macfie, J. Davies, L. Karsai, J. Greenman, M. Jacobsen, A microfluidic chip based model for the study of full thickness human intestinal tissue using dual flow, *Biomicrofluidics* 10 (2016), <https://doi.org/10.1063/1.4964813>.
244. A. Richardson, L.A. Schwerdtfeger, D. Eaton, I. McLean, C.S. Henry, S.A. Tobet, A microfluidic organotypic device for culture of mammalian intestines: ex vivo, *Anal. Methods*. 12 (2020) 297–303, <https://doi.org/10.1039/c9ay02038a>.
245. K. Tsilingiri, A. Sonzogni, F. Caprioli, M. Rescigno, A novel method for the culture and polarized stimulation of human intestinal mucosa explants, *JoVE* (2013), e4368, <https://doi.org/10.3791/4368>.
246. M.J. Workman, J.P. Gleeson, E.J. Troisi, H.Q. Estrada, S.J. Kerns, C.D. Hinojosa, G.A. Hamilton, S.R. Targan, C.N. Svendsen, R.J. Barrett, Enhanced utilization of induced pluripotent stem cell–derived human intestinal organoids using microengineered chips, *Cmgh* 5 (2018) 669–677, e2, <https://doi.org/10.1016/j.jcmgh.2017.12.008>.
247. M. Kasendra, A. Tovaglieri, A. Sontheimer-Phelps, S. Jalili-Firoozinezhad, A. Bein, A. Chalkiadaki, W. Scholl, C. Zhang, H. Rickner, C.A. Richmond, H. Li, D. Breault, D.E. Ingber, Development of a primary human small intestine-on-a-chip using biopsy-derived organoids, *Sci. Rep.* 8 (2018) 1–14, <https://doi.org/10.1038/s41598-018-21201-7>.
248. A. Sontheimer-Phelps, D.B. Chou, A. Tovaglieri, T.C. Ferrante, T. Duckworth, C. Fadel, V. Frisimantas, A.D. Sutherland, S. Jalili-Firoozinezhad, M. Kasendra, E. Stas, J.C. Weaver, C.A. Richmond, O. Levy, R. Prantil-Baun, D.T. Breault, D.
249. E. Ingber, Human colon-on-a-chip enables continuous in vitro analysis of colon mucus layer accumulation and physiology, *Cmgh*. 9 (2020) 507–526, <https://doi.org/10.1016/j.jcmgh.2019.11.008>. C. Probst, S. Schneider, P. Loskill, High-throughput organ-on-a-chip systems: current status and remaining challenges, *Curr. Opin. Biomed. Eng.* 6 (2018) 33–41, <https://doi.org/10.1016/j.cobme.2018.02.004>.
250. S. Halldorsson, E. Lucumi, R. Gomez-Sjöberg, R.M.T. Fleming, Advantages and challenges of microfluidic cell culture in polydimethylsiloxane devices, *Biosens. Bioelectron.* 63 (2015) 218–231, <https://doi.org/10.1016/j.bios.2014.07.029>.
251. S. Giusti, T. Sbrana, M. La Marca, V. Di Patria, V. Martinucci, A. Tirella, C. Domenici, A. Ahluwalia, A novel dual-flow bioreactor simulates increased fluorescein permeability in epithelial tissue barriers, *Biotechnol. J.* 9 (2014) 1175–1184, <https://doi.org/10.1002/biot.201400004>.
252. S. Sibilio, V. De Gregorio, F. Urciuolo, P.A. Netti, G. Imparato, Effect of peristaltic-like movement on bioengineered intestinal tube, *Mater. Today Bio.* 4 (2019) 1–9, <https://doi.org/10.1016/j.mtbio.2019.100027>.
253. M.J.C. Santbergen, M. van der Zande, A. Gerssen, H. Bouwmeester, M.W.
254. F. Nielen, Dynamic in vitro intestinal barrier model coupled to chip-based liquid chromatography mass spectrometry for oral bioavailability studies, *Anal. Bioanal. Chem.* 412 (2020) 1111–1122, <https://doi.org/10.1007/s00216-019-02336-6>.
255. W.M.S. Russell, R.L. Burch, *The Principles of Humane Experimental Technique*, Methuen, 1959. A. Avdeef, K.Y. Tam, How well can the caco-2/madin-darby canine kidney models predict effective human jejunal permeability? *J. Med. Chem.* 53 (2010) 3566–3584, <https://doi.org/10.1021/jm901846t>.
256. H. Lennernas, Animal data: the contributions of the Ussing Chamber and perfusion systems to predicting human oral drug delivery in vivo, *Adv. Drug Deliv. Rev.* 59 (2007) 1103–1120, <https://doi.org/10.1016/j.addr.2007.06.016>.
257. H. Li, H.E. Jin, W.S. Shim, C.K. Shim, An improved prediction of the human in vivo intestinal permeability and BCS class of drugs using the in vitro permeability ratio obtained for rat intestine using an Ussing chamber system, *Drug Dev. Ind. Pharm.* 39 (2013) 1515–1522, <https://doi.org/10.3109/03639045.2012.714787>.

258. Y.H. Zhao, J. Le, M.H. Abraham, A. Hersey, P.J. Eddershaw, C.N. Luscombe, D. Boutina, G. Beck, B. Sherborne, I. Cooper, J.A. Platts, Evaluation of human intestinal absorption data and subsequent derivation of a quantitative structure - Activity relationship (QSAR) with the Abraham descriptors, *J. Pharm. Sci.* 90 (2001) 749–784, <https://doi.org/10.1002/jps.1031>.
259. M. Iyer, Y.J. Tseng, C.L. Senese, J. Liu, A.J. Hopfinger, Prediction and mechanistic interpretation of human oral drug absorption using MI-QSAR analysis, *Mol. Pharm.* 4 (2007) 218–231, <https://doi.org/10.1021/mp0600900>.
260. K. Sugano, H. Hamada, M. Machida, H. Ushio, K. Saitoh, K. Terada, Optimized conditions of bio-mimetic artificial membrane permeation assay, *Int. J. Pharm.* 228 (2001) 181–188, [https://doi.org/10.1016/S0378-5173\(01\)00845-6](https://doi.org/10.1016/S0378-5173(01)00845-6).
261. K. Sugano, N. Takata, M. Machida, K. Saitoh, K. Terada, Prediction of passive intestinal absorption using bio-mimetic artificial membrane permeation assay and the paracellular pathway model, *Int. J. Pharm.* 241 (2002) 241–251, [https://doi.org/10.1016/S0378-5173\(02\)00240-5](https://doi.org/10.1016/S0378-5173(02)00240-5).
262. H. Yu, Q. Wang, Y. Sun, M. Shen, H. Li, Y. Duan, A new PAMPA model proposed on the basis of a synthetic phospholipid membrane, *PLoS One.* 10 (2015), e0116502.
263. K. Sugano, Y. Nabuchi, M. Machida, Y. Aso, Prediction of human intestinal permeability using artificial membrane permeability, *Int. J. Pharm.* 257 (2003) 245–251, [https://doi.org/10.1016/S0378-5173\(03\)00161-3](https://doi.org/10.1016/S0378-5173(03)00161-3).
264. E. Naderkhani, Development of Biomimetic Phospholipid Vesicle-Based Permeation Assays (PVPA) as Screening Tool in Drug Development, 2015.
265. M. Di Cagno, H.A. Bibi, A. Bauer-Brandl, New biomimetic barrier Permeapad™ for efficient investigation of passive permeability of drugs, *Eur. J. Pharm. Sci.* 73 (2015) 29–34.
266. A.C. Jacobsen, S. Nielsen, M. Brandl, A. Bauer-Brandl, Drug permeability profiling using the Novel Permeapad® 96-well plate, *Pharm. Res.* 37 (2020) 93, <https://doi.org/10.1007/s11095-020-02807-x>.
267. S.M. Fischer, G.E. Flaten, E. Hagesæther, G. Fricker, M. Brandl, In-vitro permeability of poorly water soluble drugs in the phospholipid vesicle-based permeation assay: the influence of nonionic surfactants, *J. Pharm. Pharmacol.* 63 (2011) 1022–1030.
268. A. Collett, E. Sims, D. Walker, Y.L. He, J. Ayrton, M. Rowland, G. Warhurst, Comparison of HT29-18-C1 and Caco-2 cell lines as models for studying intestinal paracellular drug absorption, *Pharm. Res.* 13 (1996) 216–221, <https://doi.org/10.1023/A:1016082829111>.
269. Y. Kamiya, H. Takaku, R. Yamada, C. Akase, Y. Abe, Y. Sekiguchi, N. Murayama, M. Shimizu, M. Kitajima, F. Shono, K. Funatsu, H. Yamazaki, Determination and prediction of permeability across intestinal epithelial cell monolayer of a diverse range of industrial chemicals/drugs for estimation of oral absorption as a putative marker of hepatotoxicity, *Toxicol. Reports.* 7 (2020) 149–154, <https://doi.org/10.1016/j.toxrep.2020.01.004>.
270. J. Westerhout, E. Van De Steeg, D. Grossouw, E.E. Zeijdner, C.A.M. Krul, M. Verwei, H.M. Wortelboer, A new approach to predict human intestinal absorption using porcine intestinal tissue and biorelevant matrices, *Eur. J. Pharm. Sci.* 63 (2014) 167–177, <https://doi.org/10.1016/j.ejps.2014.07.003>.
271. V. Pade, S. Stavchansky, Estimation of the relative contribution of the transcellular and paracellular pathway to the transport of passively absorbed drugs in the Caco-2 cell culture model, *Pharm. Res.* 14 (1997) 1210–1215, <https://doi.org/10.1023/A:1012111008617>.
272. M. Yazdaniyan, S.L. Glynn, J.L. Wright, A. Hawi, Correlating partitioning and Caco-2 cell permeability of structurally diverse small molecular weight compounds, *Pharm. Res.* 15 (1998) 1490–1494, <https://doi.org/10.1023/A:1011930411574>.
273. J. Alsenz, E. Haenel, Development of a 7-Day, 96-Well Caco-2 permeability assay with high-throughput direct UV compound analysis, *Pharm. Res.* 20 (2003) 1961–1969, <https://doi.org/10.1023/B:PHAM.0000008043.71001.43>.
274. P. Artursson, Epithelial transport of drugs in cell culture. I: a model for studying the passive diffusion of drugs over intestinal absorptive (Caco-2) cells, *J. Pharm. Sci.* 79 (1990) 476–482, <https://doi.org/10.1002/jps.2600790604>.
275. V. Fade, Link between drug absorption solubility and permeability measurements in Caco-2 cells, *J. Pharm. Sci.* 87 (1998) 1604–1607, <https://doi.org/10.1021/js980111k>.
276. X.C. Wu, J.R. Williford, S. Gokhin, S. Lee, M.R. Davis, P. Sheffels, X. Wang, J. Migeon, M.C. Bodinier, The TC7 Cell Monolayer is a Valuable in vitro Intestinal Epithelial Model for Membrane Permeability Screening, 2020.

277. E. Hellinger, S. Veszelka, A.E. Toth, F. Walter, A. Kittel, M.L. Bakk, K. Tihanyi, V. Hada, S. Nakagawa, T.D.H. Duy, Comparison of brain capillary endothelial cell-based and epithelial (MDCK-MDR1, Caco-2, and VB-Caco-2) cell-based surrogate blood–brain barrier penetration models, *Eur. J. Pharm. Biopharm.* 82 (2012) 340–351.
278. X. Jin, T.-L. Luong, N. Reese, H. Gaona, V. Collazo-Velez, C. Vuong, B. Potter, J. C. Sousa, R. Olmeda, Q. Li, Comparison of MDCK-MDR1 and Caco-2 cell based permeability assays for anti-malarial drug screening and drug investigations, *J. Pharmacol. Toxicol. Methods.* 70 (2014) 188–194.
279. Q. Wang, J.D. Rager, K. Weinstein, P.S. Kardos, G.L. Dobson, J. Li, I.J. Hidalgo, Evaluation of the MDR-MDCK cell line as a permeability screen for the blood–brain barrier, *Int. J. Pharm.* 288 (2005) 349–359.
280. K.A. Lentz, J.W. Polli, S.A. Wring, J.E. Humphreys, J.E. Polli, Influence of passive permeability on apparent P-glycoprotein kinetics, *Pharm. Res.* 17 (2000) 1456–1460.
281. I. Lozoya-Agullo, F. Araújo, I. Gonzalez- Alvarez, M. Merino-Sanjuán, M. Gonzalez- Alvarez, M. Bermejo, B. Sarmiento, Usefulness of Caco-2/HT29-MTX and Caco-2/HT29-MTX/Raji B coculture models to predict intestinal and colonic permeability compared to Caco-2 monoculture, *Mol. Pharm.* 14 (2017) 1264–1270, <https://doi.org/10.1021/acs.molpharmaceut.6b01165>.
282. J.H. Yeon, J.K. Park, Drug permeability assay using microhole-trapped cells in a microfluidic device, *Anal. Chem.* 81 (2009) 1944–1951, <https://doi.org/10.1021/ac802351w>.
283. D.W. Lee, S.K. Ha, I. Choi, J.H. Sung, 3D gut-liver chip with a PK model for prediction of first-pass metabolism, *Biomed. Microdevices* 19 (2017), <https://doi.org/10.1007/s10544-017-0242-8>.

## 4.9 Acknowledgements

This work has been developed in collaboration with: Chiara Vitale, Silvia Scaglione, Marco Massimo Fato, Giulia Ponschin, Sayeun Ayehunie, Rodolfo Repetto, Alessandro Bottaro.

# Chapter 5

## 3D Perfusable Hydrogel Recapitulating the Cancer Dynamic Environment to in Vitro Investigate Metastatic Colonization

### 5.1 Abstract

Metastasis is a complex process in which cancer cells spread through the bloodstream to different parts of the body. Despite efforts to develop an in vitro model that can help to understand this process, it still remains a challenge. In this study, I have developed an in vitro model of extravasation, which is a crucial step in metastasis. The model consists of a 3D hydrogel that mimics the metastatic site, and a circulation system that allows cancer cells to flow. I tested two different polymers (fibrin and alginate) and compared their mechanical and biochemical properties. We also used computational fluid-dynamic simulations to predict the fluid dynamics within the polymeric matrix and determine the optimal culture conditions. I validated the platform through perfusion tests by fluidically connecting the hydrogels with the external circuit. Finally, I injected highly metastatic breast cancer cells (MDA-MB-231) and exposed them to physiological wall shear stress (WSS) conditions (5 Dyn/cm<sup>2</sup>) to assess their migration toward the hydrogel. Results showed that CTCs arrested and colonized the polymeric matrix, indicating that this platform can be an effective fluidic system to model the first steps of the metastatic cascade. Furthermore, it has the potential to elucidate the contribution of hemodynamics on cancer dissemination to a secondary site in vitro. This study provides important insights into the development of new therapeutic strategies for the treatment of cancer metastasis.

### 5.2 Introduction

Circulating tumor cells (CTCs) are viable cells that circulate in the bloodstream after detaching from a primary tumor [1]. Over the past decade, different studies showed that these cells play a key role in tumor progression [2]. In fact, it was shown a correlation between the presence of circulating tumor cells with a short survival rate of patients with metastatic carcinoma [3,4]. During the process of metastasis, tumor cells intravasate into bloodstream and lymphatic vessels, translocate until reaching distant tissues, to then extravasate, attach and proliferate, giving origin to a metastatic site [5]. In this context, an improved understanding of the mechanical forces encountered by CTCs in the blood flow is crucial for fully decoding the various process of metastatic cascade and delineating vulnerable CTCs states for therapeutic intervention [6]. In fact, CTCs must be able to withstand different fluid-dynamical stresses during their circulation, in order to survive and to adhere to the endothelial wall of the potential metastatic site, to finally extravasate to origin a secondary tumor [7]. Currently, conventional studies of extravasation rely primarily on in vivo models [8]. Although these are considered the most physiologically reliable models for extravasation, they present some limitations, such as poor segmentation of the essential steps of metastatization and hard capture of the individual variables which affect the whole process. Therefore, to overcome these disadvantages, some micro-fluidic systems

(called lab-on-chip) have been employed to investigate the metastatic cascade, by manipulating small volumes of cellular material and reproducing the dynamic interactions between tumor cells and the ECM microenvironment (e.g., CTCs arrest and transmigration into a secondary site) [9,10,11]. For example, Jeon et al. fabricated a microfluidic device to investigate the cancer extravasation by analyzing the tumor cell adhesion and then the transmigration across an endothelial monolayer. In particular, they used a high-resolution imaging technique in order to detect and quantify the number of cells involved in these processes [12]. In addition, in another work, Jeon et al. realized a microfluidic device to study human metastatic breast cancer cell extravasation within a perfusable bone-mimicking microenvironment [13]. The resulting device represented a functional human multi-culture device where breast cancer cells could flow, adhere, and metastasize through a micro-vascular network. Moreover, in a further study Ma et al. investigated the breast cancer (MDA-MB-231 and MCF-7) cell extravasation toward different cell-based spheroids, by realizing a PDMS-based microfluidic device containing a Boyden-chamber-like system [14]. However, these lab-on-chip devices show some limitations, due to their small dimensions, poor cells number and limited liquid volumes used. In fact, the over-miniaturization of these models could impair the realism of the tumor microenvironment resembled *in vitro* [15]. In particular, the attachment and colonization of CTCs to a secondary tissue require a proper interaction with a surrounding extracellular matrix (ECM) [16]. In fact, once CTCs mechanically arrest close to the target tissues, the subsequent establishment of the metastasis and cells growth is highly dependent on the interaction between metastatic cancer cells and the surrounding environment [17]. In this context, the progress in tissue engineering led to design matrix-based culture systems that recapitulate the biological, biophysical and biochemical environment of the natural extracellular matrix [18,19]. Specifically, hydrogels have been widely used to model the 3D ECM, because of their advantageous properties similar to those of the native one [20,21]. In fact, they possess a high-water content, which provides biochemical and biomechanical cues similar to the physiological ECM [21,22,23,24]. Presently, vascularized 3D hydrogels are increasingly gained attention to investigate the dynamic cancer-associated phenomena. In particular, vasculogenesis-based, subtractive and bioprinter-based models can be used to realize channels within polymeric matrices [12,25,26]. Among them, vasculogenesis models allow obtaining a vascularization through a growth factors gradient, thus inducing endothelial cells (ECs) to form a capillary-like network. These are the commonest methods used to create vascularized 3D hydrogel-based models to study cancer cells extravasation, as it occurs at the capillary level. For example, Chen et al. realized a two-channels device to co-culture human umbilical vein endothelial cells (HUVECs) and lung fibroblasts stimulated with inflammatory cytokines within a 3D fibrin ECM. After 2 days of culture, HUVECs organized into tubular structures characterized by tight junctions and a physiological vessels permeability [27]. However, injecting fluid flow resembling the bloodstream and controlling its biophysical properties, crucial for cancer cells migration and invasion, result in being very difficult because syringe or peristaltic pumps cannot be directly connected to the inner vasculature [28]. On the other hand, although bioprinting techniques allow creating more complex and variable sized networks, they are often hardly accessible due to the high costs. Taking together all these considerations, in this work a fluid-dynamic perfusable hydrogel-based system was fabricated, through a simple and low-cost, but effective, subtractive method, as model of cancer cells extravasation. In particular, we developed a hydrogel-based 3D fluidic system, representative of the bloodstream, where CTCs can experience physiologically relevant forces within an “ECM-like” environment, as it happens *in vivo*. Specifically, a hydrogel matrix with a vessel-mimicking channel was realized and directly connected with an external fluidic system, where it is possible to set and precisely monitor



fluid flow patterns. Two kinds of hydrogels were tested and compared: alginate and fibrin. Alginate is widely employed in many different biomedical applications, such as tissue engineering, tissue modeling and drug delivery [29,30,31]. Moreover, it was chosen because it is bio-inert, easy-to-use, cheap and has tunable mechanical properties [32,33]. Likewise, fibrin is extensively adopted in several tissue engineering fields, such as bone regeneration [34] as well as for cardiovascular applications [35,36,37], because of its higher biocompatibility and bioactivity [38]. CFD simulations were performed to quantify the fluid-dynamic stimuli at tissue scale, to predict the hydrogel mechanical response to fluid flow-associated forces, as well as to evaluate if an adequate nutrients fluxes were properly provided to the 3D hydrogels [39]. In particular, the glucose transport was modeled, as it is a fundamental nutrient for cancer cells metabolism and activity [40]. Finally, the 3D fluid-dynamic hydrogel-based system was validated with perfusion tests to experimentally demonstrate the performance of the system. In addition, highly metastatic breast cancer cells (MDA-MB-231) were injected in the circuit, flowing under WSS conditions, and their viability upon circulation as well as their capability to invade the surrounding ECM-like hydrogel were assessed, finally mimicking one of the crucial steps of the metastatic cascade.

## 5.3 Materials and Methods

### 5.3.1 Channel-Based Hydrogels Realization

Firstly, we realized a mold through 3D printing technology (Form 2, Formlabs, Lecco, IT) composed by a sphere (diameter = 1 cm), where the hydrogel representing the metastatic tumor mass was placed, and two lateral cylinders to easily connect the hydrogel spherical central body to an external fluidic circuit. The mold was fabricated with a biocompatible resin (Dental LT Resin, Formlabs, Lecco, IT) by using a resolution of 100  $\mu\text{m}$ . After printing, it was washed with isopropyl alcohol for 5 min and then photocured through UV light for 20 min to eliminate resin residues and to optimize the photo-linking process, respectively. Two distinct materials were selected to prepare the hydrogels: alginate and fibrin. For each polymer and cross-linking agent, different concentrations and precursor solution/cross-linking agent ratios were tested. Briefly, alginate powder (Manugel GMB, FMC Biopolymer, Girvan, UK) was dissolved in physiological solution (0.9% w/v NaCl) at the final concentration of 1% v/v, 1.5% v/v, 2% v/v and 2.5 w/v; then, the hydrogel were crosslinked into the mold by adding a calcium chloride solution ( $\text{CaCl}_2$ ), by varying three concentrations: 0.5 M, 0.75 M and 1 M. Moreover,  $\text{CaCl}_2$ /alginate 1:1 v/v, 1:3 v/v and 1:6 v/v ratios were assessed. The cross-linking occurred after 15 min at room temperature (25  $^\circ\text{C}$ ). Fibrin hydrogel was realized by combining fibrinogen from human plasma (F3879 Sigma Aldrich, Saint Louis, MO, USA) (20 mg/mL or 40 mg/mL) diluted in phosphate buffered saline solution (PBS)) with thrombin from human plasma (T6884 Sigma Aldrich, Saint Louis, MO, USA) (25 U/mL or 10 U/mL) diluted in  $\text{CaCl}_2$  5 mM solution. Furthermore, we tested the thrombin/fibrinogen ratio from 1:1 v/v to 1:3 v/v. The cross-linking occurred after 15 min at 37  $^\circ\text{C}$ . The channel was formed by inserting a 21-gauge needle (800  $\mu\text{m}$ ) inside the mold, where the polymeric solutions were added, respectively. The cross-linking agents were poured within the mold and, after cross-linking, the needle was gently removed, leaving a hollow round canal within the gel.

### 5.3.2 Channel-Based Hydrogels Characterization

#### 5.3.2.1 Diffusion measurements

Glucose diffusion coefficients in alginate and fibrin hydrogels were experimentally measured. Hydrogels were formed by pouring alginate and fibrin in a CaCl<sub>2</sub> and thrombin bath, respectively. Then, hydrogel beads were soaked in 4 mL of deionized water containing glucose at the initial concentration of 200 mg/mL and 1 mL of solution was sampled every hour for 8 h. Glucose absorbance was read at 193 nm by using a spectrophotometer and the glucose diffusivity within the two hydrogels was calculated through the best fitting of the data obtained from the experimental release studies. Briefly, a simulation of the mass transport process occurring between the medium and the hydrogels was performed by employing the Transport of the diluted species (TDS) module of Comsol Multiphysics (COMSOL AB, Stockholm, Sweden) in order to fit the raw data (not shown) and thus to get the optimal glucose diffusion coefficient by comparing the two resulting curves. The implemented model in Comsol Multiphysics was based on the second Fick law assuming that only the diffusion process in the bath could occur:

$$\frac{\delta c}{\delta t} + \nabla \times (J) = 0 \quad (1)$$

where  $c$  is the component concentration and  $J$  is the mass diffusive flux vector, defined by the Fick law as:

$$J = -D \nabla c \quad (2)$$

where  $D$  is the diffusion coefficient of the metabolite. Experiments were performed in triplicates and the results were expressed as mean and standard deviation.

### 5.3.2.2 Mechanical characterization

Both hydrogels were mechanically tested through a dynamic mechanical analysis (DMA) at the physiological frequency of 1 Hz. Briefly, the instrument was composed by a plate supporting the sample, a mini-shaker that generate a vertical oscillation, connected to a cylindrical indenter (diameter = 5 mm), which thus apply a sinusoidal stress on the cylindrical sample (diameter = 5 mm, height = 3 mm), linked with a force transducer, and finally by a laser measuring the displacement. Before all tests, samples were 10% pre-deformed. Measurements were recorded in triplicate and the results were expressed as mean and standard deviation. When the stress is applied the following equations hold:

$$\begin{cases} \sigma = \sigma_0 \sin \omega t \\ \varepsilon = \varepsilon_0 \sin \omega t + \delta \end{cases} \quad (3)$$

where  $\sigma$  is the stress tensor,  $\varepsilon$  the strain tensor,  $\omega$  the frequency,  $t$  the time and  $\delta$  the lag. The storage modulus  $E$  (or Young modulus) measuring the stored energy and representing the elasticity of the material, and the loss modulus  $E''$  (or viscous modulus) measuring the dissipated energy as heat and representing the viscosity, have been evaluated and defined as follows:

$$\begin{cases} E = \frac{\sigma_0}{\varepsilon_0} \cos \delta \\ E'' = \frac{\sigma_0}{\varepsilon_0} \sin \delta \end{cases} \quad (4)$$

The damping properties were also analyzed by calculating the loss factor ( $\tan \delta$ ), as ratio between the viscous modulus over the storage one [41]:

$$\tan \delta = \frac{E''}{E} \quad (5)$$

Furthermore, considering the rubber elasticity theory, the following equation defines the gel crosslink density  $\rho_x$  as [20],

$$\rho_x = \frac{E}{3RT} \quad (6)$$

where  $R$  is the universal gas constant ( $8.314 \text{ J K}^{-1} \text{ mol}^{-1}$ ),  $T$  the absolute temperature ( $298.15 \text{ K}$ ).

### 5.3.2.3 CFD analysis of the Fluid-Hydrogels Interactions

Firstly, in order to obtain desired WSS range values inside the channel ( $1\text{--}10 \text{ Dyn/cm}^2$ ) a theoretical analysis, assuming (i) a laminar flow regime, (ii) an incompressible Newtonian fluid, was carried out. Based on these hypotheses, the inverse formula of Poiseuille's law for a cylindrical tube is:

$$Q = \frac{\pi r^3 \tau}{4\mu} \quad (7)$$

where  $Q$  is the flow rate,  $r$  the channel radius,  $\tau$  the shear stress and  $\mu$  is the fluid dynamic viscosity of water. Next, the fluid-dynamics inside the channel were simulated. This analysis was performed using the Single-Phase Laminar Fluid Flow model of Comsol Multiphysics 5.5 assuming (i) a laminar flow regime, (ii) an incompressible Newtonian fluid. The solving equations are the Navier-Stokes ones for conservation of momentum (8a) and the continuity one for conservation of mass (8b):

$$\begin{cases} \rho \left[ \frac{\partial u_f}{\partial t} + u_f \times (\nabla u_f) \right] = -\nabla p + \mu(\nabla^2 u_f) & (8a) \\ (\nabla \times u_f) = 0 & (8b) \end{cases}$$

where  $u_f$  is the fluid velocity and  $p$  the pressure across the circuit. The density  $\rho$  ( $1000 \text{ kg/m}^3$ ) and viscosity  $\mu$  ( $10^{-3} \text{ Pa}\cdot\text{s}$ ) values of water at room temperature ( $25 \text{ }^\circ\text{C}$ ) were used. A flow rate was set as input according to Equation (7) to create a pressure gradient within the channel, in order to generate the fluid motion, whereas as output the atmospheric pressure was set as null, avoiding a backflow. A no-slip boundary condition was set, thus assuming no flow across channel walls. Moreover, the shear stress distribution within the channel was estimated. Since the steady state flow is reached almost instantaneously for our flow rate range, we considered only a steady state analysis. Indeed, an iterative geometric multigrid (GMRES) algorithm was used to solve the equations. The interaction between the fluid and the hydrogel solid structure, including both fluid pressure and viscous forces, was investigated. According to the Fluid-Structure Interaction (FSI) Multiphysics module, the interplays between the fluid (cell culture medium) and a deformable solid (3D hydrogel) were examined. In particular, the fluid-dynamic load on the structure, i.e., the hydrogel, especially focusing on the channel deformation in order to determine the fluid flow-associated forces effects on the polymer matrix, was analyzed. According to the DMA results (Table 11), the solid structure was approximated to an isotropic linear elastic material since the elastic component was found to be predominant respect to the viscous one.

Table 11: Hydrogels chemical-physical characteristics. Data are reported as mean  $\pm$  s.d.

Material	Elastic Modulus [kPa]	Viscous Modulus [kPa]	Loss Factor	Crosslinking Density [mol/cm <sup>3</sup> ]	Diffusivity [m <sup>2</sup> /s]
Alginate	167.3 $\pm$ 9.0	30.4 $\pm$ 0.5	0.18 $\pm$ 0.01	2.2 $\pm$ 0.1 $\cdot$ 10 <sup>-5</sup>	5.0 $\pm$ 0.8 $\cdot$ 10 <sup>-10</sup>
Fibrin	7.2 $\pm$ 0.8	0.9 $\pm$ 0.1	0.13 $\pm$ 0.02	9.7 $\pm$ 1.1 $\cdot$ 10 <sup>-7</sup>	4.4 $\pm$ 0.5 $\cdot$ 10 <sup>-10</sup>

Therefore, the multiphysics model equations are:

- Equation of motion, an expression of Newton's second law:

$$\nabla \times \sigma_s + F_v = \rho_h \frac{\partial u_2}{\partial t^2} \quad (9)$$

where  $\sigma_s$  is the Cauchy stress tensor,  $F_v$  the body force per unit volume,  $\rho_h$  is the hydrogel density and  $u_2$  the channel displacement vector.

- Strain-displacement equation:

$$\varepsilon = \frac{1}{2} [\nabla u_2 + (\nabla u_2)^T] \quad (10)$$

where  $\varepsilon$  is the strain tensor.

- Constitutive law for the structural material:

$$\sigma_s = \left[ \frac{Ev}{(1+v)(1-2v)} \nabla \times u_2 \right] I + \left[ \frac{E}{1+v} \right] \varepsilon \quad (11)$$

where E is the Young Modulus, measured through DMA analysis, and  $\nu$  the Poisson coefficient.

- Equation of normal components, which allows coupling the fluid-dynamics with the solid mechanics:

$$\sigma_s \times n = \sigma_f \times n \quad (12)$$

where  $n$  is the normal vector on the channel walls and  $\sigma_f$  the fluid stress tensor.

Constitutive law for a Newtonian fluid:

$$\sigma_f = -p_f I + \mu \left[ \nabla u_f + (\nabla u_f)^T \right] - \frac{2}{3} \mu (\nabla \times u_f) I \quad (13)$$

As initial condition, the channel displacement was assumed null.

#### 5.3.2.4 Cell Viability Analysis within Channel-Based Hydrogels

Alginate and fibrin hydrogels were tested and compared to model the ECM environment mimicking the metastatic site. Breast cancer cells from adenocarcinoma (MDA-MB-231) were embedded within the two polymers and cultured in Dulbecco's Modified Eagle's Medium (DMEM; Invitrogen, Carlsbad, CA, USA) enriched with 10% Fetal Bovine Serum (FBS), 1% L-glutamine and 1% penicillin/streptomycin (all from Sigma Aldrich, Saint Louis, MO, USA) at the concentration of  $2 \cdot 10^6$  cells/mL. After 24 h, the cells viability was evaluated by washing the hydrogels three times with PBS and by incubating them in 2 mM calcein AM and in 4 mM EthD-1 in PBS for 15 min at 37 °C in a dark environment, to identify live and dead cells, respectively. All images were obtained using fluorescence microscope (Nikon H550L, Nikon, Tokyo, Japan) and processed with ImageJ® software. Cell viability is derived as ratio between alive cells and the total number of cells for image. Measurements were recorded in triplicates and the results were expressed as mean and standard deviation.

### 5.3.3 Channel-Based Hydrogels Validation under Dynamic Conditions

#### 5.3.3.1 Perfusion Tests

Perfusion tests were carried out to verify the two materials capability to resist to the fluid passage, previously examined through FSI analysis, and thus the fluidic continuity between

the hydrogel inner channel and an external fluidic circuit. This circuit was composed by silicone tubes connected to a syringe pump (Harvard apparatus PHD2000, Holliston, MA, USA), which allowed to accurately control the flow rate and keep it constant. The pump flow rate was set in the range predicted by the CFD analysis to obtain a physiological WSS values in the 1–10 Dyn/cm<sup>2</sup> range. Furthermore, we injected a dye into the entire fluid circuit and dipped the hydrogel into a colored PBS bath, to identify any liquid leakage from the channel.

### 5.3.3.2 Computational Glucose Transport Simulation

A glucose mass transport analysis was carried out, by using the TDS Multiphysics module. In addition to the diffusive mechanism, other two processes were considered: the convection transport, due to the presence of a velocity field ( $u_f$ ), and the metabolite consumption/production because of the cellular respiration. The glucose metabolism is accurately described by the Michaelis-Menten reaction:

$$R = \frac{V_{max}c}{K_m + c} \quad (14)$$

where R is the reaction term, c is the concentration of the component,  $V_{max}$  represent the maximum consumption/production rate (equal to  $2.57 \times 10^{-4}$  mol/m<sup>3</sup>·s) and  $K_m$  represents the component concentration when the rate is  $V_{max}/2$  (equal to 2.9 mol/m<sup>3</sup>) [42]. Thus, the general form to describe the mass transport can be written as:

$$\frac{\delta c}{\delta t} + \nabla \times (J) + u_f \times \nabla c = R \quad (15)$$

where J is the mass diffusive flux vector previously defined Equation (2).

In particular, this study was conducted by considering two opposite scenarios to monitor the presence of concentration gradients inside the hydrogels: (i) a continuous refilling of the culture medium within the culture chamber and (ii) no culture medium refilling, both in static and dynamic conditions. In both cases, 5.5 mol/m<sup>3</sup> was set as culture medium initial glucose concentration.

### 5.3.3.3 Metastatic Breast Cancer Cells Circulation

The mold was sterilized in ethanol 70% v/v for 30 min, washed with sterile DI water and connected to the syringe pump using autoclaved connectors (Bio-rad, Milan, IT) and Tygon tubes (i.d. = 800 μm; Saint-Gobain, Courbevoie, France). Fibrin hydrogels were prepared by using the protocol described above. The tubes inner surface was treated with 1% Pluronic F-127 (Sigma Aldrich, Saint Louis, MO, USA) for 30 min to reduce cell adhesion during circulation.

Highly metastatic breast cancer cells (MDA-MB-231) from breast adenocarcinoma were expanded in DMEM enriched with 10% FBS, 1% L-glutamine and 1% penicillin/streptomycin (all from Sigma Aldrich, Saint Louis, MO, USA). Cells were enzymatically detached with 0.05% trypsin, counted, and injected within the circuit at a density of  $1 \cdot 10^5$  cells/mL. The pump flow rate was set to 1.5 mL/min to reproduce the physiological WSS value of 5 Dyn/cm<sup>2</sup>. As controls, MDA-MB-231 cells were injected in a circuit composed of Tygon tubes (i.d. = 800 μm) where cells could circulate at the same WSS and cultured in static conditions over surfaces pre-treated with Pluronic.

### 5.3.3.4 Recovered Cells Viability Assay and Cells Migration in the Hydrogel under Circulation

Cells viability was analyzed after 24 h of circulation by using the Live/Dead assay (Sigma Aldrich, Saint Louis, MO, USA). Shortly, MDA-MB-231 were recovered from the circuits

(petri dish for the static control) and counted. Then, cells were placed in 96 well plates, where they could adhere. After 24 h, supernatant was collected to count the cells which did not adhere on the plastic surfaces, while the remaining cells were incubated with 2 mM calcein AM and in 4 mM EthD-1 in PBS for 15 min at 37 °C in a dark environment, to identify live and dead cells, respectively. Cells were washed three times in PBS and observed under microscope. All images were obtained by using fluorescence microscope (Nikon H550L, Nikon, Tokyo, Japan) and processed with ImageJ® software. Cells' viability was derived as the ratio between the number of alive cells and the total number of cells for each picture. A toluidine blue staining on the hydrogel was performed to establish the presence of the cells within the hydrogel after 24 h of circulation. Briefly, fibrin hydrogel was fixed in 4% paraformaldehyde and next washed three times with PBS. Then, the gel was immersed in a 0.2% toluidine blue (Sigma Aldrich, Saint Louis, MO, USA) solution for 15 min and, subsequently, washed in PBS until the excess toluidine was removed. Images were captured using light transmitted microscope (Nikon H550L, Nikon, Tokyo, Japan).

## 5.4 Results

### 5.4.1 Hydrogels Realization

To obtain a tumor ECM-like model traversed by a perfusable channel, a hydrogel matrix with a single inner vessel-like channel fluidically connected to an external circuit was realized (Figure 22) in order to study the first steps occurring during the metastatic cascade (i.e., cells circulation and survival within the bloodstream, extravasation, spreading and colonization of the metastatic site).

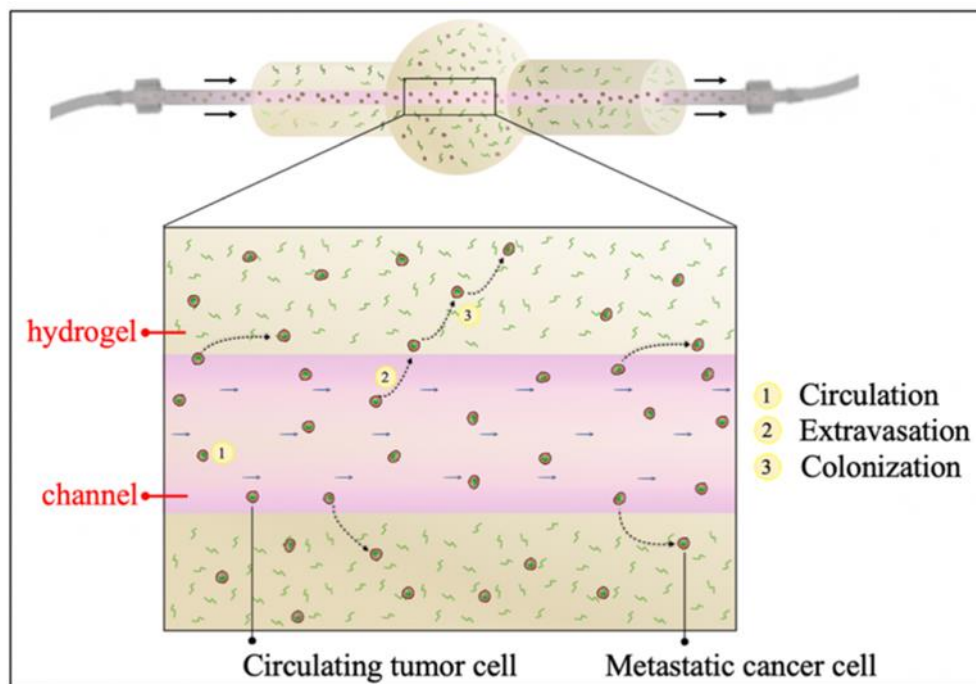


Figure 22: Schematic representation of the main steps of the metastatic cascade.

Two kinds of polymers were used and compared to realize the channel-based hydrogel by using two different precursors (alginate solution and fibrinogen, respectively). The polymers were respectively poured into a mold after the insertion of a 21G-needle in an appropriate support. The mold was necessary to create and mechanically sustain the hydrogels. Once alginate or fibrin were cross-linked, the needle was gently removed from the mold leaving

cylindrical cavities within the hydrogel. Different fabrication parameters (polymeric precursor and cross-linking agent concentrations, precursor/cross-linking agent ratios) were tested for the two polymers, respectively. As result, we observed that highest concentration of fibrinogen (40 mg/mL) and alginate precursor in a weight/volume ratio higher than 1.5% were difficult to pour into the mold due to the high viscosity of the solutions. On the other hand, the hydrogel collapsed by using alginate concentrations lower than 1.5 % w/v. Accordingly, we chose alginate 1.5% w/v and fibrinogen 20 mg/mL as precursor concentrations. Regarding the cross-linker agent, 1 M CaCl<sub>2</sub> was selected, to guarantee performant mechanical properties without impairing cells viability [43]. Thrombin concentration of 10 U/mL was chosen because it was enough to enable a good manipulation of the final hydrogel. Therefore, the final protocol of alginate realization consisted of alginate 1.5% w/v, CaCl<sub>2</sub> 1 M and a CaCl<sub>2</sub>/alginate ratio of 1:3 v/v, whereas the fibrin hydrogel was prepared by mixing fibrinogen 20 mg/mL and thrombin 10 U/mL at 1:1 v/v ratio.

## 5.4.2 Hydrogels Characterization

Firstly, the chemical-physical characteristics of alginate and fibrin hydrogels without channel were assessed. To successively examine the glucose distribution within the hydrogels, experimental glucose diffusion measurements were carried out, by performing a CFD mass transport analysis. The mass transport process occurring between the medium and the hydrogel was simulated by using Comsol Multiphysics in order to obtain the best fitting of the raw data (not shown) and thus to identify the optimal glucose diffusion coefficient. Results are reported Table 11. Subsequently, both polymers were mechanically characterized: the storage and viscous moduli were evaluated by performing a DMA analysis at a physiological frequency (1 Hz). Results reported in Table 11 show the elastic and viscous moduli for both the hydrogels. The alginate elastic and viscous moduli resulted in being considerably higher than the fibrin ones. The elastic modulus values are directly correlated with the degree of crosslinking of the polymeric compounds. It can be observed that the crosslinking density of the alginate was higher than the fibrin one, reflecting the different mechanical properties of the two polymers. The damping properties, represented by the Loss factor, showed that for both the hydrogels the elastic component was more dominant than the viscous one (loss factor  $\ll 1$ ). This means that these materials can be considered simple linear elastic ones. Accordingly, the Young modulus was used as input hydrogel parameter in the following computational simulations. These values were used as input in the further CFD simulations, performed to predict the mechanical response of the channel-based hydrogels in presence of a fluid flow. Newtonian incompressible fluid was considered and, according to the theoretical analysis Equation (7), the 0.3–3 mL/min range was imposed as input flow rate for the CFD simulations. In particular, the fluid-dynamic load transmitted from the fluid to the hydrogel was quantified through the FSI Multiphysics. Alginate or fibrin channel-based hydrogels were modeled as linear isotropic elastic materials, as results of the mechanical characterization (Table 11). The radial channel displacement was compared to the initial diameter size (800  $\mu\text{m}$ ) to evaluate the channel deformation respect to its initial dimensions. Both polymers showed a low channel deformation and to properly withstand the fluid flow-dynamic load. It can be noticed in Figure 23 that the fluid flow-associated stress and the resulting deformation were higher at the beginning of the channel, both for alginate and fibrin, showing that such area is crucial to ensure a fluidic continuity between the hydrogel and the external circuit.

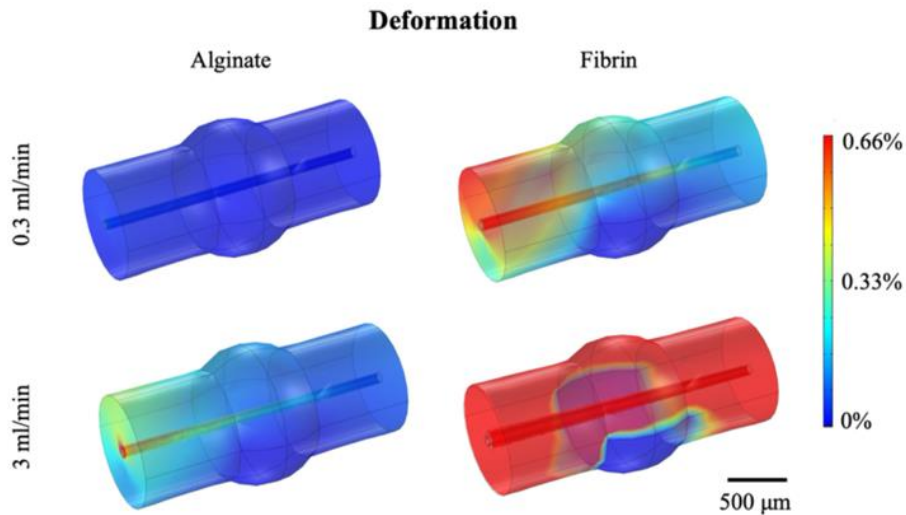


Figure 23: Channel displacement within alginate and fibrin models evaluated at minimum flow rate (0.3 mL/min) and maximum flow rate (3 mL/min).

Finally, alginate and fibrin 3D samples were tested and compared to evaluate their biocompatibility. Breast cancer cells from adenocarcinoma (MDA-MB-231) were embedded within the two polymers. After 24 h of culture, cells viability was evaluated by using the live/dead assay to discriminate live and dead cells, revealing a cell viability higher than 90% in both cases ( $93.5\% \pm 2.2\%$  for alginate hydrogels and  $95.7\% \pm 1.2\%$  for fibrin ones). Moreover, cancer cells were characterized by a round shape typical of the in vivo native tumor environment, as shown in Figure 24. Despite the different chemical composition and mechanical properties of the two polymers, no substantial differences were highlighted in cells viability and organization within the matrix, confirming that alginate and fibrin are both suitable candidates to mimic the tumor extracellular surrounding environment, as widely documented in the literature [44,45] and that our protocol of hydrogels fabrication is not harmful for cells' viability.

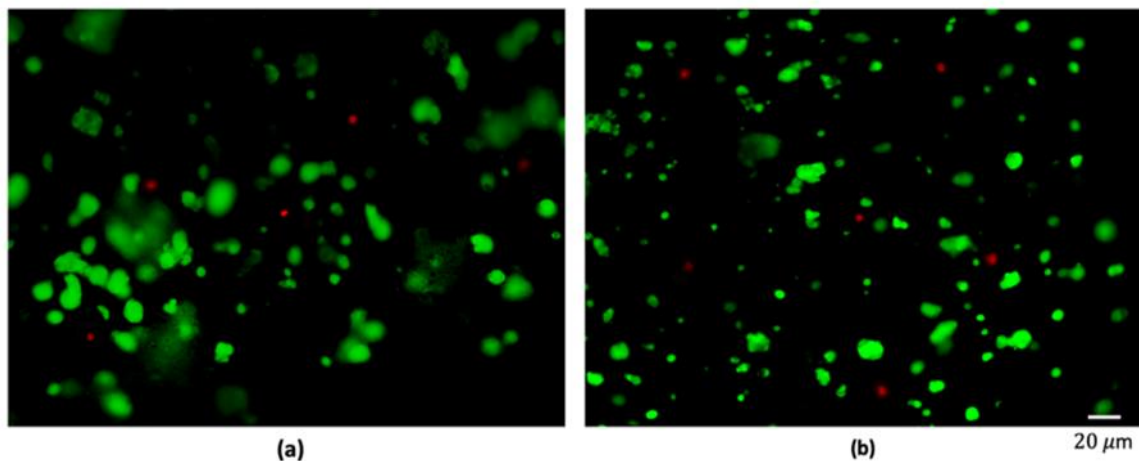


Figure 24: Live/dead staining on MDA-MB-231 cultured in channel-based alginate (a) and fibrin (b) hydrogels.

### 5.4.3 Perfusion tests

Perfusion tests were performed to experimentally compare the capability of alginate and fibrin to withstand the fluid flow at the same flow rate. According to the theoretical and CFD analyses, the 0.3–3 mL/min range, corresponding to a WSS of 1 Dyn/cm<sup>2</sup> and 10



Dyn/cm<sup>2</sup> respectively, was imposed as input flow rate at the pump level. Fibrin revealed to be the most performing material. In fact, as it is shown in Figure 25b, the dye flowing into the channel, at flow rate values equal or lower than 1 mL/min, did not disperse within the fibrin polymeric matrix, differently from in presence of alginate (Figure 25a), where the fluid rapidly permeated from the channel to the hydrogel. Moreover, it was possible to carry out tests up to 24 h by using fibrin, whereas alginate collapsed after only a few hours.

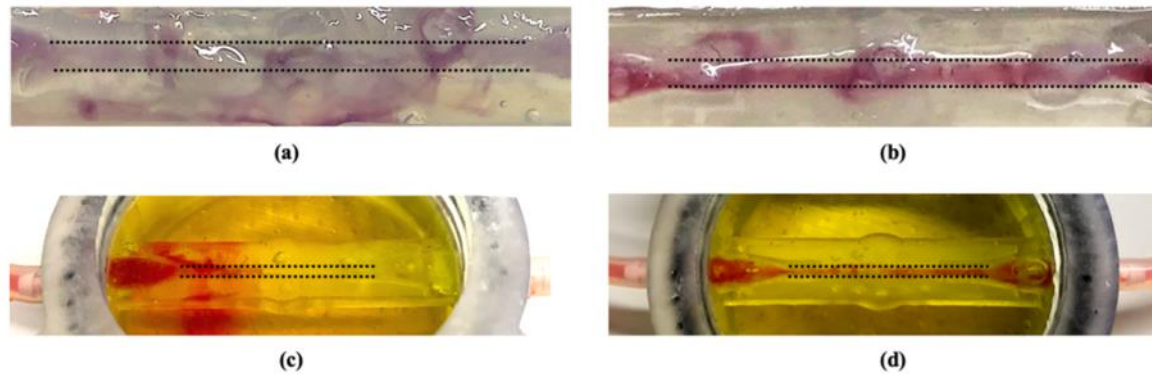


Figure 25: Hydrogels perfusion tests. The dotted line indicates where the channel is located. Comparison between alginate (a) and fibrin (b) capability to withstand the fluid passage at the same flow rate (1 mL/min); comparison between 3 mL/min (c) and 1.5 mL/min.

Therefore, further perfusion tests only on fibrin hydrogels were executed to experimentally investigate effects of different input flow rates in the established range. As the FSI analysis predicted, the first tract of the channel was confirmed to be the critical point for the fluidic continuity with the external circuit, since liquid leakages occurred only in this area. In addition, as it is shown in Figure 25c, flow rate values higher than 1.5 mL/min, therefore higher than 5 Dyn/cm<sup>2</sup> of WSS, often caused channel damaging, yielding to a liquid leakage. On the other hand, a perfect fluidic continuity was obtained by setting a flow rate of about 1.5 mL/min (Figure 25d), corresponding to a WSS of 5 Dyn/cm<sup>2</sup>, as CFD simulations predicted which is a physiological micro-vessel WSS [25].

#### 5.4.4 Glucose Diffusion Analysis

Two different culture conditions were simulated by employing the TDS module of COMSOL Multiphysics 5.5: the so-called “continuous refill” culture condition, characterized by a continuous medium refresh over time, and the “no refill” condition. In addition, the static and dynamic scenarios for the “no refill” condition were investigated. The simulation was carried out up to 8 h, by using as input values the physical parameters found by performing the experimental absorption studies (Table 11). Figure 26 shows glucose distribution over time for all the culture conditions. A homogeneous spatial distribution in the refill condition just after 4 h was achieved, whereas in the other scenarios (no refill, both static and dynamic) a higher glucose accumulation around the vessel can be observed, since in these cases the nutrients renewal could occur only through the fluid flow within the channel.

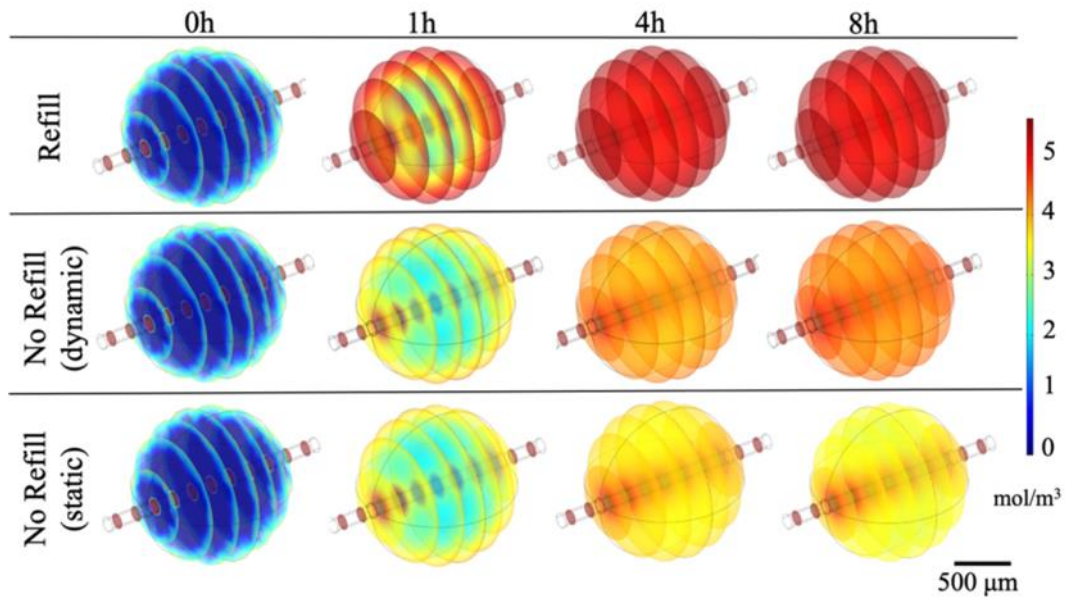


Figure 26: Glucose concentration within fibrin hydrogels modeled simulating three different scenarios: (i) continuous culture medium refilling, (ii) dynamic no culture medium refilling, (iii) static no culture medium refilling within the chamber. Four different time points are reported:  $t_0 = 0$  h,  $t_1 = 1$  h,  $t_2 = 4$  h,  $t_3 = 8$  h.

Finally, we calculated the glucose concentration gradient as the difference between the maximum and the minimum glucose concentration values for each time point considered (Figure 27). If the glucose is not homogeneously distributed, the concentration gradient is higher, since this last is representative of the concentration discrepancies within the polymeric matrix. The results reported confirm the trends previously described.

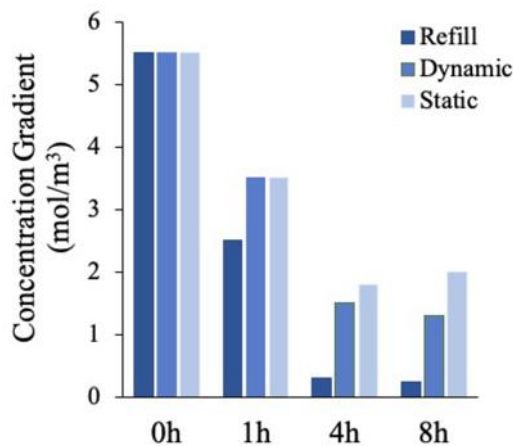


Figure 27: Glucose concentration gradients values in the three culture scenarios considered at different time points:  $t_0 = 0$  h,  $t_1 = 1$  h,  $t_2 = 4$  h,  $t_3 = 8$  h.

In summary, a constant monotone decreasing glucose gradient was observed in the refill and dynamic no refill mode, meaning that the glucose was uniformly delivered to the cells in the gel over time, whereas in the static condition, an initial decrease, due to the initial large disparity between the surrounding culture medium rich in glucose and the glucose-free polymer matrix, was followed by a gradient increase, indicating a non-homogenous glucose profile.

#### 5.4.5 Recovered Cells Number and Viability after Circulation

High metastatic potential breast adenocarcinoma cells (MDA-MB-231) circulated within the hydrogel-based fluidic platform under physiological WSS (5 Dyn/cm<sup>2</sup>) conditions. Cell suspension was collected after 24 h of circulation from the circuits and cells were counted. The percentages of recovered cells from the hydrogel-based circuit, the plastic tube one and the static control, respect to the total number of cells injected, were 57.5% ± 1.3%, 80.1% ± 1.9%, 91.3% ± 1.2%, respectively (Figure 28).

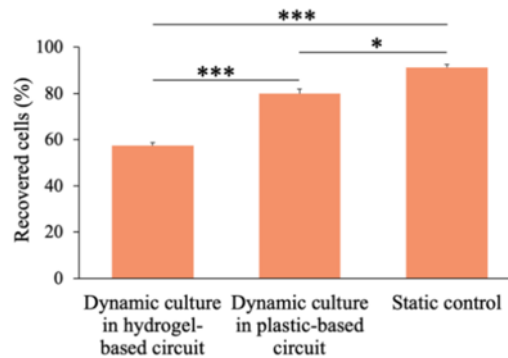


Figure 28: Number of recovered cells from the hydrogel-based circuit, the plastic tube-based one and the static control after 24 h. Values are reported as mean ± s.d., N = 3, student's t-test: \* p < 0.05, \*\*\* p < 0.001.

After counting the recovered cells, they were plated in 96 well plates and cultured to allow their adhesion. After 24 h, the supernatant containing the dead cells, which were not able to adhere on the plastic surface (or detached), was collected, while a fluorescent staining (live/dead) was performed on the remaining adherent cells (Figure 29).

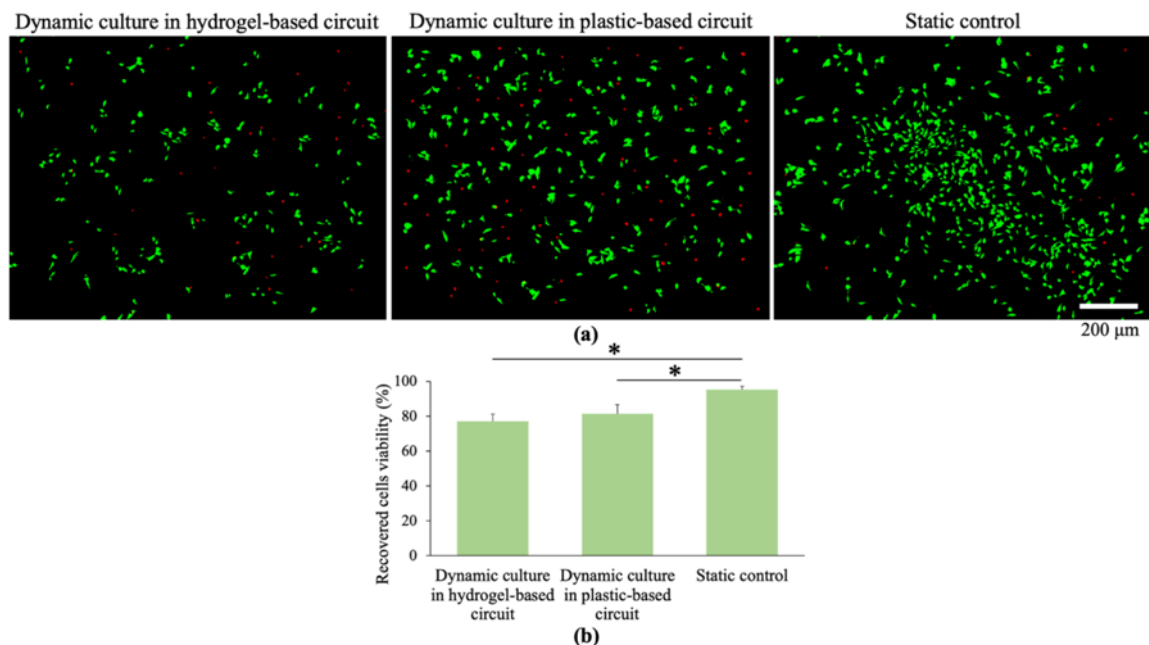


Figure 29: Recovered cells viability measured by live/dead staining of cells after 24 h of circulation within the hydrogel-based circuit (WSS = 5 Dyn/cm<sup>2</sup>), plastic-based circuit (dynamic control, WSS=5 Dyn/cm<sup>2</sup>) and culture within petri dish (static control) (a); quantitative analysis of the images, values are reported as mean ± s.d., N = 3, student's t-test: \* p < 0.05 (b).

Image post-processing analysis of fluorescent images (Figure 29a) revealed a cell viability of 77.3% ± 4.1% after cells circulation within the hydrogel-based circuit under a WSS of 5 Dyn/cm<sup>2</sup>, and of 81.3% ± 5.3% at the same WSS 5 Dyn/cm<sup>2</sup> in the hydrogel-free plastic

circuit, whereas in the static control resulted equal to  $95.2\% \pm 1.9\%$ . This means that the WSS affected cells viability, although at this physiological value (5 Dyn/cm<sup>2</sup>) the cells viability was still high (around 80%) after 24 h of culture. It is important to note that the number of dead cells which did not adhere on the well plates after recovery from the circuits was not significantly different (data not shown) in all cases suggesting that the cells viability is not altered respect that represented in Figure 29. Interestingly, no significant differences in cells viability were found after cells circulation in the fluidic platform with and without the hydrogel. The lower number of cells recovered in the hydrogel-based circuit could be due to the presence of a bioactive fibrin surface where breast cancer cells could adhere. Therefore, we then investigated the presence of cells within the hydrogel, to evaluate if they migrated toward the fibrin.

#### 5.4.6 Cells Migration within the Hydrogel under Fluid Flow

CTCs migration within the hydrogel-based surrounding environment was qualitatively evaluated by performing a toluidine blue staining on the fibrin hydrogel. As can be observed in Figure 30, MDA-MB-231 extravasated from the channel and migrated in the hydrogel. The high presence of embedded cells within the fibrin hydrogel confirmed that the difference between the absolute number of cells recovered from the hydrogel-based circuit and from the hydrogel-free one was due to the cells migration toward the hydrogel. Most of the migrated cells were found in the polymeric matrix portions closer to the channel where they circulated.

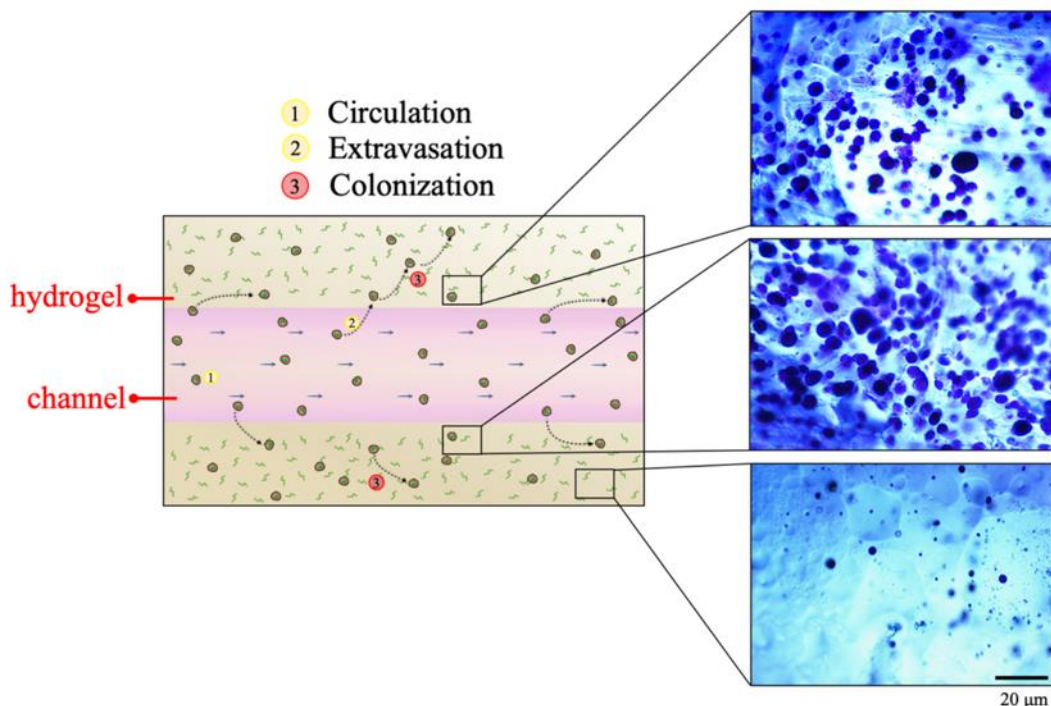


Figure 30: Toluidine blue staining on fibrin hydrogel identifying cells extravasated and migrated within the fibrin hydrogel.

## 5.5 Discussion

Cancer metastasis represents one of the leading causes of death. Despite recent advances in cancer research, the establishment of a reliable *in vitro* platform to accurately explore the crucial mechanisms involved during the metastatic dissemination remain still a challenge. To meet this need, here we realized a novel *in vitro* fluidic platform to deeply investigate

the cancer cells extravasation and colonization in a 3D hydrogel-based metastatic model under physiological hematogenous forces. Firstly, a 3D printer was employed to fabricate a plastic mold to realize 3D hydrogels provided with an inner channel directly connected to an external fluidic circuit. Alginate and fibrin were tested and compared as bulk polymers for the hydrogel realization. Hydrogels fabrication protocols were optimized to obtain a balance between the feasibility of the channel-based system and the performance of the final hydrogel-based structure. Specifically, the two polymeric concentrations were optimized to be low enough to be easily handled in the molds and high enough to guarantee a suitable stiffness of the final hydrogels, able to withstand the hydraulic pressure generated by the fluid flow. In fact, mechanical properties are fundamental at the macroscale level as well as at the microscale one. In this context, it is widely recognized that the mechanical properties condition cell activity [46]. For example, breast cancer cells showed a decreased viability by increasing alginate hydrogels elasticity, while soft hydrogels ( $E < 200$  kPa) were more permissive to cell proliferation [44]. Here, DMA results reported that alginate and fibrin hydrogels stiffness was in this range. Besides the biocompatibility, it was important to predict, through CFD simulations, the hydrogels mechanical response to external fluidic stimuli. In fact, fluid flow-derived stimulation within compliant and deformable materials, such as soft hydrogels, may lead to structural deformations [47]. FSI results indicated that both polymers endured the flow-associated stresses, preventing matrix collapses and liquid leakages of the circulating medium, by imposing a flow rate range of 0.3–3 mL/min, corresponding to the physiologic WSS of 1–10 Dyn/cm<sup>2</sup> within the channel. In fact, such WSS values establish a physiologically relevant range of fluid forces experienced by CTCs in microvascular vessels [48]. Furthermore, it is commonly accepted that fluid flow patterns have a regulatory effect on tumor cells adhesion, proliferation, and invasion. In particular, the shear stress can influence the CTCs survival during the vascular transport and thus their metastatic potential [25]. Therefore, it is important to resemble the cancer hemodynamics, especially the biophysical properties experienced by the CTCs during the metastatic migration in the bloodstream. As first platform validation, experimental perfusion tests were carried out by fluidically connecting the hydrogels to the external fluidic circuit to verify the real capability of the 3D hydrogels to withstand the fluid flow stimuli. Interestingly, results revealed that fibrin was the most performing material, since liquid dispersion within the matrix was absent and the channel was clearly visible after perfusion. This behavior can be due to the well-known adhesive properties of the fibrin that make it widely adopted in the surgical field as a sealant to promote tissues bonding [49,50]. Another major current challenge in designing 3D hydrogel-based culture systems relies on the mass transport limitations experienced when using clinically relevant length scales (centimeters) [51]. In fact, one of the major common limitations of the hydrogel-based constructs is represented by the passive cell culture medium diffusion, which is inadequate to deliver nutrients over large length scale, thus resulting in nutrient and waste discrepancies within the constructs, reducing cell viability as well as altering cellular phenotypes [52,53]. In fact, ideally, once the CTCs have colonized the hydrogel representing the metastatic site, they need an adequate nutrients supply, present in the culture medium, to carry on their metabolic activity. Therefore, we simulated three different scenarios: the medium “continuous refill” culture condition, characterized by a continuous medium refresh over time in the culture chamber and the “no refill” condition, in static and in dynamic culture, respectively. As reported, in each of these configurations, an initial (first 4 h) increase of the glucose concentration inside the hydrogel occurred, due to a massive medium diffusion to the gel, caused by the high glucose concentration difference between inside (0 mol/m<sup>3</sup>) and outside (5.5 mol/m<sup>3</sup>) the polymer. After 4 h, a change in the trend occurred for the “no refill” static scenario. In fact, a small decrease of glucose concentration was shown in the following h (up to 8 h), resulting

in higher concentration inhomogeneities within the entire matrix. On the contrary, for the “no refill” dynamic culture mode, an enhanced glucose spatial uniformity within the hydrogel was reached, demonstrating that the dynamic stimuli had a clear effect on improving the hydrogel glucose supply due to the additional convection process occurring within the system. Accordingly, the “no refill” dynamic scenario was more similar to the “continuous refill” one, which represented the ideal culture condition. Finally, once the platform was fluidically validated and the nutrient transport mechanisms optimized, highly metastatic breast cancer cells (MDA-MB-231) were injected within the circuit and exposed to physiological WSS conditions of 5 Dyn/cm<sup>2</sup>, to assess their viability upon circulation as well as their capability to migrate toward the hydrogel and colonize the metastatic model. Since a lower number of cells was recovered from the hydrogel-based circuit (57.5% ± 1.3%), respect the hydrogel-free one (80.1% ± 1.9%), we supposed that this remarkable difference was due to the presence of the bioactive fibrin [49], where breast cancer cells could adhere. Hence, we investigated the presence of cells within the hydrogel, to evaluate if they migrated toward the fibrin. As Figure 30 shows, a large presence of cells within the polymeric matrix can be shown, confirming that invasion and adhesion to the hydrogel occurred under physiological WSS conditions. Moreover, it is well-known that vasculature structure plays a pivotal role on CTCs extravasation and that the complex interplay between the ECs and cancer cells needs to be reproduced to fully elucidate the mechanisms of cells invasion in a secondary tissue [28,54]. Furthermore, the endothelium is susceptible to different shear stresses by altering morphology, gene expression profiles, ECs-ECM interactions and barrier transport capabilities [25]. Based on these considerations, further studies could be performed aimed at increasing the level of accuracy of our fluidic platform by associating multiple components typical of the metastatic niche (e.g., chemical signals, cells recreating the tumor stroma, endothelial cells to re recreate the endothelial barrier functions). In addition, biomolecules, as vascular endothelial growth factor (VEGF), can be incorporated in our system, since, for example, VEGF gradients together with shear forces may promote ECs sprouting and vasculogenesis of capillary-sized networks within the ECM [28,55]. Here, we realized a 3D hydrogel-based fluidic platform by coupling an experimental approach to an in silico analysis to assess the optimal culture conditions and precisely control fluid patterns within a ECM-based channel, thus providing the scientific community a low-cost and efficient in vitro model to carry out systematic studies on the development and progress of the metastatic process.

## 5.6 References

1. Song, P.; Ye, D.; Zuo, X.; Li, J.; Wang, J.; Liu, H.; Hwang, M.T.; Chao, J.; Su, S.; Wang, L.; et al. DNA Hydrogel with Aptamer-Toehold-Based Recognition, Cloaking, and Decloaking of Circulating Tumor Cells for Live Cell Analysis. *Nano Lett.* **2017**, *17*, 5193–5198, doi:10.1021/acs.nanolett.7b01006.
2. Pantel, K.; Alix-Panabières, C. Functional Studies on Viable Circulating Tumor Cells. *Clin. Chem.* **2016**, *62*, 328–334, doi:10.1373/clinchem.2015.242537.
3. Myerowitz, R.L.; Edwards, P.A.; Sartiano, G.P. Carcinocythemia (carcinoma cell leukemia) due to metastatic carcinoma of the breast. Report of a case. *Cancer* **1977**, *40*, 3107–3111.
4. Rodríguez-Salas, N.; Jiménez-Gordo, A.M.; González, E.; de las Heras, B.; Zamora, P.; Espinosa, E.; de Castro Fernández, M.F.; Gonzalez-Baron, M. Circulating Cancer Cells in Peripheral Blood. *Acta Cytol.* **2000**, *44*, 237–241, doi:10.1159/000326367.
5. Chaffer, C.L.; Weinberg, R.A. A Perspective on Cancer Cell Metastasis. *Science* **2011**, *331*, 1559–1564, doi:10.1126/science.1203543.
6. Follain, G.; Herrmann, D.; Harlepp, S.; Hyenne, V.; Osmani, N.; Warren, S.C.; Timpson, P.; Goetz, J.G. Fluids and their mechanics in tumour transit: Shaping metastasis. *Nat. Rev. Cancer* **2020**, *20*, 107–124, doi:10.1038/s41568-019-0221-x.

7. Mitchell, M.J.; King, M.R. Computational and Experimental Models of Cancer Cell Response to Fluid Shear Stress. *Front. Oncol.* **2013**, *3*, 44, doi:10.3389/fonc.2013.00044.
8. Al-Mehdi, A.B.; Tozawa, K.; Fisher, A.B.; Shientag, L.; Lee, A.; Muschel, R.J. Intravascular origin of metastasis from the proliferation of endothelium-attached tumor cells: A new model for metastasis. *Nat. Med.* **2000**, *6*, 100–102, doi:10.1038/71429.
9. Song, J.W.; Cavnar, S.P.; Walker, A.C.; Luker, K.E.; Gupta, M.; Tung, Y.C.; Luker, G.D.; Takayama, S. Microfluidic Endothelium for Studying the Intravascular Adhesion of Metastatic Breast Cancer Cells. *PLoS ONE* **2009**, *4*, e5756, doi:10.1371/journal.pone.0005756.
10. Shin, M.K.; Kim, S.K.; Jung, H. Integration of intra- and extravasation in one cell-based microfluidic chip for the study of cancer metastasis. *Lab Chip* **2011**, *11*, 3880–3887, doi:10.1039/c1lc20671k.
11. Bersini, S.; Jeon, J.S.; Dubini, G.; Arrigoni, C.; Chung, S.; Charest, J.L.; Moretti, M.; Kamm, R.D. A microfluidic 3D in vitro model for specificity of breast cancer metastasis to bone. *Biomaterials* **2014**, *35*, 2454–2461, doi:10.1016/j.biomaterials.2013.11.050.
12. Jeon, J.S.; Zervantonakis, I.K.; Chung, S.; Kamm, R.D.; Charest, J.L. In Vitro Model of Tumor Cell Extravasation. *PLoS ONE* **2013**, *8*, e56910, doi:10.1371/journal.pone.0056910.
13. Jeon, J.S.; Bersini, S.; Gilardi, M.; Dubini, G.; Charest, J.L.; Moretti, M.; Kamm, R.D. Human 3D vascularized organotypic microfluidic assays to study breast cancer cell extravasation. *Proc. Natl. Acad. Sci. USA* **2014**, *112*, 214–219, doi:10.1073/pnas.1417115112.
14. Ma, Y.; Pan, J.Z.; Zhao, S.P.; Lou, Q.; Zhu, Y.; Fang, Q. Microdroplet chain array for cell migration assays. *Lab Chip* **2016**, *16*, 4658–4665, doi:10.1039/c6lc00823b.
15. Shin, Y.; Han, S.; Jeon, J.S.; Yamamoto, K.; Zervantonakis, I.K.; Sudo, R.; Kamm, R.D.; Chung, S. Microfluidic assay for simultaneous culture of multiple cell types on surfaces or within hydrogels. *Nat. Protoc.* **2012**, *7*, 1247–1259, doi:10.1038/nprot.2012.051.
16. Pathak, A.; Kumar, S. Independent regulation of tumor cell migration by matrix stiffness and confinement. *Proc. Natl. Acad. Sci. USA* **2012**, *109*, 10334–10339, doi:10.1073/pnas.1118073109.
17. Chen, W.; Hoffmann, A.D.; Liu, H.; Liu, X. Organotropism: New insights into molecular mechanisms of breast cancer metastasis. *npj Precis. Oncol.* **2018**, *2*, 1–12, doi:10.1038/s41698-018-0047-0.
18. Prestwich, G.D. Simplifying the extracellular matrix for 3-D cell culture and tissue engineering: A pragmatic approach. *J. Cell. Biochem.* **2007**, *101*, 1370–1383, doi:10.1002/jcb.21386.
19. Marrella, A.; Aiello, M.; Quarto, R.; Scaglione, S. Chemical and morphological gradient scaffolds to mimic hierarchically complex tissues: From theoretical modeling to their fabrication. *Biotechnol. Bioeng.* **2016**, *113*, 2286–2297, doi:10.1002/bit.25994.
20. Marrella, A.; Lagazzo, A.; Barberis, F.; Catelani, T.; Quarto, R.; Scaglione, S. Enhanced mechanical performances and bioactivity of cell laden-graphene oxide/alginate hydrogels open new scenario for articular tissue engineering applications. *Carbon N. Y.* **2017**, *115*, 608–616, doi:10.1016/j.carbon.2017.01.037.
21. Marrella, A.; Giannoni, P.; Pulsoni, I.; Quarto, R.; Raiteri, R.; Scaglione, S. Topographical Features of Graphene-Oxide-Functionalized Substrates Modulate Cancer and Healthy Cell Adhesion Based on the Cell Tissue of Origin. *ACS Appl. Mater. Interfaces* **2018**, *10*, 41978–41985, doi:10.1021/acsami.8b15036.
22. Tibbitt, M.W.; Anseth, K.S. Hydrogels as extracellular matrix mimics for 3D cell culture. *Biotechnol. Bioeng.* **2009**, *103*, 655–663, doi:10.1002/bit.22361.
23. Marrella, A.; Dondero, A.; Aiello, M.; Casu, B.; Olive, D.; Regis, S.; Bottino, C.; Pende, D.; Meazza, R.; Caluori, G.; et al. Cell-Laden Hydrogel as a Clinical-Relevant 3D Model for Analyzing Neuroblastoma Growth, Immunophenotype, and Susceptibility to Therapies. *Front. Immunol.* **2019**, *10*, 1876, doi:10.3389/fimmu.2019.01876.
24. Sood, D.; Tang-Schomer, M.; Pouli, D.; Mizzoni, C.; Raia, N.; Tai, A.; Arkun, K.; Wu, J.; Black, L.D.; Scheffler, B.; et al. 3D extracellular matrix microenvironment in bioengineered tissue models of primary pediatric and adult brain tumors. *Nat. Commun.* **2019**, *10*, 1–14, doi:10.1038/s41467-019-12420-1.
25. Buchanan, C.F.; Verbridge, S.S.; Vlachos, P.P.; Rylander, M.N. Flow shear stress regulates endothelial barrier function and expression of angiogenic factors in a 3D microfluidic tumor vascular model. *Cell Adhes. Migr.* **2014**, *8*, 517–524, doi:10.4161/19336918.2014.970001.
26. Miller, J.S.; Stevens, K.R.; Yang, M.T.; Baker, B.M.; Nguyen, D.H.T.; Cohen, D.M.; Toro, E.; Chen, A.A.; Galie, P.A.; Yu, X.; et al. Rapid casting of patterned vascular networks for perfusable engineered three-dimensional tissues. *Nat. Mater.* **2012**, *11*, 768–774, doi:10.1038/nmat3357.

27. Craik, C. Mechanisms of tumor cell extravasation in an in vitro microvascular network platform. *Bone* **2008**, *23*, 1–7, doi:10.1038/jid.2014.371
28. Bittner, K.R.; Jiménez, J.M.; Peyton, S.R. Vascularized Biomaterials to Study Cancer Metastasis. *Adv. Healthc. Mater.* **2020**, *9*, e1901459, doi:10.1002/adhm.201901459.
29. Sun, J.; Tan, H. Alginate-Based Biomaterials for Regenerative Medicine Applications. *Materials* **2013**, *6*, 1285–1309, doi:10.3390/ma6041285.
30. Drury, J.L.; Mooney, D.J. Hydrogels for tissue engineering: Scaffold design variables and applications. *Biomaterials* **2003**, *24*, 4337–4351, doi:10.1016/s0142-9612(03)00340-5.
31. Kim, A.R.; Hwang, J.H.; Kim, H.M.; Kim, H.N.; Song, J.E.; Yang, Y.I.; Yoon, K.H.; Lee, D.; Khang, G. Reduction of inflammatory reaction in the use of purified alginate microcapsules. *J. Biomater. Sci. Polym. Ed.* **2013**, *24*, 1084–1098, doi:10.1080/09205063.2012.735100.
32. Kaklamani, G.; Cheneler, D.; Grover, L.M.; Adams, M.J.; Bowen, J. Mechanical properties of alginate hydrogels manufactured using external gelation. *J. Mech. Behav. Biomed. Mater.* **2014**, *36*, 135–142, doi:10.1016/j.jmbbm.2014.04.013.
33. Lee, K.Y.; Mooney, D.J. Alginate: Properties and biomedical applications. *Prog. Polym. Sci.* **2012**, *37*, 106–126, doi:10.1016/j.propolymsci.2011.06.003.
34. Noori, A.; Ashrafi, S.J.; Vaez-Ghaemi, R.; Hatamian-Zaremi, A.; Webster, T.J. A review of fibrin and fibrin composites for bone tissue engineering. *Int. J. Nanomed.* **2017**, *12*, 4937–4961, doi:10.2147/ijn.s124671.
35. Ye, Q.; Zünd, G.; Benedikt, P.; Jockenhoevel, S.; Hoerstrup, S.P.; Sakyama, S.; Hubbell, J.A.; Turina, M. Fibrin gel as a three dimensional matrix in cardiovascular tissue engineering. *Eur. J. Cardio-Thoracic Surg.* **2000**, *17*, 587–591, doi:10.1016/s1010-7940(00)00373-0.
36. Jockenhoevel, S.; Zund, G.; Hoerstrup, S.P.; Chalabi, K.; Sachweh, J.S.; Demircan, L.; Messmer, B.J.; Turina, M. Fibrin gel—Advantages of a new scaffold in cardiovascular tissue engineering. *Eur. J. Cardio Thorac. Surg.* **2001**, *19*, 424–430, doi:10.1016/s1010-7940(01)00624-8.
37. Shaikh, F.M.; Callanan, A.; Kavanagh, E.G.; Burke, P.E.; Grace, P.A.; McGloughlin, T.M. Fibrin: A Natural Biodegradable Scaffold in Vascular Tissue Engineering. *Cells Tissues Organs* **2008**, *188*, 333–346, doi:10.1159/000139772.
38. Haugh, M.G.; Thorpe, S.D.; Vinardell, T.; Buckley, C.T.; Kelly, D.J. The application of plastic compression to modulate fibrin hydrogel mechanical properties. *J. Mech. Behav. Biomed. Mater.* **2012**, *16*, 66–72, doi:10.1016/j.jmbbm.2012.10.009.
39. Li, R.H.; Altreuter, D.H.; Gentile, F.T. Transport characterization of hydrogel matrices for cell encapsulation. *Biotechnol. Bioeng.* **1996**, *50*, 365–373, doi:10.1002/(sici)1097-0290(19960520)50:43.0.co;2-j.
40. Annibaldi, A.; Widmann, C. Glucose metabolism in cancer cells. *Curr. Opin. Clin. Nutr. Metab. Care* **2010**, *13*, 466–470, doi:10.1097/mco.0b013e32833a5577.
41. Capurro, M.; Barberis, F. Evaluating the mechanical properties of biomaterials. In *Biomaterials for Bone Regeneration*; Dubruel, P., Van Vlierberghe, S.B.T.-B., Eds.; Woodhead Publishing: Cambridge, UK, 2014; pp. 270–323. ISBN 978-0-85709-804-7.42.
42. Schornack, P.A.; Gillies, R.J. Contributions of Cell Metabolism and H<sup>+</sup> Diffusion to the Acidic pH of Tumors. *Neoplasia* **2003**, *5*, 135–145, doi:10.1016/s1476-5586(03)80005-2.
43. Cao, N.; Chen, X.B.; Schreyer, D.J. Influence of Calcium Ions on Cell Survival and Proliferation in the Context of an Alginate Hydrogel. *ISRN Chem. Eng.* **2012**, *2012*, 1–9, doi:10.5402/2012/516461.
44. Cavo, M.; Fato, M.; Peñuela, L.; Beltrame, F.; Raiteri, R.; Scaglione, S. Microenvironment complexity and matrix stiffness regulate breast cancer cell activity in a 3D in vitro model. *Sci. Rep.* **2016**, *6*, 35367, doi:10.1038/srep35367.
45. Rowe, S.L.; Lee, S.Y.; Stegemann, J.P. Influence of thrombin concentration on the mechanical and morphological properties of cell-seeded fibrin hydrogels. *Acta Biomater.* **2007**, *3*, 59–67, doi:10.1016/j.actbio.2006.08.006.
46. Vedadghavami, A.; Minooei, F.; Mohammadi, M.H.; Khetani, S.; Kolahchi, A.R.; Mashayekhan, S.; Sanati-Nezhad, A. Manufacturing of hydrogel biomaterials with controlled mechanical properties for tissue engineering applications. *Acta Biomater.* **2017**, *62*, 42–63, doi:10.1016/j.actbio.2017.07.028.
47. Gillentine, M.A.; Berry, L.N.; Goin-Kochel, R.P.; Ali, M.A.; Ge, J.; Guffey, D.; Rosenfeld, J.A.; Hannig, V.; Bader, P.; Proud, M.; Shinawi, M.; et al. 3D microvascular model recapitulates the diffuse large B-cell lymphoma tumor microenvironment in vitro. *J. Autism Dev. Disord.* **2017**, *47*, 549–562, doi:10.1097/CCM.0b013e31823da96d.Hydrogen.



48. Ma, S.; Fu, A.; Chiew, G.G.Y.; Luo, K.Q. Hemodynamic shear stress stimulates migration and extravasation of tumor cells by elevating cellular oxidative level. *Cancer Lett.* **2017**, *388*, 239–248, doi:10.1016/j.canlet.2016.12.001.
49. Ahmed, T.A.E.; Dare, E.V.; Hincke, M. Fibrin: A Versatile Scaffold for Tissue Engineering Applications. *Tissue Eng. Part B Rev.* **2008**, *14*, 199–215, doi:10.1089/ten.teb.2007.0435.
50. Spicer, P.P.; Mikos, A.G. Fibrin glue as a drug delivery system. *J. Control. Release* **2010**, *148*, 49–55, doi:10.1016/j.jconrel.2010.06.025.
51. Soltani, M.; Chen, P. Effect of tumor shape and size on drug delivery to solid tumors. *J. Biol. Eng.* **2012**, *6*, 4, doi:10.1186/1754-1611-6-4.
52. Cuchiara, M.P.; Allen, A.C.B.; Chen, T.M.; Miller, J.S.; West, J.L. Multilayer microfluidic PEGDA hydrogels. *Biomaterials* **2010**, *31*, 5491–5497, doi:10.1016/j.biomaterials.2010.03.031.
53. Malda, J.; Rouwkema, J.; Martens, D.E.; Le Comte, E.P.; Kooy, F.K.; Tramper, J.; Van Blitterswijk, C.A.; Riesle, J. Oxygen gradients in tissue-engineered Pegt/Pbt cartilaginous constructs: Measurement and modeling. *Biotechnol. Bioeng.* **2004**, *86*, 9–18, doi:10.1002/bit.20038.
54. Meng, F.; Meyer, C.M.; Joung, D.; Vallera, D.A.; McAlpine, M.C.; Panoskaltsis-Mortari, A. 3D Bioprinted In Vitro Metastatic Models via Reconstruction of Tumor Microenvironments. *Adv. Mater.* **2019**, *31*, e1806899, doi:10.1002/adma.201806899.
55. Bogorad, M.I.; DeStefano, J.; Karlsson, J.; Wong, A.D.; Gerecht, S.; Searson, P.C. Review: In vitro microvessel models. *Lab Chip* **2015**, *15*, 4242–4255, doi:10.1039/c5lc00832h.

## 5.7 Acknowledgements

This work has been developed in collaboration with: Chiara Vitale, Alessandra Marrella, Gabriele Varani, Silvia Scaglione, Marco Massimo Fato.

# Chapter 6

## High blood flow shear stress values are associated with circulating tumor cells cluster disaggregation in a multi-channel microfluidic device

### 6.2 Abstract

Metastasis is a complex process that involves the spread of tumor cells through the bloodstream. These circulating tumor cells (CTCs) can exist as single cells or clusters, and the latter have a higher potential to cause metastasis. However, the effects of physical constraints such as hemodynamic wall shear stress (WSS) on CTC clusters are not well understood. To investigate this, a new multichannel microfluidic device was developed that can replicate different WSS levels characteristic of the human circulatory system. Three physiological WSS levels (i.e. 2, 5, 20 dyn/cm<sup>2</sup>) were generated to simulate the conditions of capillaries, veins, and arteries. The device was validated using triple-negative breast cancer cells (MDA-MB-231) injected as single CTCs, which showed that higher WSS values led to decreased viability. Computational simulations were also used to investigate the disaggregation of CTC clusters under different WSS levels. Finally, CTC clusters were injected into the three different circuits and subjected to the different WSS levels, showing that higher WSS levels led to increased cluster disaggregation after 6 hours. These findings suggest that the microfluidic device represents a valuable in vitro tool for studying the biological significance of blood flow mechanical forces and developing new strategies for anticancer therapy.

### 6.3 Introduction

Cancer metastasis is a biologically complex tumor dissemination process associated with a poor survival rate. During this process, circulating tumor cells (CTCs) detach from a primary tumor and exploit the physiological blood circulation to give origin to metastases at secondary sites [1,2]. In particular, cancer cell motility enables their invasion into the blood vessels, in a phase known as intravasation, to then flow through the circulatory system up to reach localized and distant sites [3,4]. Although CTCs are present in the blood of oncologic patients, the amount of these cells is very low if compared with other cells like blood cells or leukocytes [5,6]. In particular, CTCs flow the bloodstream as single cells or as multicellular aggregates (CTC clusters), which present with a higher potential to metastasize [7]. Specifically, when transported in fluids, single CTCs and CTC clusters are subjected to various fluid-dynamic forces affecting cell death or extravasation [8]. Therefore, different studies have recently investigated the role of the bloodstream on the CTCs survival and aggressiveness to better understand the metastatic cascade and to identify more effective therapeutic approaches [9–11]. In particular, physical blood parameters, including pressure, fluid velocity and shear stress, may affect the morphology, the expression of specific biomarkers and aggressiveness of CTCs [12,13]. The tumor vasculature is capillary-based with a very low fluid flow velocity, where CTCs are subjected to mild SS (10–20 dyn/cm<sup>2</sup>),

mostly due to the small section of the blood capillary. As they are transported far from the primary site, some CTCs flow through the arterial and venous system, where they encounter higher SS (4–30 dyn/cm<sup>2</sup>) and lower SS (1–4 dyn/cm<sup>2</sup>), respectively [8]. How individual CTCs and CTC clusters can withstand fluidical stimuli and survive in their way in the circulatory system is not yet fully elucidated. Mathematical models and computational fluid-dynamics (CFD) analysis based on physical principles can be extremely useful for investigating single CTCs and CTC clusters behavior in the vascular microenvironment. In fact, the use of algorithms opens a wide range of scenarios for modeling biological processes and optimizing the performance of device and materials conceived to interact with biological tissues [14,15]. Moreover, CFD analysis together with experimental data may allow to predict how cellular networks and systems respond to changes in their environment and therefore can help in defining which parameters affect their activity [16,17]. Indeed, a computational-experimental approach has recently elucidated the influence of cellular biophysical properties on hemodynamic deformation and margination of CTC aggregates within the bloodstream, successfully highlighting the fluid dynamics contribution during the CTCs dissemination [18,19]. In this scenario, in vitro microfluidic systems have been emerged paving the way towards novel in vitro cell-culture formats able to better reproduce the fluid-dynamical features of the cancer environment [20,21]. In fact, although in vivo models are more physiological, they still present some experimental limitations [22]. In particular, it is difficult to in vivo independently capture the effects of individual microenvironmental variables (i.e. rigidity of the ECM matrix, bio-mechanical features of the blood vessels, blood fluid-dynamical proprieties) on the development of biological processes and extract quantitative data [23–27]. The advances in microfluidic technologies enabled in vitro modelling of tumor-related biophysical factors affecting different cell types [28–30]. Moreover, it was already shown that SS is one of the prominent physical stimuli that alters the cancer cells motility and migration, the adhesion capacity and the viability and cluster activity of CTCs within the bloodstream [31–35]. However, to date, most of the systems aimed to study in vitro the effects of fluidic stimuli (such as SS) in vitro on tumor cells are based on rudimental single-channel fluidic systems connected to a peristaltic pump or systems based on needles connected to syringe pumps, where it is possible to get different SS values, by changing the flow rate at the pump level for each experimental condition [10,11,36]. In this work, we have designed and realized a novel microfluidic device able to simultaneously reproduce different hemodynamic WSS in the same experiment, thanks to a specific design based on increasing levels of vessels ramifications, finally reducing biological (experimental) variability. To fabricate the 3D vessels interconnections, 3D printed technology was adopted to produce a 3D master with the desired fluidic pattern. Polydimethylsiloxane (PDMS) was then molded against the sacrificial 3D printed template, thus obtaining microfluidic PDMS channels, difficult to achieve through standard soft lithography. We then examined the effects of different WSS on circulating metastatic breast cancer cells (MDA-MB-231) as single cells and as clusters of cells, respectively, by injecting a cells suspension in the microfluidic device. This system can be further used to analyze the drug efficacy towards CTCs in circulation as well as to improve a deeper understanding of which factors allow single CTCs and CTC clusters to survive in the bloodstream, with the ultimate goal to design next generation therapies against the metastatic spread of cancer.

## **6.4 Materials and Methods**

### **6.5.1 Theoretical and CFD analysis**

Firstly, a theoretical model, based on the Continuity law and energy balance, was developed to reproduce different shear stress values within the device. In particular, different levels of

ramifications were designed in order to obtain multiple shear stress in three distinct circuits by setting a unique inlet flow rate at the level of the pump. The theoretical model is based on the hypothesis of i) laminar flow within vessels, i.e. channels, with rectangular geometry and with the same length; ii) the cells are dispersed in a medium similar to water as Newtonian fluid. It was then possible to calculate the number of ramifications for each circuit to get the proper wall shear stress (WSS) by following (1):

$$\frac{Q^{in}}{n} = \frac{\tau B H^2}{6\mu} \quad (1)$$

where  $Q^{in}$  is the inlet flow rate at the pump level,  $\tau$  is the WSS in the vessels,  $B$  and  $H$  the height and width of vessels, respectively,  $\mu$  is the water dynamic viscosity,  $n$  the number of vessels. Thanks to this equation it is possible to design the proper number of ramifications for each circuit to obtain the desired range of shear stress within the device, by setting a unique flow rate at the pump level. Since we wanted to reproduce the range of physiological shear stresses at the different vascular tree districts ranging from is 1–20 dyn/cm<sup>2</sup>, three independent set of branches were designed to reproduce the following different levels of WSS: 2-5-20 dyn/cm<sup>2</sup>. The obtained geometry was designed through a commercial software. The fluid was assumed to be incompressible and in laminar flow regime, therefore the fluid dynamics within the circuit was modelled by using the Laminar Fluid Flow module of Comsol Multiphysics 5.5. The equations solved are the Navier-Stokes ones for conservation of momentum (2) and the continuity one for conservation of mass (3):

$$\begin{cases} \rho \left[ \frac{\partial \mathbf{u}_f}{\partial t} + \mathbf{u}_f \times (\nabla \mathbf{u}_f) \right] = -\nabla p + \mu (\nabla^2 \mathbf{u}_f) & (2) \\ (\nabla \times \mathbf{u}_f) = 0 & (3) \end{cases}$$

where  $u$  is the velocity in the vessels and  $p$  the pressure across the circuit. The density  $\rho$  and dynamic viscosity  $\mu$  values were specified for water at room temperature (25°C). As initial conditions, the velocity field and the pressure were considered null. No-slip boundary condition was fixed because there is no flow across the device walls. An inflow laminar rate equal to 30 ml/min was set as inlet for each of the three circuits, whereas an atmospheric pressure condition with no backflow was chosen as outlet. Since the steady state flow is reached almost instantaneously (~0.005 s to ~0.01 seconds) for flow rates range between 24–36 ml/min, we considered only a steady state analysis avoiding transient laminar flow simulations. An iterative geometric multigrid (GMRES) algorithm was used to solve the equations for the steady-state condition.

## 6.5.2 Microfluidic device fabrication

### 6.4.2.1 3D printing of the masters

The device negative masters were designed through the Computer-Aided Drafting (CAD) software Sketchup 2016, accordingly with the theoretical and CFD analysis described above. The 3D masters were printed with a biocompatible photopolymer resin (Dental LT Resin) by using a 3D-printer (Form2, Formlabs) with a resolution of 100  $\mu$ m. After printing, the masters were washed with isopropyl alcohol for 10 minutes and then photo-cured through UV light for 20 minutes in order to eliminate resin residues and to optimize the photo-crosslinking process, respectively. Then, a silanization treatment was performed to facilitate the successive rapid removal of PDMS replicas from the masters during the replica molding (REM) phase [15]. Briefly, it consists in an oxygen plasma treatment for 240 seconds with 50 W (Tucano plasma reactor Gambetti Kenologia) and in the vapor phase deposition ( $p = 30$  kPa) for 30 minutes of trichloro(1H,1H,2H,2H-perfluorooctyl)silane (FOTS) antiadhesive agent (Sigma-Aldrich).

#### 6.4.2.2 PDMS molding

Positive replicas were fabricated in PDMS (Sylgard® 184 Silicone Elastomer Kit, Dow Corning) by curing the pre-polymer (a mixture of 10/1 w/w base and the curing agent) on the printed masters at 60°C for 2 hours, accordingly with the previously described protocol [16]. The PDMS mold was removed from the printed master by manually peeling it off (demolding). This procedure resulted in replicas with intruded and top-opened channels with rectangular cross-sectional geometry, as a result of the negative 3D-printed master. The patterned replica was bonded to a PDMS flat layer (i.e. a closing layer of 175 mm x 70 mm x 1 mm in size), that was previously fabricated by casting and curing PDMS pre-polymer in a proper plastic master fabricated by standard stereolithography. Both masters were then reused without additional cleaning processes. Once demolded, both the fabricated PDMS layers were irreversibly sealed together, resulting in a final polymer device. In details, the sealing procedure is the following. Firstly, a pre-polymer film was deposited directly on a 200 mm x 200 mm glass plate, with a thickness lower than 50 µm. Then, the patterned replica and coated glass were arranged to allow a fast inking contact (5 minutes) between the open-side of the replica's channels and the film. Successively, the replica was manually detached from the coated glass and exposed to partial curing at 60°C for no more than 5–8 minutes, obtaining a sticky side. Then, the sticky layer was placed in contact with the closing layer and bonded together by curing in oven at 60°C for 30 minutes. Finally, the plastic tubes of the circuit were connected to the holes at the extremities of the channel and permanently sealed by applying the pre-polymer at the interfaces, and by curing it at 60 °C for 30 minutes to fix the connection.

#### 6.4.2.3 Hydrophilic treatments

To make a hydrophilic surface layer on PDMS, the native PDMS surfaces were modified by oxidation. The oxidation process was firstly performed by plasma oxidation, placing the assembled PDMS device in the oxygen plasma chamber for 120 seconds with 50 W [17], and then by exposure to an oxidizing solution of H<sub>2</sub>O:HCl:H<sub>2</sub>O<sub>2</sub> (in a volume ratio of 1:1:5) [20]. The PDMS channels were filled with this solution and maintained for 10 minutes at 70°C, followed by two washes in DI-water, thus resulting in a hydrophilic silanol-covered (Si-OH) PDMS surface. Since in contact with air the PDMS surface reverts to hydrophobic, the oxidized channels' surfaces were treated with a silanization solution of 5% 3-aminopropyltriethoxysilane (APTES, Sigma-Aldrich) for 20 minutes at 80°C, followed by an EtOH rinse to remove the unreacted APTES. The fluidic device was then baked at 80°C for 30 minutes in an oven, followed by rinsing with a 1X-PBS (ThermoFisher Scientific) solution for 5 minutes. After this procedure, the channels' surface results in amino-grafted PDMS and glass-like surfaces that remain stable over time [21].

#### 6.4.2.4 Morphological analysis of the device

The PDMS patterned replicas were analyzed under an upright epifluorescence microscope (BX51, Olympus) to detect that no cracks were formed along channels during the PDMS removal process. The optically transparent PDMS device enabled independent channel defect or leakage verification using dispensed a dye consisted of 1% methylene blue (Alfa Aesar) in deionized water.

#### 6.4.2.5 Metastatic breast cancer cells circulation

The device was sterilized in ethanol 70% v/v for 30 minutes followed by rinsing with sterile DI water and connected to a syringe pump (Harvard apparatus PHD2000) using connectors (Biorad) and Tygon tubes (i.d = 1 mm). To reduce the cell adhesion to the inner surface of

the tubes, these were treated with 1% Pluronic F-127 (Sigma Aldrich) for 30 minutes. MDA-MB-231 cells (from breast adenocarcinoma) were expanded in Roswell Park Memorial Institute medium (RPMI) enriched with 10% Fetal Bovine Serum (FBS), 1% L-glutamine and 1% penicillin/streptomycin (all from Sigma Aldrich). The culture media was changed twice a week. At confluence, cells were enzymatically detached with 0.05% trypsin, counted and injected within the three different circuits, with a 21G needle, at a density of  $2 \times 10^5$  cells/ml. The syringe pump flow rate was set at 30 ml/min to reproduce the different WSS values. Cells cultured over non-adhesive surfaces were used as static control.

#### 6.4.2.6 Cell viability analysis of recovered cells

MDA-MB-231 viability after circulation within the device was evaluated through a live/dead assay (Sigma Aldrich). Briefly, after 6 hours of culture the same volume of cells from different circuits was placed in 96-well plates. Cells were allowed to adhere for 24 hours, were washed with PBS and incubated in 2 mM calcein AM and in 4 mM EthD-1 in PBS for 15 minutes at 37°C in a dark environment, to detect live and dead cells, respectively. Cells were washed three times in PBS. Positivity to either staining solution was observed by means of fluorescence microscopy (Nikon H550L). Viable cells were counted by using Image J® software from binarized images. In particular, cells positive to calcein were assessed through image post-processing of binarized images, by calculating the number of cells present in the green channel.

#### 6.4.2.7 CFD analysis of cell clusters disaggregation

The hemodynamic disaggregation of CTC clusters due to the blood flow-associated forces was simulated, by considering three different physiological WSS values (2-5-20 dyn/cm<sup>2</sup>). Each cluster circulating in the vascular system was assumed as a fluid with physical properties, such as density, dynamic viscosity, etc., equal to those typical of the clusters. In particular, the values were set considering the spatial average values of the cluster. Thus, the clusters motion and disaggregation within the blood vessels were simulated by considering the flow of two different immiscible fluids, one representing the blood and the other one representing the clusters. Accordingly, a two-phase flow model was set up by combining the Laminar Fluid Flow module with the Level Set one of Comsol Multiphysics 5.5, following a computational approach recently proposed and adopted by Phillips and colleagues [37]. In fact, the level-set method was used to track moving interfaces in fluid flows models taking into account differences in fluids densities and viscosities, and also including the effects of surface tension, by solving the transport equation for the level set function  $\phi$  (4):

$$\frac{\partial \phi}{\partial t} + \mathbf{u} \cdot \nabla \phi = \gamma \nabla \cdot \left( \varepsilon \nabla \phi - \phi (1 - \phi) \frac{\nabla \phi}{|\nabla \phi|} \right) \quad (4)$$

where  $\gamma$  is a reinitialization parameter, set to the maximum expected velocity magnitude, and  $\varepsilon$  the interface thickness controlling parameter, set to  $h_{\max}/2$  where  $h_{\max}$  is the maximum element size in the component. Since the velocity field is not divergent, a conservative level set method was adopted because it perfectly conserves the mass of each fluid, even if the computational time is longer. Moreover, in most level-set methods the right-hand side of (4) is zero, but in the current method it was necessarily filled to keep numerical stability and interface thickness [38]. The auxiliary function  $\phi$  (5) varies smoothly from 0 (fluid 1) to 1 (fluid 2), passing through the interface where it is equal to 0.5.

$$\phi = \begin{cases} < 0.5 & \text{water (fluid 1)} \\ 0.5 & \text{interface} \\ > 0.5 & \text{cluster (fluid 2)} \end{cases} \quad (5)$$

Finally, the incompressible formulation of the Navier-Stokes equation solved for the laminar flow regime becomes:

$$\rho \left( \frac{\partial \mathbf{u}}{\partial t} + \mathbf{u} \cdot \nabla \mathbf{u} \right) = \nabla \cdot [-p\mathbf{I} + \mu(\nabla \mathbf{u} + \nabla \mathbf{u}^T)] + \mathbf{F}_{st}, \quad (6)$$

where  $\rho$  is the density,  $\mu$  the dynamic viscosity and  $\mathbf{F}_{st}$  the surface tension force, which allows the model to incorporate the cluster deformability, defined as:

$$\mathbf{F}_{st} = \sigma \delta k \mathbf{n} + \delta \nabla_s \sigma, \quad (7)$$

where  $\sigma$  is the surface tension coefficient,  $\mathbf{n}$  the normal to the interface and  $k$  the curvature:

$$k = -\nabla \cdot \mathbf{n}, \quad (8)$$

$\delta$  a Dirac delta function located at the interface and  $\nabla_s$  the surface gradient operator:

$$\nabla_s = (\mathbf{I} - \mathbf{n}\mathbf{n}^T)\nabla. \quad (9)$$

The density is a function of  $\rho_1$  (1000 kg/m<sup>3</sup>) and  $\rho_2$  (1500 kg/m<sup>3</sup>) [39], densities of fluid 1 and fluid 2 respectively, defined as:

$$\rho = \rho_1 + (\rho_2 - \rho_1) \phi, \quad (10)$$

whereas, the dynamic viscosity, also depending on  $\phi$ , is a function of  $\mu_1$  (0.001 Pa·s) and  $\mu_2$  (1.36 Pa·s) [37], dynamic viscosities of fluid 1 and fluid 2 respectively, given by:

$$\mu = \mu_1 + (\mu_2 - \mu_1) \phi. \quad (11)$$

As initial conditions the velocity field and the pressure of each fluid were considered null, whereas a no-slip condition for boundaries was fixed. The computational domain was designed to reproduce a single device channel characterized by rectangular shape with 1 mm of width and 120 mm in length. To avoid high computational timing, the geometry was implemented in two dimensions. In order to obtain the three different levels of WSS within the channels (2-5-20 dyn/cm<sup>2</sup>), at inlet an inflow laminar rate was set to 2-5-20 ml/min respectively (1). A user-defined unstructured triangular mesh was used. In particular, an interface refinement and a boundary layers elements densification were performed by splitting them. Finally, in order to automatically initialize the level-set variable, a Phase Initialization study was performed and then a Time Dependent step was implemented, since the position of an interface always depends on its history.

#### 6.4.2.8 Experimental analysis of cell clusters disaggregation

Clusters of MDA-MB-231 were generated by detaching 80%-confluent monolayer of cells with trypsin for 1 minute. Clustered MDA-MB-231 were then counted and injected within the three different circuits, with a 21 G needle, at a density of  $1 \times 10^3$  clusters/ml. The same needle was used to add the clusters suspension in a non-adhesive 96-well plate as static control. The same procedure was also performed to remove the clusters from the device and the non-adhesive static control after 6 hours of circulation. Samples were then observed under the microscope. Images obtained by an optical microscopy were analyzed through ImageJ® software, to quantify morphological features of the clusters after circulation. In particular, the following morphological parameters were measured: cluster size, defined as the diameter of the cluster calculated as the average between the major and minor axis length; cluster area; circularity, defined as  $4\pi \text{area}/\text{perimeter}^2$ ; and perimeter. Quantification of the clusters diameter, area, circularity and perimeter was performed with ImageJ® on thresholded images through a semiautomatic image postprocessing of binarized images. Within each experiment, the same threshold was used for all the conditions.

## 6.5 Results

### 6.5.1 Theoretical and CFD analysis

Three distinct circuits composed by ramified vessels have been designed within the device to simultaneously and independently reproduce three different levels of WSS, resembling the human vascular system. Based on the theoretical mathematical model, the number of designed ramifications is 10 for the first circuit, 2 for the second circuit, and 1 for the third one (Figure 31), to obtain with a unique flow rate the desired physiological WSS values of 2, 5, 20 dyn/cm<sup>2</sup>, corresponding to those present in veins, arteries and capillaries.

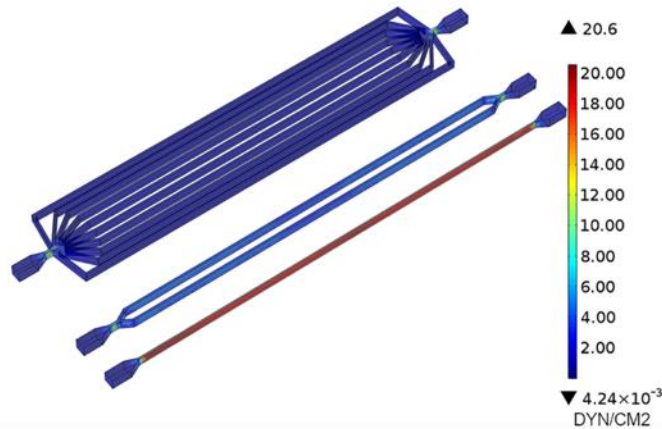


Figure 31: SS profiles of the fluid flows. SS profiles of the fluid flow within the channels with an inflow rate of 30 ml/min.

To predict the fluid dynamics within the circuits, a computational analysis of the fluid dynamics within the device was performed, and the WSS values within the microfluidic vessels evaluated. Figure 31 reports the different WSS values at the three levels of ramifications. The figure shows that the desired values of WSS are obtained by setting at inlet the same flow rate at 30 ml/min, as anticipated by the theoretical model. Table 12 reports the shear stress in the microfluidic vessels for the flow rate tested in this work. The shear stress values obtained from the simulations are close to the ones predicted with the theoretical model, showing the good reliability of the model.

Table 12: Wall Shear stress within three different ramifications.

N of ramifications	WSS [dyn/cm <sup>2</sup> ]
1	20±0.03
2	5±0.02
10	2±0.18

Wall shear stress within three different ramifications when a 30ml/min flow rate was applied.

## 6.5.2 Device Fabrication

The fluidic system was composed of different parts: the PDMS micro-channel device; plastic tubes physically connected to the device which allows cells circulation; a syringe pump which drives the fluid flow. To simultaneously reproduce different hemodynamic WSS on a single device, the microfluidic device developed in this study comprises three independent circuits composed of ramifications of channels connected respectively to three inlets and three outlets. The specific pattern of three independent circuits—composed of ramifications of channels connected respectively to three inlets and three outlets was designed according to the theoretical and CFD analysis. We utilized a procedure based on 3D-printing and soft-



lithography techniques to fabricate the flow circuits in PDMS (Figure 32), ensuring a well-defined size and shape of channels with optical transparency (down to 280 nm).

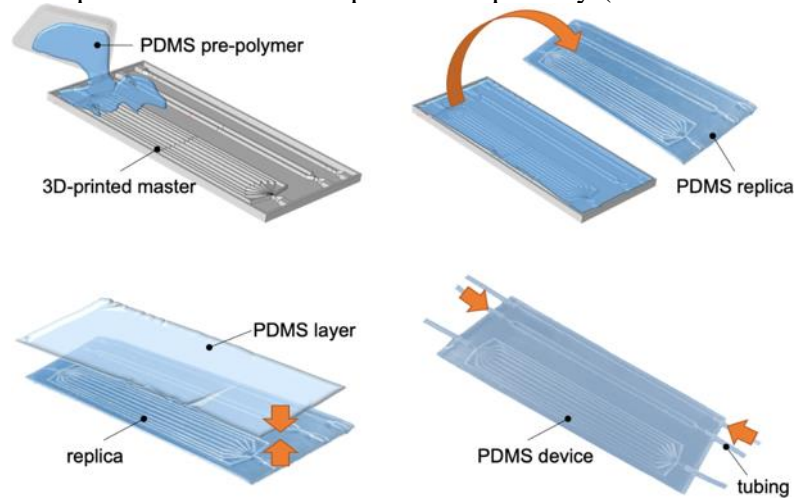


Figure 32: PDMS device fabrication process. Schematic representation of the fabrication process of the device.

In particular, after the designing step, the channels pattern was converted into 3D-printing code and printed under precise digital control as a solid polymeric three-dimensional master (Figure 32). The master contained extruded tube-shaped structures of rectangular cross-section with  $1\text{ mm} \times 3\text{ mm}$  in size and 120 mm in length. The device was then realized in PDMS by curing the pre-polymer on the printed template, then the PDMS mold was removed from the printed masters by manually peeling it off. After completing this reliable manufacture process, a fluidic device ( $175\text{ mm} \times 70\text{ mm} \times 4.5\text{ mm}$ ) was realized in PDMS (Figure 33A), to guarantee low cost, biocompatibility, gas-permeability and robustness. In particular, the channels were deep 3 mm to avoid their collapse during fabrication.

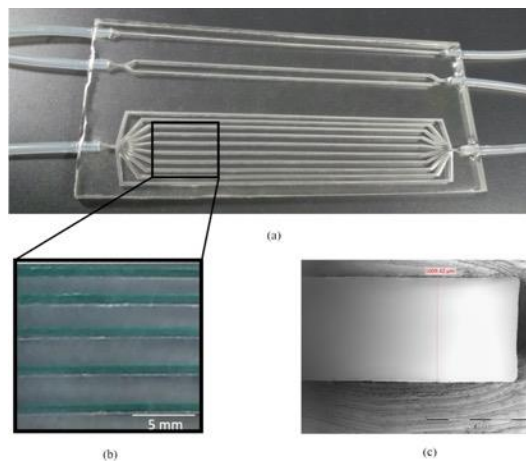


Figure 33: PDMS multi-channel device. Pictures showing (a) the 3D fluidic PDMS device with different ramifications of channels, inlets/outlets are permanently connected to tubes, (b) the same channels filled with a blue dye to demonstrate absence of leakage and (c) the cross-section of a PDMS channel.

Before and after sealing, we analyzed the integrity of the channels by injecting methylene blue and observing under an upright epifluorescence microscope. No entrance of methylene blue dye was observed into the walls of channels and the seal areas (Figure 33B). A cross-section of the channels made in PDMS after removal from the mold was evaluated (Figure 33C) and show the successful realization of 1mm wide channels.

### 6.5.3 Cell viability

MDA-MB-231 cells were cultured within the fluidic device to validate the system and analyze the effects of WSS on CTC viability. After 6 hours of circulation within the device, the cells were collected and re-plated in multi-well plates. Image post processing was performed to quantify the number of viable cells. Cell viability was inferred from the number of green (viable) cells for each sample, respectively to the number of viable cells in the static control. The fluorescent micrographs showed that a low WSS (2 dyn/cm<sup>2</sup>) didn't significantly affect cell viability, being most of the cells alive and thus able to adhere unto plastic surfaces, compared to the static control. Moreover, results showed that high WSS affected cell survival: in particular, after 6 hours of circulation at 20 dyn/cm<sup>2</sup> the cells recovered and adhered in multiwells were less in number, as effect of a reduced viability (Figure 34).

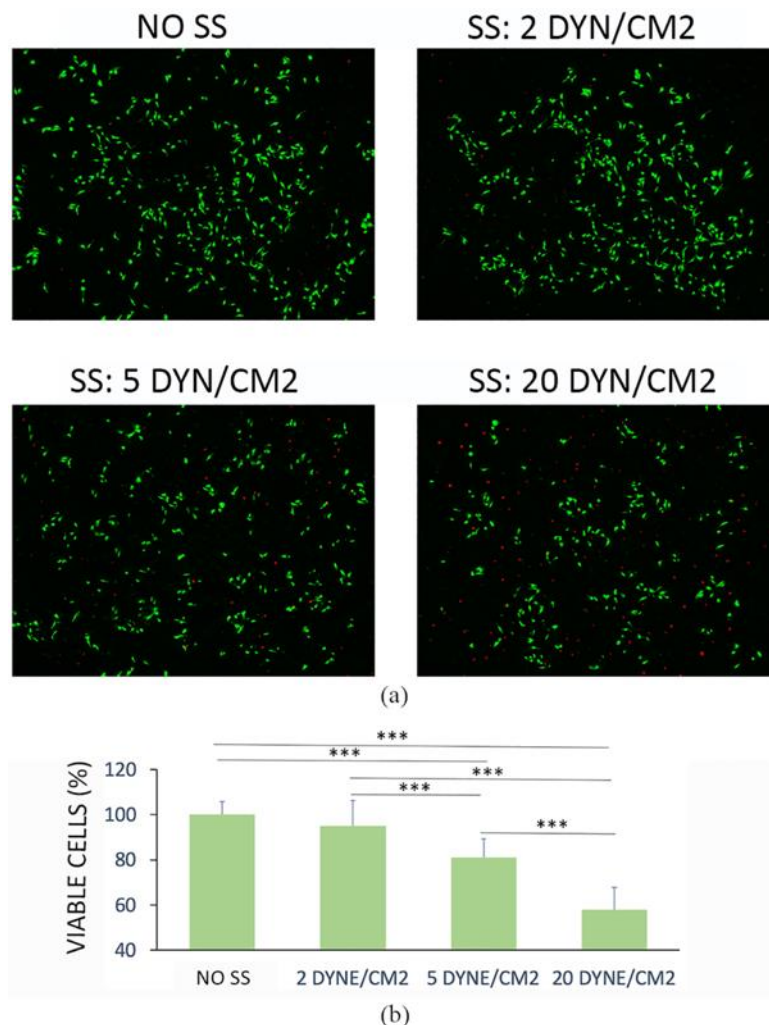


Figure 34: Cell viability. (a) Cell viability measured by live/dead staining of cells replated after 6 hours of circulation (b) Quantitative analysis of the images. Values are reported as mean  $\pm$  s.d.,  $N = 4$ . Student's  $t$ -test. \*\*\* $P < 0.001$ .

### 6.5.4 Cell clusters CFD simulations

To reproduce CTC clusters disaggregation, depending on the WSS level experienced by the clustered cells, mathematical simulations were performed in a two-dimensional (2D) domain mimicking a single micro-channel of the device. Therefore, three different physiological-

relevant WSS conditions (2, 5, 20 dyn/cm<sup>2</sup>) were investigated. Since each cluster was represented by a fluid, we implemented a two-phase flow model by using Comsol Multiphysics 5.5. Figure 35 shows the different SS effects on CTC clusters. In particular, based on the simulations, increasing SS levels should induce a major cluster disaggregation. Under a WSS equal to 20 dyn/cm<sup>2</sup>, the clusters disaggregation gives origin to bigger newly derived clusters, thus highly reducing their original size; while when the WSS is lower (5 dyn/cm<sup>2</sup>), smaller derived aggregates are observed. Moreover, no significant differences can be noticed between the 2 dyn/cm<sup>2</sup> condition and the control one (no SS).

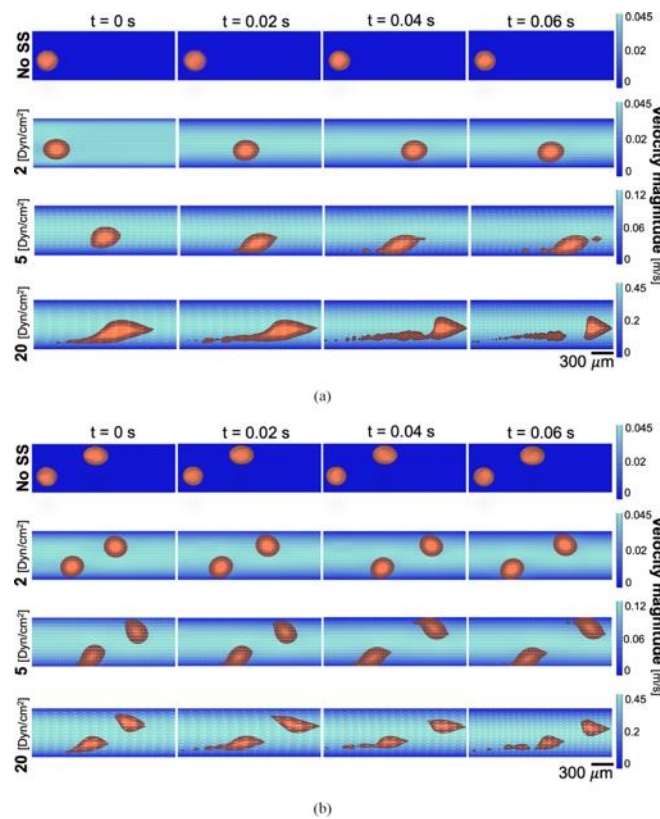


Figure 35: CTC clusters disaggregation. Fluid-dynamic simulation of CTC clusters disaggregation process under fluid flow with (A) one and (B) two clusters circulating. Clusters shape inside the vessel is reported at different time points:  $t = 0, 0.02, 0.04$  and  $0.06$  s.

Furthermore, it can be observed how the clusters align along the flow direction to decrease their hydrodynamic resistance in the first instants of experiment simulated (Figure 35). In addition, such mechanism is more evident as SS raises. In a recent study, this process was experimentally observed in human CTC clusters in xeno-transplanted zebrafish, where CTC clusters reduced their flow resistance by reorganizing into single-file chain-like clusters [40].

### 6.5.5 Cell clusters experimental analysis

The here proposed fluidic device was adopted also to culture tumor cell clusters, for resembling the in vivo pathological conditions. To this aim, the role of WSS on cluster disaggregation was also experimentally investigated. Higher WSS levels increased the disaggregation of cell clusters recovered after 6 hours of circulation, as predicted by the CFD analysis (Figure 36). At low WSS (2 dyn/cm<sup>2</sup>) a poor reduction of cluster size was observed. At high WSS (20 dyn/cm<sup>2</sup>) very few and small clusters were observed and recovered.

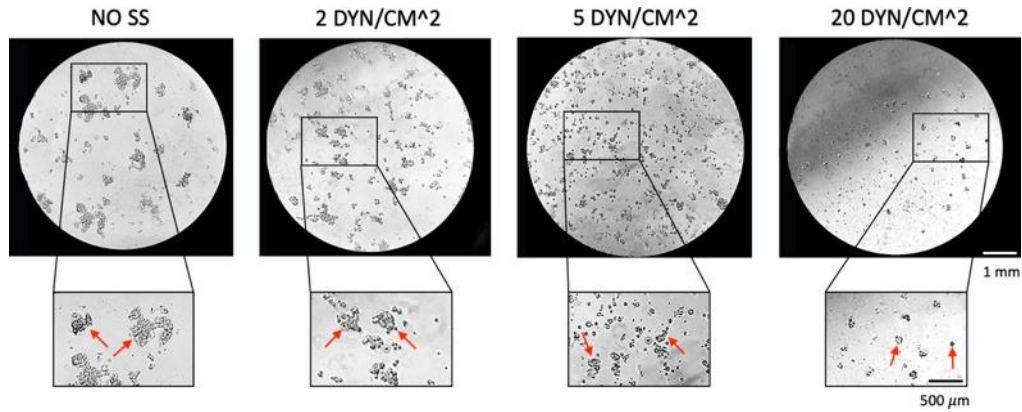


Figure 36: Clusters size reduction at different shear stress levels. Clusters size reduction after 6 hours of circulation at different shear stress.

Clusters size, area, perimeter and circularity after circulation at different SS were quantified through image post processing (Figure 37). It was found that after 6 hours of circulation at 20 dyn/cm<sup>2</sup> there was a significant reduction of the clusters size up to reach a reduction of about 70% respect to the static control. Moreover, the clusters area and perimeter decrease by incrementing the values of SS confirming that higher values of SS were able to increasingly disaggregate the CTC clusters.

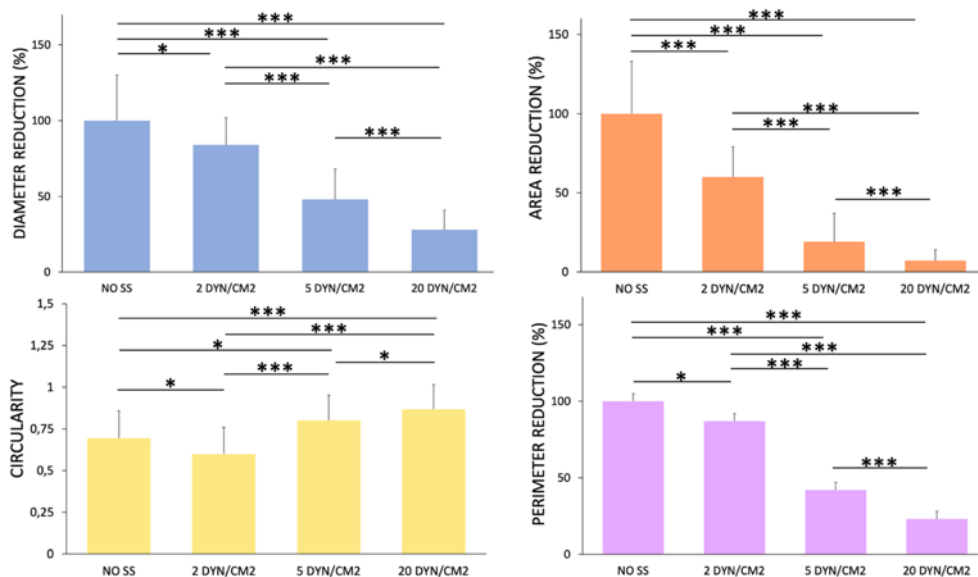


Figure 37: Quantitative analysis of the CTC clusters images. Values are reported as mean  $\pm$  s.d.,  $N = 4$ . Student's  $t$ -test. \*  $P < 0.05$ ; \*\*\*  $P < 0.001$ .

Interestingly, it can be observed a reduction of circularity after 6 hours of culture for 2 dyn/cm<sup>2</sup>, indicating a kind of cluster elongation for low values of WSS, while smaller clusters ( $WSS > 2$  dyn/cm<sup>2</sup>) were characterized by a higher circularity and rounded shape.

## 6.6 Discussion

In the present work a micro-fluidic device able to simultaneously reproduce different physiological SS was designed and fabricated. During the first phase, theoretical and CFD models were respectively implemented. They allowed the design of three independent circuits composed by a set number of ramified channels. The number of ramifications at

each entry was determined to obtain within the same fluidic device the SS values reached in vivo in capillaries, veins and arteries that together form the blood vessel circulation feeding tissues and organs. In the different anatomical sites of the vascular tree (i.e. capillaries, veins, arteries) shear stress are deeply different, reaching the highest values both in arteries, mostly due to the high flow velocities values close to 100–500 mm/s (8), and in capillaries where blood velocities are 3 orders of magnitude less but the vessel geometrical dimensions are significantly smaller. Therefore, decoupling in vivo the distinctive role of shear stress and velocities on CTCs behavior is still an open issue. For these reasons, we here have developed an alternative in vitro approach aimed to properly tune the number of ramifications for reducing the velocities differences in the three independent circuits, that are within the veins range (10–200 mm/s), and better understanding the role of the shear stresses. The technique adopted for the device fabrication is 3D printing combined with soft-lithography. Although both 3D-printing and the PDMS-molding procedures require individual skill and expertise, they were combined to boost the respective advantages offered by 3D-printing in terms of time efficiency and complexity of the models and by PDMS-molding, due to the superior physico-mechanical properties of PDMS as substrate for microfluidic applications [41]. The fluidic device here fabricated is optically transparent and sufficiently thick to sustain pressures necessary to perform dynamic experiments and, at the same time, to allow microscopic observation. For this application, it was also necessary to make each PDMS channel hydrophilic. since the cell culture medium should easily be injected and flow within the channels. This is challenging, due to the fast hydrophobic recovery of the PDMS surface after modification [42]. We used plasma treatment combined with the exposure to an oxidizing solution, and a coating with APTES aminosilane compound, to provide a hydrophilic functional film covalently bonded to the PDMS surfaces. In fact, such treatment reduces the nonselective adsorption of hydrophobic molecules, which is a typical limit of the hydrophobic nature of PDMS [43]. Among various methods, we opted for this one since it is suitable for a fully bonded fluidic device and ensures hydrophilicity over an extended period of time. As first validation, we tested the viability of CTCs within the device, subjected to the different WSS reproduced. The results obtained are consistent with previous studies reporting a decreasing cell viability along with increased WSS values of stimulation [11,36]. In particular, it was previously shown that MDA-MB-231 cells viability was about 85% and 60% after 4 hours of stimulation with WSS of 15 and 30 dyn/cm<sup>2</sup>, respectively [11]. In this context, the molecular pathway of WSS-mediated apoptosis was clarified by Hope et al. [44]. In particular, they identified mechanosensitive ion channels called Piezo1 as key players in WSS-induced TRAIL-mediated apoptosis of cancer cells (COLO 205 and MDA-MB-231 cell lines), decoding one of the possible WSS-induced mechanism impairing CTCs survival in the bloodstream. Interestingly, in a further study it was also demonstrated that if most of highly aggressive metastatic breast cancer cells were resistant to physiological WSS (15 and 30 dyn/cm<sup>2</sup>), these stimuli could kill non-metastatic breast cancer cells (MCF7) by inducing apoptosis [36]. Moreover, the fluidical stimuli have a role also in the survived CTCs extravasation potential, even if the exact mechanisms are still not fully understood [32,45]. In particular, a recent work reported that cancer cell migration efficacy was 3-fold higher after a fluidic stimulation with a WSS of 15 dyn/cm<sup>2</sup> if compared to a static control group [32]. Along this line, WSS around 15 dyn/cm<sup>2</sup> seemed to promote also metastatic cells adhesion to extracellular matrix and endothelial monolayer. This means that WSS also conditions the effective adhesion of the extravasated tumor cells to a secondary organ with a pro-metastatic effect [33]. Therefore, these studies together with our work suggest a dual role of WSS on CTCs: if it has the capability to kill CTCs in circulation, it is also able to modulate the aggressiveness of the survived cells, fostering their capability to migrate, extravasate and adhere to a metastatic site. Other studies showed the importance

of increasing the level of complexity of the model. In fact, in a recent work authors examined the fluid WSS effects on CTC clusters by realizing a spheroid-based 3D mono and co-culture model formed by prostate cancer cells and cancer associated fibroblasts (CAFs), respectively. They demonstrated that CAFs play a pivotal role in promoting CTC survival and migration during the vascular transport, conferring shear resistance to CTC clusters through heterotypic cell-cell interaction [46]. However, despite recent advances in the understanding of biological features of CTCs, the effects of physiological WSS levels on single and clustered CTCs remain to be investigated. In this context, our device may represent a valid system to study the hydrodynamical effects of the blood flow on human single or aggregated CTCs (Figure 38) and where also different co-cultures or cells derived from metastatic patients can be incorporated and analyzed.

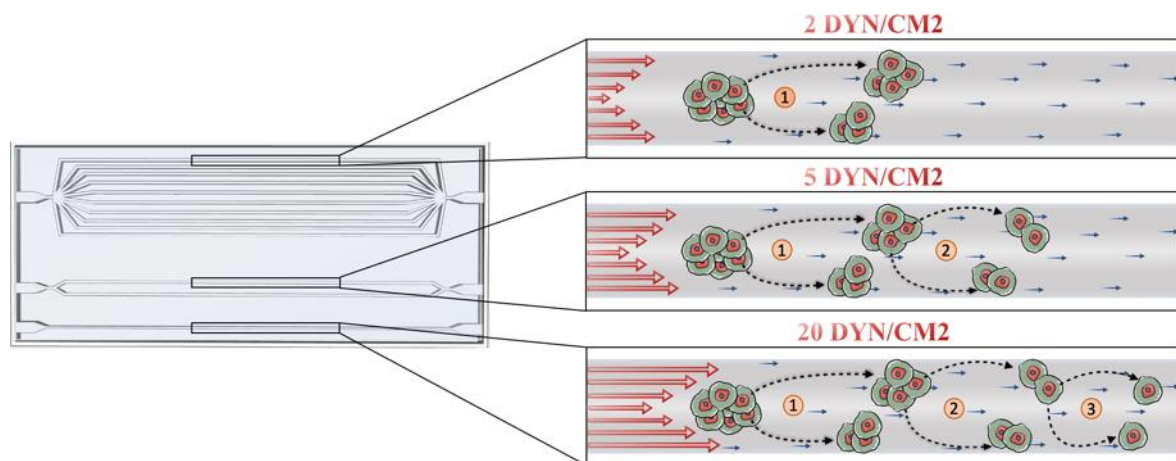


*Figure 38: SS induce CTC clusters disaggregation. Schematic representation of the observed effects of increasing levels of SS on the disaggregation of CTC clusters.*

Furthermore, CFD simulations, based on the laminar two-phase modelling, were coupled to an experimental approach to investigate the hemodynamic disaggregation of CTC clusters in response to different physiologically relevant WSS within the vessels. In the past years, the CTCs and CTC clusters dynamics within the vasculature was modeled with other mathematical models, for example by adopting the analytical Green's function formulation [47], where CTCs are designed as non-deformable particles, or by using the immersed finite element method (IFEM) [18], which takes into account the Young's module of the CTC. However, in this works CTCs were modeled as spheres composed of a simple linear-elastic material and the CTC clusters as aggregations of spheres with a non-deformable structure. Therefore, it was not possible to evaluate the possible CTC clusters morphology changes that can be induced by the blood flow-associated stimuli within the bloodstream, such as the shape reorganization into single-file chain-like geometries that substantially reduce the clusters hydrodynamic resistance [40], by using this computational approach. Hence, in our work, we employed the laminar two-phase modelling, provided by Comsol Multiphysics, following the approach proposed by a recent paper which adopted this method to in silico study the CTC clusters circulation and deformability within the vasculature [37]. In particular, each CTC cluster circulating was assumed as a fluid immiscible with the primary one (i.e. blood) with physical properties, such as density and dynamic viscosity, known from the literature [3,37,39]. Importantly, the two-phase model allowed to take into account the CTC cluster membrane deformability by considering a surface tension at the interface between the two fluids and thus to investigate the CTC cluster deformation, reorganization and disintegration in response to different physiologically relevant WSS. Here, the results suggest that in our model the WSS has a role on the disaggregation of CTC clusters, as

resumed in Figure 35 and experimentally shown in Figure 36. Specifically, MDA-MB-231 clusters were injected within the three independent circuits and their morphology after 6 hours of dynamic culture was observed. In particular, while the clusters size decreases by increasing the values of WSS, an increased circularity of the clusters was observed. This observation can suggest that the cells within the aggregates were subjected to a kind of elongation aligning in the direction of the flow at low WSS, to then disaggregate at higher WSS values assuming the original more rounded conformation. The capability of clusters to modulate their morphology in transit has already been demonstrated [40]. It was shown that clusters act as individual cells in series, which elongate to pass through capillary-size vessels, to then reform into the typical “rounded” organization. Accordingly, from our results it can be hypothesized that at low WSS values (2 dyn/cm<sup>2</sup>) CTC clusters undergo reorganization forming chain-like structures in order to escape to the blood flow-associated forces avoiding the disaggregation process. On contrary, at higher WSS (> 5 dyn/cm<sup>2</sup>) cluster cells disaggregate by assuming their original rounded morphology.

## 6.7 References

1. Reymond N, d’Agua BB, Ridley AJ. Crossing the endothelial barrier during metastasis. *Nat Rev Cancer*. 2013; 13: 858–870. <https://doi.org/10.1038/nrc3628> PMID: 24263189
2. Nguyen DX, Bos PD, Massague J. Metastasis: from dissemination to organ-specific colonization. *Nat Rev Cancer*. 2009; 9: 274–284. <https://doi.org/10.1038/nrc2622> PMID: 19308067
3. Phillips KG, Kuhn P, McCarty OJT. Physical biology in cancer. 2. The physical biology of circulating tumor cells. *Am J Physiol—Cell Physiol*. 2014; 306: 80–88. <https://doi.org/10.1152/ajpcell.00294.2013> PMID: 24133063
4. Friedl P, Alexander S. Cancer invasion and the microenvironment: Plasticity and reciprocity. *Cell*. 2011; 147: 992–1009. <https://doi.org/10.1016/j.cell.2011.11.016> PMID: 22118458
5. Yu M, Stott S, Toner M, Maheswaran S, Haber DA. Circulating tumor cells: approaches to isolation and characterization. *J Cell Biol*. 2011; 192: 373–382. <https://doi.org/10.1083/jcb.201010021> PMID: 21300848
6. Maheswaran S, Haber DA. Circulating tumor cells: a window into cancer biology and metastasis. *Curr Opin Genet Dev*. 2010; 20: 96–99. <https://doi.org/10.1016/j.gde.2009.12.002> PMID: 20071161
7. Aceto N, Bardia A, Miyamoto DT, Donaldson MC, Wittner BS, Spencer JA, et al. Circulating tumor cell clusters are oligoclonal precursors of breast cancer metastasis. *Cell*. 2014; 158: 1110–1122. <https://doi.org/10.1016/j.cell.2014.07.013> PMID: 25171411
8. Follain G, Herrmann D, Harlepp S, Hyenne V, Osmani N, Warren SC, et al. Fluids and their mechanics in tumour transit: shaping metastasis. *Nat Rev Cancer*. 2019; 1–18. <https://doi.org/10.1038/s41568018-0093-5> PMID: 30532011
9. Lee HJ, Diaz MF, Price KM, Ozuna JA, Zhang S, Sevick-Muraca EM, et al. Fluid shear stress activates YAP1 to promote cancer cell motility. *Nat Commun*. 2017; 8: 1–14. <https://doi.org/10.1038/s41467-0160009-6> PMID: 28232747
10. Barnes JM, Nauseef JT, Henry MD. Resistance to fluid shear stress is a conserved biophysical property of malignant cells. *PLoS One*. 2012/12/03. 2012; 7: e50973–e50973. <https://doi.org/10.1371/journal.pone.0050973> PMID: 23226552
11. Regmi S, Fu A, Luo KQ. High shear stresses under exercise condition destroy circulating tumor cells in a microfluidic system. *Sci Rep*. 2017; 7: 1–12. <https://doi.org/10.1038/s41598-016-0028-x> PMID: 28127051
12. Wirtz D, Konstantopoulos K, Searson PC. The physics of cancer: the role of physical interactions and mechanical forces in metastasis. *Nat Rev Cancer*. 2011; 11: 512–522. <https://doi.org/10.1038/nrc3080> PMID: 21701513
13. Levental KR, Yu H, Kass L, Lakins JN, Egeblad M, Erler JT, et al. Matrix crosslinking forces tumor progression by enhancing integrin signaling. *Cell*. 2009; 139: 891–906. <https://doi.org/10.1016/j.cell.2009.10.027> PMID: 19931152
14. Hossain MS, Chen XB, Bergstrom DJ. Investigation of the in vitro culture process for skeletal-tissue engineered constructs using computational fluid dynamics and experimental methods. *J Biomech Eng*. 2012; 134: 1–12. <https://doi.org/10.1115/1.4007952> PMID: 23363205

15. Marrella A, Aiello M, Quarto R, Scaglione S. Chemical and morphological gradient scaffolds to mimic hierarchically complex tissues: From theoretical modeling to their fabrication. *Biotechnol Bioeng.* 2016; 113: 2286–2297. <https://doi.org/10.1002/bit.25994> PMID: 27093435
16. Sung JH, Wang Y, Shuler ML. Strategies for using mathematical modeling approaches to design and interpret multi-organ microphysiological systems (MPS). *APL Bioeng.* 2019; 3: 021501. <https://doi.org/10.1063/1.5097675> PMID: 31263796
17. Mitchell MJ, King MR. Computational and experimental models of cancer cell response to fluid shear stress. *Front Oncol.* 2013;3 MAR: 1–11. <https://doi.org/10.3389/fonc.2013.00003> PMID: 23386995
18. King MR, Phillips KG, Mitrugno A, Lee TR, de Guillebon AME, Chandrasekaran S, et al. A physical sciences network characterization of circulating tumor cell aggregate transport. *Am J Physiol—Cell Physiol.* 2015; 308: C792–C802. <https://doi.org/10.1152/ajpcell.00346.2014> PMID: 25788574
19. Vitale C, Fedi A, Marrella A, Varani G, Fato M, Scaglione S. 3D perfusable hydrogel recapitulating the cancer dynamic environment to in vitro investigate metastatic colonization. *Polymers (Basel).* 2020; 12: 1–19. <https://doi.org/10.3390/polym12112467> PMID: 33114344
20. Sung KE, Beebe DJ. Microfluidic 3D models of cancer. *Adv Drug Deliv Rev.* 2014; 79: 68–78. <https://doi.org/10.1016/j.addr.2014.07.002> PMID: 25017040
21. Yesil-Celiktas O, Hassan S, Miri AK, Maharjan S, Al-kharboosh R, Quiñones-Hinojosa A, et al. Mimicking Human Pathophysiology in Organ-on-Chip Devices. *Adv Biosyst.* 2018; 2: 1–25. <https://doi.org/10.1002/adbi.201800109>
22. Marrella A. 3D fluid-dynamic ovarian cancer model resembling systemic drug administration for efficacy assay. *ALTEX.* 2020; 37: 1–14. <https://doi.org/10.14573/altex.2003131> PMID: 32754773
23. Marrella A, Iafisco M, Adamiano A, Rossi S, Aiello M, Barandalla-Sobrados M, et al. A combined lowfrequency electromagnetic and fluidic stimulation for a controlled drug release from superparamagnetic calcium phosphate nanoparticles: potential application for cardiovascular diseases. *J R Soc Interface.* 2018; 15: 20180236. <https://doi.org/10.1098/rsif.2018.0236> PMID: 29997259
24. Bersini S, Jeon JS, Dubini G, Arrigoni C, Chung S, Charest JL, et al. A microfluidic 3D invitro model for specificity of breast cancer metastasis to bone. *Biomaterials.* 2014; 35: 2454–2461. <https://doi.org/10.1016/j.biomaterials.2013.11.050> PMID: 24388382
25. Marrella A, Giannoni P, Pulsoni I, Quarto R, Raiteri R, Scaglione S. Topographical Features of Graphene-Oxide-Functionalized Substrates Modulate Cancer and Healthy Cell Adhesion Based on the Cell Tissue of Origin. *ACS Appl Mater Interfaces.* 2018; 10: 41978–41985. <https://doi.org/10.1021/acsami.8b15036> PMID: 30479135
26. Marrella A, Dondero A, Aiello M, Casu B, Olive D, Regis S, et al. Cell-laden hydrogel as a clinical-relevant 3D model for analyzing neuroblastoma growth, immunophenotype, and susceptibility to therapies. *Front Immunol.* 2019; 10: 1–15. <https://doi.org/10.3389/fimmu.2019.00001> PMID: 30723466
27. Trujillo-de Santiago G, Flores-Garza BG, Tavares-Negrete JA, Lara-Mayorga IM, Gonza lez-Gamboa I, Zhang YS, et al. The tumor-on-chip: Recent advances in the development of microfluidic systems to recapitulate the physiology of solid tumors. *Materials (Basel).* 2019; 12: 2945. <https://doi.org/10.3390/ma12182945> PMID: 31514390
28. Abhyankar VV, Toepke MW, Cortesio CL, Lokuta MA, Huttenlocher A, Beebe DJ. A platform for assessing chemotactic migration within a spatiotemporally defined 3D microenvironment. *Lab Chip.* 2008; 8: 1507–1515. <https://doi.org/10.1039/b803533d> PMID: 18818806
29. Zuchowska A, Jastrzebska E, Zukowski K, Chudy M, Dybko A, Brzozka Z. A549 and MRC-5 cell aggregation in a microfluidic Lab-on-a-chip system. *Biomicrofluidics.* 2017; 11: 24110.
30. Ayuso JM, Virumbrales-Muñoz M, Lacueva A, Lanuza PM, Checa-Chavarria E, Botella P, et al. Development and characterization of a microfluidic model of the tumour microenvironment. *Sci Rep.* 2016; 6: 1–16. <https://doi.org/10.1038/s41598-016-0001-8> PMID: 28442746
31. Shields JD, Fleury ME, Yong C, Tomei AA, Randolph GJ, Swartz MA. Autologous Chemotaxis as a Mechanism of Tumor Cell Homing to Lymphatics via Interstitial Flow and Autocrine CCR7 Signaling. *Cancer Cell.* 2007; 11: 526–538. <https://doi.org/10.1016/j.ccr.2007.04.020> PMID: 17560334
32. Ma S, Fu A, Chiew GGY, Luo KQ. Hemodynamic shear stress stimulates migration and extravasation of tumor cells by elevating cellular oxidative level. *Cancer Lett.* 2017; 388: 239–248. <https://doi.org/10.1016/j.canlet.2016.12.001> PMID: 27965040



33. Ma S, Fu A, Lim S, Chiew GGY, Luo KQ. MnSOD mediates shear stress-promoted tumor cell migration and adhesion. *Free Radic Biol Med.* 2018; 129: 46–58. <https://doi.org/10.1016/j.freeradbiomed.2018.09.004> PMID: 30193891
34. Weth A, Krol I, Priesner K, Donato C, Pirker S, Wolf C, et al. A novel device for elimination of cancer cells from blood specimens. *Sci Rep.* 2020; 10: 1–10. <https://doi.org/10.1038/s41598-020-67071-w> PMID: 32576883
35. Aceto N, Bardia A, Miyamoto DT, Donaldson MC, Wittner BS, Spencer JA, et al. Circulating tumor cell clusters are oligoclonal precursors of breast cancer metastasis. *Cell.* 2014; 158: 1110–1122. <https://doi.org/10.1016/j.cell.2014.07.013> PMID: 25171411
36. Fu A, Ma S, Wei N, Tan BXX, Tan EY, Luo KQ. High expression of MnSOD promotes survival of circulating breast cancer cells and increases their resistance to doxorubicin. *Oncotarget.* 2016; 7: 50239. <https://doi.org/10.18632/oncotarget.10360> PMID: 27384484
37. Phillips KG, Lee AM, Tormoen GW, Rigg RA, Kolatkar A, Luttmgen M, et al. The thrombotic potential of circulating tumor microemboli: Computational modeling of circulating tumor cell-induced coagulation. *Am J Physiol—Cell Physiol.* 2015; 308: C229–C236. <https://doi.org/10.1152/ajpcell.00315.2014> PMID: 25411332
38. Olsson E, Kreiss G, Zahedi S. A conservative level set method for two phase flow II. *J Comput Phys.* 2007; 225: 785–807. <https://doi.org/10.1016/j.jcp.2006.12.027>
39. Heyden S, Ortiz M. Investigation of the influence of viscoelasticity on oncotripsy. *Comput Methods Appl Mech Eng.* 2017; 314: 314–322. <https://doi.org/10.1016/j.cma.2016.08.026>
40. Au SH, Storey BD, Moore JC, Tang Q, Chen YL, Javaid S, et al. Clusters of circulating tumor cells traverse capillary-sized vessels. *Proc Natl Acad Sci U S A.* 2016. <https://doi.org/10.1073/pnas.1524448113> PMID: 27091969
41. Roy E, Pallandre A, Zribi B, Horny M-C, Delapierre FD, Cattoni A, et al. Overview of Materials for Microfluidic Applications. *Adv Microfluid—New Appl Biol Energy, Mater Sci.* 2016. <https://doi.org/10.5772/65773>
42. Senzai T, Fujikawa S. Fast hydrophobicity recovery of the surface-hydrophilic poly(dimethylsiloxane) films caused by rechemisorption of dimethylsiloxane derivatives. *Langmuir.* 2019. <https://doi.org/10.1021/acs.langmuir.9b01448> PMID: 31286768
43. Shirure VS, George SC. Design considerations to minimize the impact of drug absorption in polymerbased organ-on-a-chip platforms. *Lab Chip.* 2017; 17: 681–690. <https://doi.org/10.1039/c6lc01401a> PMID: 28102869
44. Hope JM, Lopez-Cavestany M, Wang W, Reinhart-King CA, King MR. Activation of Piezo1 sensitizes cells to TRAIL-mediated apoptosis through mitochondrial outer membrane permeability. *Cell Death Dis.* 2019;10. <https://doi.org/10.1038/s41419-019-2063-6> PMID: 31685811
45. Follain G, Osmani N, Azevedo AS, Allio G, Mercier L, Karreman MA, et al. Hemodynamic Forces Tune the Arrest, Adhesion, and Extravasation of Circulating Tumor Cells. *Dev Cell.* 2018; 45: 33–52.e12. <https://doi.org/10.1016/j.devcel.2018.02.015> PMID: 29634935
46. Ortiz-Otero N, Clinch AB, Hope J, Wang W, Reinhart-King CA, King MR. Cancer associated fibroblasts confer shear resistance to circulating tumor cells during prostate cancer metastatic progression. *Oncotarget.* 2020; 11: 1037–1050. <https://doi.org/10.18632/oncotarget.27510> PMID: 32256977
47. Lee AM, Tormoen GW, Kanso E, McCarty OJT, Newton PK. Modeling and simulation of procoagulant circulating tumor cells in flow. *Front Oncol.* 2012; 2 SEP: 1–9. <https://doi.org/10.3389/fonc.2012.00108> PMID: 23050240

## 6.8 Acknowledgments

This work has been developed in collaboration with: Alessandra Marrella, Gabriele Varani, Silvia Scaglione, Marco Massimo Fato, Ivan Vaccari, Nicola Aceto, Giuseppe Firpo, Patrizia Guida.

# Chapter 7

## **A multi-organ-on-chip to recapitulate the infiltration and the cytotoxic activity of circulating NK cells in 3D matrix-based tumor model**

### **7.1 Abstract**

The efficacy of immunotherapy for cancer treatment relies heavily on the interaction between immune cells and cancer cells. However, conventional in vitro cell cultures lack the complexity and dynamic nature of the tumor microenvironment, while animal models do not accurately reflect the anti-tumor activity of the human immune system. Therefore, the development of reliable preclinical models is essential for screening immunotherapeutic approaches. Here, it is presented an organ-on-chip (OOC) approach that recreates the migration of Natural Killer (NK) immune cells in a physiologically flowing environment, their infiltration within a 3D tumor matrix, and activation against neuroblastoma cancer cells in a humanized setting. The circulating NK cells actively migrate towards the tumor niche and maintain their ability to interact with matrix-embedded tumor cells, leading to a cytotoxic effect (tumor cell apoptosis). The phenotype of the NK cells is also examined since it correlates with prognosis and response to immunotherapy. The model reveals a significant decrease in CD16-positive NK cells within the migrated and infiltrated population. The proposed immune-tumor OOC-based model is a promising approach for faithfully replicating human pathology and efficiently testing immunotherapies, potentially in a personalized manner. This immune-organ on chip approach can recreate the tumor-mediated infiltration of circulating immune cells within a 3D tumor model.

### **7.2 Introduction**

Immunotherapies represent one of the current most promising challenges in cancer treatment. These are based on the concept of boosting the host's immune system toward the elimination of cancer and include several strategies such as the use of monoclonal antibodies (mAb) targeting tumor-associated molecules or blocking immune checkpoints, anti-cancer vaccines and cell-based therapies (Ringquist et al., 2021; Shelton et al., 2021). The success of immunotherapeutic approaches aimed to unleash the activity of cytotoxic cells such as CD8+ T lymphocytes or Natural Killer (NK) cells strictly depends on their interaction with cancer cells and other immune cells. Such interaction might be profoundly affected by the highly complex niche of the tumor microenvironment (TME), which is populated by different type of cells (i.e., stromal cells, tumor cells, immune cells), interconnected within a complex three-dimensional vascularized matrix. Given these premises, the development of reliable preclinical human models has become crucial for the assessment of the best immune therapeutic approaches (Boucherit et al., 2020; Ando et al., 2021; Ringquist et al., 2021). To date, preclinical safety and efficacy assessment of immunotherapies are carried out through 1) extensive in vitro cultures, addressing the cellular and molecular basis of immune responses, cancer initiation and development, and its interactions with immune cells

2) *in vivo* xenografts and genetically engineered animal models, for a necessary systemic contextualization. However, both approaches show limitations. Conventional *in vitro* models use 2D cultures that under-represent the complexity of the TME (three-dimensionality, shear stresses due to fluidic exposure, irroration affecting molecule distribution) (Rodrigues et al., 2021). On the other side, the animal models classically used in oncology often rely on immunodeficient mice xenografted with human cell lines or patient-derived tumor cells (PDX). These models, although useful for testing anti-tumor drugs, do not allow to obtain information regarding the anti-tumor activity of the human immune system. Other *in vivo* approaches are based on syngeneic mice with a fully competent immune system with results that not always recapitulate the human setting (Franklin et al., 2022). The more sophisticated and informative animal models to date are the so called “humanized mice” having a human HSC-derived immune system which can be engrafted with human tumors. However, some limitations are related to the often incomplete reconstitution of the human immune system, in terms of cell lineage development, wrong proportion of the various immune cell subtypes and degree of their activity and maturation. These defects are due to the presence of a mouse-specific microenvironment lacking human stroma and growth factors (Cogels et al., 2021). Moreover, such models are very expensive, time-consuming, and hardly usable in personalized medicine. Therefore, 3D, human *in vitro* tumor models, including spheroids and organoids, as well as microfluidics approaches integrating the human immune components, are increasingly being developed and adopted (Rodrigues et al., 2021; Vitale et al., 2022). 3D tumor models have advantages over conventional 2D cultures, such as an increased cellular and architectural cancer complexity, like the presence of a biomimetic TME with the proper chemical and biomechanical features (Cavo et al., 2016), beside to the possibility of coculturing stromal, endothelial and cancer cells where cells can migrate and infiltrate in a 3D space. Moreover, from a technical point of view, the adoption of 3D cancer models allows to scale up cell yields, with a sample size compatible with a wide variety of standard downstream analysis, such as molecular and cytofluorimetric analysis, beside immunohistochemistry maintaining a possible anisotropic cells behavior (Ballester-Beltran et al., 2015). The arising microfluidic platforms display the potential to recapitulate the physiological blood flows affecting the survival of circulating tumor cells (Marrella et al., 2021a), the intra/extravasation of circulating cells (tumor cells or activated immune cells), besides a reliable drug distribution (Marrella et al., 2021b). However, some microfluidic models used to co-culture immune and tumor cells in physically separated compartments are currently adopted in static conditions (Lee et al., 2018). Moreover, the over-miniaturization of some organ on chips (OOC) allow to host only few cells and very small amount of tumor samples, thus limiting the downstream analytical approaches. From a manufacturing point of view, the conventional OOC models and microfluidic models under development are typically fabricated using the polydimethylsiloxane (PDMS) elastomer, in which UV lithography is utilized to create an overall chip architecture with microscale fluid channels across the compartments where few microliters of media circulate without any sampling/injection port (Amin et al., 2016; Lee et al., 2018). Besides suffering the difficulty of mimicking the complex structures of the microenvironment *in vivo* (Amin et al., 2016), these PDMS-based devices lead to the adsorption of small hydrophobic compounds on the chip, causing the reduction of their bioavailability, finally resulting in issues in terms of cellular responses and/or bias in biochemical analysis. In this paper, we present a unique and promising approach aimed at recapitulating the immune cell infiltration and activation against cancer cells in a humanized, fluid-dynamic and 3D environment. An organ-on-chip technology (MIVO®) has been recently adopted by authors for recapitulating the systemic administration of anticancer drugs and for carrying out efficacy assays in comparison with

the standard xenograft model, demonstrating the high predictability of this in vitro 3R approach (Marrella et al., 2021b). Similarly, the same technological platform has been adopted for culturing aggressive breast cancer models and recapitulating the cancer cells migration and infiltration in the fluid flow circuit, which represents the first physiopathological step towards the metastatic onset (Cavo et al., 2018). Here, the generation of a humanized and immunocompetent in vitro cancer model (Marrella et al., 2019), where tumor cells are cultured in a compartment physically separated through a porous permeable membrane from the fluid flow compartment, relies on the capability to emulate the microcirculation as well as the circulatory behavior of immune cells within the TME. The possible access to both the tumor and the circulating compartments allows to monitor and quantify the changes that occur in the TME (soluble molecules, cell death, tumor cell invasion), in circulating immune cells, and potentially in additional compartments physically connected each other through the circulating fluid flows (i.e., evaluation of the metastatic site). The flexibility of this approach carries the important potential of better recapitulating a clinical scenario, opening the way for a more reliable platform for 1) a personalized investigation of the specific migratory and infiltrative capacity of immune cells, 2) the analysis of the anti-tumor activity of both drug-based and cell-based therapies, 3) the investigation of the effects of tumor-immune cell cross-talk often leading to the onset of resistant tumor variants (Bottino et al., 2021).

## **7.3 Materials and Methods**

### **7.3.1 Cell cultures**

The MYC-N amplified neuroblastoma (NB) cell line HTLA-230 was provided by Dr. E. Bogenmann (Children's Hospital Los Angeles, CA) (Corrias et al., 1996) and cultured in RPMI-1640 medium supplemented with 10% heat-inactivated FCS (Biochrom, Berlin, Germany), 50 mg/ml streptomycin, 50 mg/ml penicillin (Sigma-Aldrich), and 2 mm glutamine (Euroclone). The cells were cultured in a humidified environment (95% air/5% CO<sub>2</sub>) at 37°C and were used to generate 3D tumor models. Peripheral blood mononuclear cells (PBMCs) were obtained from blood of volunteer healthy donors by Ficoll-Hypaque gradients (Sigma Aldrich). NK cells were purified by using the NK-cell isolation kit II (Miltenyi Biotec) and were cultured on irradiated PBMCs in RPMI-1640 supplemented with 10% heat-inactivated FCS, 50 mg/ml streptomycin, 50 mg/ml penicillin (Sigma-Aldrich), 2 mm glutamine (Euroclone), 600 IU/ml rhIL-2 (Proleukin; Chiron, Emeryville, CA) and 0.5% v/v phytohemagglutinin (Gibco, Paisley, United Kingdom). After 10 passages, NK cells were checked for purity (>95%) analyzing classical NK cell markers (Castriconi et al., 2007b).

### **7.3.2 Computational fluid-dynamic simulations**

Fluid dynamics within Single-Flow MIVO® device was investigated to predict 1) the fluid velocity profiles within the device and 2) the fluid flow-driven NK cells trajectories. First, the analysis was performed by using the Single-Phase Laminar Fluid Flow model of Comsol Multiphysics 5.6 assuming 1) a laminar flow regime, 2) an incompressible Newtonian fluid (Vitale et al., 2020; Pulsoni et al., 2022). The equations to be solved are the Navier-Stokes ones for the conservation of momentum Equation (1) and the continuity law for conservation of mass Equation (1):

$$\left\{ \begin{array}{l} \rho \left[ \frac{\partial \mathbf{u}_f}{\partial t} + \mathbf{u}_f \times (\nabla \mathbf{u}_f) \right] = -\nabla p + \mu (\nabla^2 \mathbf{u}_f) \quad (1a) \\ (\nabla \times \mathbf{u}_f) = 0 \quad (1b) \end{array} \right.$$

where  $\mathbf{u}_f$  is the fluid velocity and  $p$  the pressure across the circuit. The values of the density  $\rho$  (1,000 kg/m<sup>3</sup>) and the viscosity  $\mu$  (10<sup>-3</sup> Pa·s) was selected as water at room temperature (25°C). A flow rate of 0.3 ml/min was set as input according to the value impose experimentally to generate the fluid motion, whereas as output the atmospheric pressure was set as null, avoiding a backflow. A no-slip boundary condition was set. Finally, an iterative geometric multigrid (GMRES) algorithm was used to solve the equations. Subsequently, the particle tracing module for fluid flow was added to the model to identify the position and velocity of the NK cells dispersed in the moving fluid as a function of time. The Newtonian model was used to estimate the behaviour of the particles in the fluid flow. Such model is based on the conservation of total momentum:

$$\frac{d(m_p \mathbf{v}_p)}{dt} = \mathbf{F}_d + \mathbf{F}_g, \quad (2)$$

where  $m_p$  is the mass of the particle,  $\mathbf{v}_p$  its velocity,  $\mathbf{F}_d$  and  $\mathbf{F}_g$  the drag force and the gravity force, respectively. The drag force was calculated through the Stokes drag law:

$$\mathbf{F}_d = 6\pi\mu r_p (\mathbf{u}_f - \mathbf{v}_p), \quad (3)$$

where  $\mu$  is viscosity defined above,  $r_p$  is the particle radius (assuming NK cells as spheres) equal to 0.006 mm (Dickinson et al., 2015) The gravity force was calculated as:

$$\mathbf{F}_g = m_p \mathbf{g} \frac{(\rho_p - \rho)}{\rho_p}, \quad (4)$$

where  $\mathbf{g}$  is the gravity acceleration,  $\rho_p$  the particle density equal to 1,080 kg/m<sup>3</sup> (Zhao et al., 2015) and  $\rho$  the fluid density defined above. A rebound condition on the walls was set, meaning that the momentum of the particles that encounter the wall is preserved.

### 7.3.3 3D cultures

Three-dimensional NB models were generated as previously described (Marrella et al., 2019). Briefly, HTLA-230 cells were resuspended in DMEM (Euroclone) supplemented with 10% heat-inactivated FBS, 1% penicillin/streptomycin and 1% glutamine and mixed with a 1% alginate solution (1:1 V/V), to obtain a final 0.5% alginate concentration (w/V). This cell suspension was dropped into a 0.5 M CaCl<sub>2</sub> gelling bath gel spheroids formation. The hydrogels were then washed with sterile distilled water and transferred in a 96-well plate, cultured in DMEM supplemented with 10% FBS, 1% penicillin/streptomycin and 1% glutamine, and 5 mM CaCl<sub>2</sub>, ensuring gel maintenance. For the establishment of NK cell 3D cultures, after thawing NK cells were recovered for 72 h, and then cultured for additional 24 h in the standard 2D setting (96-well plate) or embedded within the alginate matrix. Specifically, the 3D culture was obtained resuspending NK cells in DMEM supplemented with 10% FBS, 1% penicillin/streptomycin, 1% glutamine and 600 UI/ml IL2, and mixed with a 1% alginate solution (1:1 V/V). The 3D hydrogels were obtained following the procedure described above. The cells were then analyzed by flow cytometry in terms of cell viability through staining with a Cell Viability Dye. For NB/NK cell 3D co-cultures, HTLA-230 cells or NK cells were resuspended in DMEM supplemented with 10% FBS, 1% penicillin/streptomycin and 1% glutamine or DMEM supplemented with 10% FBS, 1% pen/strep, 1% glutamine and 600 UI/ml IL2, respectively, and then mixed at different E:T ratios (1:1; 1:10). The 3D hydrogels were obtained following the procedure described above

and kept in culture over/night before analyzing the expression of the NK marker CD16 through flow cytometry.

### 7.3.4 Dynamic culture

The dynamic co-cultures were performed by using the Single-Flow MIVO® device, with the aim to recapitulate the complexity of a 3D, dynamic TME. NK cells were counted, eventually stained with CFSE Cell Proliferation Kit (ThermoFisher Scientific), resuspended in RPMI-1640 medium (Euroclone) supplemented with 10% FBS, 1% penicillin/streptomycin, 1% glutamine and 600 UI/ml IL2, and loaded within the MIVO® chamber (1.5 ml/chamber), to get an effector: target (E: T) ratio of 10:1 with tumor cells. The circulation of NK cells was allowed by a pumping system, through the imposition of a fluid flow rate of 0.3 ml/min, simulating capillary flows, while 3D NB hydrogels were cultured with the maintenance medium physically separated through a permeable porous membrane. For extravasation experiments, after 4 h dynamic co-culture, both circulating (within the capillary circuit) and extravasating (within the tumor niche) NK cells were harvested and counted by means of a hemocytometer. NK cells were also cultured when the MIVO chamber contained either DMEM w/o supplement (negative control) or an alginate gel w/o NB cells supplemented with 40% FBS as a chemoattractant factor (positive control).

### 7.3.5 Immunofluorescence analysis of 3D cultures

For 3D dynamic or static NK/NB co-cultures, NK cells were used unlabeled or labeled with carboxyfluorescein succinimidyl ester (CFSE) (CellTrace CFSE Cell proliferation kit, Molecular Probes). Briefly, NK cells were washed three times with RPMI-1640 and resuspended at  $1 \times 10^7$ /ml in the same medium. CFSE was added at the final concentration of 100uM and incubated for 10 min at 37°C in water bath. The reaction was stopped by adding complete culture medium and cells were washed twice before performing the experiments. For NK cell or NB staining, 3D cultures, either from dynamic or static conditions, were washed with a 0.9% sodium chloride solution supplemented with 5 mm CaCl<sub>2</sub> and fixed in 4% paraformaldehyde supplemented with 1 mm CaCl<sub>2</sub>. For experiments performed with unlabeled NK cells, after incubation with blocking solution (2% BSA, 5 mm CaCl<sub>2</sub> in 0.9% sodium chloride solution), the hydrogels were stained for the NK-associated marker DNAM-1 (Castriconi et al., 2004) (F5, mouse anti-human, IgM) primary antibody for 2 h, followed by a goat anti-mouse IgM FITC-conjugated secondary antibody (Southern Biotech, Birmingham, AL). Cell nuclei were counterstained with DAPI. The hydrogels were mounted on a microscope slide, squeezed with a glass coverslip, and then observed under a fluorescence microscope (Nikon ECLIPSE Ts2-FL). For experiments performed with CFSE-labelled NK cells, after incubation with blocking solution (2% BSA, 5 mm CaCl<sub>2</sub> in 0.9% sodium chloride solution), the hydrogels were stained for the NB-specific marker GD2, by using a direct Alexa Fluor 647 mouse anti-human Disialoganglioside GD2 (IgG2a, BD Biosciences) antibody. Cell nuclei were counterstained with DAPI. The 3D hydrogels were layered on a 0.17 mm-thick microscope coverslip (optically clear borosilicate glass) and examined on the laser scanning confocal microscope SP2-AOBS (Leica Microsystems, Mannheim, Germany), using either a 20x/0.70 (Plan Apochromat) objective or a HCX PL APO  $\times 40/0.75$ –1.25 oil immersion objective, on a DM IRE2 inverted microscope. Fluorescent dye excitation was performed using a 488 nm laser for CFSE excitation (emission detection range 500–560 nm), a 633 nm laser for Alexa 647 excitation (emission detection range 655–760 nm), a 405 nm diode laser for DAPI excitation (emission detection range 410–480). Image merging was performed with Leica proprietary software or ImageJ.

To provide a formal proof of the NK cell-mediated tumor killing in 3D cultures, NB and NK cells were cultured alone or in co-cultures overnight (E:T 1:1). After cell recovering, cells were stained with direct Alexa Fluor 647 mouse anti-human GD2 (IgG2a, BD Pharmingen) and direct APC-H7 mouse anti-human CD45 (IgG1, BD Pharmingen) antibodies to discriminate NB cells (GD2+CD45-) from NK cells (GD2-CD45+). Then, cells were stained with Fixable Viability Stain 510 (BD Horizon) following manufacturer's procedures and analyzed by flow cytometry (FACSVerse flow cytometer-BD).

### 7.3.6 Flow cytometry analysis

To assess NK cell viability, cells were recovered from the 2D standard (96-well plate) culture or from the 3D culture. The latter was achieved by hydrogel dissolution, through incubation in an alginate solubilizing solution (0.15 M NaCl, 100 mM trisodium citrate dihydrate), for 10 min in a 37°C water bath. Cells were then washed with PBS w/o Ca<sup>2+</sup> and Mg<sup>2+</sup> and stained with a PE-TexasRed Fixable Cell Viability dye (ThermoFisher Scientific), following manufacturer's protocol. To assess NK cell infiltration within the 3D tumor culture, as well as their phenotype, the cells were recovered from the alginate scaffold as described above. Cells were also recovered from the medium surrounding the hydrogels within the transwell inserts (to analyze extravasated NK cells) and from the circulating compartment (to analyze circulating NK cells). The cells were then washed with PBS w/o Ca<sup>2+</sup> and Mg<sup>2+</sup> and incubated with the staining solutions, for 30 min: the cells were stained with an anti-human CD45-APC and an anti-human CD16-PacificBlue antibody (ThermoFisher Scientific). For the analysis of tumor cell death after dynamic co-culture, the cells were recovered from the alginate scaffold and subsequently stained with an anti-human CD45-APC antibody and an Annexin V-FITC Apoptosis Detection Kit (eBioscience). After incubation with the staining solution, the cells were washed and run through a NovoCyte3000 Flow Cytometer System. Data were analyzed with the NovoExpress software (Agilent Technologies).

## 7.4 Results

### 7.4.1 Assessment of natural killer cell viability in standard 2D culture vs. 3D alginate embedding

High-risk neuroblastoma (NB) is an aggressive, metastatic pediatric cancer difficult to treat and still characterized by poor overall survival. We have recently developed an alginate-based 3D NB culture as in vitro model characterized by a more physio-pathological setting showing only a partial overlap with the standard 2D culture in terms of expression of immune-related molecules (Marrella et al., 2019). We also demonstrated that the NB cell viability and proliferation are preserved after embedding NB cells within the 3D alginate matrix. The aim of the present work is the implementation of such three-dimensional culture with features mimicking 1) the dynamic microcirculation within the tumor microenvironment and 2) the circulatory behavior of immune cells. Then, a reliable dynamic culture, consisting in the 3D NB model cultured with circulating NK cells, has been generated as a suitable tool for analyzing immune cell migration and infiltration, as well as tumor cell killing. Given the hypothesis that circulating NK cells could be able to specifically infiltrate the alginate-based NB culture, we wanted to verify whether the alginate matrix per se could be detrimental for the NK cell viability. NK cells were cultured in standard conditions (suspended culture within a 96-well plate) or embedded in the

alginate-based 3D matrix; the cells were then collected from the standard culture by pipetting or recovered from the 3D culture through alginate dissolution, stained with a Viability Dye, and analyzed by flow cytometry. In the NK 3D culture, a clear population of unstained (thus viable) cells is shown beside to a clear stained population of dead cells (Figure 39A); conversely, in the 2D culture the presence of a mid-stained population might be indicative of early cell death/structural degradation of the cell, enriching the population of non-viable cells (Figure 39A). According to the clearly viable population, a significant difference was observed in cell viability between the standard suspended NK culture and the 3D embedding (Figure 39B,C).

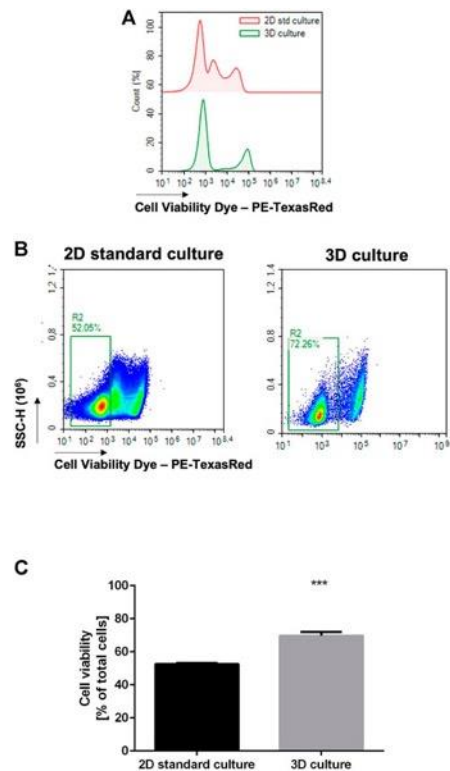


Figure 39: 3D alginate embedding does not negatively affect cell viability. NK cells were cultured in the standard setting ( $n = 6$ ) or in 3D alginate hydrogel ( $n = 6$ ) for 24 h. The cells were then recovered and stained with a Fixable Cell Viability Dye (PE-TexasRed). (A) Flow cytometry analysis on NK cells, histograms: three distinct populations are observed in the 2D standard culture. (B) Flow cytometry analysis on NK cells showing % of low-staining population. (C) Statistical analysis of (B).

#### 7.4.2 Assessment of natural killer cell viability in standard 2D culture vs. 3D alginate embedding

Flow cytometry is one of the most widely adopted approaches for quantitative and qualitative assessment of the composition of TME. With the aim to generate a reliable in vitro model, to support some preclinical studies in a 3Rs perspective, we wanted to check if flow cytometry could be successfully employed to analyze heterogeneous cell populations recovered from the alginate scaffold, as a model of a complex 3D tumor. We started by analyzing simple NK monocultures. NK cells were cultured in standard 2D conditions or in 3D embedding overnight, and the cells directly collecting from the cell suspension or dissociating the alginate, respectively. We assessed the expression of the NK-associated marker CD16, being aware that such marker is highly expressed in polyclonal NK cells (Figure 40). Indeed, as expected, we found high percentage (70%) of CD16+ positive cells



(Figure 40A,B). No significant differences were observed between the 2D and 3D culture setting in terms of percentage (Figure 2C) of positive cells (69.91% vs. 70.39%).

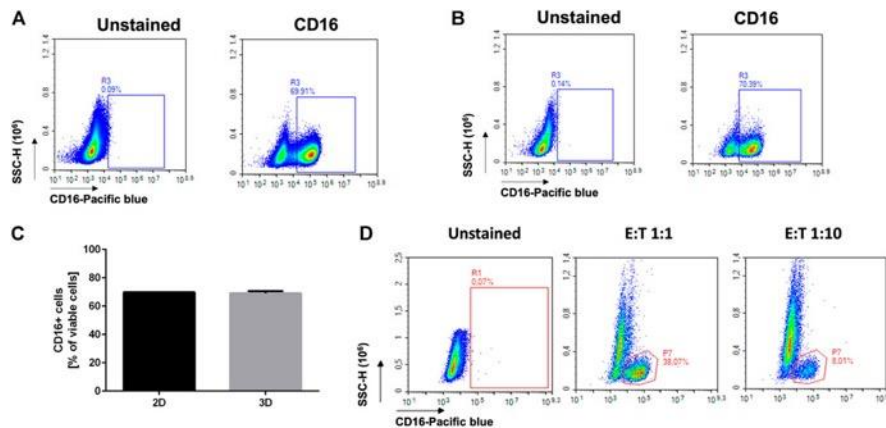


*Figure 40: Reliability of flow cytometry analysis after cell recovery. NK cells were cultured in the standard 2D setting (A), in 3D alginate embedding (B), or co-cultured with tumor cells in the 3D alginate matrix (C). The cells were then recovered and analyzed for the expression of the NK marker CD16. (A) CD16 expression on NK cells cultured in standard conditions (96-well plate, n=6). (B) CD16 expression on NK cells cultured in a 3D alginate scaffold (n=6). (C) No significant difference in CD16 expression is highlighted by flow cytometry in standard vs. 3D culture. (D) CD16 expression on NK cells recovered from a 3D alginate-based co-culture with HTLA-230 cells, at different E:T ratios (n=12).*

We then prepared cocultures with NK and the HTLA-230 NB cell line, to assess the reliability of the staining of hetero-cultures. In particular, we performed cocultures with two different effector/target (E: T) ratio (1:1 and 1:10). The lowest NK: NB ratio was specifically chosen with the aim to get closer to in vivo scenario where few NK cells generally infiltrate the most aggressive solid tumors including NB (Balsamo et al., 2012; Castriconi et al., 2018; Melaiu et al., 2020). We then verified by flow cytometry the percentage of CD16-positive cells, gated on total cells. Considering that, in the NK monocultures, approximately 70% of the cells show CD16 positivity (Figure 40–C), as expected, we detected around 38% CD16+ cells in the 1:1 coculture and around 8% CD16+ cells in the 1:10 coculture.

### 7.4.3 Assessment of natural killer-tumor cell interaction within the 3D model

To verify if NK cells could infiltrate the alginate matrix and interact with tumor cells, we co-cultured NK cells and NB at different E:T ratios (1:1 and 1:10). When embedded in the alginate matrix, NK cells and tumor cells are homogeneously dispersed in a single-cell suspension. To assess the ability of NK cells to move within the matrix for reaching the tumor cells, we performed a confocal microscopy analysis. NK cells were labelled with the cell tracker CFSE (green) and then co-embedded with the unlabeled tumor cells. Then, the 3D co-culture was fixed in paraformaldehyde and stained with a mAb specific for the NB-specific marker GD2 (red). We observed several NK cells start to interact with NB cells (Figure 41).

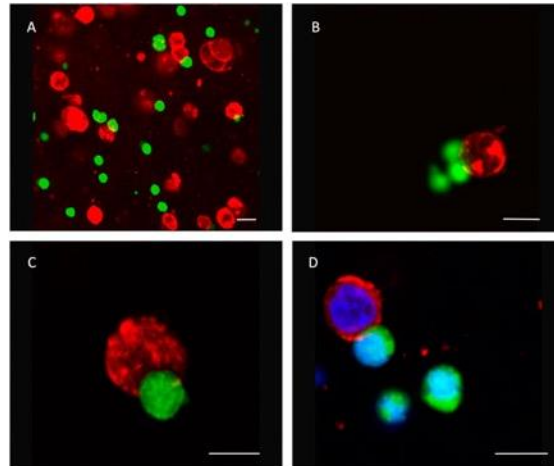


Figure 41: NK cells and NB cells coembedded in a 3D alginate scaffold. Confocal Microscopy Acquisition and Analysis of CFSE-labeled NK cells (green) and GD2-positive NB cells (red) coembedded in 3D alginate scaffold and cultured for 24 h. In panel D, nuclei have been stained with DAPI. (A)  $\times 20$  magnification (representative square field of  $\times 173173$  micron); (B–D)  $\times 40$  magnification. Scale bar: 10 micron.

This leads to a significant tumor cell death paralleled by a high NK cell viability (Figure 42) cells co-culture analysis showed that tumor cell death significantly increased when NB cells were co-cultured with NK cells in 3D models, indicating that NK cells are able to interact and effectively kill tumor cells grown in 3D cultures. As expected, the percentage of dead tumor cells in the presence of NK cells was also significantly increased in 2D culture, whereas at T = 0 was negligible. Moreover, NK cells recovered from hydrogels showed a high viability, demonstrating that 3D alginate spheres are suitable models for testing NK cell-mediated immunotherapy.

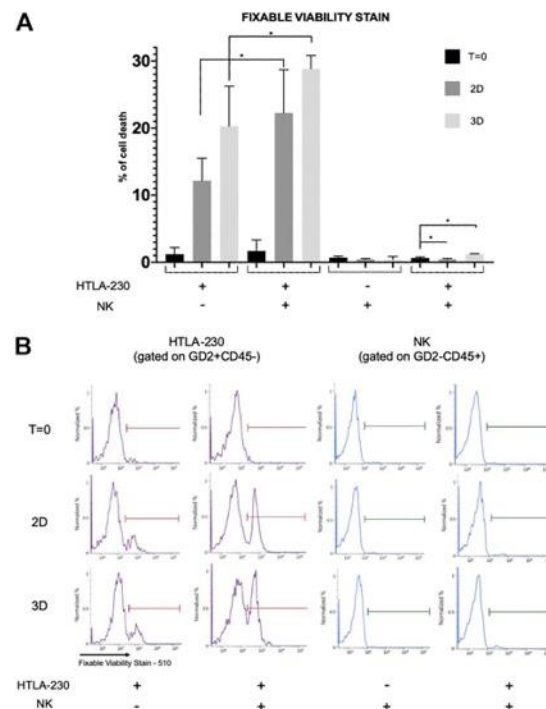


Figure 42: Viability assessment of NB and NK cells in 2D and 3D cultures. (A) Percentage of dead NB or NK cells (i.e., Fixable Viability Stain 510 positive cells) recovered from 2D cultures or 3D alginate spheres, both in monoculture and coculture, gated on GD2+CD45- and CD45+GD2-, respectively. Mean fluorescence intensity with 95% CI is reported (n = 4, \*p < 0.05). (B) Representative experiment.

#### 7.4.4 Dynamic culture and assessment of natural killer cell “extravasation”

Once we have analyzed the feasibility of 3D cultures in static conditions, we carried out the dynamic co-culture by using MIVO®. The dynamic culture has been specifically planned to allow the circulation of NK cells below hydrogel-embedded tumor cells (E:T ratio 10:1), which are accommodated in a standard 24-well plate transwell insert, fitting the MIVO® chamber (Figure 43).

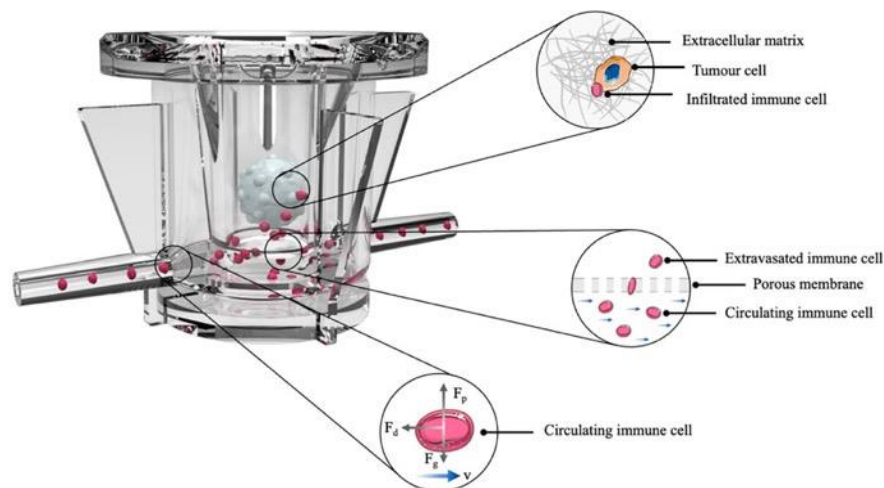


Figure 43: Organ on chip platform for immune-tumor cells cross-talk. Representative scheme of the experiment: HTLA-230 cells were embedded in a 3D alginate scaffold and cultured above a microcirculation of NK cells, for 4 h.

The device has been connected to a pumping system, which enable the imposition of a fluid flow, driving NK cells throughout the circulation, thus mimicking the circulatory system within the tumor microenvironment. The MIVO material is PDMS free, to avoid any molecule binding issues, and no immune cells adhesion at the walls was observed (data not shown). As evidence of that, Computational Fluid Dynamics (CFD) simulations have been performed. Results show that velocity values within MIVO® range from 0 to 1.2 cm/s, which are characteristic of capillary blood flow, when the imposed inlet flow rate is 0.3 ml/min (Figure 44A).

We then verified the ability of NK cells to migrate upward (thus against the gravity force), following an active, chemoattractant-driven “extravasation”, with no driving forces dependent on the fluid flow per se. To this purpose, additional experimental groups included 1) a positive control of cell migration (“empty” 3D alginate scaffolds, without tumor cells, in culture medium enriched with 40% FBS as a chemoattractant), and 2) a negative control (without alginate scaffolds, with culture medium without any chemoattracting supplement). The tumor samples were represented by 3D alginate cultures of HTLA-230 cells, kept in standard conditions (cell culture medium with 10% FBS). After co-culturing the cells for 4 h in a dynamic microenvironment, the supernatants into the transwell inserts were collected, and the migrated cells were counted by means of a hemocytometer. As shown in Figure 44B, we did observe a significant increase of cell migration in the tumor group as well as in the positive control, whereas little or no NK cell migration was observed in the negative control group, demonstrating an active, tumor-specific, NK cell “extravasation”. The biochemical-driven specificity of the “extravasation” process is further corroborated by the CFD simulation aimed at investigating fluid flow-driven NK cells trajectories: the simulation does

not report cells “extravasation” events from the bottom chamber towards the tumor, because of the fluid motion alone, as shown in Figure 44C.

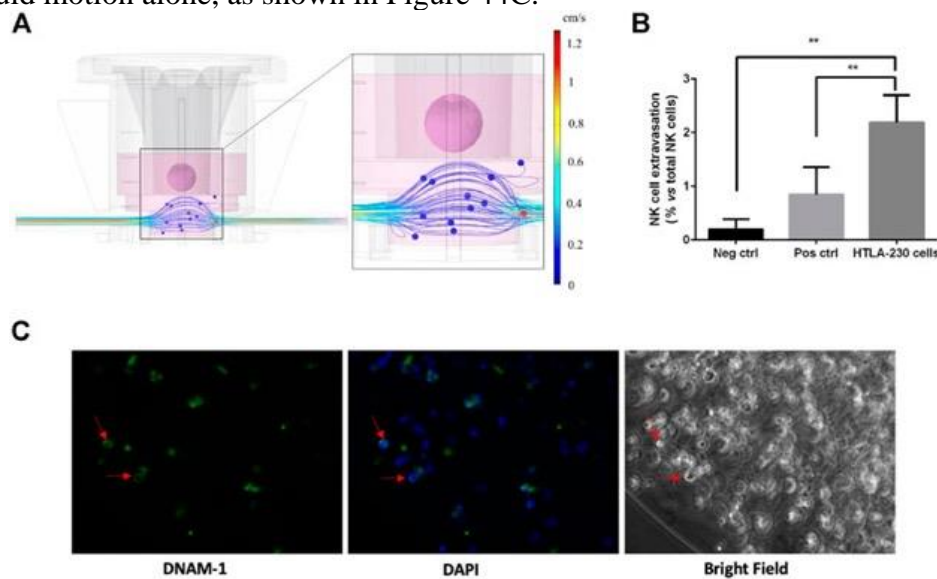
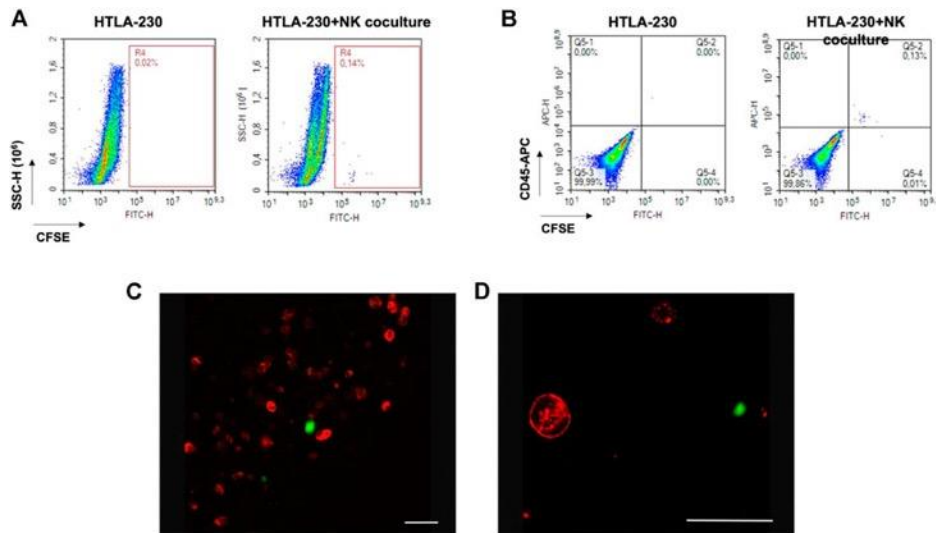


Figure 44: Dynamic culture with circulating NK cells (4 h coculture). (A) CFD simulation of the fluid velocity profiles within the organ on chip and the fluid flow-driven immune cells trajectories. (B) Tumor-specific NK cell extravasation (neg ctrl: DMEM w/o supplements; pos ctrl: alginate gels w/ HTLA-230 cells, plus 30% FBS; HTLA-230 gels with standard 10% FBS) ( $n = 6$ ). (C) NK cell infiltration within the gel, as indicated by DNAM-1-positive cells highlighted by red arrows.

#### 7.4.5 Natural killer cell infiltration

To understand if the migrated NK cells were capable to infiltrate the 3D tumor despite the presence of the alginate matrix, and eventually to interact with tumor cells, we performed the same dynamic culture described above. After co-culturing the cells for 4 h under microcirculation, the 3D alginate cultures were recovered, fixed with 4% PFA, NK cells stained for the DNAM-1 marker (Castriconi et al., 2004), and observed under a fluorescence microscopy. As shown in Figure 44D, DNAM-1+ cells were mostly located along the border of the gels. This is indicative of the ability of NK cells not only to specifically migrate toward the tumor culture, but also to infiltrate the alginate matrix. The same experiment was performed by labelling NK cells with the cell tracker CFSE before the establishment of the coculture, and then following their journey toward the NB culture (Figure 45A,B). This served also as a proof of concept that all the cells found within the transwell inserts during the dynamic culture were CFSE-positive, thus NK only. No tumor cells migrated outside the alginate gels, excluding a bias in the quantification of the “extravasation” of immune cells (data not shown). After 4 h dynamic co-culture, the 3D alginate gels were recovered, fixed and stained for the tumor marker GD2, and observed under confocal microscopy, with the aim to highlight possible effector-to-tumor cell interactions. As shown in Figure 45C,D, CSFE-positive NK cells were found among the GD2-positive tumor ones within the alginate cultures.



*Figure 45: Over/night dynamic co-culture of alginate-embedded neuroblastoma cells with circulating NK cells. (A) Representative experiment showing a flow cytometry analysis of the cells recovered from the gels. A clear population of CFSE-labelled cells (corresponding to NK cells) is visible in the co-cultured sample ( $n = 6$ ). (B) Perfect concordance between CFSE-labelling and CD45 expression ( $n = 6$ ). (C AND D) Confocal Analysis of different 3D alginate scaffold isolated from 3D dynamic cultures (4 h). Representative confocal microscopy xy fields ( $370 \times 370$  micron) acquired in 3D alginate scaffolds containing GD2-positive NB cells (red) that were previously embedded in the gel, and subjected to 4 h of dynamic flow of CFSE-labeled NK cells (green). Merged fluorescence images show that NK cells were able to infiltrate the gel. Scale bar is 50 micron.*

#### 7.4.6 Assessment of the natural killer cell phenotype in circulating, extravasating, and infiltrating populations

NK cells being related to a high cytotoxic activity. However, because of the tumor microenvironment, the CD16-negative infiltrating NK cells may prevail, which are characterized by low-cytotoxicity. Given these premises, we sought to verify if our dynamic culture could recapitulate the selection of a specific NK cell phenotype in the extravasated and infiltrated NK cell fraction. We then performed a dynamic culture, incubating HTLA-230 3D hydrogels with circulating, CFSE labelled NK cells over/night (10:1 E:T ratio). Then, we collected 1) the 3D tumor hydrogels, 2) the migrated NK cells, found into the transwell inserts, and 3) the circulating NK cells, which were analyzed for CD45 and CD16 expression through flow cytometry. The hydrogels were dissociated as described above, and the single cell suspension was analyzed identifying the CSFE-labelled NK cells infiltrating the tumor model. As shown in Figure 45A a clear, although small, CSFE-labeled cell population was present within the hydrogel, corroborating the findings (Figure 45C,D) on the ability of the “extravasated” NK cells to infiltrate the 3D tumor culture. As a further demonstration, CD45 staining confirmed that all and only the CFSE-positive cells were belonging to the immunity lineage (Figure 45B). Moreover, Figure 8 shows the proportion of CD45 and CD16 co-expressing NK cells, gated out on the total CFSE-positivity. We compared the standard NK culture (positive control), the circulating NK cells recovered from the MIVO® devices, the migrated NK cells recovered from the transwell inserts, and the infiltrated NK cells recovered from the hydrogels. As highlighted in the representative plots in Figure 46A, as well as in Figure 46B, the proportion of NK cells expressing CD16 is markedly reduced in the “extravasated” and infiltrated groups, if compared with the circulating group, which conversely is similar to the standard NK culture. This might reflect a preferential recruitment of CD16-negative NK cell population, recapitulating data

observed in different solid tumors (Balsamo et al., 2012; Castriconi et al., 2018; Melaiu et al., 2020).

Finally, we aimed at analyzing the induction of apoptosis in tumor cells, after overnight coculturing with circulating NK cells. Figure 46C shows a significant increase in the exposure of annexin-V on tumor cells membrane, indicating that the migrated infiltrating NK cells are able to specifically induce tumor cell death, thus retaining, at least in part, their cytotoxic potential.

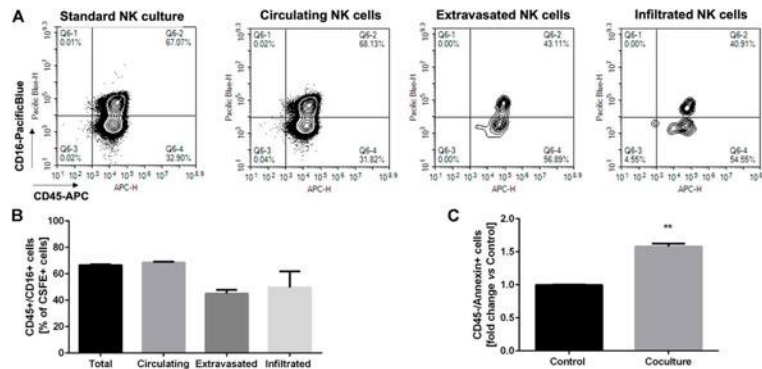


**Figure 46:** Phenotypic characterization of the different fractions of NK cells (A) Representative plots showing the phenotypic characterization of the different fractions of NK cells recovered from the dynamic culture (infiltrated, extravasated, circulating vs. the standard NK culture) based on CD45/CD16 expression, gated on the CFSE-positive population ( $n = 6$ ). (B) Statistical analysis of CD16 expression in the different fractions of NK cells, recovered from the dynamic culture ( $n = 6$ ). (C) Induction of apoptosis in tumor cells, assessed through flow cytometry as annexin-V staining on CD45-negative cells ( $n = 6$ ). Control: HTLA-230 3D monoculture.

## 7.5 Discussion

The improvement of preclinical cancer models represents the basis for the acceleration of the development of more effective and personalized therapeutic strategies, and the reduction of clinical failure rate of oncology drugs, mainly due to the lack of both 1) complex clinically relevant in vitro models that better recapitulate the physio-pathological features occurring in patients (Jardim et al., 2017; Wong et al., 2019; Honkala et al., 2021), and 2) fully humanized animal models (Mak et al., 2014; Maulana et al., 2021; Bjornson-Hooper et al., 2022). For instance, and importantly, immune-oncology therapies would need a fully integrated human microenvironment to be tested, given the intricate interplay between the different immune cell subsets, tumor cells, and other cells within the TME. Moreover, the vascularization state, the accessibility of the tumor bulk and the presence of immunosuppressive signals within the human TME must be considered for both drug-based and cell-based immunotherapies. Starting from a two-dimensional “flat biology”, across the development of three-dimensional cultures and co-cultures, the current rise of microfluidic technologies enables the implementation of a “fourth dimension”, with the introduction of fluid flows mimicking the tissue dynamic environment. In this context, the organ-on-chip technology represents a new generation of in vitro models, which consists in the realization of hyper organized cell cultures building tissue-level structures, the corresponding physiological functions (Bhatia and Ingber, 2014; Sontheimer-Phelps et al., 2019) and different cellular compartments which can cross-communicate through channels interconnection, and/or porous membranes (Maulana et al., 2021). For instance, the cultivation of cancer cells and immune cells in two separated compartments, connected through microchannels within the same planar chip, allows the establishment of a biochemical gradient for immune cell recruitment from the first chamber toward the side

chamber, hosting tumor cells. However, most of these tumor-on-chip are used either in static conditions (Hsu et al., 2012; Businaro et al., 2013; Parlato et al., 2017; Pavesi et al., 2017; Lee et al., 2018; Guo et al., 2019; Um et al., 2019; Yu et al., 2019; Ren et al., 2020; Ayuso et al., 2021), or through simple gravity-driven flow (Song et al., 2021), or perfusion with very low fluid flow rates, being far from physiological conditions. For instance, in a tumor-on-chip model, Aung et al. perfused T cells applying a fluid flow rate of 50 ul/hr (corresponding to 0,8 ul/min) (Aung et al., 2020); similarly, in an immune system-on-chip recently developed by Goyal et al., immune cells were cultured through a flow rate of 60 ul/hr (corresponding to 1 ul/min) (Goyal et al., 2022). Instead, these devices could be further implemented with microfluidic motion, generating more reliable cell culture models with shear stresses and stimuli associated with fluid flows mimicking the dynamics of real tissues (e.g., interstitial flows, blood flows) as well as the biological and biochemical processes that physiologically rely upon dynamic flows (e.g., circulation of immune cells, drug kinetics). Here, we provide a fluid-dynamic technology for performing dynamic experiments with a 300 ul/min flow rate, corresponding to a physiological capillary blood flow velocity (Marrella et al., 2020; Marrella et al., 2021b), for mimicking the microcirculation of the TME. Specifically, NK cells were driven by the fluid flow motion below the tumor model, which was in turn cultured in a 3D matrix. NK cells and the tumor model were physically separated in two different compartments through a porous permeable membrane supporting the adoption of different culture media (e.g. serum percentage, selective growth factors), while NK cells were free to sense the chemo-attractive gradient exerted by tumor cells and to actively initiate a spontaneous “extravasation” process toward the tumor cells themselves. Importantly, NK cells were able to migrate upward, against the gravity and viscous forces exerted by the fluid flow, demonstrating that their migration is specifically mediated by soluble factors released by tumor cells, as little or no migration has been observed in the negative control group (w/o chemo attractants, w/o tumor cells). In particular, the gradient of chemoattractant molecules activates the inner filament network of the cells, leading to a cell chemotactic response (Yang et al., 2015). This force that drives the cells to move towards the chemoattractant source is also named protrusion force. In our experiments, the protrusion force generated by the presence of tumor cells led to a migration of immune cells that was significantly higher than that obtained with increased serum percentage in the medium, demonstrating for the first time a tumor-mediated migration of immune cells in a biologically relevant organ-on-chip platform. Interestingly, NK cells and tumor cells were co-cultured in the dynamic setting in a standard 10:1 E:T ratio (Ayuso et al., 2019; Sargenti et al., 2020; Gopal et al., 2021; Morimoto et al., 2021). However, we observed that only around 2% of circulating NK cells were able to specifically extravasate in the upper compartment, in line with the low number of NK cells generally observed in tumor tissues (Balsamo et al., 2012; Castriconi et al., 2018; Melaiu et al., 2020); then, only this cellular subset had the potential to really interact with tumor cells, highlighting the limitations of the current static co-culture modalities, where often high E/T ratios are used simply adding NK cells into the well/circuit, leading to a possible overestimation of their efficacy in tumor control. This technical issue of the current approaches might lead to a deep impact in the preclinical evaluation of immunotherapies, in which the activation and recruitment of specific subsets of immune cells (for drug-based therapies) as well as of infused, often engineered cells (for cell-based therapies) represent the crucial first step for their efficacy. Furthermore, this may explain at least in part the high success rate of immunotherapies at the preclinical level, which is not mirrored by the same success once translated into the clinic. The second step for activated immune cells to be effective against the tumor is their capability to infiltrate the tumor bulk, keeping an activation state without being affected by the adverse/immunosuppressive signals from the TME. This is, for instance, the main

challenge of CAR-T (and -NK) cell therapy for solid tumors: indeed, despite being successful for hematological malignancies, such cell-based therapy has not found a successful application for solid tumors yet (Guerra et al., 2021; Kumari et al., 2021). In this context, our experiments show that, beside the importance of determining the extravasation rate as indicative of immune cell recruitment, it is mandatory to assess the immune cell infiltration within real three-dimensional matrix-based tumor cultures, where the chemophysics and biomechanics (i.e. stiffness) of the matrix itself better resemble the immune-tumor cross talk occurring *in vivo*. Importantly, the over-miniaturization of the “classical” microfluidic devices, beside failing in recapitulating the biological and clinical features of TME, possibly leads to the underrepresentation of the tumor heterogeneity occurring into the clinic. Moreover, this also carries some technical limitations related to downstream biochemical assays and to small volumes/bubbles handling (Ayuso et al., 2021; Song et al., 2021): indeed, the use of very small cell numbers (e.g., 1,000 cells/spheroid (Ayuso et al., 2019), 2,500 cells/well (Gopal et al., 2021)) and/or very small volumes (e.g., 10–20  $\mu$ l containing  $10^5$ – $2 \times 10^5$  cells (Ren et al., 2020)) are not always suitable for standard analytical methods such as immunofluorescence and flow cytometry analysis. Consequently, the user adaptation to a different cell culture technology, with a less comfortable handling with respect to the standard cultures and a narrowed range of analytical methods (i.e., often confined to cell imaging) make these microfluidic devices not easy to adopt in conventional laboratory practices. On the contrary, following the approach here described, 3D cultures were obtained with more cells (min.  $3 \times 10^4$  cells/matrix) co-cultured with 10-fold higher NK circulating cells. Furthermore, given the increased sample size (up to 5 mm), our experiments represent the proof-of-concept for the use of this platform with more complex 3D cultures (i.e., based on bioprinted scaffolds and/or seeded with different cell types) to better mimic the TME, as well as with patient biopsies. The latter could have a profound impact on personalized screening, for tailoring patients based on the better response or for assessing the efficacy of cell-based therapies. We already demonstrated the reliability of alginate-based cultures for different tumors (Cavo et al., 2018; Marrella et al., 2019; Marrella et al., 2021b), and in particular for NB cultures, where the susceptibility to therapies and the tumor cells immune-phenotype were properly predicted and recapitulated (Marrella et al., 2019). Here, we demonstrated that the alginate matrix is suitable also for culturing NK cells, without affecting their viability or their phenotype. Moreover, when NK cells and NB cells were co-embedded in alginate matrix, we observed that NK cells retained their ability to interact with tumor cells and to kill them, providing evidence of their migratory/infiltrating behavior within the hydrogel. After co-culturing NK cells and the 3D tumor in dynamic conditions, we also assessed the cytotoxic effect of infiltrated NK cells: since we observed a significant increase of annexin-V exposure on tumor cells, we demonstrated that NK cells also retained their killing capacity within the alginate matrix. Importantly, we analyzed NK cell phenotype in terms of CD16 expression, within the circulating environment (administered NK cells), the migrated and infiltrated fractions, after 24 h of dynamic co-culture: we observed a clear decrease in CD16-positive NK cells within the recruited populations (both migrated and infiltrated). CD16+ cells represent a subpopulation of NK cells displaying cytotoxic activity higher than that exerted by the CD16–population (Orange, 2008; Myers and Miller, 2021). Since the infiltration and phenotype of NK cells have been correlated with prognosis and response to immunotherapy in NB tumors (Melaiu et al., 2020; Szanto et al., 2021), it is crucial to dispose of a preclinical model that faithfully recapitulates the human pathology. In this context, our NB/NK model represents a paradigm for the establishment of advanced *in vitro* models that can be efficiently employed for testing immunotherapies also in different tumors, eventually in a personalized perspective. Here, by using HTLA-230, a human cell line highly recapitulating



the most aggressive NB disease (Castriconi et al., 2007a), we provided a humanized and immunocompetent platform bridging the gap between standard in vitro methods, advanced miniaturized organ-on-chips and animal models. With its further optimization by the addition of cells and molecules characterizing the TME, this model could be more successfully utilized for deciphering or consolidating the mechanisms supposed to drive the quality and the amount of human NK cell infiltration in tumors (Castriconi et al., 2013; Regis et al., 2017). In the present model this infiltration could depend on the activity of factors such as TGF- $\beta$ , MIF, or VEGF shown to be highly secreted by HTLA-230 cells line (Castriconi et al., 2013). Finally, these mechanisms could be finely tuned in combined personalized strategies to potentiate the efficacy of immunotherapies.

## 7.6 References

1. Amin, R., Knowlton, S., Hart, A., Yenilmez, B., Ghaderinezhad, F., Katebifar, S., et al. (2016). 3D-printed microfluidic devices. *Biofabrication* 8, 022001. doi:10.1088/1758-5090/8/2/022001
2. Ando, Y., Mariano, C., and Shen, K. (2021). Engineered in vitro tumor models for cell-based immunotherapy. *Acta Biomater.* 132, 345–359. doi:10.1016/j.actbio.2021.03.076
3. Aung, A., Kumar, V., Theprungsirikul, J., Davey, S. K., and Varghese, S. (2020). An engineered tumor-on-a-chip device with breast cancer-immune cell interactions for assessing T-cell recruitment. *Cancer Res.* 80, 263–275. doi:10.1158/0008-5472.can-19-0342
4. Ayuso, J. M., Rehman, S., Virumbrales-Munoz, M., McMinn, P. H., Geiger, P., Fitzgerald, C., et al. (2021). Microfluidic tumor-on-a-chip model to evaluate the role of tumor environmental stress on NK cell exhaustion. *Sci. Adv.* 7, eabc2331. doi:10.1126/sciadv.abc2331
5. Ayuso, J. M., Truttschel, R., Gong, M. M., Humayun, M., Virumbrales-Munoz, M., Vitek, R., et al. (2019). Evaluating natural killer cell cytotoxicity against solid tumors using a microfluidic model. *Oncoimmunology* 8, 1553477. doi:10.1080/2162402x.2018.1553477
6. Ballester-Beltran, J., Biggs, M. J. P., Dalby, M. J., Salmeron-Sanchez, M., and Leal-Egana, A. (2015). Sensing the difference: The influence of anisotropic cues on cellbehav. *Front. Mat.* 2, 39. doi:10.3389/fmats.2015.00039
7. Balsamo, M., Vermi, W., Parodi, M., Pietra, G., Manzini, C., Queirolo, P., et al. (2012). Melanoma cells become resistant to NK-cell-mediated killing when exposed to NK-cell numbers compatible with NK-cell infiltration in the tumor. *Eur. J. Immunol.* 42, 1833–1842. doi:10.1002/eji.201142179
8. Bhatia, S. N., and Ingber, D. E. (2014). Microfluidic organs-on-chips. *Nat. Biotechnol.* 32, 760–772. doi:10.1038/nbt.2989
9. Bjornson-Hooper, Z. B., Fragiadakis, G. K., Spitzer, M. H., Chen, H., Madhireddy, D., Hu, K., et al. (2022). A comprehensive atlas of immunological difference between humans, mice, and non-human primates. *Front. Immunol.* 13, 867015. doi:10.3389/fimmu.2022.867015
10. Bottino, C., Dondero, A., and Castriconi, R. (2021). Inhibitory axes impacting on the activity and fate of Innate Lymphoid Cells. *Mol. Asp. Med.* 80, 100985. doi:10.1016/j.mam.2021.100985
11. Boucherit, N., Gorvel, L., and Olive, D. (2020). 3D tumor models and their use for the testing of immunotherapies. *Front. Immunol.* 11, 603640. doi:10.3389/fimmu.2020.603640
12. Businaro, L., De Ninno, A., Schiavoni, G., Lucarini, V., Ciasca, G., Gerardino, A., et al. (2013). Cross talk between cancer and immune cells: Exploring complex dynamics in a microfluidic environment. *Lab. Chip* 13, 229–239. doi:10.1039/c2lc40887b
13. Castriconi, R., Carrega, P., Dondero, A., Bellora, F., Casu, B., Regis, S., et al. (2018). Molecular mechanisms directing migration and retention of natural killer cells in human tissues. *Front. Immunol.* 9, 2324. doi:10.3389/fimmu.2018.02324
14. Castriconi, R., Dondero, A., Bellora, F., Moretta, L., Castellano, A., Locatelli, F., et al. (2013). Neuroblastoma-derived TGF- $\beta$ 1 modulates the chemokine receptor repertoire of human resting NK cells. *J. I.* 190, 5321–5328. doi:10.4049/jimmunol.1202693
15. Castriconi, R., Dondero, A., Cantoni, C., Della Chiesa, M., Prato, C., Nanni, M., et al. (2007). Functional characterization of natural killer cells in type I leukocyte adhesion deficiency. *Blood* 109, 4873–4881. doi:10.1182/blood-2006-08-038760

16. Castriconi, R., Dondero, A., Cilli, M., Ognio, E., Pezzolo, A., De Giovanni, B., et al. (2007). Human NK cell infusions prolong survival of metastatic human neuroblastoma-bearing NOD/scid mice. *Cancer Immunol. Immunother.* 56, 1733–1742. doi:10.1007/s00262-007-0317-0
17. Castriconi, R., Dondero, A., Corrias, M. V., Lanino, E., Pende, D., Moretta, L., et al. (2004). Natural killer cell-mediated killing of freshly isolated neuroblastoma cells. *Cancer Res.* 64, 9180–9184. doi:10.1158/0008-5472.can-04-2682
18. Cavo, M., Caria, M., Pulsoni, I., Beltrame, F., Fato, M., Scaglione, S., et al. (2018). A new cell-laden 3D Alginate-Matrigel hydrogel resembles human breast cancer cell malignant morphology, spread and invasion capability observed “in vivo”. *Sci. Rep.* 8, 5333. doi:10.1038/s41598-018-23250-4
19. Cavo, M., Fato, M., Peñuela, L., Beltrame, F., Raiteri, R., Scaglione, S., et al. (2016). Microenvironment complexity and matrix stiffness regulate breast cancer cell activity in a 3D in vitro model. *Sci. Rep.* 6, 35367. doi:10.1038/srep35367
20. Cogels, M. M., Rouas, R., Ghanem, G. E., Martinive, P., Awada, A., Van Gestel, D., et al. (2021). Humanized mice as a valuable pre-clinical model for cancer immunotherapy research. *Front. Oncol.* 11, 784947. doi:10.3389/fonc.2021.784947
21. Corrias, M. V., Scaruffi, P., Occhino, M., De Bernardi, B., Tonini, G. P., and Pistoia, V. (1996). Expression of MAGE-1, MAGE-3 and MART-1 genes in neuroblastoma. *Int. J. Cancer* 69, 403. doi:10.1002/(SICI)1097-0215(19961021)69:5<403::AID-IJC9>3.0.CO;2-9
22. Dickinson, A. J., Meyer, M., Pawlak, E. A., Gomez, S., Jaspers, I., Allbritton, N. L., et al. (2015). Analysis of sphingosine kinase activity in single natural killer cells from peripheral blood. *Integr. Biol.* 7, 392–401. doi:10.1039/c5ib00007f
23. Franklin, M. R., Platero, S., Saini, K. S., Curigliano, G., and Anderson, S. (2022). Immuno-oncology trends: Preclinical models, biomarkers, and clinical development. *J. Immunother. Cancer* 10, e003231. doi:10.1136/jitc-2021-003231
24. Gopal, S., Kwon, S.-J., Ku, B., Lee, D. W., Kim, J., Dordick, J. S., et al. (2021). 3D tumor spheroid microarray for high-throughput, high-content natural killer cell-mediated cytotoxicity. *Commun. Biol.* 4, 893. doi:10.1038/s42003-021-02417-2
25. Goyal, G., Prabhala, P., Mahajan, G., Bausk, B., Gilboa, T., Xie, L., et al. (2022). Ectopic lymphoid follicle formation and human seasonal influenza vaccination responses recapitulated in an organ-on-a-chip. *Adv. Sci.* 2022, 2103241. doi:10.1002/advs.202103241
26. Guerra, E., Di Pietro, R., Basile, M., Trerotola, M., and Alberti, S. (2021). Cancer homing CAR-T cells and endogenous immune population dynamics. *Int. J. Mol. Sci.* 23, 405. doi:10.3390/ijms23010405
27. Guo, Z., Song, J., Hao, J., Zhao, H., Du, X., Li, E., et al. (2019). M2 macrophages promote NSCLC metastasis by upregulating CRYAB. *Cell. Death Dis.* 10, 377. doi:10.1038/s41419-019-1618-x
28. Honkala, A., V Malhotra, S., Kummur, S., and Junttila, M. R. (2021). Harnessing the predictive power of preclinical models for oncology drug development. *Nat. Rev. Drug Discov.* 21, 99–114. doi:10.1038/s41573-021-00301
29. Hsu, T.-H., Kao, Y.-L., Lin, W.-L., Xiao, J.-L., Kuo, P.-L., Wu, C.-W., et al. (2012). The migration speed of cancer cells influenced by macrophages and myofibroblasts co-cultured in a microfluidic chip. *Integr. Biol.* 4, 177–182. doi:10.1039/c2ib00112h
30. Jardim, D. L., Groves, E. S., Breitfeld, P. P., and Kurzrock, R. (2017). Factors associated with failure of oncology drugs in late-stage clinical development: A systematic review. *Cancer Treat. Rev.* 52, 12–21. doi:10.1016/j.ctrv.2016.10.009
31. Kumari, R., Ouyang, X., Wang, J., Xu, X., Zheng, M., An, X., et al. (2021). Preclinical pharmacology modeling of chimeric antigen receptor T therapies. *Curr. Opin. Pharmacol.* 61, 49. doi:10.1016/j.coph.2021.08.008
32. Lee, S. W. L., Adriani, G., Ceccarello, E., Pavesi, A., Tan, A. T., Bertolotti, A., et al. (2018). Characterizing the role of monocytes in T cell cancer immunotherapy using a 3D microfluidic model. *Front. Immunol.* 9, 416. doi:10.3389/fimmu.2018.00416
33. Mak, I. W. Y., Evaniew, N., and Ghert, M. (2014). Lost in translation: Animal models and clinical trials in cancer treatment. *Am. J. Transl. Res.* 6, 114.
34. Marrella, A., Buratti, P., Markus, J., Firpo, G., Pesenti, M., Landry, T., et al. (2020). In vitro demonstration of intestinal absorption mechanisms of different sugars using 3D organotypic tissues in a fluidic device. *ALTEX* 37, 255–264. doi:10.14573/altex.1908311

35. Marrella, A., Dondero, A., Aiello, M., Casu, B., Olive, D., Regis, S., et al. (2019). Cell-Laden hydrogel as a clinical-relevant 3D model for analyzing neuroblastoma growth, immunophenotype, and susceptibility to therapies. *Front. Immunol.* 10, 1876. doi:10.3389/fimmu.2019.01876
36. Marrella, A., Fedi, A., Varani, G., Vaccari, I., Fato, M., Firpo, G., et al. (2021). High blood flow shear stress values are associated with circulating tumor cells cluster disaggregation in a multi-channel microfluidic device. *PLoS One* 16, e0245536. doi:10.1371/journal.pone.0245536
37. Marrella, A., Varani, G., Aiello, M., Vaccari, I., Vitale, C., Mojzisek, M., et al. (2021). 3D fluid-dynamic ovarian cancer model resembling systemic drug administration for efficacy assay. *ALTEX-Alternatives Anim. Exp.* 38, 82–94. doi:10.14573/altex.2003131
38. Maulana, T. I., Kromidas, E., Wallstabe, L., Cipriano, M., Alb, M., Zaupa, C., et al. (2021). Immunocompetent cancer-on-chip models to assess immuno-oncology therapy. *Adv. Drug Deliv. Rev.* 173, 281–305. doi:10.1016/j.addr.2021.03.015
39. Melaiu, O., Chierici, M., Lucarini, V., Jurman, G., Conti, L. A., De Vito, R., et al. (2020). Cellular and gene signatures of tumor-infiltrating dendritic cells and natural-killer cells predict prognosis of neuroblastoma. *Nat. Commun.* 11, 5992. doi:10.1038/s41467-020-19781-y
40. Morimoto, T., Nakazawa, T., Matsuda, R., Nishimura, F., Nakamura, M., Yamada, S., et al. (2021). Evaluation of comprehensive gene expression and NK cell-mediated killing in glioblastoma cell line-derived spheroids. *Cancers (Basel)* 13, 4896. doi:10.3390/cancers13194896
41. Myers, J. A., and Miller, J. S. (2021). Exploring the NK cell platform for cancer immunotherapy. *Nat. Rev. Clin. Oncol.* 18, 85–100. doi:10.1038/s41571-020-0426-7
42. Orange, J. S. (2008). Formation and function of the lytic NK-cell immunological synapse. *Nat. Rev. Immunol.* 8, 713–725. doi:10.1038/nri2381
43. Parlato, S., De Ninno, A., Molfetta, R., Toschi, E., Salerno, D., Mencattini, A., et al. (2017). 3D Microfluidic model for evaluating immunotherapy efficacy by tracking dendritic cell behaviour toward tumor cells. *Sci. Rep.* 7, 1093. doi:10.1038/s41598-017-01013-x
44. Pavesi, A., Tan, A. T., Koh, S., Chia, A., Colombo, M., Antonicchia, E., et al. (2017). A 3D microfluidic model for preclinical evaluation of TCR-engineered T cells against solid tumors. *JCI Insight* 2, 89762. doi:10.1172/jci.insight.89762
45. Pulsoni, I., Lubda, M., Aiello, M., Fedi, A., Marzagalli, M., von Hagen, J., et al. (2022). Comparison between Franz diffusion cell and a novel micro-physiological system for in vitro penetration assay using different skin models. *SLAS Technol.* 27 (3), 161–171. doi:10.1016/j.slas.2021.12.006
46. Regis, S., Caliendo, F., Dondero, A., Casu, B., Romano, F., Loiacono, F., et al. (2017). TGF- $\beta$ 1 downregulates the expression of CX3CR1 by inducing miR-27a-5p in primary human NK cells. *Front. Immunol.* 8, 868. doi:10.3389/fimmu.2017.00868
47. Ren, X., Alamri, A., Hipolito, J., Lin, F., and Kung, S. K. P. (2020). *Methods in enzymol.* Amsterdam, Netherlands: Elsevier, 357.
48. Ringquist, R., Ghoshal, D., Jain, R., and Roy, K. (2021). Understanding and improving cellular immunotherapies against cancer: From cell-manufacturing to tumor-immune models. *Adv. Drug Deliv. Rev.* 179, 114003. doi:10.1016/j.addr.2021.114003
49. Rodrigues, J., Heinrich, M. A., Teixeira, L. M., and Prakash, J. (2021). 3D in vitro model (R)evolution: Unveiling tumor–stroma interactions. *Trends Cancer* 7, 249–264. doi:10.1016/j.trecan.2020.10.009
50. Sargenti, A., Musmeci, F., Bacchi, F., Delprete, C., Cristaldi, D. A., Cannas, F. et al. (2020). Physical characterization of colorectal cancer spheroids and evaluation of NK cell infiltration through a flow-based analysis. *Front. Immunol.* 11, 564887. doi:10.3389/fimmu.2020.564887
51. Shelton, S. E., Nguyen, H. T., Barbie, D. A., and Kamm, R. D. (2021). Engineering approaches for studying immune-tumor cell interactions and immunotherapy. *iScience* 24, 101985. doi:10.1016/j.isci.2020.101985
52. Song, J., Choi, H., Koh, S. K., Park, D., Yu, J., Kang, H., et al. (2021). High-throughput 3D in vitro tumor vasculature model for real-time monitoring of immune cell infiltration and cytotoxicity. *Front. Immunol.* 12, 733317. doi:10.3389/fimmu.2021.733317
53. Sontheimer-Phelps, A., Hassell, B. A., and Ingber, D. E. (2019). Modelling cancer in microfluidic human organs-on-chips. *Nat. Rev. Cancer* 19, 65. doi:10.1038/s41568-018-0104-6
54. Szanto, C. L., Cornel, A. M., Tamminga, S. M., Delemarre, E. M., de Koning, C. C. H., van den Beemt, D. A. M. H., et al. (2021). Immune monitoring during therapy reveals activity and regulatory immune responses in high-risk neuroblastoma. *Cancers (Basel)* 13, 2096. doi:10.3390/cancers13092096

55. Um, E., Oh, J. M., Park, J., Song, T., Kim, T.-E., Choi, Y., et al. (2019). Immature dendritic cells navigate microscopic mazes to find tumor cells. *Lab. Chip* 19, 1665–1675. doi:10.1039/c9lc00150f
56. Vitale, C., Fedi, A., Marrella, A., Varani, G., Fato, M., Scaglione, S., et al. (2020). 3D perfusable hydrogel recapitulating the cancer dynamic environment to in vitro investigate metastatic colonization. *Polym. (Basel)* 12, 2467. doi:10.3390/polym12112467
57. Vitale, C., Marzagalli, M., Scaglione, S., Dondero, A., Bottino, C., Castriconi, R., et al. (2022). Tumor microenvironment and hydrogel-based 3D cancer models for in vitro testing immunotherapies. *Cancers (Basel)* 14, 1013. doi:10.3390/cancers14041013
58. Wong, C. H., Siah, K.W., and Lo, A. W. (2019). Estimation of clinical trial success rates and related parameters. *Biostatistics* 20, 273–286. doi:10.1093/biostatistics/kxx069
59. Yang, H., Gou, X., Wang, Y., Fahmy, T.M., Leung, A. Y.-H., Lu, J., et al. (2015). A dynamic model of chemoattractant-induced cell migration. *Biophys. J.* 108, 1645–1651. doi:10.1016/j.bpj.2014.12.060
60. Yu, J., Berthier, E., Craig, A., de Groot, T. E., Sparks, S., Ingram, P. N., et al. (2019). Reconfigurable open microfluidics for studying the spatiotemporal dynamics of paracrine signalling. *Nat. Biomed. Eng.* 3, 830–841. doi:10.1038/s41551-019-0421-4
61. Zhao, Q., Shirinzadeh, B., Cui, M., Sun, M., and Zhao, X. (2015). A simple weighing method for spherical cells. *SLAS Technol.* 20, 471–480. doi:10.1177/2211068215583629

## 7.7 Acknowledgments

This work has been developed in collaboration with: Silvia Scaglione, Monica Marzagalli, Maurizio Aiello, Giorgia Pelizzoni, Roberta Castriconi, Cristina Bottino, Silvia Bruno, Alessandro Poggi, Chiara Vitale, Fabrizio Fontana, Alessandra Dondero.

# Chapter 8

## A Human Ovarian Tumor & Liver Organ-on-Chip for Simultaneous and More Predictive Toxo-Efficacy Assays

### 8.1 Abstract

The limited success rate of clinical trials in oncology is due to the inadequate predictability of preclinical assays, which fail to replicate the complexity of human tissues (in vitro tests) or produce species-specific outcomes (animal testing). Therefore, the development of new approaches is necessary to better evaluate novel anti-cancer treatments. In this study, a multicompartmental organ-on-chip (OOC) platform was used to connect 3D ovarian cancer tissues to hepatic cellular models and mimic the systemic administration of cisplatin to investigate drug efficacy and hepatotoxic effects in a physiological context. Computational fluid dynamics was used to impose capillary-like blood flows and predict cisplatin diffusion. After conducting a cisplatin concentration screening using 2D/3D tissue models, cytotoxicity assays were performed in the multicompartmental OOC and compared with static co-cultures and dynamic single-organ models. Increasing cisplatin concentration resulted in a linear decrease in SKOV-3 ovarian cancer and HepG2 liver cell viability. Additionally, the 3D ovarian cancer models displayed higher drug resistance than the 2D model in static conditions. Importantly, the experimental approach combining 3D culture, fluid-dynamic conditions, and multi-organ connection showed the most predictive toxicity and efficacy results when compared to clinical therapy. This demonstrates that OOC-based approaches are reliable alternatives to the 3Rs (Replacement, Reduction, Refinement) in preclinical research.

### 8.2 Introduction

In medical and pharmaceutical research, there is an urgent challenge related to the evident and increasingly low rate of successful research results being translated from bench to bedside [1,2,3]. In particular, there is a disproportion between the huge investments in new medicines and their impact on population health [4] since about 90% of early clinical trials fail [5,6,7]. This problem is particularly significant in oncology, where the statistics are more dramatic [7,8]. The main reason for this failure is related to the lack of clinical efficacy and unmanageable organ toxicity [9,10], and these poor predictive results are often attributed to the poor ability of preclinical models to generate results of human relevance [7,11,12,13,14,15]. Indeed, current 2D models are far from representative of human complexity, and while emerging 3D models more closely resemble chemical and biomechanical environmental in vivo-like cues [16], they are still insufficient in recapitulating human disease progression and tissue–drug dynamic interaction [17,18,19,20,21]. On the other hand, while animal tests are required by regulatory organizations, playing a pivotal role in evaluating the safety and efficacy of drugs [6,22],

there is still a severe mismatch in the diversity of animal species that explain this poor animal-to-human predictability. As a result, less than 8% of animal trials are successfully translated to clinical cancer trials [1,11,23,24,25,26,27,28,29,30]. Indeed, animal studies have been demonstrated to overestimate the likelihood of a treatment being effective by about 30%, while toxic outcomes at sub-clinical and lower doses than those found to be safe in animals have been reported [31,32]. Hereafter, although *in vivo* models continue to provide useful information about drug safety and potency, it is crucial to keep in mind that their findings are rarely applicable to humans [1,6,33,34]. To circumvent these shortcomings, alternative human-relevant approaches have emerged, the most significant being organ-on-chip (OOC) systems [35]. These technologies are capable of accurately decoupling biological mechanisms behind the cytotoxic effects of testing molecules through a highly reproducible and less time- and cost-consuming *in vitro* approach. In particular, it is hoped that OOCs will advance biological contexts and thus potentially produce physiologically-relevant outcomes translatable to clinical scenarios [20,36,37,38]. OOC systems exploit the advances made in the last decade in microfabrication and biomimicry of materials, as well as novel methodologies for using primary cells or patient-derived biopsies *in vitro* [35,39,40,41]. These unprecedented multidisciplinary combinations allow the recapitulation of the functionality, architecture and dynamics at the organ level, setting the stage for more efficient preclinical predictions of human responses and thus potentially diminishing the high attrition rates of clinic trials [42]. However, many human diseases, such as cancer, involve multiple organs, and thus 2D static models used to manage spatiotemporally separated organs are too simplistic and fail to simulate the dynamic interrelated physiology of tissues and their interaction with the tested drugs [43,44]. Indeed, tissues and cells within the body are anatomically connected by a network of vessels, where fluids flow and communicate by the secretion of signaling factors (e.g., extracellular vesicles, soluble molecules) [40]. Hence, organ-organ interplays are crucial to our understanding of human disease and they should also be introduced to model and achieve appropriate responses to investigational drugs. Moreover, it is well known that drugs may cause multi-organ side effects and when they enter the human body, they are bio-transformed (e.g., ADME processes) [30,43]. Thus, to properly emulate the pharmacokinetics and pharmacodynamics of drugs, systemic approaches must be pursued. Specifically, multi-organ-on-chip (MOOC) systems have been recently developed to address this need, reproducing the multicellular nature of organs and their connections, which would not have been possible to implement in single OOCs [43,45]. Particularly, multi-organ platforms with medium recirculation emulate systemic and cross-organ communication and reciprocal influences, better reproducing the *in vivo* context [39,43]. For example, MOOCs incorporating a liver model may bring essential information about hepatic metabolism and the hepatotoxicity of the compounds tested, as has been reported for many conventional therapies [46,47]. Moreover, MOOCs can be valuable tools for developing metastasis models for the online monitoring of cancer cells extravasation from the primary mass and their circulation and intravasation into one or multiple specific metastatic sites [44,47]. However, although they are promising tools in cancer research, these approaches are currently based on miniaturized cell culture, allowing the adoption of a small number of cells, which may not accurately represent phenotypic or microenvironmental characteristics or tiny tumor samples, thus limiting the use of analytic techniques [17,20]. Moreover, fluid flow is mostly driven by gravity or capillary forces, preventing important fluidic cues, such as velocity and shear forces of the human bloodstream, from modulating through a pumping system [17,48]. Finally, both conventional and advanced microfluidic devices are made of polydimethylsiloxane (PDMS), which is known to be potentially harmful to cells by causing biocompatibility loss

due to the gradual release of non-crosslinked oligomers and the adsorption of small hydrophobic molecules [20,48,49]. In this study, to overcome these limitations, we adopted a multicompartamental PDMS-free OOC technology (MIVO®) for testing the efficacy of on-target and simultaneously measuring off-target toxicity, determining the therapeutic index in a pathophysiological scenario. The system enables the combination of 3D clinically relevant-sized tumor tissue cultures with a fluidic circuit controlled by a peristaltic low flow rate pump that accurately mimics the capillary bloodstream, allowing systemic drug administration to be simulated. Specifically, a 3D hydrogel-based ovarian cancer model [17] was generated and fluidically connected to a hepatocellular culture; cisplatin was injected in circulation and the anti-cancer effects and hepato-toxicity were assessed after 48 h of treatment, respectively. Computational fluid-dynamic (CFD) simulations have been performed to (i) set capillary-like blood flow dynamics and (ii) investigate the mass transport profiles of cisplatin within the cell culture models. Finally, toxo-efficacy results derived from the dynamic multi-organ system were compared with (i) static single-organ models, (ii) dynamic single-organ models, and (iii) static multi-organ models.

## 8.3 Materials and Methods

### 8.3.1 Liver and Ovarian Cancer Cell Cultures

The human liver HepG2 cell line (ATCC No. HB8065) was expanded in Eagle's Minimum Essential Medium (EMEM), supplemented with 10% heat-inactivated Fetal bovine serum (FBS), 2 mM L-glutamine (L-glu), and 1% penicillin/streptomycin (Pen/Strep), and plated at a density of  $1 \times 10^5$  cells/cm<sup>2</sup>. The human ovarian cancer SKOV-3 cell line (ATCC) was expanded Dulbecco's modified Eagle's medium (DMEM) high glucose supplemented with 10% FBS, 2 mM L-glu and 1% Pen/Strep and plated at a density of  $1 \times 10^5$  cells/cm<sup>2</sup>. The cells were incubated in a humidified, 5% CO<sub>2</sub> atmosphere at 37 °C. Media were changed twice a week. When culture dishes were nearly confluent, liver, and ovarian cancer cells were detached with 0.25% trypsin-EDTA solution, after two washes with Phosphate Buffered Saline (PBS) and replated until the next confluence. FBS, L-glu, Pen/Strep solution, DMEM, EMEM, trypsin-EDTA solution, trypsin solution, Live/Dead assay, Phalloidin Fluorescein Isothiocyanate Labeled, DAPI, and cisplatin were purchased from Sigma Aldrich. A first set of cells culture in 2D was adopted to preliminary investigate the cytotoxic effect of cisplatin on HepG2 and SKOV-3 that were cultured as monolayers at a density of  $1 \times 10^5$  cells/mL in 96-well plates. Cells were left to adhere overnight in a humidified, 5% CO<sub>2</sub> atmosphere at 37 °C. The day after (T<sub>0</sub>), cisplatin was added to the culture medium at a final concentration of 10, 25, 50, and 100 μM.

### 8.3.2 Ovarian Cancer Model

A 3D hydrogel-based ovarian cancer model was developed as in our previous publication [17]. Briefly, Alginate powder (React4life) was dissolved in physiologic solution at 1% w/v and filtered under sterile conditions. SKOV-3 cells suspension was mixed with the alginate solution to obtain a final concentration of 0.5% w/v. The SKOV-3/alginate suspension was dripped into a sterile 0.5 M Calcium-based crosslinker bath to form hydrogel spheres with a final density of cells of  $1 \times 10^6$  cells/mL. After washing the spheres with DI water to remove the excess of calcium, the hydrogels were gently moved into the culture systems, placed in 96-well plates, and cultured with DMEM supplemented with 10% FBS, 1% Pen/Strep, and CaCl<sub>2</sub> 5 mM. The day after (T<sub>0</sub>), cisplatin was added to the culture medium at a final concentration of 10, 25, 50, and 100 μM.

### 8.3.3 Static vs. Dynamic In Vitro Model

A co-culture model was implemented by cultivating SKOV-3 cells within 24-well Transwell inserts accommodated within the 24-well plates where HepG2 cells were plated on the bottom. Cells were left to adhere overnight in a humidified, 5% CO<sub>2</sub> atmosphere at 37 °C. The day after (T0), cisplatin was added to the culture medium at a final concentration of 10, 25, and 50 μM. A compartmental fluidic device (MIVO® by React4life) was adopted to simultaneously assess the on-target and off-target cytotoxic activity of cisplatin under dynamic conditions. Briefly, inserts containing either HepG2 cells or SKOV-3 cancer spheres were placed within the MIVO® chamber, producing two fluidically independent compartments: (i) the tissue culture chamber, and (ii) the circulatory one. The device was connected to a pumping system imposing a fluid flow predicted by CFD simulations through a closed-loop fluidic circuit that mimics the circulatory system disseminating the drug. Cisplatin was injected into the fluidic circuit, resembling systemic drug administration and extravasation. For the dynamic multi-organ condition, two independent chambers hosting liver and ovarian cancer models were fluidically connected by the external fluidic circuit, reproducing the in vivo-like tissues arrangement and interconnections. Mono-culture or co-culture of HepG2 cells and SKOV-3 cells provided with the same amount of culture medium with or without cisplatin were used as static controls.

### 8.3.4 Computational Fluid-Dynamic Analyses

Fluid dynamics within the organ-on-chip was investigated to predict (i) the fluid velocity profiles within the device, and (ii) the transport kinetics of cisplatin, as the anticancer drug tested. First, the analysis was performed by using the Single-Phase Laminar Fluid Flow model of Comsol Multiphysics 5.6, assuming (i) a laminar flow regime and (ii) an incompressible Newtonian fluid. The equations to be solved include Navier–Stokes for the conservation of momentum (1a) and the continuity law for the conservation of mass (1b):

$$\begin{cases} \rho \left[ \frac{\partial \mathbf{u}_f}{\partial t} + \mathbf{u}_f \times (\nabla \mathbf{u}_f) \right] = -\nabla p + \mu (\nabla^2 \mathbf{u}_f) & (1a) \\ (\nabla \times \mathbf{u}_f) = 0 & (1b) \end{cases}$$

where  $\mathbf{u}_f$  is the fluid velocity, and  $p$  is the pressure across the circuit. The values of the density  $\rho$  (1000 kg/m<sup>3</sup>) and the viscosity  $\mu$  (10<sup>-3</sup> Pa·s) were selected as water at room temperature (37 °C). A flow rate of 2 mL/min was set as input according to the value imposed experimentally to generate the fluid motion, whereas as output the atmospheric pressure was set as null, avoiding a backflow. A no-slip boundary condition was set. Finally, an iterative geometric multigrid (GMRES) algorithm was used to solve the equations. Subsequently, cisplatin mass transport analysis was carried out by using the Transport of the diluted species (TDS) module of Comsol Multiphysics. In addition to the diffusive mechanism, an additional two processes were considered: the convection transport, due to the presence of a velocity field ( $\mathbf{u}_f$ ), and the metabolite and drug consumption due to cellular activity. The reaction term  $R$  for the drug was defined according to the Michaelis–Menten kinetics:

$$R = \frac{V_{max} c}{K_m + c} \quad (2)$$

where  $c$  is the concentration of the component,  $V_{max}$  represents the maximum consumption rate (equal to 1.66 × 10<sup>-12</sup> mol/m<sup>3</sup>·s for cisplatin) and  $K_m$  represents the component concentration when the rate is  $V_{max}/2$  (equal to 6.64 × 10<sup>-3</sup> mol/m<sup>3</sup> for cisplatin) [17,19]. Thus, the general form to describe mass transport can be written as:

$$\frac{\delta c}{\delta t} + \nabla \times (\mathbf{J}) + \mathbf{u}_f \times \nabla c = \mathbf{R} \quad (3)$$



where  $c$  is the component concentration and  $J$  is the mass diffusive flux vector, defined by Fick's law:

$$J = -D \nabla c \quad (4)$$

where  $D$  is the diffusion coefficient of the molecule, previously reported in the literature [17,19]. This study was conducted by considering 2D and 3D alginate hydrogel-based culture scenarios to monitor the transport profiles of the compounds over time, both in static and dynamic conditions, with the same culture medium volume. In both cases, 0.1 mol/m<sup>3</sup> was set as the initial culture medium concentration for cisplatin [19].

### 8.3.5 Cell Viability and Pharmacodynamic Evaluation

Cell viability and proliferation of both HepG2 and SKOV-3 were quantitatively assessed through Alamar Blue Assay. After 48 h of drug treatments, culture media were changed with fresh medium containing 10% v/v of Alamar Blue solution. Samples were incubated at 37 °C for 4 h in the dark, the supernatants were collected, and absorbance was measured spectrophotometrically (Infinite 200 Pro). Cell viability was calculated as the percentage of live cells normalized to the untreated controls. The proliferation rate was derived as the ratio between the time point of interest and the number of cells at T<sub>0</sub>. A pharmacodynamic evaluation was performed by calculating the cisplatin half maximal effective concentration (EC<sub>50</sub>) for SKOV-3 and median lethal dose (LD<sub>50</sub>) for HepG2 cells under different culture conditions. These parameters were estimated as best-fit values of a non-linear fitting dose-response model by GraphPad Prism software (La Jolla, CA, USA). To investigate possible SKOV-3 and HepG2 cells crosstalk, a conditioned media experiment was carried out. Briefly, a conditioned culture medium was produced by culturing HepG2 cells as monolayers and SKOV-3 cells as monolayers or embedded in a 3D alginate hydrogel with or without cisplatin (10, 25, 50 μM) for 48 h. After, this culture medium was collected and administered to the other cell type (i.e., culture medium collected from HepG2 cells was administered to SKOV-3 cells and vice versa) to evaluate the possible impact on the cellular growth rate. HepG2 and SKOV-3 cells cultured with fresh culture medium were used as the negative control.

### 8.3.6 Immunofluorescence

SKOV-3 viability, both cultured as monolayers and embedded within alginate, was qualitatively evaluated through live/dead assay. Briefly, after 48 h of treatment, samples were washed with PBS and incubated in 2 mM Calcein-AM and 4 mM EthD-1 in PBS for 15 min at 37 °C in a dark environment to detect live and dead cells, respectively. Then, samples were washed three times in PBS and observed by means of fluorescence microscopy (Nikon H550L). HepG2 clusters disaggregation and morphological changes upon cisplatin treatments were evaluated by visualizing cytoskeleton alteration with Phalloidin Fluorescein Isothiocyanate Labeled. Briefly, cells were fixed with 4% paraformaldehyde in PBS (PFA; pH 7.4) for 15 min and permeabilized with 0.1% Triton X-100 for 5 min. Subsequently, cells were incubated with 1% bovine serum albumin (BSA). Then, cells were incubated with Phalloidin Fluorescein Isothiocyanate Labeled (1:5 in DI) for 1 h at RT. Nuclei were counter-stained with DAPI. Then, samples were washed three times in PBS and imaging was performed by using fluorescence microscopy (Nikon H550L). All images obtained were analyzed through ImageJ software.

## 8.4 Results

### 8.4.1 Static Cisplatin Toxo-Efficacy Evaluation

### 8.4.1.1 Mono-Culture vs. Co-Culture Conditions

A screening of cisplatin concentrations was conducted to investigate both the efficacy and toxicity on ovarian cancer and liver cells, respectively. Regarding the cancer model, both the 2D and the 3D models were investigated, both in monoculture and co-culture. For mono-culture efficacy assays, Skov-3 cells were grown in 2D monolayers or embedded within 3D alginate-based spheres [17] and treated with cisplatin (10  $\mu\text{M}$ , 25  $\mu\text{M}$ , 50  $\mu\text{M}$  and 100  $\mu\text{M}$ ) for 48 h. As expected, the percentage of alive cells decreased with increasing cisplatin concentrations, and it was significantly higher in 3D models than in 2D. Consequently, the derived EC50 parameter shifted from 15  $\mu\text{M}$  (2D model) to 32.5  $\mu\text{M}$  (3D model), showing a higher drug resistance of cells when they are surrounded with an extracellular matrix (ECM)-mimicking matrix (Figure 47).

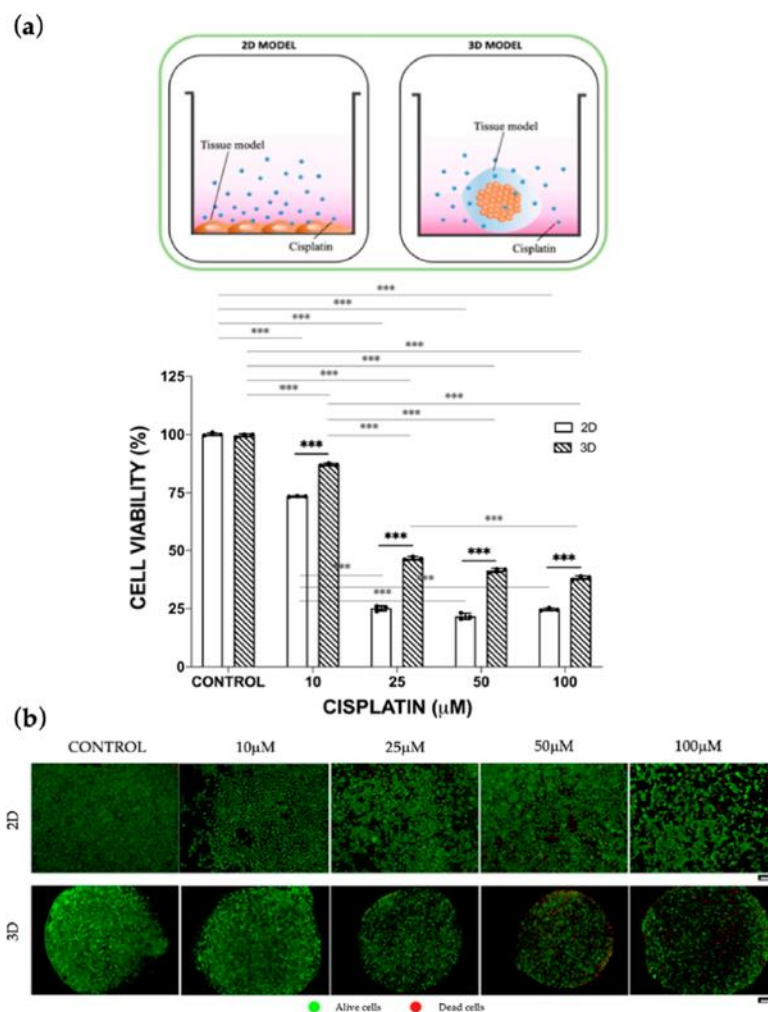


Figure 47: Cisplatin efficacy after 48 h of treatment. (a) SKOV-3 viability was assessed by Alamar Blue assay both in 2D and in 3D static mono-culture models treated with the 10, 25, 50, 100  $\mu\text{M}$  cisplatin concentrations. Cell viability was derived as the percentage of alive cells normalized to the untreated controls. Values are reported as mean  $\pm$  SD. Student's paired t-test between each experimental condition was performed and statistical significance was set at \*\*\*  $p < 0.001$  ( $N = 3$  biological replicates;  $n = 3$  technical replicates). (b) Cell viability upon cisplatin treatment represented by live/dead assay. Scale bar is 100  $\mu\text{m}$ .

For the mono-culture toxicity assays, the same concentrations of cisplatin were administered to HepG2 cell monolayers. As can be seen from Figure 48a, cisplatin was revealed to be highly toxic for HepG2 cells, with a remarkable reduction in cell viability up to 25% that was detected at the lowest cisplatin concentration (10  $\mu\text{M}$ ). The LD50 parameter was 4  $\mu\text{M}$ . Interestingly, the cisplatin cytotoxic activity against HepG2 cells was also shown through a DAPI-Phalloidin staining: an increasing disaggregation of typical HepG2 cell clusters was noted with the increase in drug doses, indicating that this anticancer drug leads also to a cytoskeletal destructive effect on actin filaments (Figure 48b).

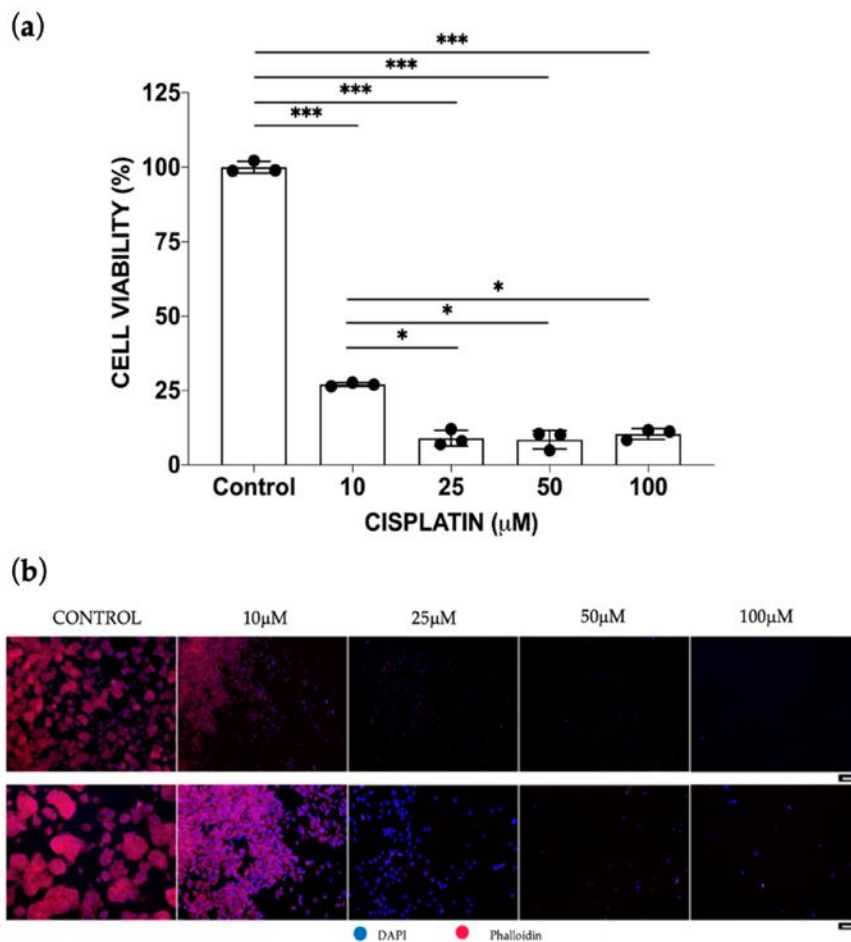


Figure 48: Cisplatin toxicity after 48 h of treatment. (a) HepG2 viability was assessed by Alamar Blue assay in 2D static mono-culture models treated with the 10, 25, 50, 100  $\mu\text{M}$  cisplatin concentrations. Cell viability was derived as the percentage of alive cells normalized to the untreated controls. Values are reported as mean  $\pm$  SD. Student's paired t-test between each experimental condition was performed and statistical significance was set at \*  $p < 0.05$  and \*\*\*  $p < 0.001$  ( $N = 3$  biological replicates;  $n = 3$  technical replicates). (b) Images of nuclei (DAPI) and cytoskeleton (Phalloidin) of HepG2 cells upon cisplatin treatment. Scale bar is 100  $\mu\text{m}$ .

A co-culture of HepG2 and SKOV-3 cells was then realized to evaluate whether the co-presence of multiple tissue models could affect a single cell-type response to cisplatin. SKOV-3 cells grown in 2D monolayers or embedded within 3D alginate-based spheres were cultured onto porous permeable inserts and placed above HepG2 cell monolayers (Figure 49). Cisplatin directly added to the culture medium generated a significant dose-dependent inhibition in cell viability for both cell lines as occurred for mono-cultures. Intriguingly, considering the 10  $\mu\text{M}$  dose, which is in line with cisplatin plasma concentrations observed in clinics [50], the hepato-toxicity in the co-culture model was reduced in respect to the

mono-culture condition. On the other hand, the ovarian cancer cells displayed significantly higher drug resistance when encapsulated in 3D alginate hydrogels, whereas their viability in 2D cultures was reduced when cancer cells were co-cultured compared to the mono-culture 2D, showing a more significant effect of the cell culture dimensionality (2D vs. 3D) than the presence of a concurrent cellular model (mono-culture vs. co-culture).

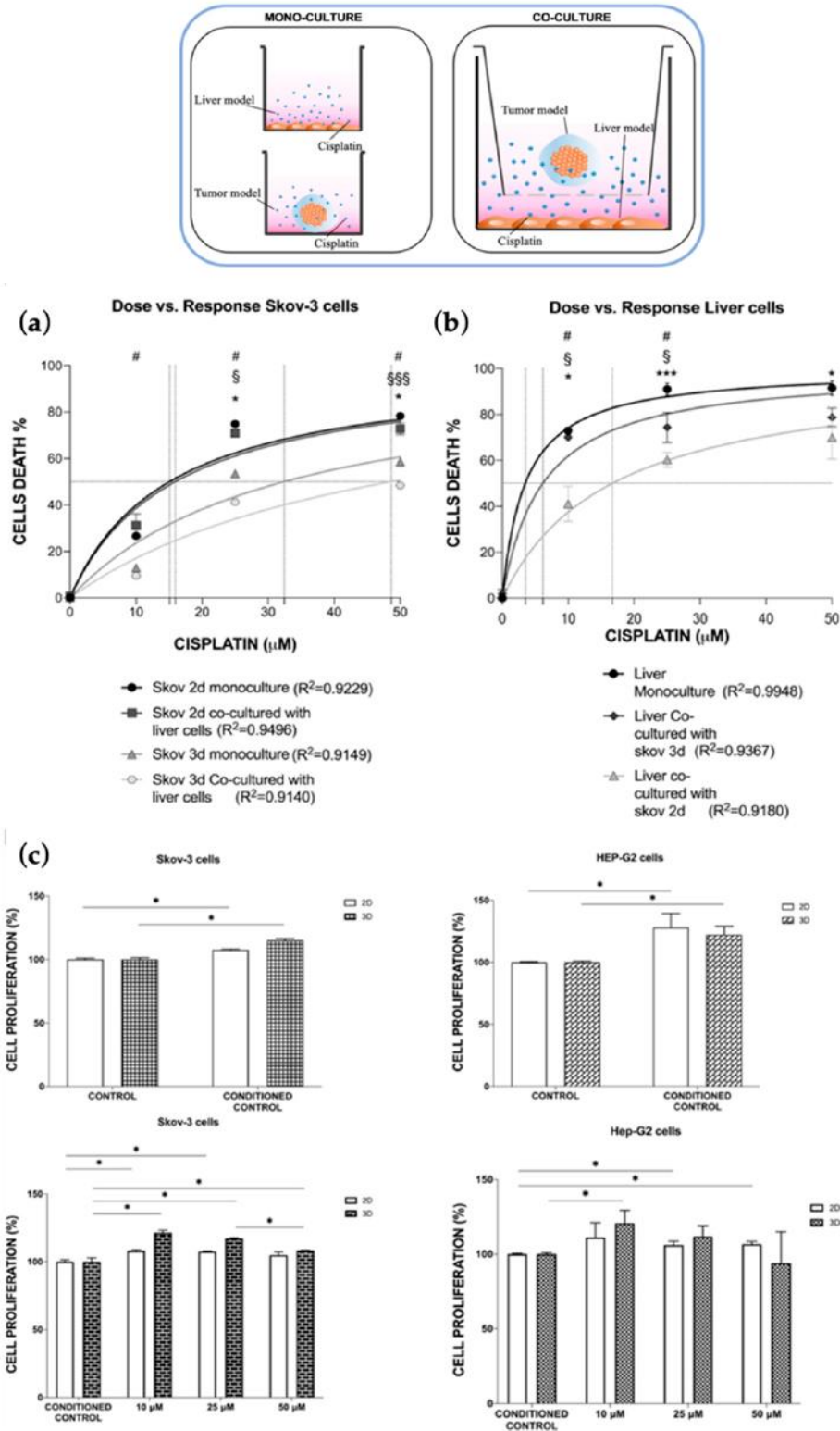


Figure 49: Cisplatin response in mono-culture vs. co-culture conditions and conditioned media effect. Cisplatin dose-response of SKOV-3 (a) and HepG2 (b) cells under different culture conditions. Values are reported as mean  $\pm$  SD. For each condition, the EC50 (vertical dotted lines, left image) and LD50

parameters (vertical dotted lines, right image) were calculated as best-fit values of a non-linear fitting dose-response model (solid curves) by GraphPad Prism software. Statistical significance was set at \*, §, #  $p < 0.05$  and \*\*\*, §§§  $p < 0.001$  ( $N = 3$  biological replicates;  $n = 3$  technical replicates). (c) SKOV-3 (left) and HepG2 (right) cell proliferation were assessed after the conditioned media administration. Control is the negative control (i.e., cells that received fresh culture medium); conditioned control: cells with culture medium w/o cisplatin previously conditioned with the other cell type for 48 h; 10, 25, 50  $\mu\text{M}$  are values of cells with conditioned culture medium with cisplatin. Statistical significance was set at \*  $p < 0.05$  and \*\*\*  $p < 0.001$  ( $N = 3$  biological replicates;  $n = 3$  technical replicates).

To further inspect cell interplays and tissue crosstalk, conditioned media experiments were carried out: a higher proliferation rate was observed for Skov-3 (107% and 115%) and HepG2 (128% and 122%) cells fed with a drug-free medium—previously used for culturing the other cell type—than those that received fresh culture medium (Figure 49c), pointing out the possible presence of soluble signaling molecules (e.g., cytokines) released by the cells during the first culture that stimulates the growth of the second ones, and thus the occurrence of cell interactions. Furthermore, this phenomenon was more noticeable when cisplatin was present in the conditioned medium in a dose-dependent manner; intriguingly, enhanced cell proliferation was identified with respect to the case of drug-free medium treatment, with a decreasing trend as the administered concentration increased. Particularly, both SKOV-3 and HepG2 cells in all culture configurations displayed a higher proliferation rate (108% and 121% for SKOV-3, 11% and 120% for HepG2) when cisplatin was administered at 10  $\mu\text{M}$  as the initial concentration. This could suggest that further and/or diverse mechanisms of cell-cell communication and protection occur when cisplatin induces apoptosis.

## 8.4.2 Dynamic In Vitro Cisplatin Toxo-Efficacy Evaluation

### 8.4.2.1 Fluid-Dynamic and Mass Transport Analysis

First, fluid dynamics within a Single-Flow MIVO® device was investigated. The results show a capillary flow dynamic beneath the tissue cultured within inserts (Figure 50a); in particular, streamlines illustrating the flow field of the circulating medium in the basal chamber are associated with velocity values ranging from 0 to 1.5 cm/s, faithfully recapitulating capillary bloodstream when the imposed inlet flow rate is 2 mL/min. Subsequently, cisplatin mass transport analysis was carried out for 2D and 3D static and dynamic culture conditions (Figure 50b).

The maximal cisplatin percentages reached were lower in static conditions (64% and 95% for 3D and 2D, respectively) than in dynamic ones (100% for 3D and 2D). In static conditions, they were revealed to be higher in the 2D cell model than in the 3D sphere, whereas in dynamic conditions, no differences were noted. All curves present a constant increase in concentration until reaching a plateau value, which differs much more between the 3D static model than the 3D dynamic one. Moreover, the kinetics transport was very fast in all 2D scenarios and the 3D static one, whereas a slower rising over time developed in the 3D fluid-dynamic model.

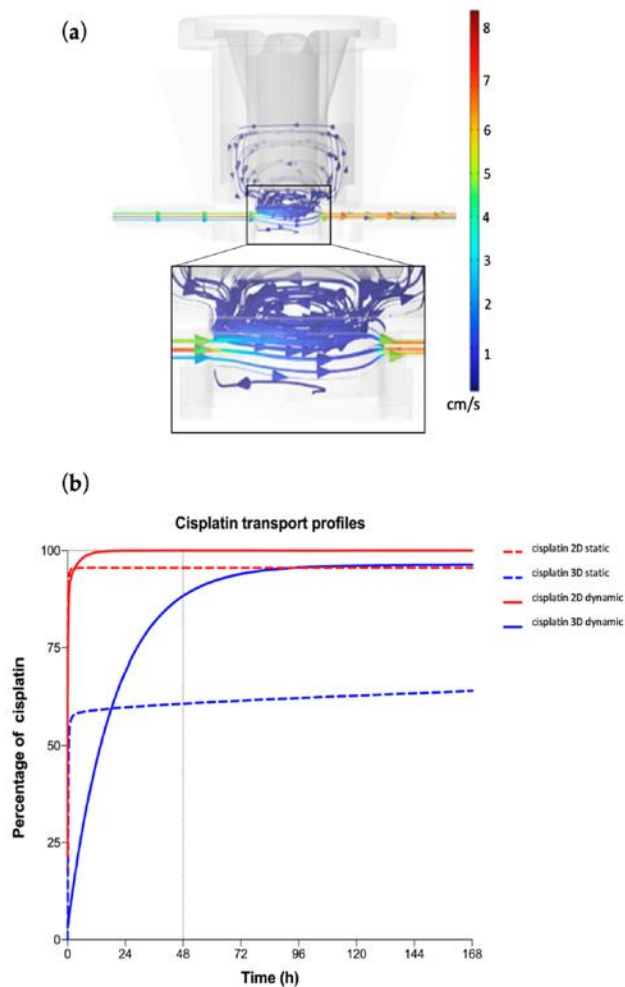


Figure 50: CFD simulations. (a) CFD streamlines illustrating the flow field of the circulating fluid within the MIVO® chamber in terms of velocity profile when a flow rate of 2 mL/min is imposed. (b) Molecule mass transport was derived up to 7 days by using the TDS module of Comsol Multiphysics. The percentage of the cisplatin molecule that is indicated on the ordinate axis was calculated as the ratio between the concentration measured at the center of the considered model (2D cell monolayer or 3D hydrogel sphere) and the initial concentration in the culture medium.

#### 8.4.2.2 Cisplatin Toxo-Efficacy Evaluation in Static vs. Dynamic Conditions Models

The cytotoxicity of cisplatin was also investigated in the 2D liver cells model and 3D cancer cells model by introducing a physiological flow circulation, mimicking systemic drug administration. Data obtained by using the dynamic cell culture were compared with those obtained in static mono-culture conditions (Figure 51).

Interestingly, while in the 2D cellular model (i.e., liver) non-significant differences were noticed in LD50, cancer cells cultured within a 3D ECM displayed an effect of the drug that was significantly higher under flow, in line with the computational model. The EC50 parameter was revealed to be 25.9  $\mu\text{M}$  and 15.4  $\mu\text{M}$  for the static and dynamic culture conditions, respectively, meaning that fluid flow enhances drug diffusion through the 3D ECM-mimicking alginate hydrogel.

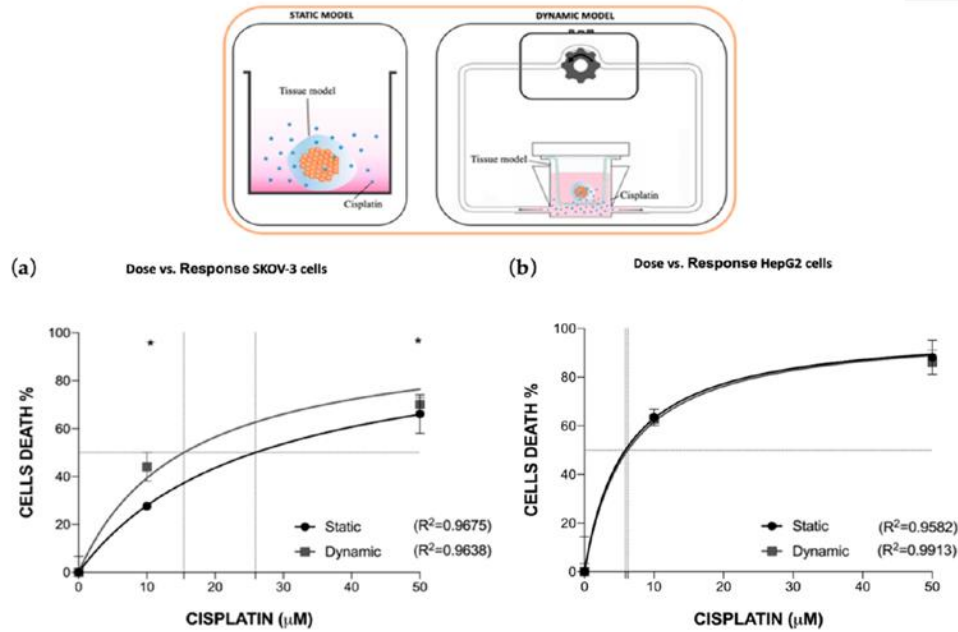


Figure 51: Dynamic culture condition impact on cisplatin pharmacodynamics in mono-culture models. Cisplatin dose-response of SKOV-3 (a) and HepG2 (b) cells under static or dynamic culture conditions. Values are reported as mean  $\pm$  SD. The LD50 and EC50 parameters were calculated, with their R2. Statistical significance was set at \*  $p < 0.05$  ( $N = 3$  biological replicates;  $n = 3$  technical replicates).

### 8.4.2.3 Multi-Organ-on-Chip Configuration Design and Development

A novel multi-organ OOC based on MIVO® tissue chamber has been developed to allow physiological communications among different organs and simulate dynamic cisplatin systemic administration through an imposed capillary-like fluid flow (Figure 52). The OOC device was adopted since it allows both planar (2D) and 3D cell culture, being compliant with commercially available inserts. The luer-lock standard connectors of tubing guarantee a flexible and modular connection between different organs connected in series. The modular design of this OOC allows tissues to be previously prepared in static conditions and then moved into a dynamic cell culture. Moreover, the flexibility of this design and the adoption of fluidic standards enable a wide range of configurations tailored to the desired experimental setup: single vs. multi-organ configuration, the type and the number of cells, and shape and dimension of scaffolds where seeding cells, flow rate, and shear stresses are generated by the flow.



Figure 52: Dynamic multi-organ platform. A novel multi-organ-on-chip configuration was developed to co-culture HepG2 cells monolayers in one chamber (1) and ovarian cancer 3D hydrogel-based models

in a second independent chamber (2) fluidically connected to the first one through an external fluidic circuit where cisplatin circulates (3), resembling the systemic drug administration.

#### 8.4.2.4 Cisplatin Toxo-Efficacy Evaluation in Single-Organ vs. Multi-Organ Conditions

The last experimental configuration achieved considered the possibility of simulating both cisplatin systemic administration through capillary blood flow conditioning and multi-organ culture by adopting the multi-compartmental setup of the MIVO® organ-on-chip. Briefly, in one chamber the liver model was cultured onto a porous insert, while in a second chamber fluidically connected with the previous one, ovarian cancer tissue was 3D cultured. Data were compared with those obtained in co-culture static conditions. Cisplatin generated a significant dose-dependent inhibition in cell viability for both co-cultured cell lines, both in static and dynamic conditions (Figure 53).

Interestingly, under plasmatic drug concentration (i.e., 10  $\mu\text{M}$ ), the hepatotoxicity was drastically reduced in dynamic multi-organ configuration, while the efficacy of the anticancer drug was shown to be significantly higher (Figure 53).

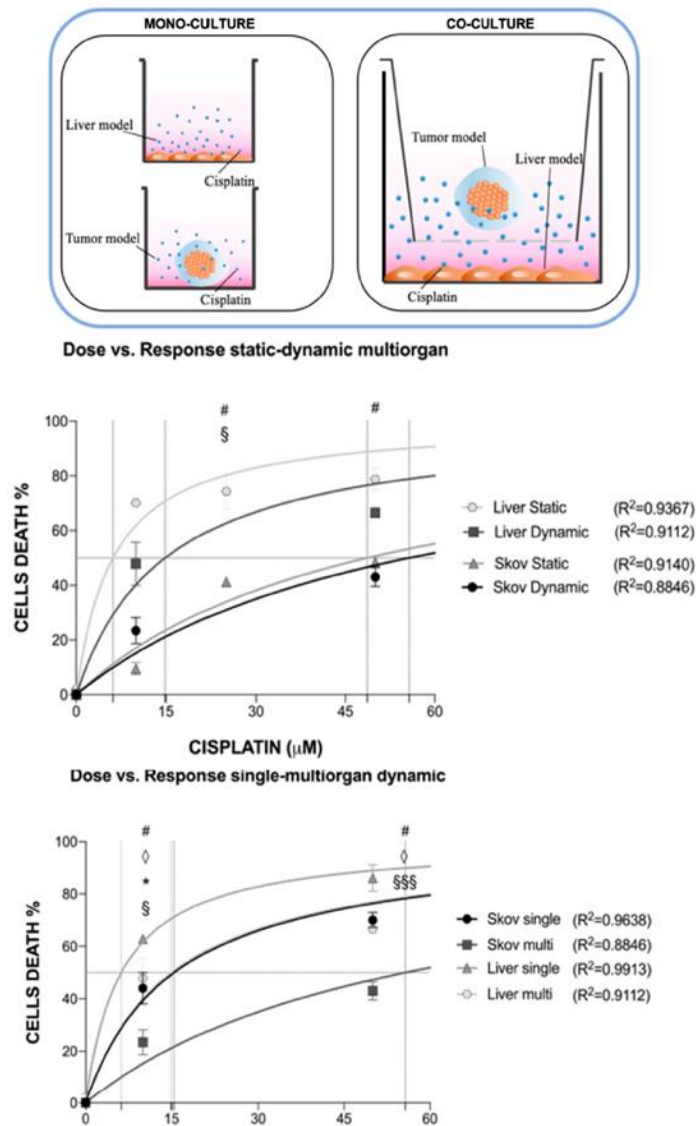


Figure 53: Cisplatin toxicity in single-organ vs. multi-organ conditions. Cisplatin dose-response of HepG2 and SKOV-3 cells when co-cultured in static vs. multi-organ dynamic conditions. Values are



reported as mean  $\pm$  SD. (a) The LD50 and EC50 parameter were calculated, with their R2; statistical significance was set at \*, §, #,  $\diamond$   $p < 0.05$ , §§§§  $p < 0.001$ . (b) The effect of cisplatin at plasma concentration was measured in both conditions for liver and ovarian cancer cells ( $N = 2$  biological replicates;  $n = 3$  technical replicates).

## 8.5 Discussion

The development of new drugs is a complex and scientifically demanding task that is also highly time and cost-consuming. In addition, only a small number of the most promising new drug candidates successfully complete the clinical test phase and are released onto the market as approved drugs. To minimize this failure of potential candidates, the introduction of more predictive and significant test systems in the preclinical phase is becoming highly demanded. To this aim, several microfluidic OOC systems have been recently designed by introducing a fluid-dynamic environment to the cells in culture to recapitulate proper human cells behavior in vitro, such as in the human body, which is fundamental for a reliable prediction of pharmaco-kinetics and pharmaco-dynamics in subsequent clinical studies. However, a great deal of work still has to be carried out to accelerate the adoption of these technological alternatives among pharma and CRO stakeholders. Indeed, OOCs are typically too difficult to be used than many other in vitro cell culture systems and their implementation needs highly specialized personnel, which can result in increasing experimental costs. To avoid these issues, some of the authors have developed a highly flexible OOC device with the ability to grow established cellular models, both in monolayer and 3D matrixes, with different sizes and shapes. In particular, during its design, proper tuning of the chamber dimensions and culture media volume in circulation was achieved to guarantee the possibility of both culturing clinically relevant size tissues and sampling the sufficient amount of media volume for more robust and modular experimental readouts. Indeed, the use of miniaturized OOCs (i.e., few thousand of cells and a few microliters of media) does not allow tumors to be recreated to scale, and the microscale volume of these OOC amplify some adverse phenomena such as bubble formations and media evaporation, besides allowing the use of a small cellular range. In previous work, authors reported a successful preclinical validation of an OOC-based drug efficacy assay in comparison with the xenograft model, which still represents the gold standard [17]. Here, a simultaneous toxo-efficacy assay has been achieved and successfully validated by co-culturing both liver and ovarian cancer tissue models in dynamic conditions, while cisplatin treatment was placed in circulation. Indeed, the unusual high modularity of this OOC makes both mono-culture and multi-organ configuration possible. The latter will allow multiple physiological niches to be built in separate chambers, where cells from different organs are cultivated under specific fluid flow-inducing shear stresses; during this multicompartmental cell culture condition, soluble molecule diffusion and cell-cell crosstalk can be successfully achieved through a serial fluidic connection among the chambers. In particular, to promote a more in vivo-like environment for cancer cells, a 3D alginate hydrogel-based matrix with the proper stiffness and mechanical stability [51] was optimized in terms of cell viability, migration, and also molecule/drug diffusion. Although in this work, a human cell line was used to recapitulate the ovarian tumor model, this matrix supports the co-culture of multiple cells (e.g., immune cells and tumor cells) [20] and also the embedding of patient-derived cells spheroids (paper in preparation). Moreover, a hepatoma cell line (HepG2) was used to mimic the liver tissue, since over the years it has represented one of the main standards in pharmacological and toxicological studies [52,53], retaining the different functionalities of the native organ [53], thus still being commonly adopted in innovative emerging pre-clinical

platforms [52]. Nevertheless, the authors are aware that it lacks some features related to the metabolic activity of the human liver (e.g., low expression of cytochrome P450 enzyme) [54,55]. However, the use of HepG2 cells allowed us to perform a proper number of assays, which were fundamental to ensure the reproducibility of the experimental outcomes and to provide the proof of concept that the novel technological approach here described is a relevant pre-clinical tool. In fact, differently from primary hepatocytes, immortalized human hepatic cell lines are much more available and easier to manipulate and maintain in cell cultures for a prolonged time, besides being much cheaper without requiring any special operator skills [55]. Furthermore, although primary human hepatocytes more closely reproduce the phenotypic and functional aspects of the human tissue [56] as well as express many drug-metabolizing enzymes better reflecting the *in vivo* scenario [55], they are also characterized by high variability, due to their origin from various donors and the different isolation methods adopted among different groups, making the standardization of models highly challenging [55]; in addition, they retain the *in vivo* characteristics for short times when cultured in 2D traditional settings, often undergoing de-differentiating processes that could limit the reliability of the data [52,54,55,56]. Interestingly, while the importance of replacing 2D cell culture with 3D structures (with or without an extracellular component) to recapitulate the behavior of the cells closer to the *in vivo* scenario is widely accepted by scientists, the key role of dynamic flow conditions has still not been deciphered, especially when such 3D tissue models are adopted. Indeed, fluid flow resembles the proper feeding of tissue culture, which helps the tissue maintain a healthy state over time if compared to the static conditions [57], but, most importantly, it guarantees the proper diffusion of molecules (i.e., drugs) within the ECM as *in vivo*, thanks to our complex vasculature structure. As also anticipated by the computational model, we have shown that only a residual part of the cisplatin is able to diffuse within the millimetric cancer tissue model cultured *in vitro*, and then to induce the expected cancer cells death. In fact, CFD showed that when a 2D model is adopted, the maximal drug concentration is rapidly reached with an over-estimated kinetic that does not recapitulate the *in vivo* scenario, where cells are not directly exposed to the drug treatment immediately after administration. Conversely, when a 3D static setting is adopted, the maximal percentage of cisplatin reaching cells is massively lower than in 2D models, since the ECM-like matrix limits the drug diffusion within the 3D structure. On the other hand, when the 3D tumor model is cultured in dynamic conditions, the slower and continuous rising of the diffusion up to 95% of the total amount better reproduces the drug delivery across the tissue, with a consequent increase in drug efficacy against the tumor as it happens *in vivo*. Moreover, if the combinatory application of 3D tissue culture and fluid flow represents the necessary path to obtain more predictive preclinical outcomes, another revolutionary step to be considered is the simultaneous culture and drug treatment of multiple organs. From this perspective, we have adopted a multi-compartmentalized OOC to investigate and quantify the dose–response both in the on-target (e.g., cancer) and off-target (e.g., liver) organs, simultaneously. Compared to the static co-culture, the multi-organ OOC configuration allowed us to obtain a lower hepato-toxicity and higher efficacy of cisplatin against cancer cells by using a drug dose of 10  $\mu\text{M}$  determined according to human plasmatic concentration. Surprisingly, these results suggest that multi-organ and dynamic 3D culture are more predictive than the traditional static models, considering the wide use of this chemotherapeutic drug for treating women affected by ovarian cancer [58,59,60,61,62]. Moreover, it is worth discussing the experimental setting that we used in the dynamic multi-organ assay. In fact, liver cells were maintained as a monolayer instead of being cultured in a more complex and reliable model such as ovarian cancer cells. In this way, it was possible to highlight the role of any variable added step-by-step in these experiments (i.e., 3D culture, fluid motion, organ-organ connection). Furthermore,

considering that hepatic cells cultured in 2D are more exposed to cisplatin than SKOV-3 cells, they should be basically more sensitive to the toxic effect of the drug; therefore, it is reasonable to conclude that by the decay of hepato-toxicity in such culture conditions, this experimental platform clearly demonstrates the importance of multi-organ connections in evaluating the systemic effects of chemical compounds.

## 8.6 References

1. Pound, P.; Ritskes-Hoitinga, M. Is it possible to overcome issues of external validity in preclinical animal research? Why most animal models are bound to fail. *J. Transl. Med.* 2018, *16*, 1–8, doi:10.1186/s12967-018-1678-1.
2. Marshall, L.J.; Austin, C.P.; Casey, W.; Fitzpatrick, S.C.; Willett, C. Recommendations toward a human pathway-based approach to disease research. *Drug Discov. Today* 2018, *23*, 1824–1832, doi:10.1016/j.drudis.2018.05.038.
3. Seyhan, A.A. Lost in translation: the valley of death across preclinical and clinical divide – identification of problems and overcoming obstacles. *Transl. Med. Commun.* 2019, *4*, 1–19, doi:10.1186/s41231-019-0050-7.
4. Jones, R.; Wilsdon, J.R. The biomedical bubble: Why UK research and innovation needs a greater diversity of priorities, politics, places and people. 2018.
5. Sun, D.; Gao, W.; Hu, H.; Zhou, S. Why 90% of clinical drug development fails and how to improve it? *Acta Pharm. Sin. B* 2022, *12*, 3049–3062, doi:10.1016/j.apsb.2022.02.002.
6. Mak, I.W.Y.; Evaniew, N.; Ghert, M. Lost in translation: Animal models and clinical trials in cancer treatment. *Am. J. Transl. Res.* 2014, *6*, 114–118.
7. Harrison, R.K. Phase II and phase III failures: 2013–2015. *Nat. Rev. Drug Discov.* 2016, *15*, 817–818, doi:10.1038/nrd.2016.184.
8. Morse, M.A.; Gwin, W.R.; Mitchell, D.A. *Vaccine Therapies for Cancer: Then and Now*; Springer International Publishing, 2021; Vol. 16; ISBN 1152302000.
9. Dowden, H.; Munro, J. Trends in clinical success rates and therapeutic focus. *Nat. Rev. Drug Discov.* 2019, *18*, 495–496, doi:10.1038/d41573-019-00074-z.
10. Chi, L.H.; Burrows, A.D.; Anderson, R.L. Can preclinical drug development help to predict adverse events in clinical trials? *Drug Discov. Today* 2022, *27*, 257–268, doi:10.1016/j.drudis.2021.08.010.
11. Dirnagl, U.; Duda, G.N.; Grainger, D.W.; Reinke, P.; Roubenoff, R. Reproducibility, relevance and reliability as barriers to efficient and credible biomedical technology translation. *Adv. Drug Deliv. Rev.* 2022, *182*, 114118, doi:10.1016/j.addr.2022.114118.
12. Duval, K.; Grover, H.; Han, L.H.; Mou, Y.; Pegoraro, A.F.; Fredberg, J.; Chen, Z. Modeling physiological events in 2D vs. 3D cell culture. *Physiology* 2017, *32*, 266–277, doi:10.1152/physiol.00036.2016.
13. Huh, D.; Hamilton, G.A.; Ingber, D.E. From 3D cell culture to organs-on-chips. *Trends Cell Biol.* 2011, *21*, 745–754.
14. Mermin, N.D. Make mouse studies work. 7–9.
15. Van Norman, G.A. Limitations of Animal Studies for Predicting Toxicity in Clinical Trials: Is it Time to Rethink Our Current Approach? *JACC Basic to Transl. Sci.* 2019, *4*, 845–854, doi:10.1016/j.jacbts.2019.10.008.
16. Hoarau-Véhot, J.; Rafii, A.; Touboul, C.; Pasquier, J. Halfway between 2D and animal models: Are 3D cultures the ideal tool to study cancer-microenvironment interactions? *Int. J. Mol. Sci.* 2018, *19*, doi:10.3390/ijms19010181.
17. Marrella, A.; Varani, G.; Aiello, M.; Vaccari, I.; Vitale, C.; Mojzisek, M.; Degrassi, C.; Scaglione, S. 3D Fluid-Dynamic Ovarian Cancer Model Resembling Systemic Drug Administration for Efficacy Assay. *ALTEX* 2021, *38*, 82–94, doi:10.14573/altex.2003131.
18. Id, A.M.; Fedi, A.; Varani, G.; Vaccari, I.; Id, M.F.; Firpo, G.; Guida, P.; Aceto, N.; Id, S.S. High blood flow shear stress values are associated with circulating tumor cells cluster disaggregation in a multi-channel microfluidic device. 2021, 1–19, doi:10.1371/journal.pone.0245536.
19. Vitale, C.; Fedi, A.; Marrella, A.; Varani, G.; Fato, M.; Scaglione, S. 3D perfusable hydrogel recapitulating the cancer dynamic environment to in vitro investigate metastatic colonization. *Polymers (Basel)*. 2020, *12*, 1–19, doi:10.3390/polym12112467.
20. Marzagalli, M.; Pelizzoni, G.; Fedi, A.; Vitale, C.; Fontana, F.; Bruno, S.; Poggi, A.; Dondero, A.; Aiello, M.; Castriconi, R.; et al. A multi-organ-on-chip to recapitulate the infiltration and the cytotoxic activity of circulating NK cells in 3D matrix-based tumor model. *Front. Bioeng. Biotechnol.* 2022, *10*, 1–15, doi:10.3389/fbioe.2022.945149.
21. Akhtar, A. The Flaws and Human Harms of Animal Experimentation. *Cambridge Q. Healthc. Ethics* 2015, *24*, 407–419, doi:10.1017/S0963180115000079.
22. Junod, S.W.; Beaver, W.T. FDA and Clinical Drug Trials: A Short History. *Quick Guid. to Clin. Trials* 2008, 25–55.
23. Matthews, R.A.J. Medical progress depends on animal models - Doesn't it? *J. R. Soc. Med.* 2008, *101*, 95–98, doi:10.1258/jrsm.2007.070164.
24. Fine, B.; Vunjak-Novakovic, G. Shortcomings of Animal Models and the Rise of Engineered Human Cardiac Tissue. *ACS Biomater. Sci. Eng.* 2017, *3*, 1884–1897, doi:10.1021/acsbomaterials.6b00662.

25. Garner, J.P.; Gaskill, B.N.; Weber, E.M.; Ahloy-Dallaire, J.; Pritchett-Corning, K.R. Introducing Therioepistemology: The study of how knowledge is gained from animal research. *Lab Anim. (NY)*. 2017, *46*, 103–113, doi:10.1038/labani.1224.
26. US, F. Innovation or stagnation: challenge and opportunity on the critical path to new medical products. <http://www.fda.gov/ScienceResearch/SpecialTopics/CriticalPathInitiative/default.htm> 2004.
27. Leenaars, C.H.C.; Kouwenaar, C.; Stafleu, F.R.; Bleich, A.; Ritskes-Hoitinga, M.; De Vries, R.B.M.; Meijboom, F.L.B. Animal to human translation: A systematic scoping review of reported concordance rates. *J. Transl. Med.* 2019, *17*, 1–22, doi:10.1186/s12967-019-1976-2.
28. Kamb, A. What’s wrong with our cancer models? *Nat. Rev. Drug Discov.* 2005, *4*, 161–165, doi:10.1038/nrd1635.
29. Rahbari, M.; Rahlfs, S.; Jortzik, E.; Bogeski, I.; Becker, K. Can animal models of disease reliably inform human studies? *PLoS One* 2017, *12*, doi:10.1371/journal.
30. Ingber, D.E. Human organs-on-chips for disease modelling, drug development and personalized medicine. *Nat. Rev. Genet.* 2022, *23*, 467–491, doi:10.1038/s41576-022-00466-9.
31. Lee, M.J.; Hatton, B.A.; Villavicencio, E.H.; Khanna, P.C.; Friedman, S.D.; Ditzler, S.; Pullar, B.; Robison, K.; White, K.F.; Tunkey, C.; et al. Hedgehog pathway inhibitor saridegib (IPI-926) increases lifespan in a mouse medulloblastoma model. *Proc. Natl. Acad. Sci. U. S. A.* 2012, *109*, 7859–7864, doi:10.1073/pnas.1114718109.
32. Attarwala, H. TGN1412: from discovery to disaster. *J. Young Pharm.* 2010, *2*, 332–336.
33. Perel, P.; Roberts, I.; Sena, E.; Wheble, P.; Briscoe, C.; Sandercock, P.; Macleod, M.; Mignini, L.E.; Jayaram, P.; Khan, K.S. Comparison of treatment effects between animal experiments and clinical trials: Systematic review. *Br. Med. J.* 2007, *334*, 197–200, doi:10.1136/bmj.39048.407928.BE.
34. Hackam, D.G.; Redelmeier, D.A. Translation of research evidence from animals to humans. *Jama* 2006, *296*, 1727–1732.
35. Ahmed, H.M.M.A.M.; Moreira Teixeira, L.S. New Endeavors of (Micro)Tissue Engineering: Cells Tissues Organs on-Chip and Communication Thereof. *Cells Tissues Organs* 2021, doi:10.1159/000516356.
36. Shinha, K.; Nihei, W.; Ono, T.; Nakazato, R.; Kimura, H. A pharmacokinetic-pharmacodynamic model based on multi-organ-on-a-chip for drug-drug interaction studies. *Biomicrofluidics* 2020, *14*, doi:10.1063/5.0011545.
37. Ronaldson-Bouchard, K.; Baldassarri, I.; Tavakol, D.N.; Graney, P.L.; Samaritano, M.; Cimetta, E.; Vunjak-Novakovic, G. Engineering complexity in human tissue models of cancer. *Adv. Drug Deliv. Rev.* 2022, *184*, 114181, doi:10.1016/j.addr.2022.114181.
38. Ko, J.; Park, D.; Lee, S.; Gumuscu, B.; Jeon, N.L. Engineering Organ-on-a-Chip to Accelerate Translational Research. *Micromachines* 2022, *13*, doi:10.3390/mi13081200.
39. Leung, C.M.; de Haan, P.; Ronaldson-Bouchard, K.; Kim, G.A.; Ko, J.; Rho, H.S.; Chen, Z.; Habibovic, P.; Jeon, N.L.; Takayama, S.; et al. A guide to the organ-on-a-chip. *Nat. Rev. Methods Prim.* 2022, *2*, doi:10.1038/s43586-022-00118-6.
40. Esch, E.W.; Bahinski, A.; Huh, D. Organs-on-chips at the frontiers of drug discovery. *Nat. Rev. Drug Discov.* 2015, *14*, 248–260, doi:10.1038/nrd4539.
41. Wikswo, J.P. The relevance and potential roles of microphysiological systems in biology and medicine. *Exp. Biol. Med.* 2014, *239*, 1061–1072, doi:10.1177/1535370214542068.
42. Low, L.A.; Mummery, C.; Berridge, B.R.; Austin, C.P.; Tagle, D.A. Organs-on-chips: into the next decade. *Nat. Rev. Drug Discov.* 2021, *20*, 345–361, doi:10.1038/s41573-020-0079-3.
43. Picollet-D’ahan, N.; Zuchowska, A.; Lemeunier, I.; Le Gac, S. Multiorgan-on-a-Chip: A Systemic Approach To Model and Decipher Inter-Organ Communication. *Trends Biotechnol.* 2021, *39*, 788–810, doi:10.1016/j.tibtech.2020.11.014.
44. Saïding, Q.; Ma, J.; Ke, C.; Cui, W. From “organs on a chip” to “patient on a chip.” *Innov.* 2022, *3*, 100282, doi:10.1016/j.xinn.2022.100282.
45. van Berlo, D.; van de Steeg, E.; Amirabadi, H.E.; Masereeuw, R. The potential of multi-organ-on-chip models for assessment of drug disposition as alternative to animal testing. *Curr. Opin. Toxicol.* 2021, *27*, 8–17, doi:10.1016/j.cotox.2021.05.001.
46. McAleer, C.W.; Long, C.J.; Elbrecht, D.; Sasserath, T.; Bridges, L.R.; Rumsey, J.W.; Martin, C.; Schnepfer, M.; Wang, Y.; Schuler, F.; et al. Multi-organ system for the evaluation of efficacy and off-target toxicity of anticancer therapeutics. *Sci. Transl. Med.* 2019, *11*, doi:10.1126/scitranslmed.aav1386.
47. Zuchowska, A.; Skorupska, S. Multi-organ-on-chip approach in cancer research. *Organs-on-a-Chip* 2022, *4*, 100014, doi:10.1016/j.ooc.2021.100014.
48. Vitale, C.; Marzagalli, M.; Scaglione, S.; Dondero, A.; Bottino, C.; Castriconi, R. Tumor Microenvironment and Hydrogel-Based 3D Cancer Models for In Vitro Testing Immunotherapies. 2022.
49. Ronaldson-Bouchard, K.; Teles, D.; Yeager, K.; Tavakol, D.N.; Zhao, Y.; Chramiec, A.; Tagore, S.; Summers, M.; Stylianou, S.; Tamargo, M.; et al. *A multi-organ chip with matured tissue niches linked by vascular flow*; Springer US, 2022; Vol. 6; ISBN 4155102200882.
50. Panteix, G.; Beaujard, A.; Garbit, F.; Chaduiron-Faye, C.; Guillaumont, M.; Gilly, F.; Baltassat, P.; Bressolle, F. Population pharmacokinetics of cisplatin in patients with advanced ovarian cancer during intraperitoneal hyperthermia chemotherapy. *Anticancer Res.* 2002, *22*, 1329–1336.
51. Cavo, M.; Fato, M.; Peñuela, L.; Beltrame, F.; Raiteri, R.; Scaglione, S. Microenvironment complexity and matrix stiffness regulate breast cancer cell activity in a 3D in vitro model. *Sci. Rep.* 2016, *6*, 1–13, doi:10.1038/srep35367.
52. Moradi, E.; Jalili-firoozinezhad, S.; Solati-hashjin, M. Microfluidic organ-on-a-chip models of human liver tissue. *Acta Biomater.* 2020, *116*, 67–83, doi:10.1016/j.actbio.2020.08.041.

53. Guo, L.; Dial, S.; Shi, L.; Branham, W.; Liu, J.; Fang, J.; Green, B.; Deng, H.; Kaput, J.; Ning, B. Similarities and Differences in the Expression of Drug-Metabolizing Enzymes between Human Hepatic Cell Lines and Primary Human Hepatocytes □. 2011, 39, 528–538, doi:10.1124/dmd.110.035873.
54. Discovery, D.; Spring, K.; Bryant, K.; Shackel, N.A. In Vitro Models of the Liver: Disease Modeling, Drug Discovery and Clinical Applications. 2019, 47–67.
55. Zeilinger, K.; Freyer, N.; Damm, G.; Seehofer, D.; Kno, F. Cell sources for in vitro human liver cell culture models. 2016, 1684–1698, doi:10.1177/1535370216657448.
56. Soldatow, V.Y.; Lecluyse, E.L.; Rusyn, I. In vitro models for liver toxicity testing. 2013, 23–39, doi:10.1039/c2tx20051a.
57. Marrella, A.; Buratti, P.; Markus, J.; Firpo, G.; Pesenti, M.; Landry, T.; Ayehunie, S.; Scaglione, S.; Kandarova, H.; Aiello, M. In vitro demonstration of intestinal absorption mechanisms of different sugars using 3D organotypic tissues in a fluidic device. *ALTEX-Alternatives to Anim. Exp.* 2020, 37, 255–264, doi:10.14573/altex.1908311.
58. Sugarbaker, P.H. Optimizing regional chemotherapy for epithelial ovarian cancer. *J. Obstet. Gynaecol. Res.* 2022, 48, 1306–1317, doi:10.1111/jog.15224.
59. Atkins, C.D.; Piccart, M.J. Randomized intergroup trial of cisplatin-paclitaxel versus cisplatin-cyclophosphamide in women with advanced epithelial ovarian cancer: Three-year results [4] (multiple letters). *J. Natl. Cancer Inst.* 2000, 92, 1446–1447, doi:10.1093/jnci/92.17.1446-a.
60. Xu, J.; Gewirtz, D.A. Is Autophagy Always a Barrier to Cisplatin Therapy? *Biomolecules* 2022, 12, 1–22, doi:10.3390/biom12030463.
61. Song, M.; Cui, M.; Liu, K. Therapeutic strategies to overcome cisplatin resistance in ovarian cancer. *Eur. J. Med. Chem.* 2022, 232, 114205, doi:10.1016/j.ejmech.2022.114205.
62. Kaye, S.B.; Lewis, C.R.; Paul, J.; Soukop, M.; Rankin, E.M.; Cassidy, J.; Davis, J.A.; Reed, N.S.; MacLean, A.; Kennedy, J.H. Randomised study of two doses of cisplatin with cyclophosphamide in epithelial ovarian cancer. *Lancet* 1992, 340, 329–333.

## 8.7 Acknowledgments

This work has been developed in collaboration with: Chiara Vitale, Silvia Scaglione, Marco Massimo Fato.



# **Part III**

## **Section Three**

# Chapter 9

## Conclusions

In conclusion, technologically advanced platforms (e.g., organ-on-chips) where to replicate biological processes in a dynamic environment have been designed and validated for investigating the efficacy and toxicity of therapeutic compounds, by combining *in vitro* and *in silico* approaches.

To realize clinically relevant scenarios, 3D tissue models and fluid dynamic stimulations have been used. Specifically, the human body fluid dynamics was simulated by performing CFD simulations (ensuring optimal flow velocity and shear stress profiles, gas and nutrients gradients and the proper time-dependent drug kinetic profile) and then experimentally applied within fluidic platform, thus integrating the use of cutting-edge technologies with *in silico* analyses establishing more reliable analytical preclinical tools.

Different case studies have been considered.

1. Skin absorption assays have been performed accordingly to the OECD Test Guidelines 428, by comparing two different diffusive chambers (Franz Diffusion Cell and the commercially available MIVO platform) in terms of penetration kinetics of hydrophilic and lipophilic molecules; their capacity to properly resemble physiological fluid flows beneath the skin was computationally and experimentally inspected (Chapter 3).

On the other hand, an extensive research analysis has been performed on the currently available intestinal models confirming that currently available intestinal preclinical models are insufficient in emulating the compounds (chemicals, food etc.) absorption profiles *in vivo* [10], therefore a mathematical model of the intestinal epithelium as novel screening strategy has been developed (Chapter 4).

2. I developed and optimized 3D ECM-like tumor (breast cancer, Chapter 5 and 6, neuroblastoma, Chapter 7, ovarian cancer, Chapter 8) models in terms of cells behavior *in vitro*; then, they were cultured under fluid-dynamic conditions (previously predicted by CFD simulations) through different fluidic platforms that allowed to mimic physiological stimuli and investigate the impact of fluid velocities and fluid-associated forces on tumor cells viability as well as the influence of a systemic multi-organ environment on drug efficacy and toxicity.

Such an approach, the combination of 3D tissue models and fluid-dynamic simulation and stimulations as well as the multi-organ test scenario, demonstrated to be pivotal to physiologically and clinically reproduce the complexity and dynamics of human phenomena (cancer onset, progression and metastasis, drug delivery and absorption) as well as to



develop and validate traditional (i.e. platin-based drugs, caffeine) or novel treatment strategies (NK cells-based immunotherapies).

Indeed, while the FDA is pushing the adoption of new alternative methods for regulatory use that can replace, reduce, and refine animal testing and improve the predictivity of non-clinical testing (FDA Modernization Act 2.0), the novel in vitro tools validated in this thesis represent an important bridge towards the implementation of 3R regulations a toxicity and efficacy assays. In this context, the technological advancements gained combining in vitro and in silico preclinical approaches, particularly employing CFD simulation and OOCs, made possible to test therapies in a more predictive ways and drastically reduce the use of animals, and thus costs and time.

If the integration of 3D biology-inspired matrixes with fluidical stimuli resembling bloodstream circulation is necessary to develop a predictive pre-clinical platform that more closely reproduces what happens during therapy, as demonstrated in this thesis, also it has been evaluated that a single-organ approach is not sufficient to determine the effective response to the drug treatment, both in terms of efficacy and toxicity.

Further studies on multi-organ clinically relevant-sized OOCs might lead to a boost in the development of personalized therapies, in which toxicity and efficacy could be tested in vitro in a highly robust, reproducible, and reliable manner. Moreover, such a MOOCs-based experimental setup will also have a strong impact on basic research, improving the understanding of biological mechanisms behind systemic diseases.



# Chapter 10

## PhD Achievements

### 10.1 List of publications

International peer-reviewed papers

1. C. Vitale\*, **A. Fedi\***, A. Marrella, G. Varani, M. Fato, S. Scaglione, 3D perfusable hydrogel recapitulating the cancer dynamic environment to in vitro investigate metastatic colonization, *Polymers*, 2020.
2. A. Marrella\*, **A. Fedi\***, G. Varani, I. Vaccari, M. Fato, G. Firpo, P. Guida, N. Aceto, S. Scaglione, High blood flow shear stress values are associated with circulating tumor cells cluster disaggregation in a multi-channel microfluidic device, *PlosOne*, 2021.
3. **A. Fedi\***, C. Vitale\*, G. Ponschin, S. Ayehunie, M. Fato, S. Scaglione, In vitro models replicating the human intestinal epithelium for absorption and metabolism studies: A systematic review, *Journal of Controlled Release*, 2021.
4. **A. Fedi \***, C. Vitale \*, P. Giannoni, G. Caluori, A. Marrella, Biosensors to Monitor Cell Activity in 3D Hydrogel-Based Tissue Models, *Sensors*, 2022.
5. I. Pulsoni, M. Lubda, M. Aiello, **A. Fedi**, M. Marzagalli, J. von Hagen, S. Scaglione, Comparison Between Franz Diffusion Cell and a novel Micro-physiological System for In Vitro Penetration Assay Using Different Skin Models, *SLAS Technology*, 2022.
6. M. Marzagalli, G. Pelizzoni, **A. Fedi**, C. Vitale, F. Fontana, S. Bruno, A. Poggi, A. Dondero. M. Aiello, R. Castriconi, C. Bottino. S. Scaglione, A multi-organ-on-chip to recapitulate the infiltration and the cytotoxic activity of circulating NK cells in 3D matrix-based tumor model, *Frontiers in Bioengineering and Biotechnology*, 2022.
7. **A. Fedi\***, C. Vitale\*, M. Fato, S. Scaglione, A Human Ovarian Tumor & Liver Organ-on-Chip for Simultaneous and More Predictive Toxo-Efficacy Assays, *Bioengineering*, 2023.

### 10.2 Participation to National and International Conferences

- **GNB2020, VII congress of the National Group of Bioengineering 2020**, Trieste, paper titled “A hydrogel channel-based system to model the blood flow dynamic stimuli” accepted and published by Pàtron editor.
- **TERMIS-EU 2020**, Manchester (postponed to 2023), abstract titled “A 3D fluid-dynamic cancer model to resemble the in vivo drug administration as a new platform for drug testing”
- **SLAS Europe 2022 Conference and Exhibition**, Dublin, poster presentation “A novel multi-organ model for performing more reliable preclinical toxo-efficacy assays”.
- **Micro Physiological System World Summit 2023**, New Orleans, poster presentation “A novel multi-organ in vitro model for combined and more predictive toxo-efficacy assays”.

### **10.3 Collaboration to funded projects**

As CNR research fellow during my PhD I collaborated to the European FET-OPEN project B2B (from Breast To Bone) (2018-2022); I was involved in the design and realization of a multi-chamber bioreactor to study the metastatic process starting from a breast organoid to a bone tissue (CAD design, 3D printing, and CFD simulations).

This activity was carried out in collaboration with the biotech company React4Life s.r.l.